GREEN AND SUSTAINABLE SYNTHESIS OF SILVER NANOWIRES USING BATCH AND MILLIFLUIDIC PROCESSES AND THEIR APPLICATIONS IN CONDUCTIVE INKS

By

SINA KAABIPOUR

Bachelor of Science in Chemical Engineering
Shiraz University
Shiraz, Iran
2015

Master of Science in Chemical Engineering
Lamar University
Beaumont, TX
2018

Submitted to the Faculty of the
Graduate College of the
Oklahoma State University
in partial fulfillment of
the requirements for
the Degree of
DOCTOR OF PHILOSOPHY
May, 2023

GREEN AND SUSTAINABLE SYNTHESIS OF SILVER NANOWIRES USING BATCH AND MILLIFLUIDIC PROCESSES AND THEIR APPLICATIONS IN CONDUCTIVE INKS

Dissertation Approved:

Dr. Shohreh Hemmati

Dissertation Adviser

Dr. Josh Ramsey

Dr. James Smay

Dr. Toby Nelson

Name: SINA KAABIPOUR

Date of Degree: MAY, 2023

Title of Study: GREEN AND SUSTAINABLE SYNTHESIS OF SILVER NANOWIRES USING BATCH AND MILLIFLUIDIC PROCESSES AND THEIR APPLICATIONS IN CONDUCTIVE INKS

Major Field: CHEMICAL ENGINEERING

Abstract: This dissertation focuses on the solution-based synthesis of one-dimensional (1D) silver nanostructures (mainly silver nanowires) using green, sustainable, and cost-efficient materials and processes, and application of 1D silver nanostructures in conductive inks formation for printed circuit boards (PCBs) application. Conventional chemical and physical processes used for the synthesis of metallic nanostructures, in general, suffer from hazardous waste production, usage of unsustainable reagents, high energy consumption, and high production cost. However, recent research proves that plant-based products such as polyphenols can serve as proper alternatives (as the reducing/capping/stabilizing agents) to produce nanostructures with different sizes and morphologies, if the process parameters are controlled properly. In such processes, hazardous waste production can be significantly limited if not eliminated, and energy consumption can be minimized. This research firstly investigates the synthesis of silver nanostructures with different sizes and morphologies by sustainable and environmentally-friendly—aka. "green"—reagents (reducing/capping agents), and discusses possibilities for the green synthesis of 1D silver nanostructures, such as silver nanowires (AgNWs). Afterward, a novel procedure for the synthesis of AgNWs, with moderate yield (~50%), using tannic acid in a batch process is introduced. Then, the effect of different parameters such as pH, silver precursor/reducing agent concentration ratio, light, and stirring rate on the yield of silver nanowires, and the size and morphology of silver nanostructures, was investigated. The synthesis procedure is then tried in a continuous millifluidic reactor to increase the yield of silver nanowires by ~32%. The millifluidic process can improve mass and heat transfer, thanks to its miniaturized environment, and a more consistent control over the size and morphology of nanostructures. The silver nanowires synthesized using tannic acid were then used for conductive ink preparation. The rheological behavior of the conductive ink was investigated, which provides valuable information about the flow of the ink and its behavior during screen printing and direct writing. It was demonstrated that the direct writing method can be a simple and efficient procedure to print silver nanowire-based conductive ink. The environmentally-friendly, sustainable, and inexpensive synthesis of AgNWs, and the direct-write printing process, can significantly reduce the production cost of silver nanowire-based PCBs.

TABLE OF CONTENTS

Chapter Page

Chapter Page

Chapter Page

LIST OF TABLES

Table Page

LIST OF FIGURES

Figure Page

Figure Page

Figure Page

Figure Page

.

CHAPTER I

PREFACE

With nanotechnology being at the forefront of novel science and interdisciplinary areas including materials science, engineering, and chemistry, the synthesis/production process of nanomaterials from raw materials is a crucial aspect to be considered. Despite noticeable advancements in the field of nanomaterials science, there are still many issues and challenges that need to be addressed fundamentally as the field itself is still in its infancy, and there is substantial room for development. I, as a researcher in this field focusing on silver nanostructures synthesis, have attempted to address some of the considerable challenges by offering improved methods that are scalable, simpler, more cost-efficient, and more sustainable compared to conventional methods. I will discuss each of the challenges in detail, and propose the proper tools and methods to address such challenges in each chapter. This dissertation includes 6 chapters considering the "PREFACE" (Chapter I) and "CONCLUSION" (Chapter VI) chapters. Chapters II[1] ,III[2], and IV[3] are published articles in peer-reviewed journals. The second chapter is a published work in the Beilstein Journal of Nanotechnology, and third and fourth chapter are published in Colloids and Surfaces A: Physiochemical and Engineering Aspects.

One of the major challenges in the area of nanomaterials synthesis, especially in the industrial sector, is the lack of a sustainable and environmentally-friendly production/development processes.

Most nanomaterial-producing processes, in the case of solution-based synthesis, use unsustainable materials (i.e. reagents), that are commonly derived from fossil-fuel products. In addition, many of such reagents are harmful to the environment, and therefore handling their waste after the synthesis process is a credible challenge. Another challenge is energy consumption per process, which can increase energy costs for large-scale industrial production.

Another challenge is a weak atom economy. Atom economy is considered as the capability of a chemical reaction to convert the reactant atoms into products, without resulting in unwanted byproducts. If the reaction is efficient and produces minimal waste, it has high atom economy. These challenges can be overcome by using sustainable, renewable, and natural products in the synthesis process of nanomaterials such as metal nanostructures. The second chapter in this dissertation discusses this matter in detail and offers sustainable alternatives that can be easily developed, especially for the synthesis of silver nanostructures.

Despite all the advantages of sustainable process development in metal nanostructure synthesis, a common challenge is the lack of control over the size and morphology of synthesized nanostructures, which occurs due to the complexity of sustainable and renewable (i.e. plant-based) products. The third chapter offers a novel “batch synthesis” method for the synthesis of silver nanowires (AgNWs) in an environmentally-friendly, sustainable, and an inexpensive manner. This method is carried out by using tannic acid, a natural, plant-based, and renewable reducing agent, that is inexpensive and imposes no hazards to the environment. It is also demonstrated that tannic acid can be used as both the reducing and capping agents simultaneously, and how different parameters can be tuned to increase the yield of silver nanowires (portion of nanostructures with nanowire morphology with respect to other morphologies).

A major challenge that can arise from “batch synthesis” methods, including the one discussed in the third chapter, is the lack of proper mixing due to large diffusion periods, which can lead to

nanostructures with non-uniform morphologies and wide size distribution. The lack of mixing may be compensated in a more miniaturized environment (such as in a milli/micrometer-size fluidic channel), where mass and heat transfer are more efficient. The fourth chapter in this dissertation offers a process for the production of AgNWs using tannic acid by using a helically-coiled millifluidic reactor. It is demonstrated that the millifluidic reactor, thanks to its more efficient mass and heat transfer, can provide better mixing and increase the yield of AgNWs in the process.

Finally, the application of sustainably-synthesized AgNWs in printable conductive inks are investigated in chapter 5. Printable silver nanowire-based conductive inks are useful for manufacturing wearable electronics. A crucial aspect of such conductive inks is their rheological behavior, and how they behave under different shear stresses in various printing processes. This behavior determines the consistency of the printed patterns, and whether they can meet the desired standard based on the application. The fifth chapter investigates this rheological behavior for common printing processes such as screen printing and direct writing.

The sustainable, environmentally-friendly, inexpensive, and material-efficient synthesis of AgNWs can facilitate their scale-up for industrial manufacturing as well as their applications in different areas including but not limited to transparent conductive films and wearable electronics. The proposed millifluidic reactor can also be used for the synthesis of other metal nanostructures as well as other type of nanomaterials such as protein polymer nanoparticles as I illustrated that in one of my published studies in the European Journal of Pharmaceutics and Biopharmaceutics[4].

CHAPTER II

GREEN AND SUSTAINABLE SYNTHESIS of SILVER NANOPARTICLES AND ONE-DIMENSIONAL SILVER NANOSTRUCTURES: PREFERENCES, METHODOLOGIES, POTENTIALS, AND OUTLOOK

2.1. Introduction

Nanotechnology has been immensely practiced in almost every scientific discipline. Nanomaterials have been utilized in innumerable applications due to their unique characteristics. Novel successful applications of nanomaterials and nanostructures can be seen in drug delivery [5–10], nanomedicine [11–14], food packaging [15–17], aseptic procedures [18–20], correlative microscopy [21], imaging [22–26], optics [27,28], microelectronics [29–31], three dimensional (3D) printing [31–35], renewable energy [36–40], wastewater remediation [41,42], and catalysis [43–47] to name a few. Currently, the success of nanotechnology has been proved and the promising outcomes cannot be overlooked; however, the main principles behind the production of nanomaterials are yet to be examined more closely in terms of economy as well as effects on health and environment.

Among metal nanostructures, silver nanostructures have demonstrated promising potential in many applications and have contributed significantly to the advancement of nanoscience. The concept of using silver is not unprecedented; silver was used broadly by many nations and

dynasties throughout ancient history. The early applications of silver are dated back to 4000 B.C.E, by the Caldeans [48], and throughout ancient history, Persians, Romans, Egyptians, and Greeks utilized silver for food storage purposes [49]. Silver was also extensively used in utensils for eating and drinking, most probably due to the antimicrobial activities of silver which were discovered by experience during ancient centuries [49]. Later on, there were further instances where silver was used for medical purposes. For instance, Avi-Cenna applied silver filings for blood purification and to inhibit heart palpitations [48]. Silver was used in forms of aquatic solutions, coins, and plates for aseptic and antibacterial applications, as well as in food and dairy preservation up until the 19th century, as it was agreed that food and dairy products kept in silver containers lasted longer than those in other types of containers [48]. Since then, silver has been and is still in use continuously in accordance with the old traditions even today. Although silver has proved its potentials and advantages, the functions by which it had become so beneficial were not well understood in the past. Nanotechnology has emerged as a means to delve further into the usefulness of this precious element.

Silver nanostructures can be categorized based on their shape and morphology. Different shapes and morphologies of silver nanostructures have been synthesized, including cubes [50,51], spheres [52–54], triangles [55–57], prisms [58,59], sheets [60–62], disks [63,64], rods [65,66], bars [67,68], and wires [69–72].

Silver nanostructures have been receiving significant attention in the last decades due to their improved properties compared to bulk silver and their unique intrinsic characteristics including antimicrobial activity, electrical conductivity, thermal conductivity, optical characteristics, and mechanical properties. The antimicrobial characteristic of silver nanoparticles (AgNPs) has made them highly applicable in the biomedical and therapeutic fields [73–75]. Currently, antimicrobial AgNPs can potentially act as alternatives for current antibiotics due to increased bacterial resistance [75]. In addition, the development of new generations of antibiotics is costly, which prevents pharmaceutical companies from manufacturing new classes of antibiotics [76,77].

Furthermore, the physicochemical characteristics of AgNPs can be tuned in a way to avoid cellular toxicity [75,78,79], which facilitates their biomedical applications. The small size of AgNPs (<100 nm) allows them to accumulate on the extracellular membrane of the bacteria and penetrate inside, which alters the membrane permeability and leads to bacterial death [75,80]. Another therapeutic approach lies in the bactericidal activity of functionalized silver nanoparticles coated on surfaces. This method is applicable in developing aseptic catheters to prevent catheter-related infections such as urinary tract and venous infections, and also inhibit the growth of bacterial biofilms [18–20].

AgNPs were also used in developing strong thermally conductive materials. They were used in polymer composites to increase thermal conductivity (K) [81,82] for cooling applications in electronic equipment. Furthermore, AgNPs have demonstrated unique electrical properties. AgNPs coated on polycarbonate substrates were previously used to increase the electrical conductivity of polycarbonate composites [83]. AgNPs have also demonstrated minimum or no adverse effects on mechanical strength when embedded in polymeric materials or composites [84–86]. For instance, the utilization of AgNPs in bone cement is meant to prevent bacterial infection while sustaining the mechanical strength of the cement connected to the prosthesis [86]. AgNPs have also demonstrated significant optical properties. They possess substantial characteristics of surface plasmon resonance (SPR) and generally have a broad absorption spectrum [87]. This enables applications in optoelectronics and surface-enhanced Raman scattering [88,89]. AgNPs were also applied effectively in solar cell matrices [36,90,91]. AgNPs can enhance the current density in solar cells due to their far-field effect and localized surface plasmon resonance (LSPR) [36].

There are several applications in which use of 1D silver nanostructures such as nanowires (NWs) and nanorods (NRs) (at the same concentration) are preferred to other nanostructures due to stronger conductivity. For instance, the 1D silver nanostructures can provide desired electrical characteristics in conductive adhesives at lower concentrations compared to other silver

nanostructures and micron-sized ones [92]. The research being conducted on the synthesis of silver nanowires (AgNWs) is currently gaining a lot of attention due to their promising applications in electronics. This happens to be a result of outstanding electrical, optical, and mechanical properties of AgNWs. 1D silver nanostructures, such as AgNWs are more advantageous compared to other silver nanostructures due to several reasons. They can enable free movement of electrons in one direction [93], and can form networks of wires that facilitate the passage of electrical current. They can also improve transmittance characteristics due to their high aspect ratio [94]. The novel applications can be seen in transparent conductive films (TCFs) [95], wireless technology [96,97], touchscreen devices [98], organic light emitting diodes (OLED) [99], transparent conductive electrodes [100,101], artificial skin [102], liquid crystal display (LCD) [103,104], and smart windows [105,106]. AgNWs can be embedded in flexible touch-screen substrates and electronic displays to provide an enhanced decrease in sheet resistance and to increase touch sensitivity [93]. Furthermore, AgNWs can be used to prepare AgNW-based conductive inks that have remarkable rheological characteristics such as thixotropic shear thinning and thus, can be simply used for screen printing without the addition of polymeric rheological additives [107]. AgNW-coated conductive films have been considered as a promising alternative over conventional indium tin oxide (ITO)-coated conductive films which are currently being used in touchscreens [93].

The synthesis of silver nanostructures, and generally all types of nanostructures, are categorized in two approaches [108]. The first one is the top-down approach where particles are produced from the bulk material, and the second one is the bottom-up approach where nucleation sites are formed and finally grow into a nano-sized particle. The first approach consists of a set of techniques also known as “physical” synthesis methods. Several physical methods for top-down synthesis of silver nanostructures including ball milling [109–111], laser ablation [112–116], evaporation-condensation [117,118], electromagnetic levitation gas condensation (ELGC) [119], ultrasonication [120–123], lithography [124,125], spray pyrolysis [126–128], radiolysis [129–132], arc discharge [133–137], and

photoirradiation [138–140] have been utilized to synthesize various morphologies of silver nanostructures with varied size and size distribution. The physical synthesis method is primarily used for large-scale production in a short amount of time [141].

The bottom-up approach, however, mostly relies on the use of reducing agents for the production of silver nanoparticles. This approach is also categorized into two distinguishable, but not completely disparate, set of methods. The first category consists of techniques that use chemical reagents to reduce Ag cations into zero-charged Ag atoms, which then mount on top of the nuclei, serving as templates for crystal growth into particles at the nanoscale [142,143]. This set of techniques is also known as the "chemical" synthesis method. These techniques are usually accompanied by the addition of stabilizers to provide stability, prevent aggregation, control morphology, and provide physiologically-compatible properties [144–146]. Chemical methods were previously used to produce silver nanoparticles including sol-gel processes [147–150], conventional chemical reduction [151–155], reverse micelle [156–158], co-precipitation [159], chemical vapor deposition [160–162], solvothermal [163–165], and electrochemical reduction [166–169]. Chemical synthesis methods are currently among the most widely used approaches [108,170]. The second category in bottom-up synthesis methods consists of a set of techniques that incorporate the use of non-chemical reagents for the synthesis of silver nanostructures. Those techniques rely on the use of biological agents or bio-extracted compounds. The term used for addressing these methods is also referred to as "biological" synthesis. Previous studies have used bacteria [171–174], fungi [175–178], viruses [179,180], yeasts [181–183], plants [184–187] and plant extracts [170,188–192], microalgae [193–197], enzymes [198–200], saccharides [201–205], and vitamins [206–208] to synthesize Ag nanostructures with controlled size and morphology. These methods can also be referred to as a subcategorization of "green" synthesis.

Numerous works in the literature have focused on synthesis of AgNPs without giving much attention to the disadvantages such as cost, time, and hazards. Nevertheless, other essential factors such as cost-effectiveness, eco-friendliness, energy consumption, and human well-being

can easily be overlooked. For instance, hydrazine, as a strong and common reductant [209–211] for the synthesis of AgNPs [153,212–215] is a highly toxic, cancerous, and lethal chemical [209]. Although some works have incorporated green synthesis techniques [115,116,139,168,216,217], they do not completely eliminate the need for chemicals, nor do they rule out high energy consumption in physical synthesis methods, thereby increasing costs greatly [141,218].

Due to the disadvantages of physical and chemical methods, the focus has been directed towards the use of facile methods and materials that are less detrimental and more cost-effective. A common subject of interest in this area has been the selection of naturally occurring processes, widely known as "green" processes. However, green synthesis of silver nanostructures is a general term defined as the production of silver nanostructures by using environmentally-friendly techniques. Therefore, this method is not limited to synthesis by biological agents. For instance, alternative reagents such as ascorbic acid and sodium citrate are considered to synthesize AgNPs in a green and environmentally-friendly manner [219]. The green synthesis of silver nanostructures has been receiving significant attention and is expected to rule out the use of hazardous chemical substances to a great extent [49,220–222], and also to disregard the use of high-energy consuming devices for the top-down synthesis of silver nanostructures [108,189]. Green synthesis of silver nanostructures has demonstrated great advances in the last decade, yet there are still issues regarding stability, size distribution, morphology, unknown biological functions[144], and the consideration that some biological processes cannot become industrially feasible due to strict and time-consuming aseptic procedures [189].

In this review, we first aim to discuss the most common AgNP synthesis methodologies and to compare them based on their cost, eco-friendliness, and energy consumption to show why and how green chemistry can improve the process and act as an alternative compared to physical and chemical synthesis. The physical and chemical synthesis methods are discussed only in terms of the process structure, advantages, and disadvantages. Therefore, a detailed study of physical and

chemical methods for the synthesis of AgNPs is out of the scope of this review. Among the green synthesis procedures, significant attention has been recently given to plant-mediated synthesis because of its simple culturing procedures and potential for scale-up [185,223]. Various green synthesis studies from the literature were gathered and compared, giving one a clear and broad overview of the green synthesis processes. We then show how plant-mediated synthesis can emerge as a novel and alternative methodology towards the synthesis of 1D silver nanostructures, which have several applications in electronics. Finally, novel future directions including application of *in-situ* characterization techniques in the course of reaction, continuous green and sustainable synthesis of silver nanostructures adaptable for *in-situ* characterization, and incorporation of Artificial Intelligence (AI) in green silver nanostructures synthesis are discussed.

2.2. Physical and chemical synthesis methodologies of silver nanoparticles

In this section, chemical and physical synthesis methodologies of silver nanostructures have been reviewed and their advantages and disadvantages have been discussed. This section is reviewed to provide a comparison between chemical/physical synthesis and green synthesis of silver nanostructures. Since the main focus of this article is on reviewing the green synthesis of silver nanostructures as an alternative over chemical and physical methods, only the most common physical and chemical methods have been reviewed and the major part of our review has been dedicated to green synthesis of silver nanostructures.

2.2.1. Physical synthesis

Physical synthesis of silver nanoparticles includes methods that produce particles in the dimensions of 1-100 nm from bulk silver, typically in the solid phase. It is also referred to as the top-down synthesis of silver nanoparticles. Unlike chemical and biological methods, physical techniques do not necessarily require using a reducing agent or stabilizer; however, they may be incorporated with other techniques.

2.2.1.1. Ball milling process

As one of the conventional processes, the ball milling process (mostly used as mechanochemical ball milling) is a method that is used commonly to produce AgNPs in a solid state [224]. Previously, AgNPs were produced using high energy planetary ball milling [109,110,225]. Khayati et al. [109] utilized planetary ball milling in a mechanochemical process by adding organic process control agents (PCA). In this work, depending on the type of PCA used, particle sizes varied from 14 to 34 nm, and were in crystallite shape. In another work, AgNP crystallites were produced with an average size of 10-12 nm using the mechanochemical ball milling process by utilizing polyethylene glycol as the stabilizing agent [111]. The relatively small size of the produced AgNPs allowed effective antibacterial activity against gram-positive and gram-negative bacteria. The ball milling method is a cheap approach for the synthesis of AgNPs in a solid state[144], and can be used for the synthesis of AgNPs in ambient temperature, with a fair control over particle size [111]. It is a useful technique and synthesized nanoparticles may be used for antimicrobial applications [111]; however, there are several downsides with this method. The most common approach, provided by the literature, for the synthesis of NPs—especially AgNPs—is by laboratory-based planetary ball milling, which is insignificant for large-scale production [226]. In addition, the milling process itself may result in creation of agglomerated products, especially in long processes, due to the large specific surface area of the produced NPs [226,227]. Furthermore, this technique is associated with substantial energy consumption—considering the milling period—compared to alternative methods [226].

2.2.1.2. Evaporation-condensation process

Evaporation-condensation is another conventional method used for the synthesis of AgNPs. This technique is applied by using a furnace processing chamber where the metal of interest is vaporized into a low-density gas phase, becomes supersaturated by decreasing temperature, and

then is condensed to form nuclei which then grows into nanoparticles [117,141]. The chamber gas usually contains an inert gas such as Helium or Argon [117,228]. AgNPs synthesized using this technique were in crystalline shape with sizes from 7 to 55 nm [117,228]. One of the advantages of this method is that it can potentially produce NPs in large-scale [141], and can be used for long-term experiments [108,229]; however, there are significant disadvantages while using this technique. The required equipment is rigorous, highly costly, and occupies a significantly large space [108,141,218]. Furthermore, due to high operation temperature, a significant preheating time is required, and the process needs considerable time to achieve thermal stability [218,229]. There are also safety issues due to the high processing temperature which will elevate the surrounding environment temperature [141,230]. Additionally, the process consumes high degrees of energy[218,229] due to very high operating temperatures; thus, making it uneconomical.

2.2.1.3. Arc discharge process

Another physical method widely used for the synthesis of AgNPs is the arc discharge method. In this method, two electrodes—a cathode and an anode—are connected in a high current DC circuit and submerged in a solvent—mostly deionized water—to run the process [133,135]. These electrodes can be either composed of an inert metal, such as titanium, or any metal of interest by which the nanoparticles will be produced, for instance, silver for the synthesis of AgNPs [133,135]. In the case of titanium electrodes, $AgNO_3$ is used as the precursor, an electric discharge takes place between cathode and anode, and an electron exchange takes place in the plasma region where silver ions are reduced [133]. In the case of silver electrodes, silver will be melted and vaporized from the electrode ends, and as a result, nanoparticles are formed from the silver condensates [135]. Tien et al. [231] synthesized AgNPs from 5 to 45 nm using the same method. In more recent works by Tseng et al. [136,137], AgNPs were produced using a micro-electrical discharge machining system and by adding polyvinyl alcohol (PVA) as the capping agent. They obtained AgNPs with a diameter of 50-100 nm when PVA was not used, and a diameter in the range of 25-75 nm when

PVA was used [136]. The arc discharge method is advantageous in terms of the simplicity of the apparatus and equipment, low impurity due to the mere use of water, and fewer production steps [133]. In addition, this process can reach high NPs synthesis rates in a short time [133,135]. However, size distribution is large [133,136,137], and NPs produced have a fairly large size distribution compared to NPs produced by chemical methods.

2.2.1.4. Laser Ablation Process

A promising physical synthesis method used widely in recent years is laser ablation. This method is typically used for the synthesis of stable silver colloids either in solutions or in open air without utilizing any additional reagents [112,116]. AgNPs synthesized with this method are maintained in high purity due to the inexistence of chemical stabilizers and ligands, which provide NPs with unique surface characteristics [232]. Therefore, for safe biological implications (i.e in the medical and food industry), this approach can be preferred as an alternative for methods that necessarily require the use of chemical stabilizers [112,116]. In addition, small NP size, low agglomeration rate, and narrow size distribution can be achieved by this method [112]. The process uses a laser beam at high energy to ablate pure Ag from which the separated AgNPs, either in liquid or vapor form, are attained and confined in the surrounding ambient [113]. The formation of nanoparticles by laser ablation depends on the thermal and optical properties of the utilized metal and the surrounding ambient [232,233]. Despite its significant advantages, laser ablation represents some disadvantages that limit their use. In general, this method does not have high productivity and the utilization of laser ablation at an industrial scale is difficult. To achieve desired concentrations, high-energy lasers should be considered, which increase the costs significantly [116].

2.2.1.5. Spray pyrolysis process

Spray pyrolysis is another method used earlier to produce AgNPs with an average size of 10 nm embedded into amorphous calcium phosphate particles for enhanced adhesive applications [128].

The spray pyrolysis process requires using an atomizer, a tube furnace, a reaction tube, a collection filter, and a vacuum pump [128]. This method is also highly used for production of metal powders, and demonstrates less agglomeration, higher purity, and more crystallinity compared to those produced by chemical methods [234]. The method is simple and reproducible [234]; however, the process runs using high operating temperatures, and more specifically, the center of the reaction tube may not reach the setpoint temperature due to the short residence time inside the reactor and finite heat transfer from the wall [128].

In general, although physical methods can produce nanoparticles with high purity, most of them are highly expensive and may lead to agglomeration of products [144]. Based on all the disadvantages explained, the mere use of physical methods may not be adequate for most cases to produce AgNPs with desired size, morphology, size distribution, and characteristics. Moreover, most physical approaches should be accompanied with chemical or green methodologies to compensate for deficiencies.

2.2.2. Chemical synthesis

Chemical reduction, or conventional chemical synthesis, is the most common approach for the synthesis of AgNPs [218]. This is performed by the presence of a metal precursor such as $AgNO_3$, a reducing agent such as hydrazine, sodium borohydride, ethylene glycol, or dimethylformamide (DMF) as well as the presence of stabilizers such as polyvinylpyrrolidone (PVP) or polyvinylalcohol (PVA). Chemical synthesis of nanoparticles is one of the bottom-up techniques due to the fact that particles are formed from collective atoms in a nucleus rather than from the bulk [108].

2.2.2.1. Sol-gel process

The sol-gel method is one of the most common techniques to synthesize AgNPs. The sol-gel process is considered as a multifaceted approach for the synthesis of nanoparticles in various forms—especially complex compounds—such as metal-complex oxides, inorganic nanocomposites, and chalcogenides [148]. In the sol-gel method, a gel-like mixture is first prepared by mixing the silver precursor solution with a metal complex compound (i.e comprised of Ca, Ti, Sr, etc.) [147,148] in a solvent such as water or alcohol. Then the product is heated in order for the nucleation and reaction to take place [147,235]. In most cases, AgNPs are synthesized in metal oxide thin films such as TiO_2, SiO_2, and ZrO_2 where the average particle size is almost 10 nm when the heating temperature is 600 °C in the case of SiO_2 thin films, and 500 °C in the case of TiO_2 and ZrO_2 [235]. Kumar et al. [149] synthesized AgNPs using the hydrolytic sol-gel method at 400, 600, and 800 °C with particles with an average size of 20 nm and crystallite shape. The sol-gel technique can also be performed at lower temperatures as well. Jadalannagari et al. [147] synthesized silver doped hydroxyapatite nanorods using the sol-gel technique at 100 °C and produced particles with an average diameter of 25 nm with hexagonal cross section. In the sol-gel process, besides temperature and gel composition, the solvent plays an important role in determining the size, morphology, and surface characteristics of the synthesized AgNPs [236]. Organic solvents are generally more advantageous, as they can act as an oxygen supplying agent for the metal oxide and result in more uniform structures and smaller size distribution [236]. One important advantage of the sol-gel technique is the large freedom for choosing different precursors with various combinations (i.e. hybrid compounds), allowing the process to be adjusted accordingly in order to yield the desired complex product with tuned physiochemical characteristics [150]. In addition, combined with the hydrothermal approach (synthesis in a hot aqueous environment under high pressure), it can synthesize AgNPs at a lower temperature compared to the sol-gel process alone [148]. Nevertheless, there are some disadvantages regarding the application and feasibility of sol-

gel-produced nanoparticles and nanocomposites. For instance, in industrial applications of nanoparticle-doped glasses such as those in the automotive industry, there exists some difficulty in the production of thick films larger than 1 μm because of possible film cracks and shrinkage [237]. In addition to that, the film quality itself depends highly on process and environmental conditions such as temperature and humidity [237]. The sol-gel process is associated with costly precursors, process longevity, and difficulties regarding reproducibility [238].

2.2.2.2. Reverse-micelle process

Reverse micelle is another approach for synthesis of AgNPs. Reverse micelles are produced from surfactants such as sucrose fatty acids in a hydrophobic solvent such as alkanes [239]. There is a water phase inside the microemulsions which is also referred to as the water pool where the reactants are present [239]. The water pool is where the silver ions are reduced into silver atoms which then form AgNPs [156]. The reverse micelle method has served as a common approach for the synthesis of AgNPs throughout the past two decades [156]. Regular reducing agents used in this method include sodium borohydride ($NaBH_4$) [240], hydrazine (N_2H_4) [241], glucose [242], and quercetin [156,243], to name a few. The size and size distribution of the AgNPs is controlled by the strength of the reducing agent [156]. It was previously observed that hydrazine hydrate ($N_2H_4.H_2O$) can yield smaller AgNPs with a higher degree of dispersion compared to stronger reductants such as sodium borohydride ($NaBH_4$) [244]. Singha et al.[156] synthesized AgNPs in sodium dioctyl sulfosuccinate (AOT) reverse micelles using ascorbic acid as the reductant, and obtained particles with an average size of 6 nm. Yang et al. [158] used sodium borohydride as the reductant and octadecylamine (ODA) as the solvent and produced AgNPs with an average size of 3.38 nm. The size distribution of the synthesized nanoparticles depends on the type of solvent as well as the reducing agent. This enables the method to provide varied choices depending on the type of surfactant and solvent, which can be optimized to yield the desired size and morphology[156]. In addition, preparation of AgNPs using this method does not need any specific instrument, intense

temperature, or pressure conditions [239]. The scale-up of the system is also relatively simple[239]. However, the downside of this method is due to the low productivity of particles per system volume as a result of low reactant concentration inside the reverse micelles [239]. AOT-microemulsions have been the most common microemulsions for the preparation of micelles [156]. However, this method may result in synthesis of AgNPs with weak surface plasmon characteristics due to broad surface plasmon band [156].

2.2.2.3. Chemical vapor deposition process

Chemical vapor deposition (CVD) and atomic layer deposition (ALD) are among other chemical methods. CVD is a method that allows production of nanoparticles on a substrate [245]. The process consists of three steps. First, addition of a volatile precursor in the gas phase to the reactor chamber. Second, adsorption of the vapor on the substrate surface and establishment of medium compounds followed by formation of a layer. Third, nucleation and growth of the layer through heating [245]. The important factors that control the process and size of synthesized AgNPs include the precursor introduction method, reactor pressure, gas flow properties, deposition rate, deposition duration, and substrate surface temperature [161,245]. The type of precursor appears to be the most significant factor in the process [245]. Silver nitrate is the most widely used precursor for this purpose [245]. An important advantage of this technique is the establishment of silver-metal oxide (e.g SiO_2 or TiO_2) nanocomposite coating using only one deposition step [245]. The CVD method also provides many opportunities for the synthesis of silver-coated materials with various size distribution and morphology [245]. The disadvantages of this method are associated with the high process cost, complexity, and weak scale-up capability [162].

2.2.2.4. Wet chemical synthesis

Currently, most synthesis methods still rely on wet chemical reduction using a chemical reducing agent. The conventional wet synthesis of AgNPs using strong reductants such as sodium

borohydride, hydrazine, and dimethylformamide (DMF) is currently the most common approach in the literature compared to other techniques previously explained [218]. Although wet chemical methods can successfully offer narrow size distribution and synthesize particles with small size, there are some major disadvantages regarding those methods. Additionally, toxicity and hazards can result from using those chemical substances. For instance, hydrazine and its derivative compounds (e.g hydrazine hydrate) serve as a strong reductant in the synthesis of AgNPs [215] due to its strong reducing characteristic [246], however; hydrazine is known to be toxic and carcinogenic and cause severe damages to vital human organs such as lungs [246,247]. The Environmental Protection Agency (EPA) has ranked hydrazine as a potential carcinogen, in which threshold limits are considered as small as 10 ppb [246,248]. N,N-Dimethylformamide (DMF) is also known as a strong and common reducing agent. However, the compound is reported to cause damages to the liver and digestive system [249]. Sodium borohydride, another strong reducing agent is considered to have adverse effects on lungs and may cause pulmonary edema, which is a condition that results in fluid build-up in the lungs [250]. Besides the exposure risk during the process, an intense separation step should be considered to remove those compounds from the synthesized nanoparticles, thus making the process difficult and costly. In the case of hydrazine, the synthesized particles may potentially include some of the remnants from the reagent, thus making them hazardous or even unusable for biomedical applications. The polyol process is another common wet chemical method used for the synthesis of silver nanostructures. The polyol process is typically performed at 120-160 °C by utilizing ethylene glycol as the solvent and reducing agent and PVP as the capping agent in the presence of a small amount of salt mediator [251–253]. Although the polyol process is a non-hazardous and widely accepted method for the synthesis of silver nanostructures, there are some disadvantages associated with it. First, the polyol process is typically performed at temperatures higher than 120 °C, which is associated with high energy consumption. Second, this process requires dilute concentrations of silver precursors (0.1 M or lower) in order to maintain a uniform morphology and size distribution [254],

which limits their scale-up capability. Third, the yield of the silver nanostructures is highly sensitive to reaction conditions, such as temperature, concentration ratio of PVP to $AgNO_3$, salt mediator concentration, and the stirring type and rate [94]. On the other hand, natural compounds can be utilized to synthesize silver nanostructures in a much simpler fashion by enabling synthesis at room temperature and using only one reagent, as both reducing and capping agent in addition to providing non-hazardous and environmentally friendly routes towards the synthesis of different silver nanostructures.

2.3. Green synthesis of silver nanoparticles

Green synthesis of nanoparticles can be defined as a set of techniques which utilize non-chemical reagents or non-hazardous methods for the production of nanoparticles. The main purpose of such methodologies is to minimize environmental toxicity and health-related hazards [108,218,255–257]. In most green silver nanostructure synthesis processes, reduction of Ag^+ to Ag^0 is performed either by biological species or by bio-based compounds derived from a desired type of plant or organism [256]; which is also called biological synthesis. Bio-based reducing agents include microorganisms or biologically-produced material. Microorganisms consisting of viruses, microalgae, fungi, yeast, and bacteria were previously used to synthesize AgNPs. Unlike physical synthesis, but similar to chemical synthesis, biological synthesis of nanoparticles is classified under bottom-up approaches [108]. However, green synthesis is not limited to synthesis by bio-based compounds or biological species. For example, laser irradiation can also be used without using any reducing agent in order to synthesize AgNPs [256]. In addition, AgNPs were synthesized by microwave irradiation [258,259], ionizing irradiation [256,260], and pulse radiolysis [256]. Since these techniques may be utilized to produce nanoparticles with harmless procedures, they may also be classified under green synthesis methodologies. However, they have drawbacks in terms of energy consumption. A general comparison between chemical, physical, and green synthesis

methods has been outlined in Table 2.1. Figure 2.1 provides a clear overview of the classification of synthesis methods.

Table 2.1: Classification and comparison of various synthesis methodologies of silver nanostructures based on their advantages and disadvantages reported by the literature.

Method	Advantages	Disadvantages	Ref.
Physical methods			
Ball milling	• Cheap • Process can be done at ambient temperature	• Insignificant for large-scale synthesis • Agglomeration of particles • High energy consumption	144,226,227,261,262
Evaporation-condensation	• Large-scale synthesis • Useful for long-term experiments	• Rigorous equipment • Expensive equipment • Expensive process • Long preheating times • High operating temperatures • High energy consumption	108,141,218,229
Arc discharge	• Simple equipment • High purity of nanoparticles • Few process steps • High synthesis rates	• Large size distribution of nanoparticles	133,135–137
Laser ablation	• High purity of nanoparticles • Small size of nanoparticles • Low agglomeration rate • Narrow size distribution	• High energy consumption • Low productivity • Insignificant for large-scale synthesis	116,232,233
Spray pyrolysis	• High purity of nanoparticles • Process simplicity	• High operating temperatures • Low heat transfer to the reaction tube due to low residence time	128,144,234
Chemical methods			
Sol-gel process	• High purity and homogeneity of nanoparticles • Can be efficiently used for preparation of composites and complex materials	• Limited industrial applicability • Costly precursors • Process longevity • Difficulties regarding the synthesis of monoliths • Reproducibility difficulties	237,238
Reverse micelle	• Process simplicity • Scale-up simplicity	• Low productivity of particles per system volume • Large size distribution of nanoparticles • Use of toxic and hazardous chemicals such as hydrazine and sodium borohydride	156,239
Chemical vapor deposition	• Preparation of nanocomposites by only one deposition step	• High process cost • Process complexity • Weak scale-up capability	162,245
Wet chemical synthesis	• Process simplicity • Narrow size distribution of nanoparticles • Small size of nanoparticles	• Use of highly toxic and hazardous substances such as hydrazine, sodium	246–249

			borohydride, and N,N-Dimethylformamide (DMF) • Limited biomedical applications	
Green/Biological methods				
Bacteriogenic synthesis	• Process simplicity • Environmentally-friendliness		• Pathogenic behavior of certain species such as *E. Coli* • Significantly slow synthesis rate • Large size distribution • Unknown biological functions affecting the synthesis process	[108,263]
Fungi-mediated synthesis	• Process simplicity • Environmentally-friendliness • Faster synthesis rate compared to bacteriogenic synthesis • High bioaccumulation capacity and intracellular uptake • Less non-pathogenic behavior compared to bacteriogenic synthesis		• Process longevity • Pathogenic behavior • Unknown biological functions affecting the synthesis process	[108,182,183,264]
Virus/VLP-mediated synthesis	• Process simplicity • Environmentally-friendliness • Possibility to synthesize 1D nanostructures • Small size of nanoparticles		• lack of strong metal-binding sites along the biotemplate surface • Preparation of the biotemplate is time-consuming • Multiple coating cycles may be required to yield a uniform coating	[265–267]
Algae-mediated synthesis	• Process simplicity • Low cost • Environmentally-friendliness • Low reaction temperatures • use of non-pathogenic and non-hazardous reagents • Small size of nanoparticles • Uniform morphology of nanoparticles		• Significantly Slow synthesis rate • Unknown biological functions affecting the synthesis process	[268,269]
Plant/Plant extract-mediated synthesis	• Process simplicity • Low cost • Environmentally-friendliness • Low reaction temperatures • Use of non-pathogenic and non-hazardous reagents • They can act as both reducing and capping agent at the same time • Broad scope		• Unknown mechanisms affecting the synthesis process	[108,144,191,192]

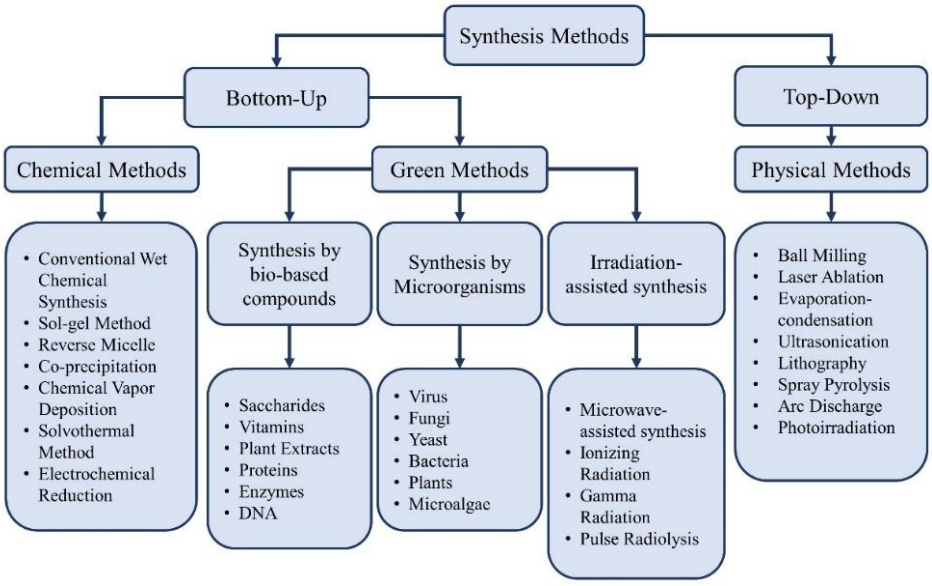

Figure 2.1: Classification of physical, chemical, and green synthesis methodologies of silver nanostructures with respect to reducing agent Type, instruments, and processes.

Nature has proven its unique ability to provide advice for synthesizing nanomaterials. The biogenic/green metal nanostructures' future is bright. Green processes are highly advantageous since they utilize naturally-occurring processes to synthesize nanoparticles. The idea was first introduced in the 19th century, when scientists discovered the reducing ability of biological materials [134]. Green/biological methods provide several advantages over physical and chemical methods. They are eco-friendly unlike chemical methods [49,108], require less energy unlike physical methods [108,218], can be used for mass production [185], and are more economically feasible [108,185,223]. Sustainability, energy-efficiency, renewability, and reduction of chemical derivatives, are among other advantages of green synthesis processes [270]. Furthermore, nature provides a high variety of reagents that can act as reducing agents, while in chemical methods the reagents selection including reducing, stabilizing, and capping agents are more limited. Therefore, recent works in the literature are introducing highly diverse biological and green methods for the synthesis of AgNPs. However, it is critical to optimize these techniques not only in terms of scale-up

capability, but also in aspects of product quality and performance. Various green synthesis studies of Ag nanostructures are reported in table 2.2 along with the reaction conditions, size and morphology of synthesized Ag nanostructures, responsible functional groups in reduction, nucleation and growth, and applications of the synthesized Ag nanostructures.

2.3.1. Bacteriogenic synthesis

Bacteriogenic synthesis is a fairly advantageous process towards facile synthesis of AgNPs due to the reactive response of bacteria to silver. The Ag-resistant bacterial strains are utilized for the synthesis of AgNPs, as they can accumulate Ag atoms on the cell walls [108]. The bacteriogenic synthesis process can be either extracellular or intracellular type. AgNPs are synthesized either by the biomass [271], or the cell culture supernatant [263]. AgNPs synthesized using bacteriogenic pathogens are commonly spherical in morphology and range from 5-200 nm in size. The mechanism through which AgNPs are synthesized is still not well understood; however, Fourier-transform infrared (FTIR) spectroscopy results from previous studies suggest that carboxylic and hydroxylic groups, in addition to primary and secondary amides corresponding to cellular proteins and enzymes, were responsible for synthesis and stabilization of AgNPs (Table 2.2). These components are present in both the biomass and the cell culture supernatant. It was previously demonstrated that the synthesis rate can be faster for some bacterial strains including *Escherichia coli (E. coli)* and *K. Pneumonia* when the cell culture supernatant is used [272]. However, the main downside of bacteriogenic synthesis is the slow synthesis rate and large size distribution compared to other green methods [108,263]. The applications of bacteria-synthesized AgNPs can be seen in development of antimicrobial agents, biosensors, optics, solar energy, and drug delivery [271–273].

2.3.2. Fungi-mediated synthesis

Fungal species have demonstrated significant potential for the synthesis of AgNPs. Their high binding and bioaccumulation capacity, intracellular uptake, and ease of handling provide them with additional advantages compared to bacteria [264]. Previous studies have shown that fungi-synthesis processes are followed by an enzymatic process, affecting the formation of stable AgNPs in the range of 5-15 nm [274]. However, this range can vary with respect to reaction conditions. FTIR results show that similar to bacteria, carbonyl, amide, and hydroxyl groups corresponding to the cellular protein were responsible for the synthesis and stabilization of AgNPs [182,183]. The less non-pathogenic behavior of fungi and their faster synthesis rate suggest their use over bacteria. Fungi-synthesized AgNPs have proved to have noticeable anti-bacterial activity. Naqvi et al. showed that synthesized AgNPs using *A. flavus* fungi increased the biocidal effectiveness against drug-resistant bacteria significantly [275]. Fungi-assisted synthesis has proved to be a promising approach towards production of AgNPs; however, the pathogenic behavior of the fungi and long synthesis periods compared to other green methods makes it inferior among green synthesis processes.

2.3.3. Plant virus template-mediated synthesis

Plant-based viruses as biotemplate have been rarely used for the synthesis of silver nanostructures compared to other methods. To the best of our knowledge, there have been only a few studies [180,265–267] that have used plant viruses to synthesize silver nanostructures. In particular, *tobacco mosaic virus* (TMV) is used as the most common template to produce rod-shape Ag nanostructures. However, TMV is not the only template that can be used for the synthesis of Ag nanostructures. Among others, *Brome Mosaic Virus* (BMV), *Cowpea Chlorotic Mottle Virus* (CCMV), *Cowpea Mosaic Virus* (CPMV), *Hibiscus Chlorotic Ringspot Virus* (HCRSV), *Red Clover Necrotic Mosaic Virus* (RCNMV), and *Turnip Yellow Mosaic Virus* (TYMV) may also be

used for the synthesis of Ag nanostructures [276]. The AgNPs can be synthesized either inside the viral template, within the interface, or on the outer surface [276]. In one of the early works, Dujradin et al. [265] synthesized AgNPs in cylindrical matrices using TMV as the biotemplate. In this work, AgNPs were 2-4 nm in size and it was shown that AgNPs, unlike platinum and gold nanoparticles, were coated on the inner surface of the TMV channel. The synthesis process is known to be mediated by the amino acid functional groups [267]. Although viral templates have not been investigated as much as other approaches, viral template-mediated Ag nanostructures have been demonstrating promising potential in targeted imaging and therapeutic delivery systems [276]. In addition, they can be used to synthesize 1D Ag nanostructures [266,267]. This characteristic is obtained due to the rod-shape morphology of some plant viruses such as TMV. Synthesis of AgNPs using 1D templates can facilitate their application as bio-semiconductors [267]. One of the main advantages of viral templates is the simple synthesis of small AgNPs [265,266]. However, their major drawback is lack of strong metal-binding sites along the biotemplate surface [266]. In addition to that, preparation of the viral templates is time-consuming and multiple coating cycles may be required to yield a uniform coating of metal nanostructures on their surface. We have recently reviewed the engineering TMV and its virus-like-particles (VLPs) for synthesis of biotemplated nanomaterials. We also discussed the recent advances on novel barely stripe mosaic virus and its VLP as a novel template for metal nanoparticle synthesis[277,278].

2.3.4. Algae-mediated synthesis

Synthesis of AgNPs using marine-based microorganisms has emerged as one of the novel and promising routes due to their non-toxicity and eco-friendly nature [193,279]. Cyanobacteria, brown algae, and green algae are the most common types of algae used for the synthesis of AgNPs [193]. For most applications, the single-cell type of the organism known as microalgae is used to synthesize AgNPs [195]. This enables formation of homogeneous microalgal suspensions which can be used directly for the synthesis process. In the synthesis process, the microalgal biomass in the

aqueous phase, cell-free aqueous extract, aqueous supernatant of dried algae, or aqueous filtrate of the broth are mixed with the silver solution (mostly silver nitrate) to synthesize AgNPs [193]. The synthesis process is intracellular when the reaction takes place within the cells, and extracellular when biosynthesis occurs outside of cells due to the presence of biomolecules [195], which depends on the type of cell culture used. For instance, cell-wall deficient cells are typically more inclined towards intracellular biosynthesis as the cell-wall is known to act as a barrier for the diffusion of metal cations into the cytoplasm [280]. When synthesized, the AgNPs are capped by a matrix of polysaccharides in and out of the cells [195], and the size of synthesized AgNPs varies depending on the cell type; however, AgNPs with average sizes as low as 4.3 nm [196], and as high as 35 nm [281] were reported. The synthesized AgNPs are typically spherical in shape [196,282,283]; however, varied morphologies were also reported [197]. Among the applications, Algae-mediated AgNPs have shown effective antioxidant and antibacterial activity [268,279]. The advantages of the algae-mediated synthesis process are low reaction temperatures, use of non-hazardous reagents, and synthesis of relatively small particles with uniform morphology. However, the main disadvantage of this type of biosynthesis is the significantly low production rate [268,269].

Table 2.2: A Review of various green processes, reaction conditions, necessary functional groups, and characterization techniques used for the synthesis of silver nanostructures with different sizes and morphologies along with their application.

Reducing agent	Solvent	Ingredient or functional Group responsible for Ag^+ reduction/ particle stabilization	Reaction time/ temperature	Morphology / dimensions	Implemented characterization techniques	Application of the synthesized nanostructures	Ref.
Bacteria/ Bacteriogenic metabolites							
EPS (exo-polysaccharide) extract of *Bacillus safensis* LAU 13	Not explicitly mentioned	Secondary amine & amide I (responsible for stabilization)	2 hr/30 ± 2 °C	Spherical/5-30 nm	FTIR/TEM /XRD	Antimicrobial agents	[273]
Bacillus krulwichiae	Distilled water	Carboxyl, Hydroxyl, Aldehyde, Ester groups responsible for reduction and stabilization	24 hr/Room temperature	Spherical/ Ave: 25.88 ± 10.49 nm	FTIR/SEM /XRD/EDX	Antimicrobial/ Antibiofilm agents	[284]
Bacillus cellulosilyticus (EPS extract)	Distilled water	Carboxyl, Hydroxyl, Aldehyde/ Ester groups responsible for reduction and stabilization	24 hr/Room Temperature	Spherical/ Ave: 23.99± 8.43 nm	FTIR/SEM/XRD /EDX	Antimicrobial/ Antibiofilm agents	[284]
Bacillus brevis	Not explicitly mentioned	Amide (-CONH), Hydroxyl, and Carbonyl Corresponding to the protein (responsible for reduction)/ C=C and –CH on protein responsible for stabilization	24 hr/room temperature	Spherical/41 –68 nm	AFM/SEM/TLC/ FTIR	Antimicrobial agents	[172]

Enterobacter cloacae	Not explicitly mentioned	Primary amide, secondary amide	72 hr/room temperature	Spherical/ 12-30 nm	FTIR/SEM/XRD	Antibacterial activity against MDR strains	285
EPS from *Leuconostoc lactis*	Milli Q water	Hydroxyl groups	1 month/room temperature	Spherical/30-200 nm	SEM/TEM/XRD /UV-Vis/AFM/TGA-DTA	Textile industry: degradation of azo-dyes	173
Pseudomonas stutzeri	Not explicitly mentioned	Primary, secondary, and aliphatic amides	8 hr/80 °C	Spherical/ 15-20 nm	TEM/FTIR	Antibacterial activity against MDR strains	174
Bacillus methylotrophicus	Not explicitly mentioned	Extracellular Enzymes and Proteins	-/28 °C	Spherical/ 10-30 nm	FE-TEM/EDX/UV-Vis	Antibacterial activity	286
Escherichia coli (culture supernatant)	Not explicitly mentioned	Primary and secondary amines corresponding to the protein	24 hr/room temperature	Spherical/40-90 nm (unoptimized condition) & 10-40 nm (optimized condition	XRD/TEM	Conductivity/ catalytic and Antimicrobial activity	287
Staphylococcus aureus	Milli Q water	Extracellular enzymes	5 min/-	Varied Morphology/ 160-180 nm	AFM/UV-Vis	Antimicrobial activity	288
Cyanobacteria	Milli Q water	-	60 min/30-60 °C	Spherical/60-80 nm	UV-Vis/DLS/TEM	Dye decolorization property	289
			Yeast				
Cryptococcus laurentii (Culture Supernatant)	Not explicitly mentioned	Amide 1 corresponding to peptides	48 hr/28±4 °C	Spherical/ Ave: 35 & 400 nm	UV-Vis/TEM/XRD/ FTIR	Antifungal activity	182
Saccharomyces cerevisiae	Not explicitly mentioned	Cytoplasmic enzymes (Oxidoreductase & Oxidase) responsible for reduction/ Proteins responsible for stabilization	72 hr/25 °C	Spherical/2-20 nm	TEM/DLS	Cosmetics, foods, and consumer goods	183

Plant/Fruit extracts							
Green Tea Powder (*Camelia Sinensis*)	Deionized water	Tea polyphenols (responsible for stabilization)	15 min/60 °C	Spherical/34.68±4.95 nm	UV-Vis/XRD/FTIR/TGA/AFM/DLS/XPS	Antibacterial activity	[290]
Camelia Sinensis extract	Deionized water	Not mentioned	30 days/Room temperature	One-Dimensional (nanowires)/ 50 nm (diameter) & 1.3 µm (length)	FESEM/HRTEM/HAADF/UV-Vis	Antibacterial activity	[291]
Blackberry fruit extract	Deionized water	O-H and C=O groups	48 hr/25 °C	Spherical/12-50 nm	TEM/FTIR/DLS/XRD/UV-Vis	Antioxidant activity	[292]
Berberis Vulgaris leaf extract	Distilled water	Not Mentioned	1 hr/Room temperature	Spherical/30-70 nm	TEM/XRD/DLS/UV-Vis	Antibacterial activity	[191]
Origanum vulgare extract	Deionized water	Phytomolecules	2 hr/85-90 °C	Spherical/2-25 nm	UV-Vis/XRD/HRTEM/EDX/FTIR	Antibacterial and antifungal activity	[190]
Coffea Arabica seed extract	Deionized water	Phenolic Groups	2 hr/Room temperature	Spherical and Ellipsoidal/20-30 nm	UV-Vis/SEM/SEM-EDXA/FTIR/DLS	Antibacterial activity	[293]
Lignin	Milli-Q water	Phenolic Hydroxyl Groups	30 min/85 °C	Spherical/7.3 ± 2.2 nm & 14.3 ± 1.8 nm	UV-Vis/TEM	Not Mentioned	[294]
Tannin	Not explicitly mentioned	Hydroxyl Groups	2 hr/50 °C	One-Dimensional (nanowires)/ 50 nm (diameter)	UV-Vis/HRTEM/SEM/SAED/IR	Detection of Pb(II) Ions	[295]
Clove oil	Not explicitly mentioned	Hydroxyl Groups from Eugenol	Not mentioned/ Room temperature	One-Dimensional (Nanowires)/ 39±0.01 nm (Diameter) & 3 µm (Length)	UV-Vis/HRTEM/XRD/FTIR	Conductive Ink	[296]

Apple extract (Microwave-assisted)	Ultra-pure water	Not Mentioned	2.5 hr for Microwave-Assisted Reduction/ Room Temperature & 96 hr in thermally-assisted one-pot reduction/ 100 °C	Spherical/28.24± 1.15 nm for thermally-assisted and 22.05±1.05 nm for microwave-assisted reaction	UV-Vis/ XRD/ EDS	Antibacterial activity	[297]
Azadirachta indica	Not explicitly mentioned	C=O groups corresponding to alkyne groups, C-O and C-OC bonds corresponding to flavonoids and terpenoids (responsible for stabilization)	15 min/Room temperature	Spherical/ 34 nm	UV-Vis/FTIR/TEM/ DLS	Antibacterial activity	[298]
Elephantopus Scaber	Distilled water	O-H, C=O stretching of plant constituents and C=C stretching of aromatic rings	30 min/40 °C	Spherical/ 37.86 nm	UV-Vis/TEM/XRD/ FTIR	Antimicrobial and anti-Cancer activity	[259]
Cinnamon zeylanicum	Dimethyl sulfoxide (DMSO)/ Ethanol/ Distilled water	Aldehyde Content (responsible for reduction)	2 hr/60 °C	Spherical/ 2-10 nm (in ethanol), Polygonal/5-25 nm (in Distilled Water), Spherical/10-50 nm (in DMSO)	UV-Vis/HRTEM	Antibacterial activity	[299]
Banana peel extract	Distilled water	Carboxyl, Hydroxyl and amide groups (responsible for reduction)	76 hr/100 °C	Spherical/23.7 nm	UV-Vis/EDX/XRD/ SEM/TEM/ FTIR	Antibacterial activity	[300]
Turmeric extract	Milli-Q water	Hydroxyl groups present in the curcumin powder and C-H bonds in turmeric powder responsible for the reduction	24 hr/Room temperature	Spherical/18 ±0.5 nm	UV-Vis/TEM/EDX/ FTIR	Antibacterial activity	[301]

Marigold flower	Ultra purified water	N-H amid stretching, C-H stretching from vinyl disubstituted alkenes, and C-Cl stretching from alkyl halides (responsible for reduction)	24 hr/Room temperature	Varied (spherical, hexagonal, and irregular)/ 46.11 nm	UV-Vis/XRD/FTIR/ EDX/SAED /TEM	Antibacterial activity	[302]
Starch	Milli-Q water	O-H stretching (aliphatic hydroxyl group) and C=O (responsible for reduction and stabilization)	48 hr/25 °C	Spherical, Polydispersed and Amorphous/ 45.6 nm	UV-Vis/ TEM/ SAED/XRD/ FTIR/DLS	Catalytic activity	[303]
Ginger	Deionized water	Phenolic groups and flavonoids	2 hr/Room temperature	Spherical/10.10-18.33 nm	UV-Vis/TEM	Antioxidant and antimicrobial activity	[304]
			Vitamins				
Vitamin C (Ascorbic Acid)	High purity water	Not mentioned	15 min/ 30°C	Quasi-spherical/ 31 nm	UV-Vis/TEM	Not specifically mentioned	[305]
Vitamin B2 (Riiboflavin)	Milli-Q water	Not mentioned	24 hr/Room Temperature	Spherical/ 6.1±0.1 nm, Nanorods (10-20 nm Diameter, 100-200 nm length)	UV-Vis/TEM/SEM/ EDX	Catalytic polymerization of aniline and pyrrole	[208]
Vitamin B12 (Microwave-assisted)	Milli-Q water	Not mentioned	3-6 min/ 100°C	Irregular/70-600 nm	UV-Vis/XRD/TEM/ SEM	Not specifically mentioned	[306]
			Microalgae/Algae				

Chlorococcum humicola	Distilled sterile water	C-N bonds corresponding to aromatic and aliphatic amines (responsible for stabilization)	48 hr/Room temperature	Spherical/2-16 nm	SEM/TEM/ FTIR/UV-Vis/XRD	Antibacterial activity	[282]
Spirulina	sterilized double-distilled water	O-H groups, C-O bonds corresponding to COOH group, and N-H bonds corresponding to primary and secondary amines	3,6,9 and 12 hr/Room temperature	Spherical/5-50 nm	UV-Vis/FTIR/XRD/ EDX/Bio-TEM	Antibacterial activity	[283]
Chlorella Vulgaris	Not Explicitly Mentioned	C=O and -N-H (amide I and amide II) bonds corresponding to proteins (responsible for stabilization and reduction)	5 days/25°C	Spherical/9.8 ± 5.7	UV-Vis/XRD/TEM/ FTIR/EDX	Antibacterial activity	[279]
Padina pavonia	Not explicitly mentioned	N-H (Amine), C-N (primary amines) groups and O-H groups (responsible for reduction)	3 hr/Room temperature	Spherical, triangular, rectangle, polyhedral and hexagonal/ 49.58–86.37 nm	UV-Vis/TEM/DLS/ FTIR/	Not specifically mentioned	[197]
Chlamydomonas reinhardtii	Deionized water	Amine and carbohydrate groups	192 hr/Room temperature	Spherical/5.6 ± 2.4 nm	UV-Vis/XRD/TEM	Not specifically mentioned	[196]
			Viruses				
Tobacco mosaic virus	Not explicitly mentioned	Hydroxyl, carboxyl and Thiol groups (responsible for reduction)	1 hr/50 °C	Spherical/2 nm	UV-Vis/TEM	Catalytic and antibacterial activities	[180]

Fungus

Rhizopus stolonifer	Deionized water	Carbonyl group of amino-acid residue and peptide-protein	2 days/40 °C	Spherical/2.8 6 ± 0.3 nm	UV-Vis/XRD/HR-TEM/FTIR	Not specifically mentioned	[307]
Penicillium aculeatum	Milli-Q deionized water	N-H and C=O from the amide group of proteins, -C-N belonging to aromatic and aliphatic amines	4 Weeks/ Room Temperature	Spherical/4-55 nm	HR-TEM/XRD/FTIR /UV-Vis	Antibacterial activity	[178]
Penicillium chrysogenum	Deionized water	-O-H, C-H, C-O-, COO-, and -N-H stretching associated with proteins	-/28 °C	Spherical/9-17.5 nm	FTIR/TEM/DLS	Antifungal activity and ability to prevent mycotoxin production	[176]
Fusarium oxysporum	Deionized water	Not mentioned	-/37 °C	Spherical/1-50 nm	SEM/TEM	Antibacterial activity	[175]

Sugars

Brown sugar	Distilled water	C-C and C-O corresponding to sucrose. glucose and fructose	2 hr/50 °C	Varied (spheres, cubes, and bars)/-	UV-Vis/TEM/HRTEM/EDX/FTIR/ MS	Biomedical and pharmaceutical applications	[203]
White sugar	Double-distilled water	-OH groups corresponding to gluconic acid	10 min under sunlight, 2-3 hr without sunlight/ Room Temperature	Spherical/10-25 nm	UV-Vis/FTIR/NTA/ TEM	Biomedical and pharmaceutical applications	[204]

2.3.5. Plant/Plant extract-mediated synthesis

Synthesis of Ag nanostructures using plants and plant extracts has recently gained more attention. These methods can act as appropriate alternatives for other methods as a result of their simplicity, low-cost, non-toxicity, and simple scale-up capability [190]. In addition, thanks to their non-pathogenic and biocompatibility characteristics, AgNPs synthesized by plants and plant extracts are ideal for biomedical applications [308]. Plant extracts contain phenolic compounds such as flavonoids and alkaloids which are soluble in water [309]. These compounds provide the reagent with unique reducing and capping characteristics [310]. This can be proved by FTIR observations, where polyphenols are a major common functional group responsible for reduction of Ag ions and stabilization of AgNPs (Table 2.2). The AgNPs can be functionalized with respect to the type of plant or plant extract reagent and reaction conditions [311]. Plants are a natural source for the removal of heavy metals from soils and underground water [312]. The removal of heavy metals takes place by phytoremediation strategies such as phytoextraction, phytofiltration, phytostabilization, phytovolatilization, phytodegradation, rhizodegradation, and phytodesalination [313]. A variety of plants such as *Noccaea caerulescens*, *Pteris vittata*, and *Sedum plumbizincicola* were previously demonstrated to have substantial heavy-metal detoxification capability [314–316]. One of the most significant factors in the detoxification process is the redox potential [317], which is seen as an opportunity to utilize plants and their components for the reduction of metal cations and synthesis of metal nanoparticles such as AgNPs. The synthesis of AgNPs by plants and their components may be categorized into in-vivo and in-vitro synthesis processes [144]. The in-vivo synthesis would refer to synthesis of AgNPs inside the plants and the in-vitro synthesis would refer to synthesis by components extracted from the plants. In the first in-vivo synthesis study, Torresdey et al. [318] synthesized AgNPs (spherical, 2-20 nm in diameter) using *Alfalfa Sprouts*, where it was reported that silver (Ag^0) was absorbed from the agar medium

through the roots and transferred into plant shoots. It was also reported in this work that the nucleation and formation of AgNPs occur within the plant tissue. However, it is debated by other studies whether the Ag^+ ions are reduced outside or inside of the plant [144,319]. Later, several studies reported synthesis of AgNPs using *Brassica Juncea* [320–323], in which they reported the presence of AgNPs in plant biomass. It is shown that the major compounds for the synthesis of AgNPs are phytochemicals that naturally exist in plants including flavones, terpenoids, catechins, and polyphenols [187,319,324], which may also include carboxylic acids, ketones, and aldehydes functional groups. Many studies have reported synthesis of AgNPs by in-plant phytochemicals in the water-soluble form [325]. This is advantageous because the water-solubility of the phytochemical compounds simplifies the process. Various parts of plants such as roots, fruits, seeds, needles, and aerial parts may be used for extraction of phytochemicals [325]. These extracts contain a substantial amount of polyphenols which are strong antioxidants [144,190] with significant redox potential. A comprehensive mechanism for the synthesis of AgNPs by plant extracts has not yet been proposed; however, the reduction mechanism may be explained by identifying the responsible functional groups. Makarov et al. [326] hypothesized that when flavonoids, a large family of polyphenols, are used as reducing agents, reactive hydrogens are released via a tautomerization process, in which flavonoids are transformed to the keto-form, which leads to reduction of Ag^+ to Ag^0. In addition, hydroxyl (-OH) groups are known to be a prominent functional group for reduction of Ag^+ [325]. The concentration of the polyphenols varies depending on the plant from which they were extracted [325]. Therefore, the properties of the synthesized AgNPs, such as size and morphology, can be tuned by selecting the plant source, and adjustment of extract composition [184,327].

The plant-mediated synthesis of AgNPs is fairly simple. The reducing agents used for the synthesis of AgNPs are used in the form of soluble powder which was previously extracted, or obtained through a common extraction procedure [187]. For synthesis, the extract solution is simply

mixed in an aqueous environment with the silver precursor such as $AgNO_3$ and maintained at a desired temperature. A prominent advantage is that these reactions can be performed at room temperature, and successfully result in formation of AgNPs, which is reported by many studies [191,291,293,296–298,301,302,304]. However, the characteristics of the AgNPs, such as size and morphology, are highly sensitive to the reaction conditions. Parameters that dictate such characteristics are extract composition and concentration, temperature, pH, Ag^+ concentration, reaction duration, and stirring rate [187].

The studies using plant extracts as reducing agents have been increasingly growing recently and various types of plant extracts have been used as reducing, capping, and stabilizing agents for the synthesis of AgNPs. Johnson et al. [328] synthesized AgNPs using *Odontosoria Chinensis* extract and reported formation of spherical AgNPs with diameters ranging from 22.3 to 48.2 nm. The reaction occurred at 40 °C, and a complete reduction of Ag^+ after 10 minutes was reported. Agglomeration was observed in the case of temperatures higher than 40 °C. Also, the most optimal concentration ratio was reported to be at 1:9 (extract: $AgNO_3$). They reported that carboxylic acids and hydroxyl functional groups were mainly responsible for the synthesis of AgNPs, and the presence of terpenoids, tannins, polyphenols, and steroids in *Odontosoria Chinensis* extract was confirmed before the synthesis experiments. The synthesized AgNPs demonstrated successful anti-inflammatory and antidiabetic activities, which was due to polyphenols, terpenoids, and tannins in the extract in addition to AgNPs themselves. Sivakumar et al. [329] synthesized spherical AgNPs with an average size of 10.3 ± 1.7 nm using *Parthenium hysterophorus* aqueous extract. The aqueous extract was mixed with a 10 mM $AgNO_3$ solution with a volumetric ratio of 3:100. The mixture was incubated in the dark for 1 hour. FTIR characterization results showed the presence of polypeptides, amine, germinal methyl, and hydroxyl as functional groups responsible for reducing Ag^+ ions and formation of AgNPs. The synthesized AgNPs then demonstrated significant antibacterial activity against *E. coli*, *P.*

auriginosa, *B. subtillis*, *S. aureus*, *E. feacalis*, and *K. pneumonia*, and anticancer activity against HepG2 cell lines. It was later demonstrated by Nouri et al. [330] that synthesis using *Mentha Aquatic* can result in formation of small AgNPs with relatively narrow size distribution. In their study, *Mentha Aquatica* leaf extract was mixed with $AgNO_3$ solution at different reaction conditions. The most optimal reaction condition was reported to be at a pH of 9.5, temperature of 90 °C, concentration ratio of 1:1, and 60 min reaction time. However, they showed that ultrasonication can reduce both the reaction time and particle size. Without ultrasonication, the average size was observed to be 14 nm, while with ultrasonication, this size was reduced to 8 nm. In addition, the increase in ultrasonication power was proportional to the decrease in reaction time. The reaction time decreased from 60 min to 10 min by increasing the ultrasonication power from 0 to 200 W. This was attributed to the enhanced diffusion of compounds due to sonic waves. In another study, Tanase et al. [331] synthesized spherical AgNPs using aqueous bark *Picea abies L.* extract. The reaction was performed at 70 °C and pH 9 with different $AgNO_3$ and extract concentrations. Although colloidal AgNPs were synthesized, the size and size distribution were significantly high (100-500 nm). The most optimal scenario was attributed to 1 mM of $AgNO_3$ with a volumetric ratio of 1:10 (extract: $AgNO_3$) and a reaction time of 3 hours. The results demonstrated that higher $AgNO_3$ concentration results in inhibition of the synthesis process. The responsible functional groups were confirmed by FTIR to be aldehydic, carbonyl, and hydroxyl groups of phenols and carboxylic acids. The AgNPs showed strong antibacterial activity against *E. coli* and Klebsiella pneumonia, comparable to the antibacterial activity of gentamicin.

Most plant extract synthesis studies use extracts as both reducing and capping agents at the same time. However, this might not be advantageous in some cases. Soliwoda et al. [192] synthesized spherical AgNPs using cacao beans and grape seed extract and investigated the effect of sodium citrate with various molar ratios with respect to $AgNO_3$ solution (1.5-6 for sodium citrate, and 1.5-9 for the extract). Acetone and ethanol were used as a solvent for cacao beans and grape seed

extract, respectively. The initial concentration of both reagents was set to 2 wt. %, and the concentration of $AgNO_3$ was kept constant at 1 wt. %. The mixtures were heated for 15 minutes and then cooled down to room temperature. Using various molar ratios, they reported that cacao beans extract resulted in aggregation of AgNPs followed by sedimentation and therefore, cannot be used as reducing and stabilizing agents at the same time. However, monodisperse AgNPs with an average size of approximately 15 nm were obtained using sodium citrate as the capping agent. Under these conditions, the molar ratio did not have a significant effect on the size of AgNPs, and their size was maintained between 11-15 nm at different molar ratios of cacao beans extract and sodium citrate. The reason was attributed to the fact that sodium citrate is able to form stable complexes with the polyphenols present in the extract, which then acts as reducing and capping agent. This was nevertheless different for grape seed extract. Without the presence of sodium citrate, AgNPs agglomerated and had a large size distribution, but in the presence of sodium citrate, the size was maintained at 10-18 nm for different sodium citrate molar ratios, and size distribution was smaller. Furthermore, it was reported by Mohagheh et al. [332] that sodium citrate can form complexes with Ag^+ at ambient temperature, and act as reducing and capping agent at the elevated temperature. In another study, Soliwoda et al. [333] reported formation of citrate-tannic acid complexes which were responsible for reduction and stabilization of tannic acid-mediated AgNPs. They also stated that the mere use of sodium citrate could result in inhomogeneous sizes and broad size distribution. To the best of our knowledge, it has not been yet well determined what type of plant extracts can be used as reducing and capping agents at the same time. The formation of silver nanoparticles by plant extracts depends highly on the plant extract composition along with various process parameters such as pH, temperature, and concentration ratio.

2.3.5.1. Effect of pH

The pH is known to be a significant parameter in controlling size, morphology, and stability of AgNPs [334]. Singh et al. [335] synthesized spherical AgNPs using *Hibiscus* Leaves extract ranging 12-17 nm in diameter. Temperature and pH were reported to be the most significant factors in controlling the synthesis process. The effect of pH was mainly investigated in this work and it was observed that at pH 3 the AgNP formation process stops as there was not any further color change, and at pH 10 agglomeration occurs upon the addition of the $AgNO_3$ solution. At pH 6 however, the reduction process started upon the addition of $AgNO_3$ and was observed for 30 minutes. The most optimal condition to minimize the size of AgNPs was reported to be at the pH of 6, temperature of 70°C, 30 minutes of reaction time, and 5 mM $AgNO_3$ solution (1:1.5 volumetric ratio with respect to the extract). Their FTIR studies demonstrated that the hydroxyl functional groups and polysaccharides were responsible for reduction and stabilization of AgNPs. In another work by Handayani et al. [336], it was demonstrated that alkaline condition is more favorable for synthesis of smaller nanoparticles. They synthesized AgNPs using *Pometia pinnata (Matoa)* leaf extract for 24 hours with 1:2 volumetric ratio (extract: $AgNO_3$). They demonstrated that at pH 11, the AgNPs were 10-50 nm in size and of spherical and hexagonal morphologies, while at pH 4 the AgNPs were observed to be 50-80 nm with spherical and triangular morphologies. It was also reported that change in pH affects the reducing capability of the extract, which is also confirmed by other studies [337,338]. The pH is also reported to control the zeta potential [334,336], and result in particle stability adjustments [334]. The higher the value of zeta potential, the stronger the long-term stability of AgNPs, thereby preventing their agglomeration [334,339]. Alkaline pH also has the potential of increasing the reaction rate due to the enhanced deprotonation of phenolic compounds in basic condition [340]. In addition, alkaline pH enables more –OH to take part in the reduction reaction, thus increasing reduction strength [341].

2.3.5.2. Effect of temperature

Temperature is another crucial factor in controlling size and morphology of AgNPs. Increasing the temperature equals increasing the reaction rate which is favorable for rapid synthesis. However, high temperatures (more than 60 °C) may result in denaturation of the extract compound, and thus alter their reduction potential and result in a significant increase in particle size and even agglomeration [144]. The extract compound should therefore be carefully selected and tested in order to avoid denaturation. Madivoli et al. [342] synthesized AgNPs using *Lantana trifolia* extract by changing the temperature from 20 to 35 °C. It was shown that a decrease in temperature resulted in broader surface plasmon, attributing to larger size distribution contrary to higher temperatures. However, increasing the temperature resulted in formation of larger particles, 60 nm in the case of 35 °C and 48 nm in the case of 20 °C. Nevertheless, AgNPs with a size of 37 nm were obtained at 30°C. Therefore, there was a sharp increase in particle size by changing the temperature from 30 to 35°C. In addition, in a study performed by Anbu et al. [343], AgNPs were synthesized at 50 °C and were slightly larger compared to those synthesized at 37 °C. The increase in particle size due to an increase in temperature was also confirmed by previous studies [311,344–346]. Furthermore, Liu et al. [347] used *Cinnamomum Camphor* leaf extract to synthesize AgNPs. They demonstrated that an increase in temperature will result in an increase in particle size under sufficient Ag^+ ions (Ag^+ concentration equivalent or excess to the extract concentration), and result in a decrease in particle size under insufficient Ag^+ ions (extract concentration excess to Ag^+ concentration). They concluded that under sufficient Ag^+ ions, particle size is not affected by nucleation, but rather by growth. They proposed on the contrary, that under insufficient Ag^+ concentration, all the Ag^+ ions are consumed rapidly through a burst nucleation process, thus not allowing further growth. It can therefore be concluded that temperature and concentration are both significant factors and have an interactive effect on controlling the morphology and size of AgNPs.

2.3.5.3. Effect of concentration/concentration ratio

The concentration of plant extract and silver precursor, as well as their ratio, play a major role in controlling size and morphology of AgNPs. Hasnain et al. [348] synthesized spherical AgNPs using purple heart plant leaf extract and investigated the effect of various parameters using the design of experiments (DoE) approach. Their results indicated that an increase in $AgNO_3$ concentration (from 0.01 to 0.1 M) at constant purple heart plant extract volume (1.4 mL) and relatively lower temperatures (60 °C), resulted in a decrease in particle size (from ~120 to 100 nm). They also observed an initial decrease (from ~310 to 150 nm) followed by a sharp increase in particle size (from ~150 to 335 nm) at relatively higher temperatures (80 °C). In addition, an increase in $AgNO_3$ concentration at constant temperature (80 °C), and relative to various volumes of purple heart plant extract, resulted in an initial decrease (from ~310 to 150 nm) followed by an increase in particle size (from ~150 to >350 nm). However, changing the purple heart plant extract volume did not have a significant effect on the particle size. Therefore, the $AgNO_3$ concentration had a much greater effect on determining particle size. Also changing the temperature from 60 to 80 °C resulted in an approximately linear and continuous increase in particle size (from ~100 to 330 nm), meaning that temperature was a stronger parameter compared to plant extract concentration. Furthermore, Htwe et al. [349] synthesized AgNPs with quasi-spherical morphology using *Imperata* cylindrical plant extract as the reducing agent and ascorbic acid as the capping agent. They showed that increasing the $AgNO_3$ concentration (from 0.5 to 0.9 mM), at constant extract and ascorbic acid concentration, resulted in increasing the particle size (from 32.7 to 39.9 nm). Their Ultraviolet-visible (UV-vis) spectroscopy results also showed that at 0.5 mM $AgNO_3$, the absorption peak was narrower compared to 0.7 and 0.9 mM $AgNO_3$, indicating lower size distribution. Khan et al. [350] utilized *Piper Betle* leaf aqueous extract to synthesize AgNPs. They investigated the effect of concentration on the size and stability of AgNPs by testing various $AgNO_3$ concentrations (1, 2, 3, and 4 mM) and extract concentrations (1:2, 1:4, and 1:8 dilution

ratio with respect to the crude extract). They reported the most optimal conditions to be at 2 mM of $AgNO_3$ and 1:4 dilution ratio of the extract. Their results indicated that increasing $AgNO_3$ concentration leads to shifting the UV-vis peak to the higher wavelengths indicated formation of larger nanoparticles. Aggregation was also observed for higher $AgNO_3$ concentrations. They also reported that higher concentrations of the extract could result in instability and aggregation of AgNPs, which is also confirmed by a previous study [351].

2.4. One dimensional silver nanostructures and their green synthesis

One dimensional (1D) silver nanostructures are characterized as a collection of silver atoms in a one-dimensional pattern. They range from tens to a few hundreds of nanometer in diameter, and their length is in the order of tens of microns. 1D silver nanostructures could either be silver nanowires (AgNWs) or silver nanorods (AgNRs). These two are distinguished by the aspect ratio, which is the ratio of the length to the diameter. Typically, 1D silver nanostructures with an aspect ratio of 10 or higher are considered as AgNWs while those with aspect ratios lower than 10 are considered as AgNRs [94]. In general, 1D metallic nanostructures have unique plasmonic properties as they can uniquely interact with light because of their plasmonic characteristics [352,353]. AgNWs, in particular, possess great surface plasmon resonance (SPR) characteristics, high conductivity, and remarkable flexibility in addition to having a simple fabrication process [354]. Synthesis of AgNWs has been under progressive investigation during the last decade due to their broad range of applications including nanoelectronics.

AgNWs have been becoming widely applicable in electronics. In particular, there been promising developments in transparent conductive electrodes (TCEs) manufacturing for next generation touchscreens by applying AgNWs [355–358]. To name a few, C3Nano®, Cambrios®, and 3M® are among the companies that have been developing AgNW-based inks for TCEs used in the flexible touchscreens manufacturing. Currently, indium tin oxide (ITO) is still the dominant material used

in TCEs due to its high transmittance and low sheet resistance [71,359]. Its high conductivity and transmittance level made ITO a fairly appropriate candidate for TCEs; however, weak flexibility, limited supply, costly coating process, highly expensive large-scale manufacturing, and the cost of the material itself have limited a potentially broader application in optoelectronics [71,94]. As a result, ITO-embedded TCEs are gradually giving their position to AgNW-embedded TCEs. One of the most important aspects of the synthesis of AgNWs is to precisely control their size and morphology to achieve a uniform high aspect ratio that strongly affects their optical and transmittance properties [360–362]. Achieving a uniform high aspect ratio depends on the synthesis process and the reaction conditions [361]. As a result, selection of the reducing and stabilizing agents, and identifying the most important factors that control the synthesis process are essential in determining the length and diameter of the synthesized AgNWs.

There are generally two methods for the synthesis of AgNWs, which are hard template and soft template methods. In hard template methods, AgNWs are produced using cylindrical nanoporous structures such as carbon nanotubes (CNTs) [363]. On the other hand, in soft template methods, capping agents such as polyvinylpyrrolidone (PVP) or cetyltrimethylammonium (CTAB) are used to direct the growth of initially formed silver seeds to AgNWs [353]. Hard template methods have several disadvantages compared to soft template ones. The yield of AgNW is significantly low and the templates are very hard to remove [94]. On the other hand, template removal issue is nonexistent in soft template methods and soft templates can be used in the solution phase. Block copolymers [364] and polyvinyl alcohol (PVA) [365] are among the other soft templates used for the synthesis of AgNWs. Currently, the most common method for the synthesis of AgNWs is through the polyol process, in which usually ethylene glycol is used as the solvent and reducing agent, PVP as the capping agent, and in the presence of a small amount of salt mediator. This method is being used to synthesize AgNWs in large commercial scales and has proved to be simple and able to provide relatively proper control over morphology and aspect ratio [366]. Synthesis of AgNWs by

the polyol approach was first introduced in 2002 by Xia's group [367]. In early studies, synthesis was performed using Pt seeds to promote nucleation and growth of AgNWs. In order to make the process more economical and simpler while maintaining high yield and aspect ratio, further modifications were later applied in the synthesis process, such as gradual addition of $AgNO_3$ solution using syringe pumps [368], using salt mediators such as Fe [369] and Cu [370] metal salts, and increasing preheating time [361]. The combination of exceptional size and morphology dependent chemical, optical, and physical characteristics of 1D Ag nanostructures with their potential antibacterial activity, is evidence of a critical need to develop synthesis processes appropriate for their industrial-relevant scale applications. These synthesis processes must meet some criteria including being scalable, low cost, and low toxicity of the materials involved in the synthesis process. These criteria are in excellent agreement with the goals in development of green and sustainable synthesis of metal nanostructures. Polyol synthesis has a fairly high energy consumption due to high temperatures (>120°C). In addition, in more recent polyol processes, a 1- hour preheating time for ethylene glycol is required, which adds to the experiment duration at relatively high temperatures. While progress with improving the polyol process was ongoing, some studies started to use green reagents for the synthesis of AgNWs. We have recently reviewed the polyol silver nanowire synthesis and its outlook for a green process [371]. In 2009, Tian et al. synthesized single-crystalline AgNWs—25 nm large in diameter and 20 μm large in length—using tannin acting as both reducing and capping agent [372]. Tannin is a natural polyphenolic compound found in various plant extracts, such as oak barks, galls, and teas. They can act as strong reducing agents due to oxidization of –OH functional groups in their molecular structure [373]. The AgNWs were synthesized at room temperature, and it was found that an increase in the tannin concentration resulted in AgNWs with a lower aspect ratio. They reported that the slow reduction rate could favor the formation of twinned silver seeds with decahedron morphology. On the contrary, in a more recent work, Dong et al. reported that at low temperatures, tannin molecules cannot selectively adsorb on the {100} facets of AgNWs due to

lack of driving energy [295]. In this work, AgNWs were synthesized at 50 ºC for 2 hours with the same $AgNO_3$ and tannin concentrations used in Tian et al.'s study. The yield of AgNWs in this work was reported to be much higher (as high as 90%) compared to Tian et al.'s study (5-10%). The AgNWs were reported to be 60 nm thick in diameter and several tens of micrometers long. Although low temperatures were considered to be unfavorable for the growth of AgNWs, higher temperatures (higher than 50 ºC) were not favorable either, which is due to the fact that tannin molecules do not have adequate time to adsorb on the specific facets, thus resulting in formation of nanoparticles. They also reported that decreasing the pH from the basic to acidic region results in increasing the yield of AgNWs, with pH 5 being the optimal value. In another study, Lin et al. synthesized AgNWs using *Cassia fistula* as both reducing and capping agent [374]. The reaction was performed at room temperature for 48 hours, and the synthesized AgNWs were reported to be 50-60 nm in diameter and tens of micrometers in length. They reported that the Ostwald ripening process was indispensable to the accumulation of smaller nanoparticles into AgNRs and ultimately AgNWs. They also reported that increasing the temperature would result in formation of mere nanoparticles due to the alteration of interaction between the biomolecules and certain facets. Jeevika et al. used clove oil, as both reducing and capping agent to synthesize AgNWs with a diameter of 39 nm and length of 3 µm [296]. Clove oil is rich in eugenol, which is a phenolic compound. The reaction was carried out at room temperature and –OH functional groups from eugenol were found to be responsible for the synthesis of AgNWs. Eugenol molecules were also responsible for stabilizing AgNWs, as they can bind to the initially formed Ag seeds' facets and direct the growth. Soleimani et al. synthesized AgNRs with sharp and blunt ends using *F. oxysporum* as a reducing agent and starch as capping agent [375]. In their work, the reaction was carried out at 30 ºC for 3 days, with the pH adjusted at 3. For AgNRs with sharp ends, the average diameter and length were 181 nm and 4.3 µm, and for AgNRs with blunt ends, the average diameter and length were 204 nm and 3.9 µm, respectively. They reported that the initially formed Ag nucleus was single-crystal, and starch was able to cover {100} facets of the

NRs. It is also noteworthy to mention that other morphologies were obtained by changing the concentration of $AgNO_3$, temperature, pH, and reaction time. In another study, Gonzalez et al. used *Camellia Sinensis* extract in presence of a small concentration of PVP to synthesize AgNWs with dimensions of 50 nm in diameter and 1.3 µm in length [291]. *Camellia Sinensis* is a strong phenolic compound with significant antioxidant potential. The reaction was carried out at room temperature for 30 days under dark conditions. They reported that PVP was able to selectively adsorb to {100} and {111} facets, thus directing the growth of AgNWs. They also explained that the Ostwald ripening process resulted in attraction of the previously formed AgNPs, therefore leading to NW growth. However, it is important to note that at the beginning of the reaction, PVP was added to the reaction in the form of powder, and the temperature of the solution was kept at 45 ºC for complete dissolution of the PVP. Nadagouda et al. used vitamin B2 to synthesize AgNWs and AgNRs at room temperature for 24 hours [208]. In their study, AgNWs with diameters ranging from 10 to 20 nm and lengths of several hundreds of microns were obtained when isopropanol was used as solvent, and AgNRs structures were obtained with a thickness of 100 to 200 nm and lengths of tens of microns when acetone and acetonitrile were used as solvent. Hemmati et al. obtained AgNRs using brown sugar as both reducing and capping agent [203]. The AgNRs were around 50 nm thick in diameter and a few microns long. The reaction was performed at 50 °C for 2 hours.

The main advantage of the green synthesis of AgNWs is the fact that the selected green reagent can act as both capping and reducing agent at the same time, therefore triggering and continuing the reduction process while controlling growth. As a result, providing an additional capping agent such as PVP may not be required, which could reduce the overall material cost, since green reducing agents such as plant extracts are not expensive. Another important advantage is the possibility of performing the synthesis experiments at significantly lower temperatures compared to the polyol process, where temperatures of 120-200 ºC are required. Some reactions can even be

carried out at room temperature. This is quite beneficial in reducing energy consumption and risk, thus making the large-scale synthesis processes more cost-effective and safer. Another advantage is the fact that synthesis experiments may be performed without using exotic seeds and metal salts. Green reagents such as tannin and clove oil have shown that synthesis of AgNWs with high yield and aspect ratio is possible. As a result, if the responsible factors are identified properly, high aspect ratio and yield can be achieved, comparable to those achieved through the polyol process.

2.5. Effect of reaction parameters on green synthesis of 1D Ag nanostructure

The effect of reaction parameters such as pH, temperature, reducing agent concentration, and silver precursor concentration is crucial for the formation of 1D silver nanostructures such as AgNRs and AgNWs. To facilitate the growth of 1D nanostructures, the reaction conditions should be favorable to initiate an anisotropic growth of the seeds in a kinetically controlled synthesis process by adjusting and controlling the generation and deposition rate of silver atoms[376]. When the number of atoms for heterogeneous nucleation is lower than the growth sites on a seed surface, the seed is expected to undergo an anisotropic growth[377]. There are different ways to make this process possible. For instance, applying a relatively low temperature (i.e room temperature) can result in the suppression of adatomic diffusion, and consequently results in an anisotropic growth process[377]. However, this also depends on the reducing capability of the reagent at room temperature as well as its concentration, reaction pH, and metal precursor concentration. For instance, tannic acid, which is a hydrolysable form of tannin, has been used for the synthesis of both AgNPs and AgNWs[372,378,379]. Tannic acid has the potential to be hydrolyzed into glucose and gallic acid in weak basic/acidic conditions at room temperature[380,381]. Gallic acid can serve as a reducing agent while glucose serves as a stabilizing agent[382]. This promising dual property of tannic acid makes it usable as both reducing and capping agent. Reducing capability of gallic acid increases by increasing the pH[382]. In the case of AgNP synthesis at room

temperature and basic pH using tannic acid, gallic acid plays its role as a strong reducing agent while glucose acts as a strong stabilizing agent[383,384]. However, in the case of AgNW or AgNR synthesis at room temperature using tannic acid, the acidic pH is considered to be more favorable due to the slower reduction rate provided by gallic acid[379]. Three studies agree on the fact that acidic pH is more favorable for the growth of 1D nanostructures in the presence of tannic acid[295,372,379]. However, higher temperatures may not be favorable for anisotropic growth due to highly rapid nucleation. Two studies have considered the room temperature conditions to be more favorable for the growth of AgNWs in acidic pH and the presence of tannic acid[372,379]. However, only one study by Dong et al. reported elevated temperatures (50 ºC) to be more favorable for the formation of AgNWs[295]. Although they mentioned that this is due to difference in facet absorption energy at different temperatures, a clear and deep explanation remains disputed as why this difference occurs. The study on the effect of pH and temperature on the yield of 1D silver nanostructures using other green reagents remains limited.

The concentrations of the reducing agent and silver precursor are other important factors in controlling the yield of 1D Ag nanostructures. Yi et al. investigated the effect of tannic acid concentration on the yield of 1D nanostructures by changing its concentration from 5 to 1 mM while keeping the $AgNO_3$ concentration at 3 mM[379]. They demonstrated that the yield of 1D nanostructures such as nanorods increased as the tannic acid concentration decreased to 1 mM. This is also in accordance with the study by Tian et al. where they used a 1 mM tannic acid concentration[372]. This was attributed due to the sufficiently slow reduction process for the formation of single crystal nanowires. However, the mere effect of $AgNO_3$ concentration on the yield of 1D silver nanostructures was not investigated.

Considering the knowledge gap in green synthesis of 1D Ag nanostructures, it is essential to expand the number of green reducing agents for synthesis of 1D Ag nanostructures. Moreover, the future studies are expected to focus on effect of reaction parameters investigation on yield and

aspect ratio of 1D Ag nanostructures in these novel green and sustainable synthesis processes to not only tune the generation or deposition rate of silver atoms, but to control the surface diffusion rate of adatoms as well. Finally, due to the intrinsic instability of a 1D nanostructures because of their large surface to volume ratio, it is essential to manipulate the reaction conditions and parameters to preserve their 1D structure during the green synthesis process.

2.6. Current state and key challenges in green synthesis of 1D Ag nanostructures

There are few green and sustainable methods of 1D synthesis of Ag Nanostructures in which most of the synthesis are in small-scale for a feasibility study. There are also inherent challenges in batch synthesis, such as challenges in batch-to-batch reproducibility. Moreover, there is a lack of fundamental understanding behind the synthesis reaction mechanism, and the functionality and responsibility of the specific compounds are not well understood. Without this fundamental knowledge, it is not possible to control and tune the size and morphology of the synthesized 1D Ag nanostructures, and there is a broad size distribution as well. By understanding the role of each functional group in the reduction, nucleation, and growth of silver nanostructures, it would be possible to predict the applicability of the other novel green reducing agents offered by nature for silver and consequently other 1D metal nanostructures synthesis.

2.6.1. Inherent challenges in batch small-scale green synthesis of 1D silver nanostructures

A major gap in green 1D silver nanostructure synthesis processes resides in the small-scale of their production with low efficiency and predictability, which has not been implemented beyond the bench. The reasonable control of the synthesis process of green synthesized 1D silver nanostructures is still a challenge in their batch synthesis along with the challenges in batch-to-batch reproducibility. It is essential to investigate the effect of all of the reaction parameters on the size and morphology of the synthesized 1D Ag nanostructures, and find the most essential parameters that predominately control the morphology and yield of 1D Ag nanostructures.

Moreover, it is important to investigate not only the simultaneous effect of these parameters but also, to find the optimal reaction conditions at which the yield of 1D Ag nanostructures is maximized.

2.6.2. Lack of recipe in green synthesis of 1D silver nanostructures

Countless numbers of plant extracts from different parts of plants have been reported for the synthesis of silver nanoparticles. Although there are many published studies regarding the green synthesis of silver nanoparticles, there are comparatively few regarding 1D ones. Moreover, among these few studies, some of them are by the assistance of microwave or ultraviolet irradiation process and high energy requirements. Not only there are few studies, but all of them are in very small-scale reactions with low yield of 1D nanostructures compared to other nanostructures. This indicates a huge gap in green synthesis of 1D Ag nanostructures and the necessity to expand the number of green reducing agents, specifically plant-based ones offered by nature for synthesis of 1D Ag nanostructures.

2.6.3. Lack of fundamental understanding behind the green synthesis of 1D silver nanostructures

The concept of size, morphology, and shape control of silver nanostructures can be achieved by investigation of the growth mechanism and adjusting synthetic parameters. The advantages of utilizing different green reducing agents such as plants and plant-derived reagents for silver nanoparticle synthesis have been of interest in studies to evaluate the mechanism behind the synthesis process including uptake of the metal ions, their bioreduction, and the possible growth route for nanoparticle formation. However, there is a lack of fundamental knowledge regarding the reaction mechanism of green synthesis of 1D silver nanostructures, specifically environmentally friendly large-scale synthesis, a process with strong potential to overcome the challenges in chemical synthesis of 1D silver nanostructures. After finding the specific biochemical compound(s) or ingredient(s) in the green reducing agents that is responsible for the

reduction of metal ions and consequently growth of nanoparticles to a desired morphology, it is essential to investigate the reaction mechanism, which would be crucial to control the reaction and consequently control the size, shape, and morphology of the synthesized 1D silver nanostructures. This would be achievable by understanding the exact route including reduction, nucleation, and growth of their green and sustainable synthesis process.

2.7. Lessons from green Synthesis of silver nanoparticles towards green synthesis of 1D silver nanostructures

Many green reagents can act as reducing and capping/stabilizing agent at the same time. However, this depends on the reaction mechanism and molecular structure of the reagent and its ingredients including particular functional groups such as amines, aldehydes, and carboxylates, to name a few [203]. Understanding the reaction mechanism is essential to tune and control the size and morphology-dependent properties of silver nanostructures. An important aspect in achieving 1D Ag nanostructure is identifying key factors controlling the stabilization and growth of initially-formed Ag seeds. Nevertheless, a clear description of how natural organic molecules can direct growth of AgNWs remains absent and only a few studies have discussed a possible mechanism in that regard. Fortunately, the mechanism of AgNWs synthesis via the polyol process is better understood and can be a useful guide in understanding the reduction process and diagnosis of responsible functional groups and binding mechanisms which direct the growth of 1D Ag nanostructures in a green synthesis process. In the case of polyol synthesis, PVP controls the capping/stabilizing mechanism, ethylene glycol controls the reduction process, and the temperature and the pH are among the factors that control the kinetics. In the polyol process, PVP binds to {100} facets of initially-formed seeds through Ag-O bonding [203], and directs the growth through the {111} facet (figure 2.2). In fact, the adsorption on {100} facets shall be much stronger compared to {111} facets for the growth to take place [94]. In the study performed by Lin et al., polyhydroxy components such as alkaloids, flavonoids, and polysaccharides acted as

capping ligands for the growth of AgNWs [374]. Many of the mentioned components contain carbonyl groups similar to PVP, which could possibly be responsible for ligand bonding. In addition, Lin et al. stated that the Ostwald ripening process was one of the factors in growth of AgNWs, which was also reported previously in the polyol process [385].

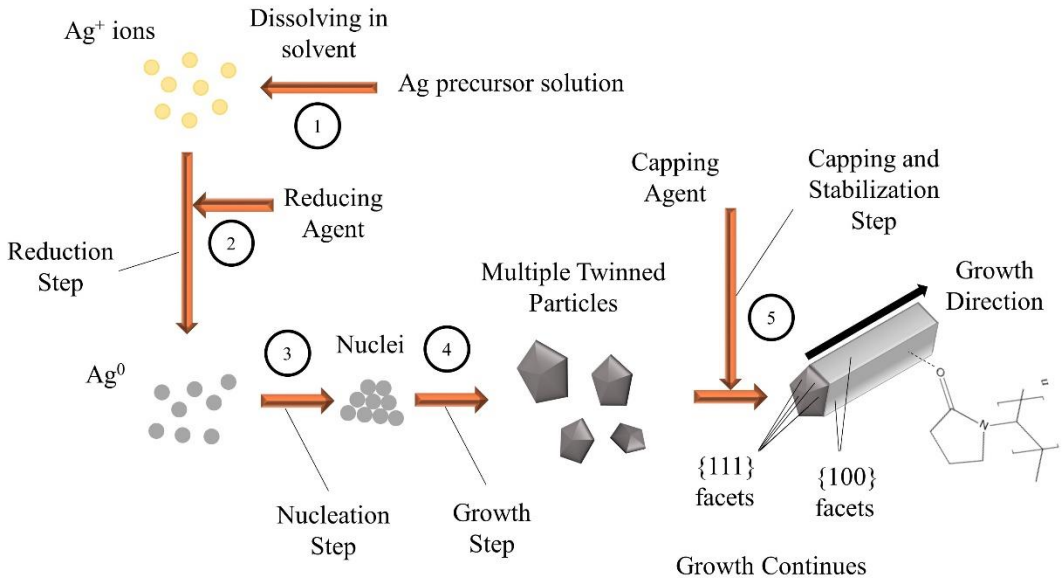

Figure 2.2: Synthesis steps and reaction mechanism for AgNWs polyol synthesis.

In another study performed by Dong et al., the tannin molecules bound to four {100} facets of AgNWs, leaving two other {100} facets free for growth [295]. Tannin molecule also has carbonyl groups, which might have been taking part in formation of ligand bonds. In a recent work, Villalpando et al. used Lavandula angustifolia extract to synthesize AgNWs [386]. They mentioned that some compounds such as saponins and glycosidics that are present in the extract [387], are responsible for 1D growth of nanostructures. However, Ag-ligand interactions are part of a larger chain in the synthesis process and are related to other factors such as reduction rate, complex formation, and temperature. For instance, as mentioned earlier in the study conducted by Dong et al., higher temperatures (>50 ºC) made the conditions difficult for tannin molecules to effectively

bind themselves (due to lack of adequate time) to {100} facets of AgNWs, in which case nanoparticles were formed instead of nanowires [295]. In addition, tannin molecules are able to form stable complexes with Ag^+ ions [373], which results in decreasing the reduction rate, paving the way for 1D anisotropic growth [388]. It was also previously mentioned that acidic pH is more in favor of AgNW formation due to moderation of reduction rate [295,379]. For instance, Dong et al. showed that the yield of AgNWs decreased by increasing the pH up to 9, while the yield increased by lowering the pH to 5 [295]. However, further decrease resulted in a smaller yield, which was attributed to an excessive decrease in reduction rate. Nadagouda et al. synthesized AgNRs in the presence of vitamin B2 in aqueous solution and reported that the self-assembly of AgNRs was due to strong interparticle Van-der-Waals and hydrophobic interactions [208]. The use of exotic seeds was therefore not needed due to the self-assembly. In addition, vitamin B2 was able to form complexes with Ag^+ ions and help to reduce the reaction rate, which leads to anisotropic growth of AgNRs. Wang et al. synthesized AgNWs using glucose in hydrothermal conditions (180 °C and under autoclave), and reported that the lower the concentration of Ag^+, the more favorable the anisotropic growth of AgNWs. They added NaCl to the $AgNO_3$ solution in order to form AgCl colloids. Due to low solubility of AgCl in water, the concentration of Ag^+ is low at 180 °C, which was favorable to growth of AgNWs. On the contrary, AgNPs were formed when only $AgNO_3$ was used. In the latter condition, the reduction rate of Ag^+ ions is higher, which does not allow growth of AgNWs. Another important factor is the diffusion of initially formed seeds. Villalpando et al. recently reported that centrifugation is able to enhance the diffusion rate and therefore favor the growth of AgNWs [386]. They reported that AgNW growth is affected by coalescence and interparticle diffusion mechanism as a result of a secondary nucleation process, where smaller particles are coalesced into forming AgNWs, as described previously [389]. Enhancement of diffusion and growth of AgNWs using magnetic stirring was also reported previously [390].

2.8. Conclusion

The synthesis process is substantial to determine the size and morphology of Ag nanostructures. The green procedures for synthesis of silver nanostructures in addition to the most common chemical and physical methods were reviewed. The advantages of green synthesis methodologies, such as their low cost, low energy consumption, scale-up capability, and simplicity that outweighs their disadvantages compared to the chemical and physical synthesis methodologies were discussed. Green synthesis processes were classified, among which synthesis of Ag nanostructures using plant extracts are considered to be a promising route due to their simple utilization, aqueous nature, and non-toxic properties. Plant extracts are likely to contain certain natural compounds such as polyphenols, flavonoids, alkaloids, and different functional groups such as hydroxyls and carboxylic acids, which can provide strong reducing and capping capability. Due to their broad scope, plant extracts are used for preparation of various Ag nanostructures with different sizes, and the literature studies on this subject have been growing during the last decade. The different green reagents based on studies in the literature at different reaction conditions to synthesize Ag nanostructures with different sizes and morphologies were outlined. In addition to reagent type, synthesis of Ag nanostructures using plant extracts is highly dependent on various process factors such as temperature, reagent concentration, and pH that were discussed. Green synthesis of AgNWs using plant extracts is gaining more attention and various compounds such as tannins, glucose, clove oil, and other natural extracts may be used as both reducing and capping agents to synthesize 1D Ag nanostructures. Unlike the polyol process, the green route consumes much less energy and is simpler. The aspect ratio of 1D Ag nanostructures is dependent on the temperature, pH, solvent, and reagent type. The 1D Ag nanostructure formation mechanism, and how those factors can be tailored to increase their yield were discussed. The advantages of the green synthesis technique make it a valid and promising

platform for facile and high-yield synthesis of 1D Ag nanostructures such as AgNRs and AgNWs.

The current advances in *in-situ* quantitative understanding using different instrumentation in the course of the reaction, including reduction, nucleation, and growth, will allow precise control of the size and morphology of metal nanostructures. *In-situ* UV-vis can be used not only to investigate the optical properties of metal nanoparticles, but to monitor their quantitative formation and size as well. *In-situ* FTIR spectroscopy can be used to find the different functional groups responsible for the reduction of metal ions and stabilization of metal nanoparticles from the peak positions in the spectrum. Future research is expected to focus on integration of these *in-situ* characterization techniques to the batch green synthesis of 1D silver nanostructures to come up with the exact reaction mechanism, and consequently not only to control their size and morphology, but to expand the number of reducing and capping agents offered by nature for the synthesis of 1D silver nanostructures as well. Moreover, future research is expected to focus on large-scale industry relevant scale 1D silver nanostructure production in a green, sustainable, and continuous manner. The design of novel laboratory flow reactors has the potential to reduce waste, minimize the building space and energy requirements, and yield more accurate predictive models during development and manufacturing. The flow reactors, such as microfluidic reactors, offer uniform heat and mass transfer, more homogenous mixing of reagents, higher yield, and throughput, and are adaptable for *in-situ* monitoring characterizations. However, microfluidic devices' fabrication is time and resource-sensitive, and requiring complicated facilities that support the advantages of millifluidic flow reactors in nanoparticle synthesis. These novel reactor systems offer similar advantages to microfluidic ones, while being easier to fabricate, simpler to reconstruct, and even more adaptable for *in-situ* monitoring characterizations. Larger surface to volume ratio and precisely controlled flow patterns that consequently increase heat and mass transfer rate, coupled with inherent safety are among other advantages of flow millifluidic

platforms [4,70,391]. Application of a continuous millifluidic reactor has potential to be a method to overcome the challenges in batch green 1D silver nanostructure synthesis through control of a uniform chemical and thermal reaction environment in a small reaction volume. Novel *in-situ* characterization techniques are essential for reaction mechanism investigation to control the morphology of the synthesized 1D Ag nanostructures in a continuous millifluidic reaction as well. *In-situ* X-ray absorption spectroscopy (XAS) is a versatile technique that provides an opportunity to investigate the reaction dynamic and mechanism of 1D metal nanostructure growth in millifluidic reactor to further control their morphology, size distribution, and crystal structures. This expected future research direction will enable a synthesis route where 1D Ag nanostructure properties can be selected and tuned by simple alteration of reaction parameters and millifluidic reactor design to produce these nanostructures in an industrial relative scale in a green and sustainable manner. Furthermore, it is critical to optimize these green and sustainable techniques, not only in terms of scale-up capability, but also in aspects of product quality and performance. Finally, the Artificial Neural Network (ANN) tools application in nanomaterial synthesis such as 1D silver nanostructures will prime to save time and expenditure by predicting the reactions' outcomes in which the most desirable nanomaterial size, morphology, and yield is achieved. Data from different characterization techniques including scanning electron microscopy (SEM), transmission electron microscopy (TEM), UV-visible spectroscopy (UV-vis), Fourier transfer infrared spectroscopy (FTIR), and X-ray absorption spectroscopy (XAS) may be utilized to train the network to optimize the green synthesis of metal nanostructures as well as to predict the size and morphology of the synthesized metal nanostructures at different reaction conditions. It will consequently have a significant impact on industrial large-scale manufacturing of metal nanostructures, in which new molecule discovery as well as the development of alternatives to existing chemical processes will be discovered. Ultimately it will address the principal need in coupling green metal nanostructure synthesis, novel *in-situ* characterization techniques, and

Artificial Intelligence (AI) tools. A schematic on future direction in green and sustainable synthesis of Ag nanostructures with focus on 1D ones is shown in figure 2.3.

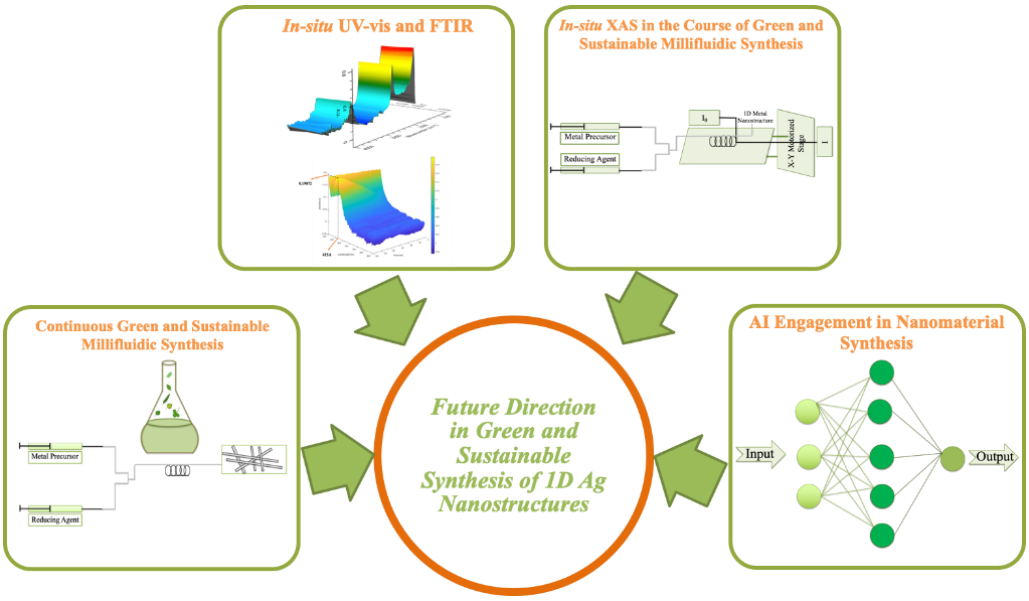

Figure 2.3: Expected future direction in green and sustainable synthesis of 1D Ag nanostructures.

CHAPTER III

GREEN, SUSTAINABLE, AND ROOM-TEMPERATURE SYNTHESIS OF SILVER NANOWIRES USING TANNIC ACID – KINETIC AND PARAMETRIC STUDY

3.1. Introduction

Commercially available nanomaterial-based goods and products have already been impacted by unique characteristics of nanomaterials such as metal nanostructures; however, inherent challenges in their precisely controlled large-scale synthesis in a sustainable manner restrain their impacts to the fullest. Uniform size, morphology, and size distribution in the synthesis processes are essential to eliminate or minimize the heterogeneity in downstream nanomanufacturing processes, which is a fundamental challenge. The additional expenditure for the safety and sustainability of large-scale metal nanostructure synthesis and their transfer from the small laboratory scale to the large industrial scale is also worth considering. The nanoscience and nanotechnology research for the green and sustainable synthesis of noble metal nanostructures has been gaining considerable attention during the last two decades. Potential environmental impacts, safety issues, scale-up challenges, and costs regarding the production of nanomaterials have led many researchers to come up with novel approaches for the synthesis of nanomaterials without needing to use hazardous substances, high-energy processes, and expensive instruments.

The green synthesis of noble metal nanostructures can be defined as a set of sustainable, environmentally friendly, and inherently safe methodologies performed under the green chemistry metrics, including inhibition of waste generation, maximizing the product yield with respect to material consumption, using less- or non-hazardous chemicals, using energy-efficient processes, and using renewable and naturally-degradable materials[270]. Although there are many published studies regarding the green synthesis of Ag nanostructures, there are comparatively few regarding 1D ones such as AgNWs. Not only are there few studies, but most are carried out in very small-scale reactions with very low yield of 1D nanostructures. This indicates a huge gap in the green synthesis of 1D Ag nanostructures and the necessity to expand the number of green reducing agents, specifically plant-based ones offered by nature. There is also a lack of fundamental knowledge regarding the kinetic and thermodynamic factors' influence on the green and sustainable synthesis of 1D Ag nanostructures. Monitoring reagent consumption and AgNW formation is essential to find out the reaction mechanism behind the synthesis to transfer to industrial-demand production through scale up. One of the first steps in the green synthesis of metal nanostructures is the selection of green reducing and capping/stabilizing agents. Thanks to more than a decade-long research, this can be achieved by selecting from a wide variety of reagents including plant-based ones such as sugars[203,392], vitamins[305,306,393], polyphenols[394,395], and other types of plant extracts, as well as microorganisms such as fungus[176,178], bacteria[284,285], microalgae[279,396], yeasts[182,183], and plant-based viruses[265,278]. Among these reagents, a strong attention has been paid to plant derivatives and extracts since microorganisms can be pathogenic (i.e. bacteriogenic and fungal species), and they often suffer from low reduction rate and low productivity[1]. Plant extracts can be more favorable due to non-pathogenic behavior, higher reduction rate, higher productivity, versatility, simplicity, low cost, and the possibility of scale-up[1,190]. Among those, polyphenols, in particular, are promising candidates to act as both reducing and capping/stabilizing agents for the synthesis of noble metal nanostructures[144,190,386] such as gold and silver[380,395], and can be found in abundance. In fact, one of

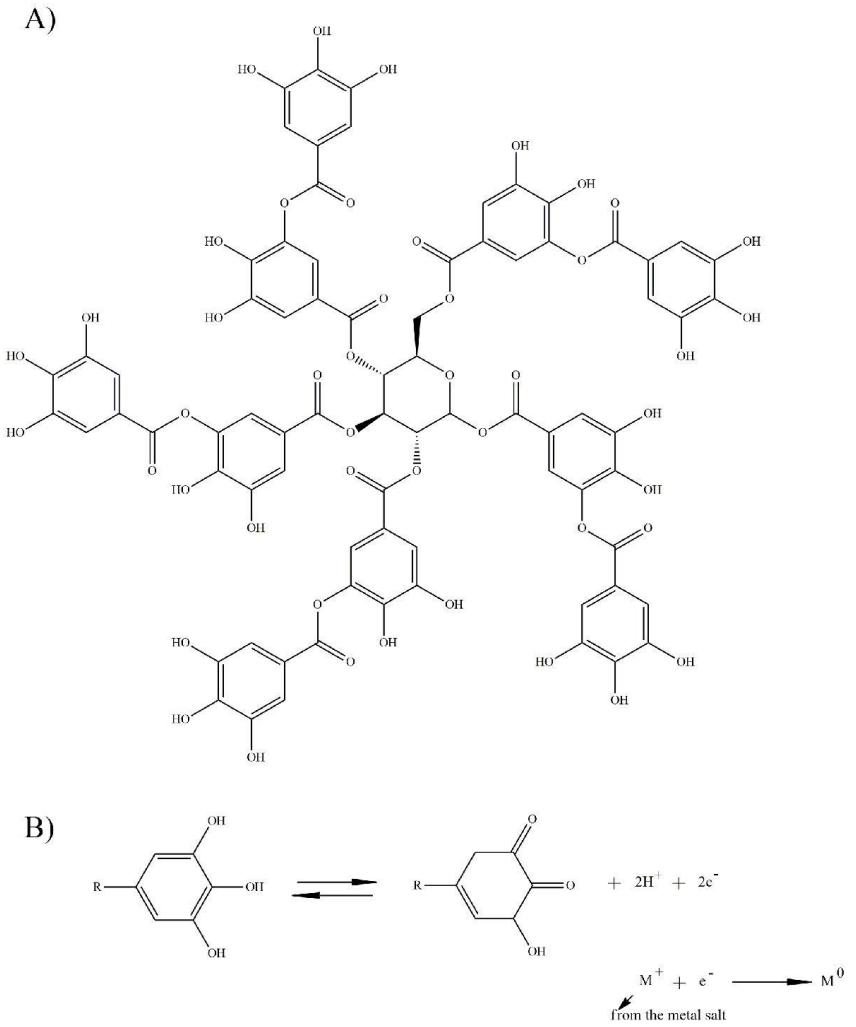

Figure 3.1: A) Chemical structure of tannic acid, B) Transformation of galloyl residues to the quinone form during the reduction of metal cations.

the reasons that plant extract-synthesis of noble metal nanostructures has emerged as a popular approach is due to the rich presence of polyphenolic compounds in most types of plant extracts[309,319,324]. Polyphenols have multiple hydroxyl functional groups, which are responsible for the reduction of positive metallic ions to the atomic form with neutral charge, which lead to nuclei formation and consequent crystal growth and ultimately the formation of metal nanostructures. In particular, tannins are highly abundant and are phenolic compounds with the ability to synthesize silver nanostructures with different morphologies. Tannins are classified into three types including hydrolyzable, condensed, and pseudo/phloro tannins[397,398]. Tannic acid that is a hydrolyzable form

of tannin, also known as a type of gallotannin, is a form in which the central position in its molecule is occupied by glucose surrounded by multiple galloyl residues (Figure 3.1.A), is a promising candidate as a reducing agent for the synthesis of silver nanostructures [382,399]. Due to the highly-dense presence of hydroxyl groups, inter- and intra-molecular hydrogen bonding occurs[378]. The intermolecular hydrogen bonds facilitate the transport of metal ions into the molecular cage of tannic acid, which then will be reduced to the neutral atomic form[378]. The reaction mechanism for the reduction of Ag^+ to Ag^0 is as follows: the phenolic groups in galloyls interfere in the redox process by transforming into the quinone form and donating electrons, which then will trigger the reduction of silver cations to silver atoms (Figure 3.1.B)[382]. Tannic acid has 25 phenolic hydroxyls with only 10 pairs of *o*-dihydroxyphenyls being capable of taking part in the redox reaction[379,399]. In fact, only two of the hydroxyls in each galloyl group at the meta and para positions of the benzene ring (ortho or para positions with respect to each other) donate electrons and transform into the quinone form (Figure 3.1.B)[379]. As a result, each tannic acid molecule is capable of donating 20 electrons to Ag^+ ions, in which a molar ratio of 0.05 (tannic acid to Ag^+ ions) satisfies the stoichiometric equivalency[399]. In addition, the electron donation and transformation to the quinone form is supported by the chelating activity of the *o*-dihydroxyphenyl derivatives and limitations on carbon valency[379,397,400]. Chelation of Ag^+ ions is important in controlling the reduction rate. Tannic acid is capable of chelating Ag^+ ions, and can decrease the number of free Ag^+ ions in the solution, which results in a decrease in the reduction rate[399,401,402].

Naturally, tannic acid has mild acidic properties and can act as a weak reducing agent for the formation of metal nanostructures at room temperature[380,399]. However, tannic acid can be partially hydrolyzed into glucose and gallic acid in weak basic/acidic conditions[380,381]. For silver nanostructure synthesis, gallic acid at room temperature and basic conditions, will enhance the reduction process and therefore, will quickly result in the formation of nanoparticles[383], while not stabilizing the nanoparticles to prevent aggregation. Glucose, on the other hand, is a weak reducing

agent but is a strong stabilizing agent, which results in the stabilization of nanoparticles[384]. By combining these two effects, tannic acid can be used as both reducing and capping/stabilizing agents for the synthesis of metal nanostructures, including silver and gold, which has been reported previously[372,403–405].

One of the first studies on the synthesis of silver nanoparticles using tannic acid was carried out in 2007 by Tian et al.[380]. They were able to synthesize silver nanoplates in a two-step process by initially synthesizing silver seeds using sodium borohydride (used for the formation of seeds) in the presence of trisodium citrate. Afterward, they mixed the tannic acid (1 mM) and $AgNO_3$ (5 mM) solutions and maintained the synthesis solution at room temperature for 12 hours. The synthesized silver nanostructures had triangular and hexagonal morphologies along with other nanostructures with irregular morphologies. They also demonstrated that a decrease in the number of seeds resulted in a lower reduction rate, which was necessary for the formation of silver nanowires (AgNWs). Two years later, they came up with the seed-free synthesis method using tannic acid without needing to use any additional capping agents or surfactants[372]. The synthesis conditions were similar to their previous study, except that the initially synthesized seeds were not used in the process. They obtained a 5-10 % yield (percentage of nanowires relative to other nanostructures) of AgNWs, which were 25 nm in diameter on average, and as long as 4 μm in length. They reported that the slow reduction rate, due to the low temperature and low tannic acid concentration was in favor of the formation of twinned silver seeds with decahedron morphologies as well as anisotropic growth. In another study, Sivaraman et al.[399] synthesized silver nanoparticles with sizes between 3.3 to 22.1 nm using tannic acid at alkaline condition (pH=8). They showed that the molar ratio of tannic acid to $AgNO_3$ was a crucial factor to control the nucleation and growth of silver nanoparticles. It was reported that a molar ratio of 0.05 resulted in a more rapid formation of nanoparticles compared to the molar ratio of 1. This was attributed to the saturation of tannic acid complexes with 20 Ag atoms at the molar ratio of 0.05, which allowed faster nucleation. In

the same year, Bulut et al.[378] synthesized silver nanoparticles with spherical morphology using tannic acid. They demonstrated using Fourier-transform infrared spectroscopy (FTIR) that the phenolic groups from the galloyl units were responsible for the reduction as well as surface stabilization of the silver nanoparticles. Later in 2011, Yi et al.[379] investigated the effect of tannic acid concentration and pH on the morphology of silver nanostructures synthesized at room temperature. They showed that acidic pH was more in favor of the formation of one-dimensional (1D) nanostructures. The relatively weak reduction rate at slightly acidic pH (6) was favorable for the growth of AgNWs. More recently, Hao et al.[406] synthesized spherical silver nanostructures using tannic acid at room temperature. They showed that an increase in the molar ratio of tannic acid to silver ions resulted in a decrease in the particle size. However, it is important to note that ammonia was used as the solvent for $AgNO_3$, and tannic acid was mixed with the silver-ammonia solution ($Ag(NH_3)_2^+$). They were able to obtain nanoparticles as small as 6.4 nm by adjusting the molar ratio of tannic acid to silver-ammonia to 0.4.

Although many studies have used tannic acid as both reducing and capping/stabilizing agents for the synthesis of silver nanoparticles, a detailed investigation on how the yield of AgNWs is affected by various reaction conditions remains absent. The tannic acid-mediated synthesis of AgNWs can be highly sensitive to certain reaction conditions such as light and pH. In addition, understanding the underlying mechanisms for how reduction kinetics control the nucleation and growth is beneficial for understanding how the anisotropic growth of AgNWs occurs when tannic acid is used as both the reducing and capping/stabilizing agents. The current polyol process, which is commonly used for the synthesis of AgNWs, is relatively energy consuming and requires an additional capping agent (PVP) and salt mediator (i.e. $CuCl_2$, NaCl), thus increasing material and energy consumption. In addition, the cost of raw materials is higher compared to tannic acid, which poses economic challenges for the large-scale synthesis of AgNWs. Despite the advantages offered by the tannic acid-mediated synthesis of AgNWs compared to the polyol

process; however, the yield of AgNWs is typically low. As mentioned previously, the synthesis of AgNWs using tannic acid has been already carried out by only a few studies previously [23,32,39], yet such processes not only suffer from a low yield (5-10% or lower), but there is also a lack of understanding regarding the underlying mechanisms, such as the reduction kinetics. In addition, it is not clear how light affected those synthesis processes, which is a crucial factor in controlling the reduction rate and the formation of AgNWs when tannic acid is used as both the reducing and capping agent based on our study. In this study, we reported the synthesis of AgNWs using tannic acid with moderate yield (~50%) and analyzed the photosensitivity of the synthesis reaction at three different illumination conditions. We provided a kinetic model that describes the Ag^{+} reduction to Ag^{0} during the course of reaction for each illumination condition. We also discussed the underlying mechanisms that favor the anisotropic growth of nanostructures and investigated the effect of different reaction parameters including tannic acid/silver nitrate molar ratio, pH, and stirring rate on the yield of AgNWs. To the best of our knowledge, this is the first study to analyze the photosensitivity of tannic acid-mediated synthesis of AgNWs, and the first study to report the synthesis of AgNWs using tannic acid with moderate yield. The cheaply-synthesized AgNWs may be used for the preparation of conductive inks used for manufacturing eco-friendly transparent conductive films (Eco-TCFs)[107,362]. Finally, the fundamental knowledge gained in this study is the critical foundation to further advance the green and sustainable metal nanostructure synthesis.

3.2. Experimental methodology

3.2.1. Materials and methods

Silver nitrate ($AgNO_3$, MW: 169.87 g/mol, product number: S0139), tannic acid (MW: 1701.2 g/mol, product number: 403040), 2,4,5,7-Tetrabromofluorescein (TBF) also commercially known as Eosin Y (MW: 647.89 g/mol, product number: E4009), 1,10 Phenanothroline (PHEN, MW:

180.21 g/mol, product number: P13002), sodium hydroxide (NaOH, MW: 40 g/mol, product number: 415413), and sodium acetate (MW:82.03 g/mol, product number: S2889) were all purchased from Sigma Aldrich. Deionized water (DIW, ASTM type II) was used as the solvent to prepare aqueous $AgNO_3$ and tannic acid solutions. The synthesis process was carried out in batch processes by mixing the $AgNO_3$ and tannic acid solutions in 100 mL round glass flasks. The mixing in the flask was controlled by a magnetic stirring bar.

3.2.2. Synthesis of silver nanostructures using tannic acid

In a typical batch experiment, 20 mL of the tannic acid solution (5 mM) was added to the 100 mL three-necked glass flasks followed by the dropwise addition of 20 mL $AgNO_3$ solution (5 mM) using Pasteur pipettes. Prior to the addition of $AgNO_3$, the pH of tannic acid was adjusted to 4 by adding sodium hydroxide (NaOH, 0.1 M solution). A magnetic stirring bar rotating at 300 RPM was also used for mixing. To investigate the effect of light on the synthesis of silver nanostructures, the reaction was carried out in three different conditions including fully illuminated, partially illuminated, and dark. In the fully illuminated condition, the glass flask was exposed to white fluorescent lamps (25 Watts T8 Philips white fluorescent lamps, provided by Energy Advantage) in the laboratory without having any physical covering. In this case, the value of the incident light intensity being irradiated to the solution inside the flask was measured to be 676 LUX. In the partially illuminated condition, the glass flask was partially covered with aluminum foil in a way that the solution was exposed to the light only through the three top necks of the flask. In this case, the value of the incident light intensity to the solution inside the reaction flask was measured to be 90 LUX. In the dark condition, the flask was completely covered with aluminum foil and the solution had no exposure to the light. For all conditions, the reaction continued for 4 hours and was maintained at room temperature. The light conditions, for all three experiments, were sustained throughout the reaction process. After the completion of the experiments, the samples were diluted with deionized water and centrifuged multiple times at 3,000 RPM for 30 minutes. Furthermore, to

do a parametric study, different tannic acid/silver nitrate concentration ratios (0.2, 0.6, 1, 1.66, and 5), pH (4, 5, and 6), and stirring rates (0, 300, and 600 rpm) were tested at partially illumination condition for the synthesis of AgNWs.

3.2.3. Ag^+ concentration measurement

To observe the change in Ag^+ consumption, the concentration of Ag^+ ions was measured using a method similar to a spectrophotometric approach first introduced by El-Ghamri and Frei[407]. In this method, TBF and PHEN were used as the compounds able to form a complex with Ag^+ ions. This complex was shown to be in the form of $[PHEN.Ag\text{-}PHEN]_2^+TBF^{2-}$ in an aqueous solution[407]. This complex is detectable by the UV-visible (UV-vis) spectroscopy by showing a peak at 550 nm. Both PHEN and TBF were used in the form of powder. The PHEN solution (4.5×10^{-3} M) was prepared by dissolving the powder in ethanol (99%). The TBF solution (1.5×10^{-3} M) was prepared in the same manner by dissolving the powder in ethanol. In addition, 40 mL of acetate buffer solution with a pH of 5.2 was prepared by dissolving sodium acetate (0.25 g) and acetic acid (54 µL) in deionized water. In order to prepare the TBF-PHEN mixture that was used to prepare the complex mixture, 1 mL of PHEN and 1 mL of TBF were added to 18 mL of the acetate buffer solution. The complex mixture was prepared by mixing 500 µL of the PHEN-TBF mixture with 500 µL of $AgNO_3$ solution with different known concentrations. The absorbance was measured using UV-vis spectroscopy, in which the absorbance peak at 550 nm for each sample corresponds to its specific Ag^+ concentration. A calibration curve

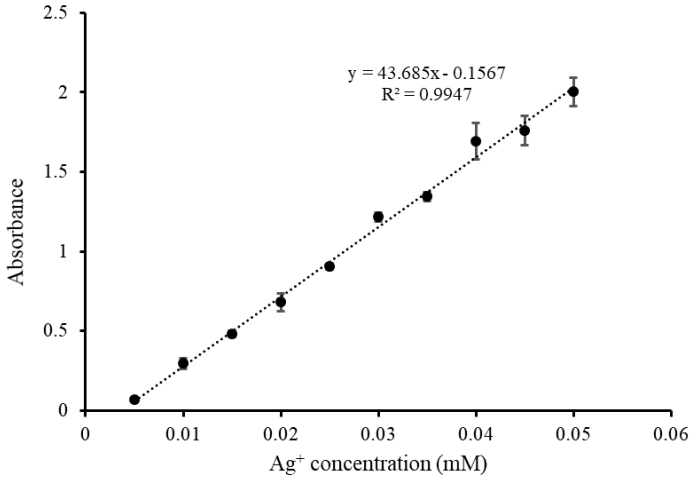

Figure 3.2: Calibration curve of Ag^+ concentration with respect to the PHEN-TBF-Ag^+ complex absorbance peak.

was obtained by correlating the absorbance peak at 550 nm to Ag^+ concentration (Figure 3.2). This calibration curve was used to calculate the Ag^+ concentration in the synthesis solution.

In order to measure the absorbance associated to Ag^+ ions in the synthesis solution, 500 µL of the diluted synthesis sample using DIW (49 times) was mixed with 500 µL of PHEN-TBF to create the PHEN-TBF-Ag^+ complex. In this case, 500 µL of deionized water was mixed with 500 µL PHEN-TBF to serve as the blank. The absorbance measurements were taken immediately after taking aliquots from the synthesis solution and repeated every 30 minutes for the three different illumination conditions. In addition, the absorbance of the synthesis solution was measured by mixing 500 µL of the diluted synthesis solution with 500 µL deionized water. In this case, deionized water was used as the blank. In order to remove the absorbance offset caused by tannic acid and the synthesized nanostructures, the absorbance of the diluted synthesis solution was subtracted from the PHEN-TBF-Ag^+ mixture absorbance. All measurements were taken in triplicates.

3.2.4. Characterization

3.2.4.1. Scanning electron microscopy (SEM)

SEM imaging was carried out by the FEI Quanta 600 field-emission gun Environmental Scanning Electron Microscope at the Oklahoma State University microscopy laboratory. To prepare the samples for imaging, 100 µL of the centrifuged sample was pipetted unto smooth carbon tabs placed on aluminum pins. The SEM samples were kept at room temperature conditions for 24 hours to allow for water evaporation. The aluminum pins containing the nanostructures were then placed inside the SEM sample holder for analysis.

3.2.4.2. Transmission electron microscopy (TEM)

TEM imaging was carried out by the JEOL JEM-2100 Scanning Transmission Electron Microscope System (200 kV accelerating voltage) at the Oklahoma State University microscopy laboratory.

The samples were prepared by pipetting 10 µL of the sample on carbon grids. The carbon grids were then placed inside the TEM sample holder for analysis after solvent removal.

3.2.4.3. Energy dispersive X-Ray spectroscopy (EDS)

The EDS analysis was carried out using a built-in Evex Nanoanalysis EDS system in the TEM instrument.

3.2.4.4. UV-visible spectroscopy (UV-vis)

The UV-visible spectroscopy was carried out using the Metler Toledo UV5 spectrophotometer. The measurements (wavelength from 190-1100 nm) were taken after pipetting the solution into 3 mL cuvettes.

3.2.4.5. X-ray diffraction (XRD)

XRD characterization was carried out using the Bruker D8 Advance XRD at the Oklahoma State University microscopy laboratory. The sample powder was obtained from the dried sample. The powder was loaded unto silicone sample holders and placed inside the sample chamber.

3.2.4.6. pH measurements

The pH of the samples was measured using the Thermo Scientific Orion Star A211 pH meter with the Orion 8102BNUWP probe.

3.2.4.7. Light measurements

The light intensity (in LUX) was measured using a Dr. Meter 1330B-V digital light meter for all illumination conditions.

3.3. Results and discussion

Tannic acid has a dual role of reduction and capping/stabilizing in the synthesis of metallic nanostructures due to the presence of gallic acid and glucose in the tannic acid molecule[295,372,378,379,382]. It is possible to tune these two effects by changing the reaction conditions such as light, pH, tannic acid concentration, and temperature. Such changes will then result in different reduction rates that affect nucleation and growth, thus resulting in different nanostructure sizes and morphologies. The concentration of $AgNO_3$ and its ratio with respect to tannic acid concentration as well as mixing are other effective factors that affect the size and morphology of silver nanostructures. As a result, a parametric study including the effect of those factors is crucial to determine how the morphology and size of the silver nanostructures are affected. This is useful in optimizing the desired yield of silver nanostructures (i.e. AgNWs in this study). Initially, in this work, the photosensitivity of the synthesis reaction has been investigated in three different illumination conditions, and the change of Ag^+ concentration with respect to time was obtained. Furthermore, the effects of tannic acid/silver nitrate molar ratio, pH, and stirring rate on the size and morphology of silver nanostructures, and more importantly on the yield of AgNWs were investigated. The morphology of silver nanostructures was varied in all scenarios and the SEM images showed polygonal, triangular, spherical, wire-shaped, and rod-shaped structures. A direct correspondence of these morphologies to specific reaction conditions and calculating their precise yield are challenging due to irregular and varied shapes; however, it is possible to see how the yield of some morphologies (i.e. wire-shaped structures) increases or decreases depending on the reaction condition.

3.3.1. Photosensitivity analysis for the synthesis of AgNWs

One of the important factors that is often ignored in most synthesis processes is the photo-induced reduction of metal ions for the synthesis of metallic nanoparticles. The photo-induced synthesis of metallic nanoparticles is advantageous in terms of being a clean process, and being able to generate reductant intermediates (i.e. free radicals) in the solution[408]. This process is highly versatile and may be used to assist the synthesis of nanoparticles regardless of the solution medium type[408]. The photo-induced reduction of metal ions can generally be classified into three different categories, including direct photoreduction, photosensitized reduction, and photocatalytic deposition[408]. The first category includes the set of processes that occur due to the excitation of either the solvent[409,410], chelate complexes[411,412], or metal acetylides[413,414], which act as electron donors. The second category includes the processes that occur due to the formation of intermediates such as excited radicals that facilitate the reduction of metal ions[415,416]. The third category is facilitated by reduction on a semiconductor surface where electrons and positive holes are generated due to the semiconductor photo-absorption[417–419]. The photo-induced reduction of metal ions is highly dependent on the light intensity (the amount of photons going into the system) and the light energy (wavelength of the photons)[420]. Upon the absorption of light by an electron-donor compound, electron transfer from a low-energy state to a high-energy state occurs (i.e. from the highest

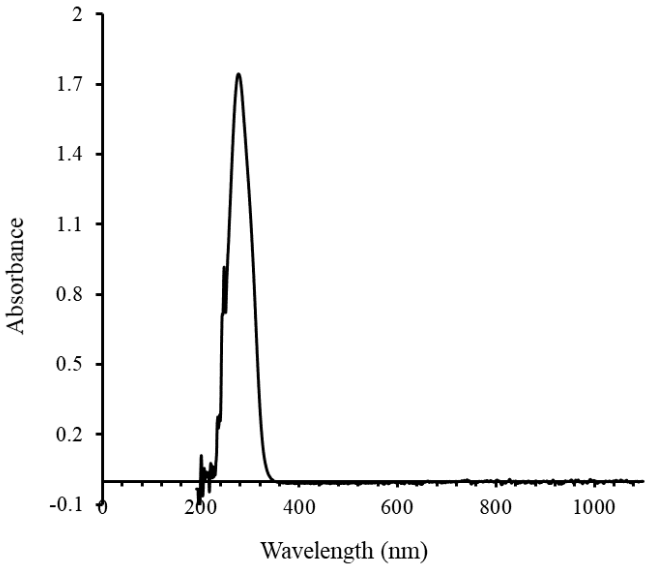

Figure 3.3: UV-vis spectra of 0.025 mM aqueous tannic acid solution.

occupied molecular orbital (HOMO) to the lowest unoccupied molecular orbital (LUMO)), which leads to charge transfer to metallic cations[421].

The photo-induced reduction process is highly dependent on the absorbance peak wavelength of the absorbent compound. A blue-shifted absorbance peak (i.e. in the ultraviolet region) means that a compound is able to absorb high-energy photons that could result in photoexcitation. In this work, we have used tannic acid as the reducing agent. Tannic acid has a UV-vis absorbance peak at approximately 280 nm (Figure 3.3), which lies in the UVB region. As a result, it is plausible that the reduction of Ag^+ to Ag^0 by tannic acid is directly affected by the photo-excited tannic acid-Ag^+ complexes. Our laboratory contains white fluorescent lamps. The white fluorescent lamps are still a source of UV emission despite the minimization of UV emission by the lamp inner phosphor coating[422–425]. As a result, white fluorescent lamps, as the source of both UV and visible light, were used as the illumination source to facilitate the synthesis of silver nanostructures. However, due to the higher energy of UV irradiation and the absorbance peak wavelength of tannic acid (280 nm), the photoexcitation of Ag^+-tannic acid complex is more likely to be affected by UV-wavelength photons rather than visible-wavelength photons.

The Ag^+ concentration curve with respect to time for all three illumination conditions is demonstrated in Figure 3.4. As it can be observed, the Ag^+ decline is sharper for the fully illuminated condition compared to the partially illuminated and dark conditions. The Ag^+ concentration decline for the partially illuminated condition is slightly sharper compared to the dark condition. The SEM images of synthesized silver nanostructures at the three illumination conditions are demonstrated in Figure 3.5. When the flask is fully illuminated, the rate of reduction compared to two other scenarios is maximum. Concordantly, since other factors are kept constant, the rate of nucleation is also highest. As shown in Figure 3.5.A, agglomerated nanostructures with irregular morphologies are synthesized at the fully illuminated condition, and

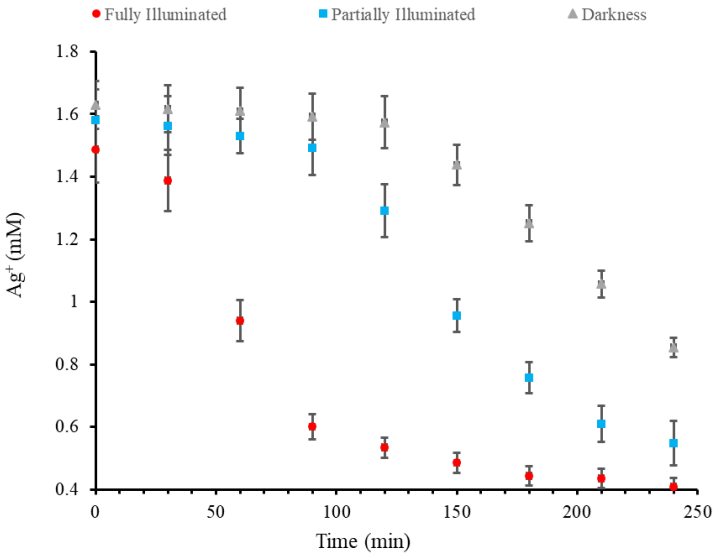

Figure 3.4: The change in Ag^+ concentration with respect to time for the three illumination conditions.

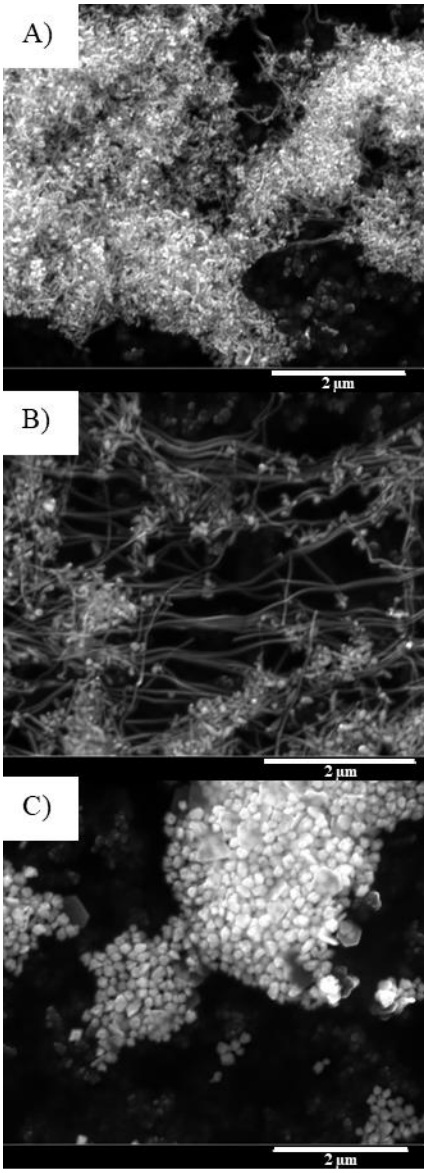

Figure 3.5: SEM images of silver nanostructures synthesized at the three illumination conditions: A) fully illuminated, B) partially illuminated, and C) dark.

the yield of AgNWs is lower compared to the partially illuminated condition. Due to the agglomerated formation of Ag nanostructures, it is challenging to identify the exact morphology and size of the Ag nanostructures; however, by estimation, the average diameter and length of the AgNWs synthesized at the fully illuminated condition were found to be 29.3±8.1 nm and 1.1±0.4 µm, respectively (by measuring the diameter and length of 50 AgNWs). In addition, the color of the solution changed from colorless to yellow just within the first 30 minutes after the addition of $AgNO_3$. The color then became darker, and gradually changed to dark green. It is plausible that the initially formed seeds underwent homogeneous nucleation resulting from high supersaturation. This is unfavorable for anisotropic growth because heterogeneous nucleation that is facilitated by maintaining the lower supersaturation limit is the most favorable condition for anisotropic growth[377]. At the partially illuminated

condition, the rate of Ag^+ concentration reduction is lower compared to the fully illuminated condition (Figure 3.4), meaning that nucleation was also slower. In this case, the color of the solution started changing after approximately 2 hours from the beginning of the reaction. The SEM image of Ag nanostructures synthesized at the partially illuminated condition is shown in Figure 3.5.B. The synthesized Ag nanostructures contain a mixture of nanowires, nanospheres, and other nanostructures with irregular morphologies. However, the yield of AgNWs is higher compared to the fully illuminated condition, meaning that anisotropic growth was more favorable than isotropic growth in this case. The size of nanospheres ranged from 50 to 80 nm, and the diameter of the AgNWs varied between 11 and 44 nm. Due to the weaker reduction of Ag^+, it is plausible that the supersaturation level was not as high as supersaturation in the fully illuminated condition, thus making the circumstances more favorable for anisotropic growth and formation of AgNWs. In the dark condition, the rate of Ag^+ concentration reduction is smaller compared to the two other conditions (Figure 3.4). As can be seen in Figure 3.5.C, the Ag nanostructures include nanotriangles, nanospheres, and nanohexagons; and almost no 1D Ag nanostructure can be observed. The Ag nanostructures had a relatively large size and size distribution with the size range varied between 90 and 500 nm.

Figure 3.6 shows the UV-vis spectra of the synthesized Ag nanostructures at the fully illuminated, partially illuminated, and dark conditions. For

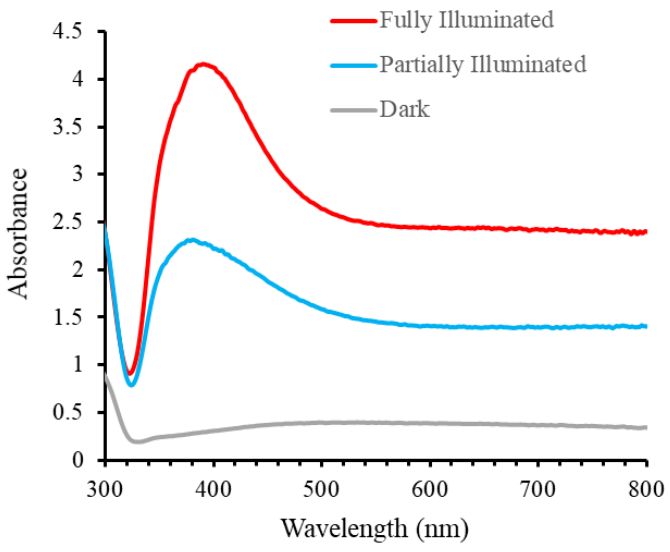

Figure 3.6: UV-vis spectra of the silver nanostructures synthesized at the three illumination conditions (the absorbance is adjusted based on the Beer-Lambert law to reflect the same dilution ratio for all samples).

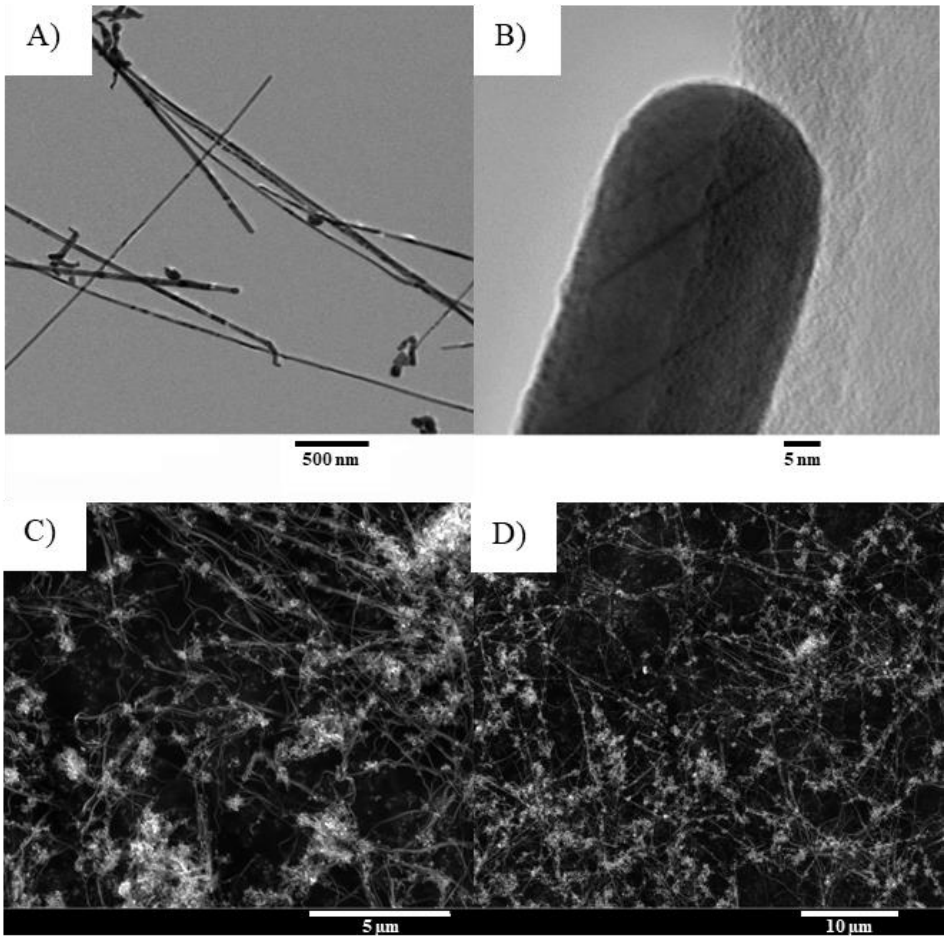

Figure 3.7: TEM and SEM images of silver nanostructures synthesized at the partially illuminated condition: A) TEM image, B) HRTEM image of a single AgNW. C) SEM image with a magnification of 15241x, and D) SEM image with a magnification of 5138x.

the fully illuminated condition, a peak can be observed at 403 nm. For the partially illuminated condition, a maximum at 390 nm and a shoulder peak at 350 nm correspond to the presence of AgNWs[372]. These peaks correspond to the transverse surface plasmon resonance (TSPR) of the AgNWs. For the dark condition, the UV-vis absorbance spectra show a broad absorption band that corresponds to different Ag nanostructures with different sizes. The results show that the partially illuminated condition was indispensable for the growth of AgNWs. Further characterization was performed for this specific reaction condition using TEM, EDX, and XRD. Figure 3.7.A shows the TEM image of the synthesized AgNWs at the partially illuminated condition. Figure 3.7.B shows the high resolution TEM (HRTEM) of a single AgNW, and figure 3.7.C and 3.7.D show the SEM

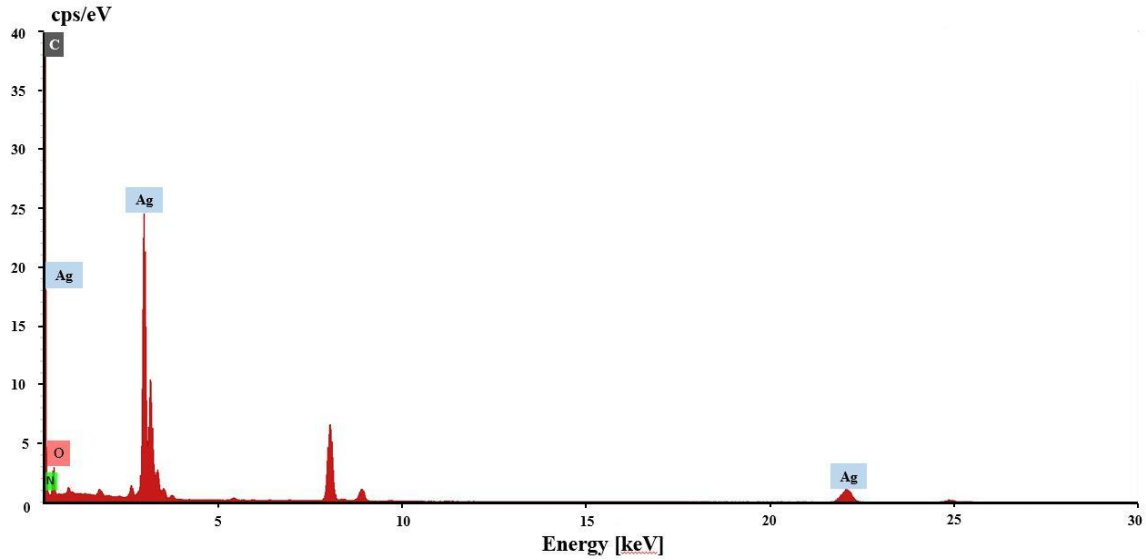

Figure 3.8: EDX spectra of the silver nanostructures synthesized at the partially illuminated condition.

images of synthesized AgNWs at different magnifications. The average diameter and length of AgNWs synthesized at the partially illuminated condition were found to be 24.4±6.6 nm and 11.4±3.2 μm, respectively. Furthermore, Figure 3.8 shows the EDX spectra of the AgNWs, confirming the presence of silver. The XRD pattern of the synthesized Ag nanostructures show four peaks that correspond to the (111), (200), (220), and (311) plane of the face-centered cubic (fcc) silver crystal structure (Figure 3.9). The yield of AgNWs synthesized at the partially illuminated condition is estimated to be approximately 50%. This illumination condition was the most favorable condition for the synthesis of AgNWs with moderate yield compared to the two other conditions. As a result, the partially illuminated condition was maintained for the investigation of the effect of other factors including tannic acid/silver nitrate molar ratio, pH, and stirring rate.

In order to understand the growth mechanism of AgNWs in this study, one should look at the main mechanisms underlying the formation of 1D nanostructures. There are two main mechanisms for the growth of 1D nanostructures, including atomic addition and random aggregation or oriented attachment[377]. In the case of atomic addition, 1D nanostructures are

formed based on atomic deposition resulting from either solution or surface reduction, while in the case of random aggregation and oriented attachment, the 1D nanostructures are formed from the adjacent nanoparticles with similar crystal structures[377]. In the atomic addition pathway, the initially formed seeds can either obtain single twin, multiply-twinned, or monocrystalline structures, while the initially formed seeds formed via the random aggregation or oriented attachment process often have monocrystalline structures. In the case of atomic addition for the formation of NWs, the crystal structure is maintained throughout the long axis of NWs. For instance, in the case of AgNW formation in the polyol process, the penta-twinned NWs are formed from decahedral seeds that are enclosed by 10 {111} facets along with five twin boundaries. The atoms are then deposited unto the twin boundaries and then diffused to the {111} facets[426–429], leaving 5 {100} facets exposed, which are capped by PVP molecules. However, this is not the case if the initially formed seeds have a monocrystalline structure. For a fcc metal such as silver, the monocrystalline seeds can grow into 1D nanostructures with a square, rectangular, or octagonal cross section[430]. Those monocrystalline 1D nanostructures can also be considered as nanocubes extended along one or two of the three axes of their corresponding fcc lattice; as a result, their surface is covered by {100} facets, similar to a nanocubes[377]. As it was previously shown by Tian et al.[372], those monocrystalline nanowires maintain the {100} facets during anisotropic growth. However, it can be hypothetically concluded that only two of such facets are exposed to atomic addition, which explains the formation of AgNWs.

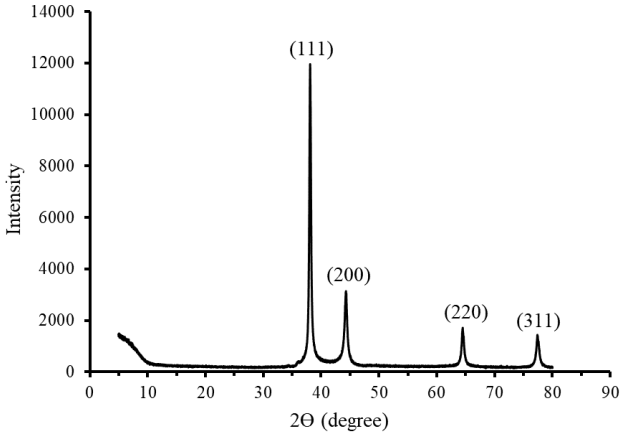

Figure 3.9: XRD pattern of the silver nanostructures synthesized at the partially illuminated condition.

In general, the exact mechanism and pathway of 1D morphology formation can be debatable. 1D silver nanostructures can be either monocrystalline or polycrystalline containing multiple monocrystalline zones along their longitudinal axis, which depends on both the type of seeds that have initiated their growth and their growth pathway. The relative concentration or population of these type of seeds depends on experimental conditions that are controlled by both kinetics and thermodynamics. Among experimental conditions, the reduction rate and consequently nucleation step is specifically critical to control this relative population, which can be controlled by reduction kinetics. One way to promote anisotropic growth (i.e. NWs) is via the manipulation of the reduction kinetics (manipulation of the metal atoms generation or deposition rate, plus the adatoms surface diffusion rate). For fcc metals such as silver, monocrystalline seeds can grow to nanorods with a square or rectangular cross section. These monocrystalline 1D nanostructures can be considered as nanocubes extended along one or two of the three axes of their corresponding fcc lattice; as a result, their surface is covered by {100} facets in which case the truncation level at their corner is controlled by the atomic addition rate[377]. The multiple twin and single twin seeds will most likely evolve into five-fold penta-twined NRs (or NWs) and nanobeams (right bipyramids), respectively. Furthermore, in the absence of a corrosive anion such as chloride or bromide and the presence of oxygen in batch synthesis using tannic acid at room temperature, it can be hypothesized that there is still adequate etching to eliminate some of the multiply twinned seeds; however, single twin seeds are preserved[431,432]. By reducing the rate of reduction or rate of atomic addition (i.e. in the partially illuminated condition) these single twin seeds will grow into nanobeams (thin nanowires). Moreover, a relatively slow reduction rate favors surface reduction over solution reduction that is favorable for 1D growth; however, the reduction rate shouldn't be too slow[377]. In the dark condition, in which the reduction rate is significantly slow, the formation of structures with stacking faults, leading to the formation of plate-like structures are dominant. In the fully illuminated condition where reduction rate is stronger, the metal ions generation or deposition rate is very fast, which makes it challenging to overcome the strong inclination of the

monocrystalline nanostructures to reduce their total surface energy by taking a highly symmetric structure (spatial arrangements of atoms). As a result, this condition is not favorable for asymmetric growth, which is why the yield of AgNWs is lower compared to the partially illuminated condition. Moreover, for 1D nanostructure growth via symmetry breaking, the ratio of the rate of deposition to the rate of surface diffusion needs to be well manipulated. When the rate of deposition is greater than rate of surface diffusion, the adatoms will stay at the deposition sites, which facilitates the site-selective growth[377]. In the partially illuminated condition, the moderate reduction rate will provide the moderate rate of atom deposition compared to the dark and fully illuminated conditions where the rate of deposition is too slow and too fast, respectively.

3.3.2. Analysis of the reduction mechanism and kinetics for the synthesis of AgNWs

The tannic acid molecule can act as a large supramolecular cage and facilitate the diffusion of Ag^+ ions by intermolecular hydrogen bonds[378]. The high density of the hydroxyl groups provide strong polarity that enables the transport and reduction of positive metal cations in those cages[378]. Bulut et al.[378] proposed a reduction mechanism in which the galloyl groups of tannic acid form a chelate complex with Ag^+ ions, which then is followed by the reduction of Ag^+ and transformation of the galloyl group from the phenolic form to the quinone form, and release of electron from the hydroxyl groups[379] (Figure 3.10).

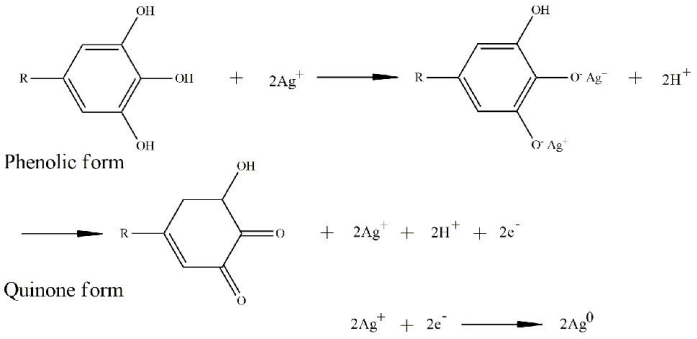

Figure 3.10: Tannic acid mediated reduction mechanism of Ag^+ to Ag^0.

Each galloyl group is able to donate two electrons for the conversion of Ag^+ to Ag^0, which enables electron transfer from the lone pairs belonging to the oxygen of the hydroxyl groups[433]. Depending

on the irradiation energy, some chelate complexes are able to reduce metal cations by photoexcitation[434]. In the case of phenolic compounds, the photoexcitation resulting from UV radiation may lead to the stretching and fission of the O-H bonds as well as proton tunneling[435–437]. This process facilitates proton elimination, which can favor the absorption and reduction of Ag^+ ions. Tannic acid has a maximum absorbance at the wavelength of 280 nm[399] (Figure 3.3). As a result, the stronger absorbance of UV-ranged photons by tannic acid will ultimately result in its photoexcitation that enhances electron donation, and reduction of Ag^+ to Ag^0. A higher number of photons resulting from a higher light intensity will further enhance this process. This is why the reduction of Ag^+ with respect to time is strongest for the fully illuminated condition. The conversion of Ag^+ to Ag^0 is a multistep process that can be divided into two major steps. First step is the monoatomic reduction of Ag^+ to Ag^0 in the solution, which leads to nucleation. The second step results in the reduction of Ag^+ to Ag^0 at the seed surface, which leads to growth. A similar mechanism was previously proposed by Tatarchuk et al.[438] for the synthesis of Ag nanoparticles. Regardless of the multi-step reduction process, the overall reduction reaction can be written as:

$$Ag^+ + e^- \rightarrow Ag^0$$

During the reduction process, measuring the reducing agent concentration during the reaction is often challenging, which makes it difficult to describe the reduction kinetics. However, if the reducing agent is added to the metal precursor in great excess, the reduction kinetics can be described by the pseudo-first order mechanism, where merely the concentration of the metal cation is required[439]. In such a scenario, the concentration of the reducing agent is considered to be constant throughout the reaction and the reduction rate is independent of the reducing agent concentration[439–443]. In this case, the reduction can be simplified as shown in Equation 3.1.

$$Rate = k[Ag^+][reductant] \cong K[Ag^+] \qquad \text{Equation 3.1}$$

Where K is the Ag^+ consumption rate constant (1/min), and $[Ag^+]$ is the concentration of Ag^+ ions at a given reaction time. Furthermore, integration yields Equation 3.2.

$$[Ag^+]_t = [Ag^+]_{t=0}\exp(-Kt) \qquad \text{Equation 3.2}$$

Where $[Ag^+]_{t=0}$ is the initial Ag^+ concentration (mM) and t is the time (min).

Equation 3.2 is the simplest form of the reduction kinetics. Several studies have demonstrated the reduction process may actually diverge from equation 3.2, particularly for those reactions with low reduction rate[444–447]. Finke and Watzky[446] came up with a modified version of the pseudo-first order kinetic model that included two steps (nucleation and growth) in the model equation. In the first step, the metal cations (M^+) are reduced to the zero-valent atoms (M^0), which is then followed by their accumulation into the nuclei via homogeneous nucleation. As a result, the reaction becomes:

$$Ag^+ + e^- \rightarrow Ag^0$$

$$nAg^0 \rightarrow Ag_n^0$$

This is then followed by surface reduction and growth on the initially-formed nuclei.

$$Ag^+ + \ Ag_n^0 + e^- \rightarrow Ag_{n+1}^0$$

In such a scenario, Finke and Watzky[446] described the rate to be as illustrated in Equation 3.3.

$$Rate = K_1[Ag^+] + K_2[Ag^+][Ag_n^0] \qquad \text{Equation 3.3}^{446}$$

Where K_1(1/min) is the rate constant in the reduction step, and K_2(1/mM.min) the rate constant in the surface growth step. $[Ag^+]$ is the silver ion concentration (mM) at a given time and $[Ag_n^0]$ is the concentration of the nuclei; and by approximation, it can also be written with respect to $[Ag^+]$ as shown in Equation 3.4.

$$[Ag_n^0] = [Ag^+]_{t=0} - [Ag^+] \qquad \text{Equation 3.4}^{439}$$

The rate reaction will then become as shown in Equation 3.5, where integration yields Equation 3.6.

$$Rate = \frac{-d[Ag^+]}{dt} = K_1[Ag^+] + K_2[Ag^+]([Ag^+]_{t=0} - [Ag^+]) \qquad \text{Equation 3.5}$$

$$[Ag^+]_t = \frac{\frac{K_1}{K_2} + [Ag^+]_{t=0}}{1 + \frac{K_1}{K_2[Ag^+]_{t=0}} exp\big((K_1 + K_2[Ag^+]_{t=0})t\big)} \qquad \text{Equation 3.6}$$

The rate constants K_1 and K_2 can be derived by fitting the Ag^+ concentration data in the course of reaction. While Equation 3.2 shows an exponential decay for the Ag^+ concentration with respect to time, Equation 3.6 exhibits a sigmoidal behavior. In order to observe how the light-dependent experiments relate to those models, both Equations 2 and 6 were used to fit the Ag^+ concentration data obtained from the three different illumination conditions, and to determine the rate constants for each condition. The rate constants are determined by non-linear regression with the Ag^+ concentration data with respect to time. Figure 3.11 shows the Ag^+ concentration data fitted using both pseudo-first order and the Finke-Watzky models. As demonstrated in Figure 3.11.A, the pseudo-first order model is most accurate for the fully illuminated condition with an R-squared of 0.923. It can be further seen that the pseudo-first order model is somewhat inaccurate for the

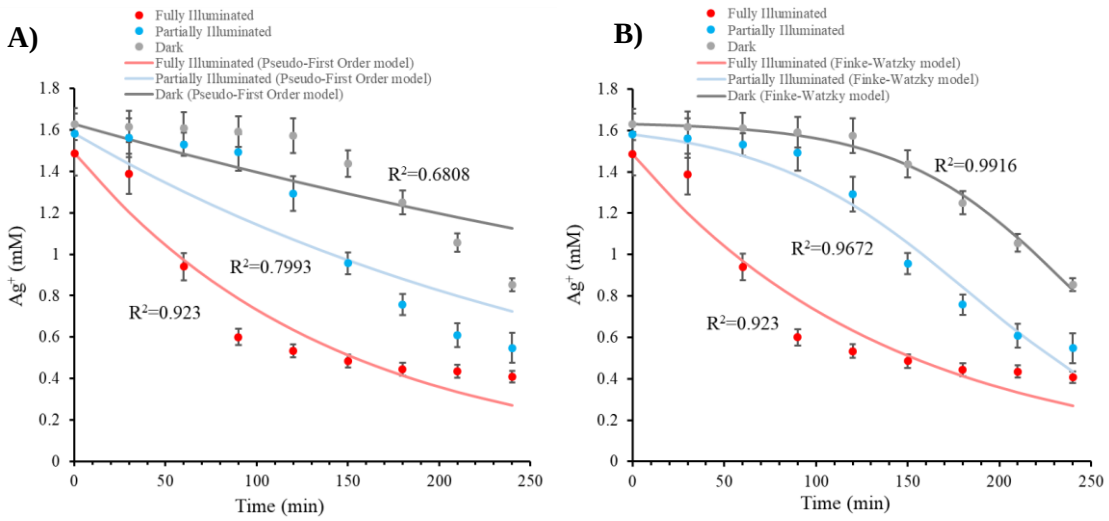

Figure 3.11: A) Ag^+ concentration change versus time fitted using pseudo-first order kinetic model (Equation 3.2), B) Ag^+ concentration change versus time fitted using Finke-Watzky kinetic model (Equation 3.6) for the three illumination conditions.

partially illuminated and dark conditions (R-squared of 0.7993 and 0.6808, respectively). It can be deduced from Figure 3.11.A that the accuracy of the pseudo-first order model decreases as the consumption rate of Ag^+ becomes smaller due to lower light intensity and lower reduction rate. Figure 3.11.B shows the Ag^+ concentration data fitted using Finke-Watzky model for three illumination conditions. Unlike the pseudo-first order model, this model is more accurate for the partially illuminated and dark conditions (R-squared of 0.9672 and 0.9916, respectively). In this case, the model is more capable of describing the data, as the consumption rate of Ag^+ becomes smaller due to lower light intensity and lower reduction rate. However, the Finke-Watzky model does not offer a better accuracy in the case of the fully illuminated condition as the R-squared is similar to that of the pseudo-first order model (0.923). This is due to the fact that the calculated K_2 is significantly small (10^{-8} 1/mM.min), and it can therefore be neglected in Equation 5. The rate constants for both pseudo-first order and the Finke-Watzky models, and for the three different illumination conditions are demonstrated in Tables 3.1 and Table 3.2, respectively. In general, the rate constants increase as the light intensity increases. This is because of the stronger reduction facilitated by higher light intensities. It is challenging to fairly compare the rate constants from the

pseudo-first order model due to the low R-squared values. However, a more reasonable comparison can be made for the rate constants in the Finke-Watzky model. It can be seen that as the illumination decreases (from partially illuminated to dark), the rate constant in the first step (nucleation) decreases from 0.000648 to 0.000126 1/min, which confirms the fact that stronger illumination will result in faster reduction and therefore faster nucleation.

Table 3.1: Pseudo-first order model (Equation 3.2) parameters for the three illumination conditions.

	Illumination condition		
Parameters	Fully-illuminated	Partially-illuminated	Dark
K (1/min)	0.007094	0.003247	0.001542
R^2	0.923	0.7993	0.6808

Table 3.2: Finke-Watzky model (Equation 3.6) parameters for the three illumination conditions.

	Illumination condition		
Parameters	Fully-illuminated	Partially-illuminated	Dark
K_1 (1/min)	0.007094	0.000648	0.000126
K_2 (1/mM.min)	10^{-8}	0.010935	0.012967
R^2	0.923	0.9672	0.9916

As shown in Table 3.2, there was a small difference in the value of K_2 for the partially illuminated and dark conditions. Considering the significant difference in the yield of AgNWs for the dark and partially illuminated conditions, this suggests that the difference in the first step (homogeneous nucleation) was mainly important in altering the course of the reaction. A small value of K_1 in the first step, which is the case for the dark condition (0.000126 1/min), leads to the formation of structures with stacking faults (not based on the minimization of surface energy), which lead to plate-like nanostructures. On the other hand, the value of K_1 for the partially illuminated condition is almost five times that of the dark condition. A higher yield of AgNWs in the partially illuminated condition implies that the first step, which is influenced by illumination, was a determining factor for the manipulation of different types of seeds and their relative concentration or population. Although the Finke-Watzky model can effectively describe Ag^+ reduction in the partially

illuminated and dark conditions, it does not offer a better fit for the fully illuminated condition compared to the pseudo-first order model. A pseudo-first order kinetics is inspired by first-order kinetics, which merely applies for elementary reactions[448]. Nevertheless, the photo-assisted synthesis process can inevitably result in the formation of radicalized intermediates in which case the reduction reaction may not follow an elementary mechanism. The production of radicalized intermediates increases as the light intensity increases. As a result, the reduction will become more complex for the fully illuminated condition to be described by either the pseudo-first order or Finke-Watzky models. In such a case, the models for Ag^+ concentration and reduction rate need to be determined experimentally[448]. An empirical model has been developed in this study that is derived mathematically from the Ag^+ concentration curve as shown in Equation 3.7.

$$[Ag^+]_t = \left([Ag^+]_{t=t_f} - [Ag^+]_{t=0}\right) \exp\left(\frac{\beta}{t^2}\right) + [Ag^+]_{t=0} \qquad \text{Equation 3.7}$$

Where $[Ag^+]_{t=t_f}$ is the final Ag^+ concentration that is collected experimentally, and β (units of min^2) is a rate constant related parameter that has a negative value. β is to be determined with non-linear regression of the experimental Ag^+ concentration data with respect to time. We can assume that after a large time has passed (t_f, in this case 240 minutes), the expression in the exponential term closes unto zero, and the exponential term will approximately reach unity; as a result, substituting t_f in equation 3.6 will

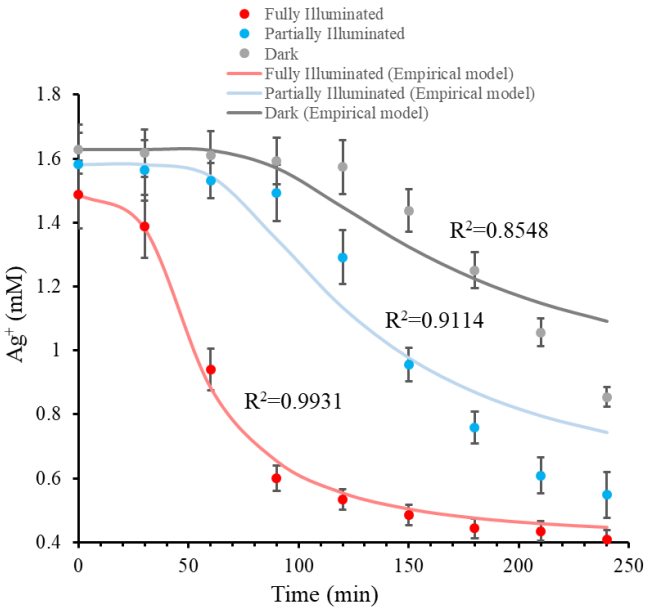

Figure 3.12: Ag^+ concentration change versus time fitted using the proposed empirical kinetic model (Equation 3.7) for the three different illumination conditions.

satisfy $[Ag^+]_{t=t_f} = [Ag^+]_{t=t_f}$. In addition, substituting $t = 0$ in Equation 3.7 will satisfy $[Ag^+]_{t=0} = [Ag^+]_{t=0}$. Figure 3.12 shows the model sketched for Ag^+ concentration with respect to time for the three different illumination conditions. As demonstrated, the model is most accurate for the fully illuminated condition with an R-squared value of 0.9931. However, the model shows an R-squared of 0.9114 and 0.8548 for the partially illuminated and dark conditions, respectively. The accuracy of the model increases as the reduction rate increases that is due to the value of β. For a faster reaction, the magnitude of β is smaller, which means that the exponential term closes unto unity more rapidly at a given reaction time.

For the fully illuminated condition, the Ag^+ concentration decreases more rapidly (lower positive value of β) in a span of 240 minutes. However, this is not the case for the partially illuminated and dark conditions, as it takes longer (>240 minutes) for the exponential term to approach unity. In order to find the relation between β and the rate constant, the rate equation shall be written with respect to $[Ag^+]$. The rate of Ag^+ consumption can be described by the derivation of $[Ag^+]$ with respect to time as shown in Equation 3.8.

$$R = -\frac{d[Ag^+]}{dt} = \frac{2\left([Ag^+]_{t=t_f} - [Ag^+]_{t=0}\right)\beta}{t^3}\exp\left(\frac{\beta}{t^2}\right) \qquad \text{Equation 3.8}$$

In order to derive an equation for the rate with respect to $[Ag^+]$, Equation 3.7 can be rewritten for t as a function of $[Ag^+]$ as shown in Equation 3.9.

$$t = \sqrt{\frac{\beta}{\ln\left(\frac{[Ag^+] - [Ag^+]_{t=t_f}}{[Ag^+]_{t=t_f} - [Ag^+]_{t=0}}\right)}} \qquad \text{Equation 3.9}$$

Substituting t (Equation 3.9) in Equation 3.8 yields Equation 3.10.

$$R = \frac{2}{\sqrt{-\beta}}\left([Ag^+] - [Ag^+]_{t=0}\right) ln\left(\frac{[Ag^+] - [Ag^+]_{t=0}}{[Ag^+]_{t=t_f} - [Ag^+]_{t=0}}\right)\sqrt{ln\left(\frac{[Ag^+]_{t=t_f} - [Ag^+]_{t=0}}{[Ag^+]_{t=t_f} - [Ag^+]_{t=0}}\right)}$$ Equation 3.10

Where $\frac{2}{\sqrt{-\beta}}$ can be considered as the rate constant K_{Ag^+}, with units of 1/min. The model parameters, including the rate constant associated with each illumination condition, is demonstrated in Table 3. It can be observed that for the fully illuminated condition, the rate constant with respect to Ag^+ consumption is highest followed by the rate constant at the partially illuminated and dark conditions, respectively.

Table 3.3: The empirical model (Equation 3.7) parameters for the three illumination conditions.

	Illumination condition		
Parameters	Fully-illuminated	Partially-illuminated	Dark
β (min^2)	-2095.975	-12070.1731	-20988.3596
K (1/min)	0.0437	0.01821	0.0138
R^2	0.9931	0.9114	0.8548

In order to evaluate the validity of the empirical model with different conditions, the experiments were carried out at different initial silver nitrate concentrations (3 and 7 mM) at the fully illuminated condition. Figure 3.13 shows the model sketched for Ag^+ concentration with respect to time for different initial silver nitrate

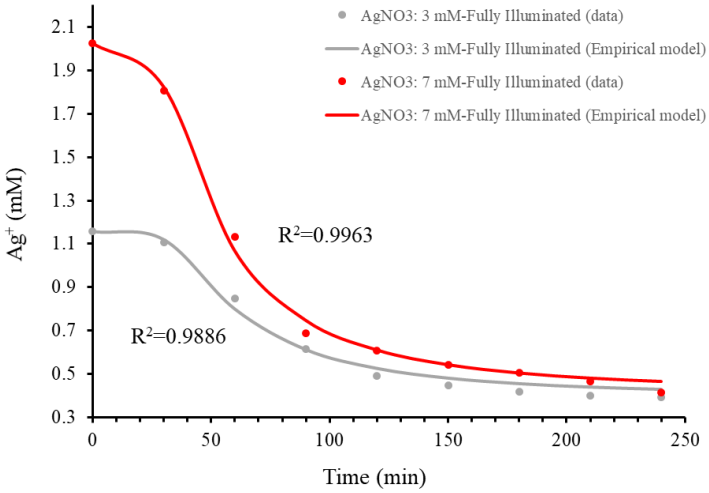

Figure 3.13: Ag^+ concentration change versus time fitted using the proposed empirical kinetic model (Equation 3.7) for the fully illuminated conditions at two silver nitrate concentrations (3 and 7 mM).

concentrations. The model shows an R-squared of 0.9963 and 0.9886 for the silver nitrate concentrations of 7 and 3 mM, respectively. This suggests that the empirical model is fairly accurate for the fully illuminated condition and the value of K may be considered to be more realistic compared to those calculated using the pseudo-first order and Finke-Watzky models. The model parameters are demonstrated in Table 3.4.

Table 3.4. The empirical model (Equation 3.7) parameters for the two other silver nitrate concentrations (3 and 7 mM) at fully illuminated condition.

	Initial silver nitrate concentration	
Parameters	3 mM	7 mM
β (min^2)	-2742.6305	-1879.6499
K (1/min)	0.0382	0.0461
R^2	0.9886	0.9963

The rate constant in the case of 3 mM silver nitrate was lower compared to when the silver nitrate concentration was 7 mM, suggesting that the reduction was faster when the silver nitrate concentration was higher. This can also be confirmed by looking at the rate constant calculated for the typical fully illuminated condition (5 mM silver nitrate), which was 0.0437 1/min. As a result, the reduction rate of Ag^+ increases as the concentration of silver nitrate increases from 3 to 7 mM. This happens due to the molar ratio of tannic acid with respect to silver nitrate. Each tannic acid molecule on average is able to chelate 20 Ag^+ ions[399]. As a result, a 1 mM tannic acid solution can satisfy a silver nitrate solution 19 times more concentrated based on stoichiometry[399]. Therefore, when the concentration of tannic acid is 5 mM, each tannic acid molecule absorbs one Ag^+ ion on average[399]. As the concentration of Ag^+ increases, more Ag^+ ions are chelated by tannic acid, which results in a faster reduction. It can be understood that the Finke-Watzky model can be considered as a good fit for the slower reductions including the partially illuminated and dark conditions, and the empirical model is a good fit for faster reductions including the fully illuminated condition. In order to better understand the reduction rate for each condition, the rate equation needs to be written with respect to time and the constants calculated by non-linear regression. For the dark and partially

illuminated conditions, the derivative of $[Ag^+]$ in Equation 3.6 shall be taken with respect to time to yield Equation 3.11.

$$R = -\frac{d[Ag^+]}{dt} = \frac{\left(\frac{K_1}{K_2} + [Ag^+]_{t=0}\right)\left(\frac{K_1(K_1 + K_2[Ag^+]_{t=0})}{K_2[Ag^+]_{t=0}} exp\left((K_1 + K_2[Ag^+]_{t=0})t\right)\right)}{\left(1 + \frac{K_1}{K_2[Ag^+]_{t=0}} exp\left((K_1 + K_2[Ag^+]_{t=0})t\right)\right)^2} \quad \text{Equation 3.11}$$

Equation 3.11 can be used to describe the rate for the partially illuminated and dark conditions. The values of K_1 and K_2 are those previously provided in Table 3.2. Furthermore, since the empirical model is a better fit for the fully illuminated condition, the rate equation is Equation 3.10. Figure 3.14 shows the reduction rates sketched with respect to time. As can be seen, each rate reaches a maximum regardless of the illumination condition. Prior to this peak, both solution and surface reduction are responsible for the consumption of Ag^+ ions. However, after this peak, surface reduction is the dominant mechanism as the color change stops and the Ag^+ concentration decreases. For the fully illuminated condition, the rate reaches a peak after 38 minutes from the beginning of the reaction, while this peak is at 184 minutes for the partially illuminated condition, and is not reached for the dark condition within the 240-minute timespan. Since this reaction is a one-pot seedless synthesis, homogeneous nucleation resulting from solution reduction is necessary for the formation of initial seeds, which grow into AgNWs via surface reduction. However, maintaining a balance between solution and surface reduction is also an important factor. In the case of the fully illuminated condition, the high reduction rate will mostly cause homogeneous nucleation and result in the formation of mostly isotropic seeds. In addition, it is possible that after solution reduction, there will not be enough silver precursor for the surface reduction which can lead to the formation of AgNWs.

In the fully illuminated condition, the solution reduction outweighs the surface reduction. In the case of the partially illuminated condition, both solution and surface reduction simultaneously play a part in the synthesis of AgNWs, which is why the yield of AgNWs is higher for the partially illuminated condition. In the case of the dark condition, both solution and surface reduction are responsible for the reduction of Ag^+ ions. However, due to the significantly slow reduction rate, stacking fault occurs in the seed growth process, which results in the formation of mostly plate-like structures. In the partially illuminated condition, the rate of reduction is controlled in such as a way as to provide the balance between the solution and surface reduction favorable for anisotropic growth. Moreover, the relatively slow reduction rate controlled by the illumination condition plays a critical role to control and manipulate the relative population of three different seeds including single crystal, single twin, and multiple twin that can grow into nanobar, nanobeam, and penta-twinned nanowire, respectively by controlling the atomic addition as well as oxidative etching. The surface capping effect of tannic acid and surface activation caused by oxidative etching can also play a role in symmetry breaking and anisotropic growth. For instance, it is hypothesized that tannic acid may absorb into only two sides on the single-crystal cubic structure and allow 1D growth[372]. It also can be hypothesized that during the reduction process, carboxylic acid groups (COOH) in the tannic acid lose their hydrogen atom to become carboxylate ion (COO−), which may attach to the silver nanoparticles surface along with the rest of the polymer to stabilize metal nanoparticles and act as surfactant by electrostatic stabilization[382]. However, its preferential absorption on all

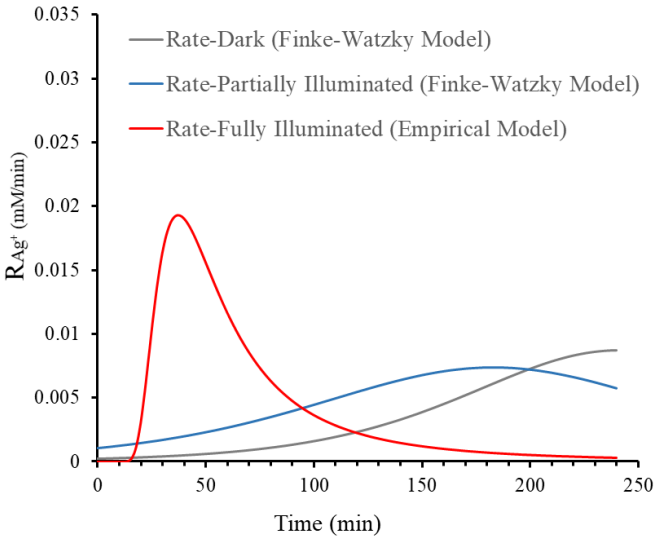

Figure 3.14: Ag^+ reduction rate for the three illumination conditions.

{100} facets of the penta-twined seeds (similar to PVP through Ag-oxygen coordination)[449] or two {100} facets of single-crystal cubic still remains a matter of debate.

3.3.3. Effect of different reaction parameters

3.3.3.1. Effect of the molar ratio of tannic acid to silver nitrate

Due to the dual role of tannic acid in the reduction of metal ions and the capping/stabilizing function of seeds/nanoparticles, its concentration is a crucial factor in controlling the size and morphology of silver nanostructures. The parametric analysis was carried out based on the most favorable illumination condition for the synthesis of AgNWs, which is the partially illuminated condition. To do so, different tannic acid/silver nitrate molar ratios (0.2, 0.6, 1, 1.67, and 5) were considered where all the other parameters (room temperature, pH of 4, and 300 rpm stirring rate) were kept constant. Figure 3.15 shows the SEM images of silver nanostructures synthesized at different tannic acid/silver nitrate molar ratios up to 1. It can be deduced from Figure 3.15 that the yield of AgNWs increases by increasing the molar ratio from 0.2 to 1. When the minimal molar ratio of 0.2 was used, the silver nanostructures assumed highly varied morphologies (Figure 3.15.A). The nanostructures also had a wide size distribution. For instance, the diameter of nanospheres varied between 20 to 100 nm. Sivaraman et al.[399] showed that as the molar ratio of tannic acid to $AgNO_3$ decreases, the incorporation efficiency of Ag^0 atoms into particles will

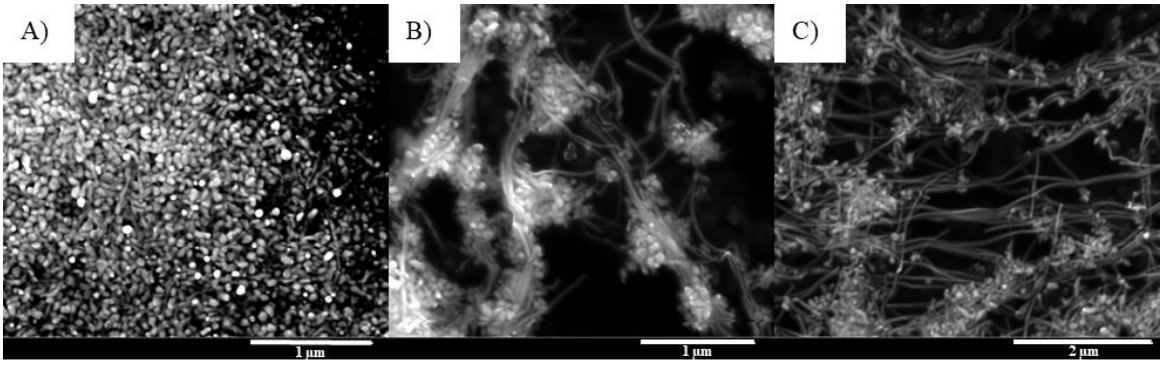

Figure 3.15. SEM images of synthesized silver nanostructures at different tannic acid/silver nitrate molar ratios up to 1. A) molar ratio of 0.2, B) molar ratio of 0.6, and C) molar ratio of 1.

increase, thus resulting in faster nucleation and growth. This is due to chelation by the tannic acid molecules. When the molar ratio is equal to 1, each tannic acid molecule can chelate one Ag^+ ion on average. As the molar ratio decreases down to 0.05, each tannic acid molecule will be able to chelate 20 Ag^+ ions on average, which increases the reduction rate. In the case of 0.2 molar ratio, the nucleation and growth rates are higher compared to the other molar ratios, making the process unfavorable for anisotropic growth and production of AgNWs. Also, a low concentration of tannic acid, due to the low molar ratio, will inevitably result in a lower rate of tannic acid absorption unto the high-energy facets (i.e. {100}). At the molar ratio of 0.6, the condition is more favorable for the growth of AgNWs (Figure 3.15.B). However, the yield of AgNWs is lower compared to when the molar ratio is 1. The yield of AgNWs is highest when the ratio is 1 (Figure 3.15.C). The UV-vis spectra of the silver nanostructures is demonstrated in Figure 3.16. For 0.2 molar ratio, a broad peak can be observed around 413 nm corresponding to Ag nanoparticles with various morphologies. In the case of 0.6 molar ratio, the peak is slightly more blue-shifted and can be observed at approximately 395 nm. In order to observe the effect of excess tannic acid, molar ratios higher than 1 were considered as well. Figure 3.17 shows how the morphology of silver nanostructures and the yield of AgNWs changes by increasing the molar ratio (1.67 and 5). All the other factors were kept constant according (room temperature, pH of 4, and 300 rpm stirring rate). It can be observed from Figure 3.17 that the yield of AgNWs decreases by increasing the molar ratio from 1 to 5. At the molar ratio of 5, there should on average be one Ag^+ ion, and as a

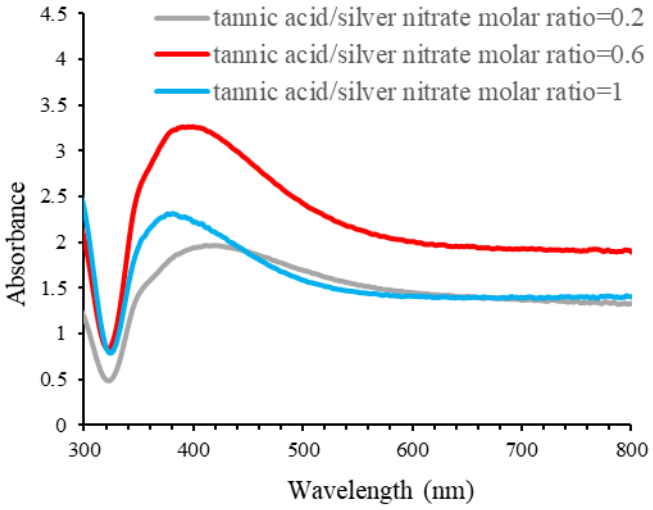

Figure 3.16: UV-vis spectra of the silver nanostructures synthesized at different tannic acid/silver nitrate molar ratios (0.2, 0.6, and 1).

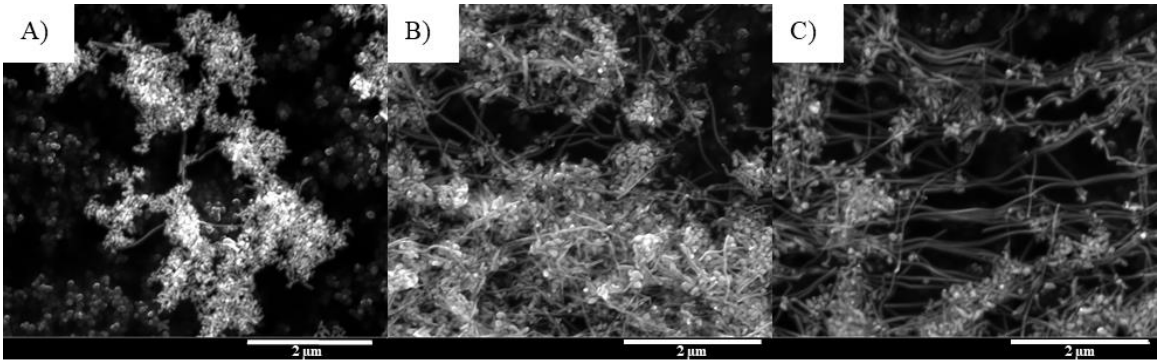

Figure 3.17: SEM images of synthesized silver nanostructures at different tannic acid/silver nitrate molar ratios higher than 1. A) molar ratio of 5, B) molar ratio of 1.67, C) molar ratio of 1.

result one Ag atom, for 5 tannic acid molecules[399]. As a result, the reduction and nucleation are slower compared to when the molar ratio is either 1.67 or 1. At the pH of 4, the rate of reduction, and consequently nucleation is already low. As a result, the nucleation and growth rates are already slow for the growth of AgNWs, which is why most nanostructures appear with irregular morphologies and plate like structures. The silver nanostructures synthesized at the molar ratio of 5, were relatively large and their size varied between 50 and 150 nm, and only a few nanowires can be observed (Figure 3.17.A). The large size and size distribution can be attributed due to the low reduction and nucleation rates. At the molar ratio of 1.67, the yield of AgNWs is higher compared to when the molar ratio is 5, but lower compared to when the molar ratio is 1 (Figure 3.17.B). At the molar ratio of 1, the concentration of Ag^+ ions (5 mM) is high enough relative to the concentration of tannic acid (5 mM) in order to maintain supersaturation and initially allow homogeneous nucleation throughout the solution. Afterward, the concentration of atoms falls from the supersaturation concentration, and the seeds continue

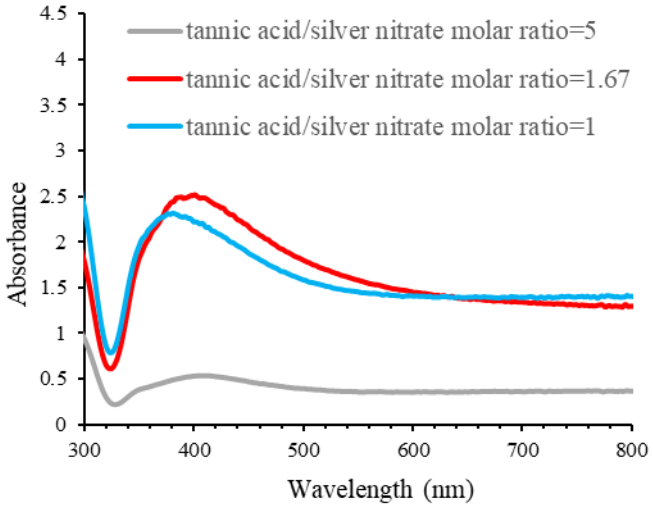

Figure 3.18: UV-vis spectra of the silver nanostructures synthesized at different tannic acid/silver nitrate molar ratios (1, 1.67, and 5).

to grow into 1D structures. Figure 3.18 shows the UV-vis spectra of corresponding molar ratios of 1, 1.67, and 5. As it can be seen for the molar ratio of 5, a broad peak at approximately 408 nm is observed, which corresponds to nanoparticles with irregular morphologies and varied sizes. At the molar ratio of 1.67, the peak is more blue-shifted compared to the previous condition, which can be observed at roughly 400 nm. The results suggest that the tannic acid/silver nitrate molar ratio of 1 is the most optimal condition for the synthesis of AgNWs.

3.3.3.2. Effect of pH

In general, pH is one of the most important factors in controlling the size and morphology of metal nanostructures during the synthesis process. A change in pH affects the redox activity of the reducing agent with respect to metal ions. For instance, basic pH can result in the deprotonation of phenolic groups of plant extracts[340]. The reduction strength (oxidation potential of the reducing agent) can directly be controlled by pH. The lower the pH, the lower the reduction rate, and the higher the pH, the higher the reduction rate (based on the pH range in our study). Tannic acid decomposes into gallic acid and glucose at a mildly acidic/basic condition, where gallic acid favors the reduction process, and glucose favors the capping/stabilization of nanostructures. Typically, alkaline condition is more favorable for the synthesis of small and monodisperse nanoparticles while acidic pH is more favorable for the synthesis of anisotropic structures such as nanowires. We have investigated the effect of pH at acidic conditions, at values of 4, 5, and 6, where the pH was adjusted before the reaction by the dropwise addition of 0.1 M NaOH solution, while other parameters ($AgNO_3$ concentration of 5 mM, tannic acid concentration of 5 mM, room temperature, and 300 rpm stirring rate) were kept constant. Figure 3.19 shows the SEM images of silver nanostructures synthesized at pH of 4, 5, and 6. At the pH of 4, the rate of reduction is adequately low, which is favorable for 1D growth. At the beginning of the reaction, the rate of reduction should be high enough to trigger supersaturation and allow homogeneous nucleation followed by a controlled growth process via atomic addition. The pH of

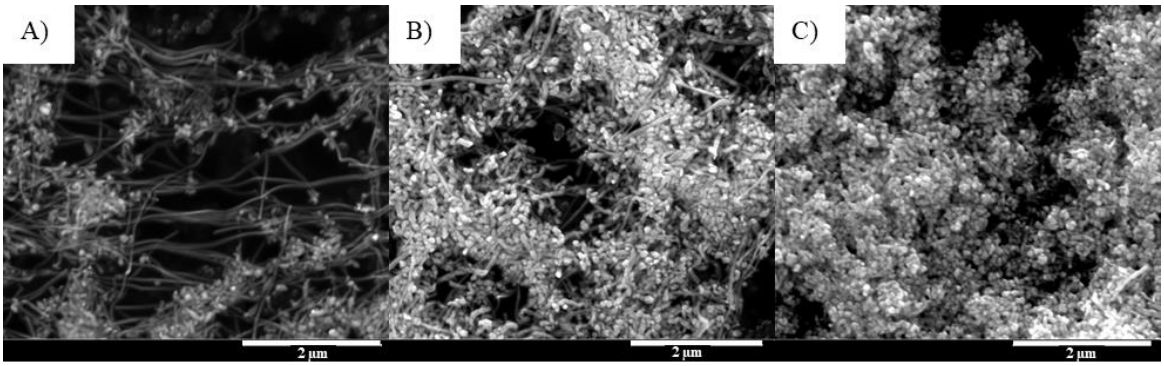

Figure 3.19: SEM images of synthesized silver nanostructures at different initial pH. A) pH=4, B) pH=5, and C) pH=6.

4 was found to be the most favorable pH for the synthesis of AgNWs with moderate yield, as demonstrated in Figure 3.19.A. When the pH is increased to 5 and then 6, the oxidation potential increases, which leads to the deprotonation of hydroxyls on the galloyl group. As a result, the reduction rate increases and aggressively results in the consumption of Ag^{+} via the solution reduction process. This leads to higher supersaturation levels and a higher deposition rate of Ag^{0} atoms, which facilitates the formation of symmetric structures due to the spatial arrangement of atoms, similar to what occurs in the fully illuminated condition. This is unfavorable for the asymmetric growth of the Ag nanostructures such as those that lead to the formation of AgNWs. Therefore, as the pH increases, the yield of AgNWs decreases. For instance, in Figure 3.19.B, the majority of nanostructures are silver nanotriangles, nanospheres, and other nanostructures with irregular morphologies. When the pH is increased to 6 (Figure 3.19.C), almost all of the synthesized nanostructures were non-1D structures with irregular morphologies. However, the size of the synthesized nanostructures was lower compared to the previous conditions (pH=4, 5). The UV-vis spectra of the Ag nanostructures synthesized at different pH values is shown in Figure 3.20. The peak is red-shifted as the pH increases. This is due to the presence of Ag nanoparticles other than AgNWs.

Lower pH values (lower than 4) result in a further decrease in the reduction rate, which may not be favorable for the synthesis of AgNWs. The reduction rate, in general, is highly sensitive to pH variations; for instance, just one degree of difference in the pH value can significantly affect the reduction rate and therefore lead to the formation of nanostructures with highly different morphologies, which is why the yield of AgNWs at the pH of 4 is significantly lower compared to when the pH is either 5 or 6. We previously showed that the rate of reduction is already low enough at the pH of 4 (at the partially-illuminated condition), and is closer to the rate for the dark condition than to the fully illuminated condition. Therefore, we hypothesize that a further decrease in the pH (i.e. from 4 to 3), at the partially illuminated condition may actually lead to a substantial drop in the reduction rate, thus mimicking the situation that occurred in the dark condition that is the formation of structures with stacking faults (not based on the minimization of surface energy), which lead to plate-like nanostructures.

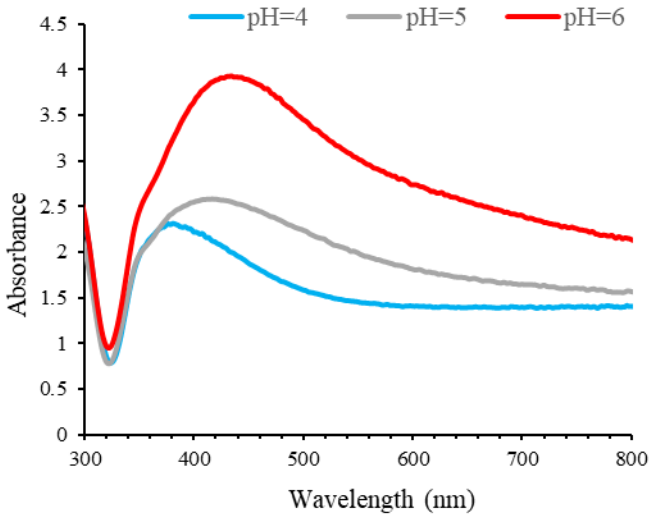

Figure 3.20: UV-vis spectra of the silver nanostructures synthesized at different pH of 4, 5, and 6.

3.3.3.3. Effect of stirring rate

Mixing is another factor that may affect the morphology of silver nanostructures and yield of AgNWs, which is controlled by the stirring rate in the flask. In this study, the stirring rate was controlled by a magnetic stirring bar placed in the solution. Figure 3.21 shows the SEM images of silver nanostructures at different stirring rates. All the other conditions ($AgNO_3$ concentration of 5 mM, tannic acid concentration of 5 mM, pH of 4, and room temperature) were kept constant. Mass and heat transfer are directly affected by mixing in the system. However, since these experiments

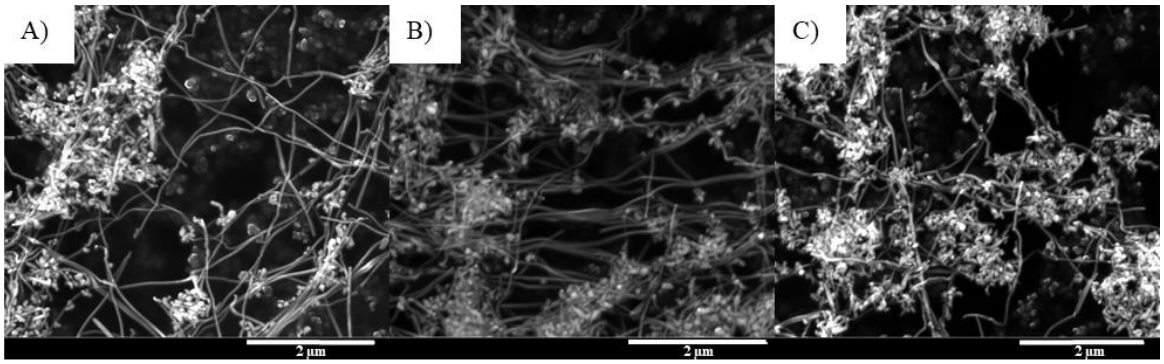

Figure 3.21: SEM images of synthesized silver nanostructures at different stirring rates. A) No stirring, B) 300 RPM, and C) 600 RPM.

were carried out at room temperature, the effect of mixing on heat transfer may be considered negligible. In the absence of mechanical mixing, the process of nucleation and growth is merely diffusion limited. This becomes challenging when the reaction volume is large, which is the case for typical batch reactions. In such a scenario, collision of molecules is weaker and the diffusion of the Ag^0 atoms into the initially formed seeds is slow. In the case of strong mechanical mixing, turbulence will increase in the system, and increases the random collision of particles. This relation can be described by the Reynolds (Re) number written with respect to the stirring bar diameter, viscosity, and density of the synthesis solution as shown in Equation 3.12[69].

$$Re = \frac{D^2 N \rho}{\mu} \qquad \text{Equation 3.12}^{69}$$

Where D is the diameter of the stirring bar, N the revolutions per minute, ρ the density, and μ the viscosity of the synthesis solution. Assuming the viscosity and density of the solution to be close to that of water, the Re value is calculated to be 0, 20,073 and 40,146 for 0, 300, and 600 RPM stirring rates, respectively. A higher stirring rate results in a higher Re number, which results in a stronger convective mass transport. As can be seen in Figure 3.21, there is not a significant difference between the yield of AgNWs for all three conditions. However, the UV-vis spectra shows a slightly more red-shifted peak for no stirring and at 600 RPM, compared to 300 RPM

(Figure 3.22). This could be due to the presence of Ag nanoparticles (other than AgNWs) along with AgNWs. The yield of AgNWs in the case of 300 RPM may be slightly higher compared to the two other conditions. As a result, both convective and diffusional mass transfer need to interfere in the process for the synthesis of AgNWs. In this case, 300 RPM may be moderately high enough to ensure both convective and diffusion controlled mass transport compared to the other two conditions. Moderate mixing will provide a better control on the manipulation of rate of deposition to the rate of diffusion that is crucial for 1D growth.

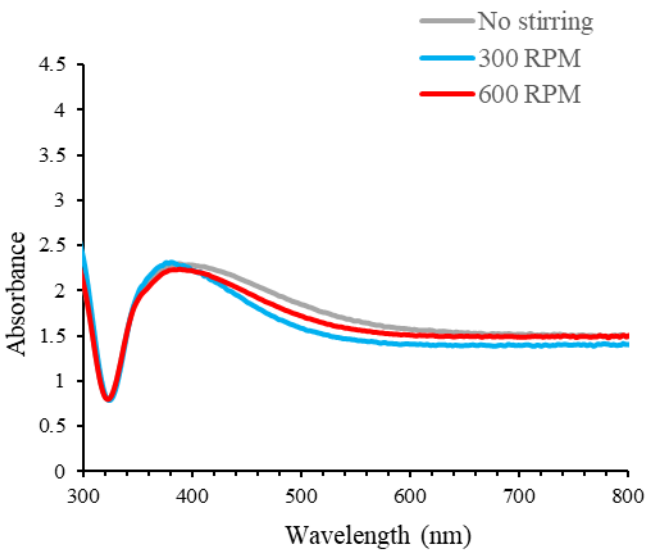

Figure 3.22: UV-vis spectra of silver nanostructures synthesized at different stirring rates.

3.4. Conclusion

This study provided the sustainable development of 1D silver nanostructures through the application of natural products while investigating the underlying effects of kinetic and thermodynamic factors in their sustainable synthesis process. In summary, we have discussed the photosensitivity of the silver nanostructure synthesis in a green and room temperature manner using tannic acid as both the reducing and capping/stabilizing agents. We discussed how photoreduction can be used to control the reduction rate of Ag^+ ions in the presence of tannic acid, and as a result the morphology of silver nanostructures for the first time to the best of our knowledge. Three different illumination conditions including fully illuminated, partially illuminated, and dark were considered. The results showed that illumination was necessary for the synthesis of AgNWs, with the partially illuminated condition being the most favorable one. Illumination highly affects the reduction of Ag^+ by tannic acid. A high exposure to light results in a strong ultraviolet absorption

by tannic acid, which significantly strengthens the reduction of Ag^+ ions. This is unfavorable for the anisotropic growth of nanostructures, which is necessary for the formation of AgNWs. With no exposure, the reduction rate is significantly low, which results in the formation of nanostructures with plate-like structures. With partial exposure, the reduction rate is adequately low to allow the control between solution and surface reduction as well as the manipulation of relative population of different types of seeds in the presence of surface passivation and surface activation caused by the capping effect of tannic acid and oxidative etching, respectively, while the rate of atomic addition is well manipulated by controlling the reduction rate. We also used three distinct models to describe Ag^+ concentration reduction during the reaction timespan for each illumination condition. The pseudo-first order kinetic model was only a fair fit for the fully illuminated condition (R-squared of 0.923), and was not accurate for the other two conditions. The Finke-Watzky model was a good fit for the dark and partially illuminated conditions (R-squared of 0.9672 and 0.9916, respectively), but did not offer a better fit for the fully illuminated condition compared to the pseudo-first order model. The proposed empirical model was a good fit for the fully illuminated condition (R-squared of 0.9931), and was validated with the other two silver nitrate concentrations. Other than illumination, the effect of other reaction parameters, including tannic acid to silver nitrate molar ratio, pH, and stirring rate were investigated. The results showed that the concentration ratio (tannic acid to silver nitrate) of 1 was necessary for the synthesis of AgNWs. A lower ratio results in a higher reduction rate that leads to the production of Ag nanoparticles. A higher ratio results in a lower reduction rate that leads to Ag nanostructures with large size distribution. We also showed that higher pH (higher than 4) was unfavorable for the formation of AgNWs due to an increase in the reduction rate. Furthermore, the effect of stirring rate was not as significant as other factors; however, a moderate rate of 300 RPM was found to be the best condition for the synthesis of AgNWs. In conclusion, we showed that AgNWs with moderate yield (50%) can be synthesized using tannic acid as both the reducing and capping/stabilizing agents, and that its yield is affected by exposure of the reaction to the light, which controls the rate of

reduction and subsequently the relative population of seeds as well as the rate of atomic addition to those seed, which all dictate the morphology of the synthesized silver nanostructures. The photosensitivity of the tannic acid-mediated synthesis of Ag nanoparticles may open a new window for the light-assisted synthesis of different nanostructures by merely changing the illumination intensity and/or wavelength. The fundamental knowledge gained from this study regarding the effect of illumination in controlling the kinetic and thermodynamic factors in metal nanostructure synthesis is critical and has not been reported before. This fundamental understanding of the kinetic behavior can be used to precisely control the reduction rate. The reduction rate then will be utilized as a quantitative measure to control the type and relative population of the initially formed seeds, and consequently the size and morphology of different metal nanostructures such as silver, gold, and palladium. This underlying discernment can provide a foundation to advance the multidisciplinary and interdisciplinary fields of green synthesis, green nanotechnology, and broadly green nanomanufacturing.

For future studies, further investigation on AgNWs synthesis using tannic acid needs to be conducted by performing the kinetic study at different reaction conditions. The final goal should be relating the reduction rate to the relative concentration or population of the three type of seeds including single crystal, single twin, and multiple twin. An important aspect in understanding how the reaction mechanisms determine the size and morphology of nanostructures is the quantitative information that can be extracted using instruments with *in-situ* analysis capabilities. For instance, acquiring *in-situ* UV-vis spectra during the course of a reaction allows one to relate certain absorbance peak wavelengths to nanostructures with certain morphologies for different reaction time lapses. Furthermore, *in-situ* FTIR spectroscopy enables one to identify functional groups that take part in the chelation and reduction of silver ions, complexation, and stabilization of nanostructures during the course of a reaction. Combining these two techniques can help obtain a detailed underlying mechanism, which is essential to control the size and morphology of the

synthesized Ag nanostructures. Furthermore, the *in-situ* FTIR characterization can make it possible to select different green reducing agents that result in similar reaction chemistry and kinetic/thermodynamic behavior for the synthesis of 1D Ag or other metal nanostructures. Considering that, especially in the area of green synthesis of metallic nanostructures, a large number of green and natural reagents may be used at room temperature to synthesize metal nanostructures with desired size and morphology (e.g. 1D nanostructures) without needing to use any additional capping agents or chemical/hazardous reducing agents.

CHAPTER IV

CONTINUOUS, GREEN, AND ROOM-TEMPERATURE SYNTHESISOF SILVER NANOWIRES IN A HELICALLY-COILED MILLIFLUIDIC REACTOR

4.1. Introduction

There has been a success in the synthesis of noble metal nanostructures with uniform size and morphology during the past decade. Due to their enhanced characteristics at the nanoscale such as electrical and thermal conductivity, optical and catalytic activities, and antibacterial properties, these nanostructures have opened up a wide window of applications in renewable energy[36,40], wastewater treatment[42,450], nanomedicine[324,451], imaging[452,453], food packaging[454,455], sensors and biosensors[456,457], microelectronics[31,458], and wearable electronics[459–461], to name a few. Despite these advancements reported in the literature, transition of the production processes from an academic setting to an industrial scale remains a major challenge[462]. This challenge is mainly due to the lack of ability to produce nanostructures in large quantities while maintaining the desired characteristics (i.e. uniformity and desired size and morphology). To produce nanostructures in batch conditions and in large scale, the volume of the reactor and the amount of reagents used should be increased to meet mass production levels.

Nevertheless, increasing the volume of the reactor imposes additional challenges on controlling the size, morphology, and uniformity, and can often lead to nanostructures with large size distribution and non-uniform structures. This is because achieving homogeneous mixing and uniform heat and mass transfer becomes more difficult as the reaction volume increases, which greatly affects both nucleation and growth of nanostructures.

It is possible to enhance mass and heat transfer and thereby tune the nanostructures' properties in a desired manner by miniaturizing the reaction environment, which is why continuous flow reactors such as micro- and millifluidic systems have been recently gaining more attention for the synthesis of nanostructures with uniform size and morphology[463,464]. Heat transfer is related to the volume of the reaction environment and it is enhanced as the diameter of channel/tube is decreased. However, mass transfer is rather more complicated and is related to mixing in the reactor. In microfluidic flow systems, the flow is laminar and mixing is mostly affected by the diffusion of the compounds in the fluid[465]. In such cases, mixing occurs at the molecular level, which is also referred to as "micromixing"[466]. In the case of single-phase flow systems, mixing occurs via molecular diffusion between the two miscible streams at very low Reynold's numbers (Re<1)[465,467]. In such a scenario, the characteristic time for the diffusion of component A in B in the case of a binary system can be described as shown in equation 4.1[465].

$$t = \frac{x^2}{D_{AB}} \qquad \text{Equation 4.1}$$

Where x is the diffusional path length, and D_{AB} is the molecular diffusivity of component A in component B. To achieve uniform concentration throughout the flow path, the value of residence time should be higher than t, which is true for micro- and millifluidic systems. This timescale can be as small as 30 s in a typical microfluidic channel with a diameter of 500 μm. Although this time may be long for fast reactions, it can be reduced by decreasing the channel diameter, thus resulting in faster mixing[465]. Application of microchannels is reported in several studies to be

more favorable for the synthesis of monodisperse nanoparticles compared to the batch synthesis[468–470]. However, flow systems with slightly larger dimensions such as millilfuidic channels/tubings are less prone to extreme pressures and clogging[471,472], require much cheaper and simpler fabrication techniques[473], and have a strong potential for large-scale applications[474]. In addition, due to their better flexibility, millifluidic channels/tubings can be curved easily in different configurations, which can create different mixing patterns in the system[475]. Furthermore, millifluidic systems are able to process larger quantities of materials and in a more rapid fashion compared to microfluidic systems.

Among various noble metal nanostructures, the synthesis of silver nanostructures in millifluidic flow systems has been gaining more attraction during the past decade thanks to their wide applications, particularly in electronics. Among silver nanostructures with different morphologies, one-dimensional (1D) ones, such as silver nanowires (AgNWs), are promising choices for electronics. One of the major applications of AgNWs is in the development of transparent conductive materials used for manufacturing conductive inks, novel electronics, and smart devices[362,476]. Indium tin oxide (ITO) has been used as the most common material in transparent conductive electrodes, due to its high optical transmittance, being more than 90%, as well as its low sheet resistance being less than 10 Ω/square[477]. However, ITO is brittle and therefore cannot be used in flexible electrodes[477]. In addition, the production of ITO is highly energy-consuming and its deposition procedure needs high temperature and vacuum, which can damage some substrates[478]. Alternatively, metal nanostructures (especially nanowires) such as gold and silver nanowires are suitable candidates due to low-cost solution processing and better mechanical flexibility characteristics[357,477]. Such characteristics enable the large-scale production of nanowire-based electrodes with high throughput[357]. AgNWs, are one of the most suitable choices due to their high conductivity, decent transmittance, and their capability to maintain conductivity while enduring a bending/folding strain[479,480]. In addition, AgNWs can form

networks, which facilitates the current flow and thus provides lower sheet resistance. They also can be used at lower concentrations compared to other nanostructures, which facilitates transmittance[94,480]. Such characteristics are highly dependent on the average diameter and length of the nanowires. In general, at similar concentrations, the higher the AgNWs length (having similar diameter), the lower the sheet resistance, and the lower the AgNWs diameter (having similar length), the higher the transparency[361,481]. Moreover, the synthesis condition of AgNWs is vital in determining the final property of the AgNW-coated conductive films. The synthesis of AgNWs via hard templates and physical methods is expensive and inefficient for large-scale applications[94]. For this reason, the synthesis of AgNWs is followed by the polyol process, which was first introduced by Xia's group in 2002[368]. There have been further modifications to this process up to this point[69,371,482]; however, the synthesis process, in general, is followed by mixing the silver precursor and ethylene glycol at temperatures around 150 °C with the assistance of a polymer stabilizer such as Polyvinylpyrrolidone (PVP)[94]. This process is currently the most widely-used method for the production of AgNWs in both lab and industrial scale. The synthesis of AgNWs in millifluidic reactors can be promising for large-scale operations. Gottesman et al.[483] synthesized AgNWs using the conventional polyol process in a millifluidic reactor. The reaction was performed at 198 °C and at different residence times (3, 15, 30, and 60 minutes). They showed that 30 minutes was the optimal residence time for the synthesis of AgNWs with maximum yield (percentage of AgNWs among nanostructures with different morphologies). The yield was shown to be higher than 90 %. Zhang et al.[484] synthesized silver nanocrystals in a droplet-flow reactor using silicone oil as the secondary phase. In that process, silver nanostructures were produced by a seed-mediated process using ascorbic acid and trisodium citrate as the reducing and capping agents, respectively, and the reaction was carried out at room temperature. Later, Hemmati et al.[471] synthesized AgNWs using the modified polyol process (using $CuCl_2$ as the salt mediator) at a lower temperature (130 °C) compared to the batch polyol process. Kinhal et al.[472] obtained different morphologies of silver nanostructures (spherical, rod-

shaped, and wire-shaped) using different configurations and tube designs (batch, straight millifluidic, and spiral millifluidic) at low cetyl trimethylammonium bromide (CTAB) concentration (1 mM), which was used as the capping agent while using ascorbic acid as the reducing agent.

The polyol process, which is used in most AgNW synthesis processes, is associated with relatively high-energy consumption due to relatively high temperatures. Although previous studies have used the polyol process in millifluidic systems for the synthesis of AgNWs, a green, sustainable, and inexpensive procedure for the continuous synthesis of AgNWs remains to be investigated. A green and sustainable synthesis process enables the use of environmentally-friendly reducing and capping agents, while also reducing energy consumption. Among environmentally-friendly reagents, polyphenols and sugar-based products have been shown to be effective compounds due to their capability to act as reducing and capping agents at the same time and minimal waste production[203,485]. In this work, we report the synthesis of AgNWs in a reusable droplet-based millifluidic reactor (milli-sized tubing bent to form a coil-like shape around a pipe), using tannic acid as both the reducing and capping agents at room temperature, and in 96 minutes residence time. To the best of our knowledge, this is the first study on room-temperature and high-yield synthesis of AgNWs in a continuous millifluidic process. We have also demonstrated the effect of silicone oil, surfactant, mixing configuration, and UV-visible (UV-vis) light on the yield of AgNWs. Furthermore, we discussed the effect of coil diameter on the reaction and on the yield of silver nanowires, and described how the mixing in the flow can be affected by changing the coil diameter. Combined with the advantages of the millifluidic system, we have demonstrated that tannic acid can be used for the synthesis of AgNWs in a green and continuous manner, and this process can be a viable sustainable technique for the large-scale production of AgNWs.

4.2. Experimental methodology

4.2.1. Materials and methods

Tannic acid (MW: 1701.2 g/mol, product number: 403040), silver nitrate ($AgNO_3$, MW: 169.87 g/mol, product number: S0139), Triton X-100 (product number: X-100), silicone oil (10 cSt, product number: 378321), sodium acetate (MW:82.03 g/mol, product number: S2889), 1,10 Phenanothroline (PHEN, MW: 180.21 g/mol, product number: P13002), and 2,4,5,7-Tetrabromofluorescein (TBF) (MW: 647.89 g/mol, product number: E4009) were all purchased from Sigma Aldrich. Deionized water (DIW, ASTM type II) was used as the solvent to prepare aqueous $AgNO_3$, tannic acid, and triton X-100 solutions. A polytetrafluoroethylene (PTFE) tube (1/16 inch inner diameter, 1/8 inch outer diameter, Fluorstore), and a polyvinylchloride (PVC) tube were used to prepare the millifluidic reactor. Three-way (tee) and cross junctions (McMasterCarr and Eldonjames) were used to combine streams into the reactor. The tee and cross junctions were made of polypropylene plastic and Polyvinylidene fluoride (PVDF), respectively. An electric syringe pump (CHEMYX, Fusion 200-X) was used to inject the solutions into the millifluidic reactor.

4.2.2. Reactor design

To prepare the millifluidic reactor, the PTFE tube was tightly wrapped around the PVC pipe to form a coil-shaped design (figure 4.1), in which case the coil diameter can be considered as the pipe's outer diameter. The tube was adhered to the pipe to maintain its position. For a typical experiment, the length

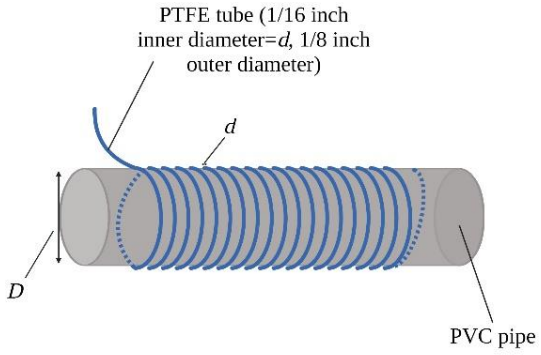

Figure 4.1: The helically-coiled millifluidic reactor design. Created with BioRender.com.

of the reactor was 50 feet and the inner diameter of the tube was 1/16 inches. For comparison, PVC pipes with different outer diameters were used (1.33, 2.37, and 5 inches).

4.2.3. Synthesis of AgNWs in the millifluidic reactor

To prepare the initial samples, 20 mL of silver nitrate (5 mM), and 20 mL of tannic acid (5 mM) were prepared by dissolving the powders in DIW. Additionally, an aqueous solution of triton X-100 was prepared (10% v/v) by adding 18 mL of DIW to 2 mL of the original triton X-100. The solutions, along with silicone oil, were each then loaded into 20 mL syringes and placed on the syringe pump, which pumped the solutions into the reactor at a given flow rate. Mixing was carried out in three different configurations. In configuration A, silver nitrate, tannic acid, and silicone oil streams met at the first junction (cross junction), and then mixed with the surfactant, triton X-100, at the second junction (tee junction). The cumulative flow was then pushed into the reactor (figure 4.2). Silicone oil is mainly used to prevent fouling inside the tube and triton X-100 is used to prevent the migration of nanostructures to the water-oil interface, which occurs due to the tendency for surface energy minimization. In configuration B, tannic acid and triton X-100 were mixed prior to syringe loading. The mixture stream met the silicone oil and silver nitrate streams at the cross junction and then entered the reactor (figure 4.3). Configuration C was similar to configuration B, but triton X-100 was rather mixed with silver nitrate prior to syringe loading to yield concentrations of 10 % (v/v) and 5 mM, respectively (figure 4.4). At the end of the reactor, the nanostructure suspensions were then collected in a falcon tube, which was placed in an ice bath to quench the reaction solution. At typical conditions, all reactions were carried out in the dark, this was done by covering all of the reactor with aluminum foil. Furthermore, the flowrates were adjusted so that the residence time inside the reactor was 96 minutes for all conditions. The flowrate values for each configuration are provided in the figures. In all conditions, the PVC tube (coil) diameter was 2.37 inches. After the reaction was completed, the silicone oil was removed from the falcon tube and the sample was centrifuged six times at 3,000

rpm for 30 minutes, supernatant was removed, and obtained nanostructures were suspended in deionized water.

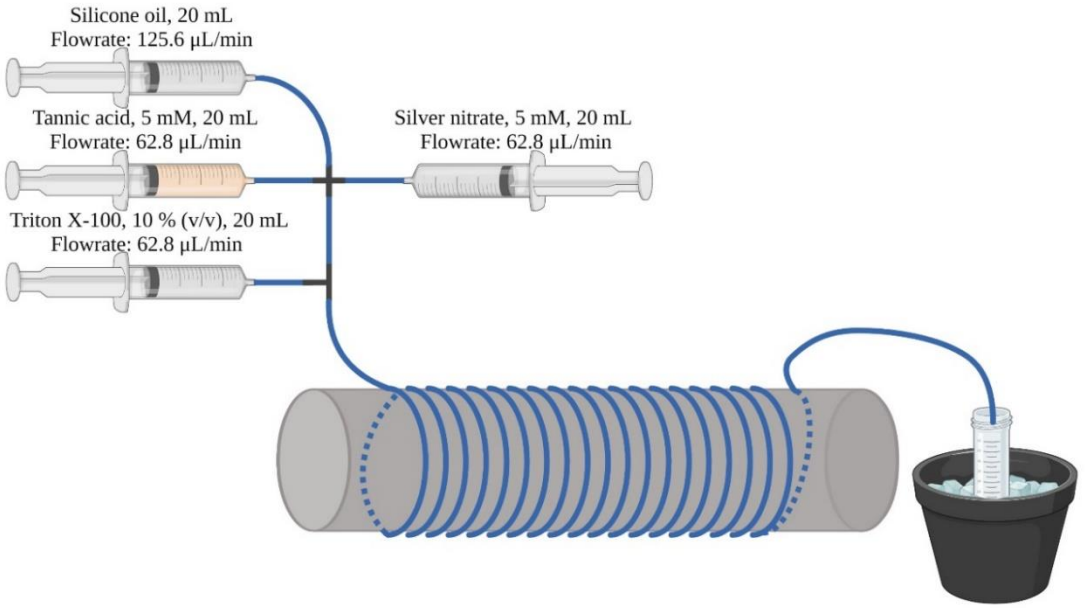

Figure 4.2: Configuration A of the millifluidic reactor: separate addition of the triton X-100 stream. Created with BioRender.com.

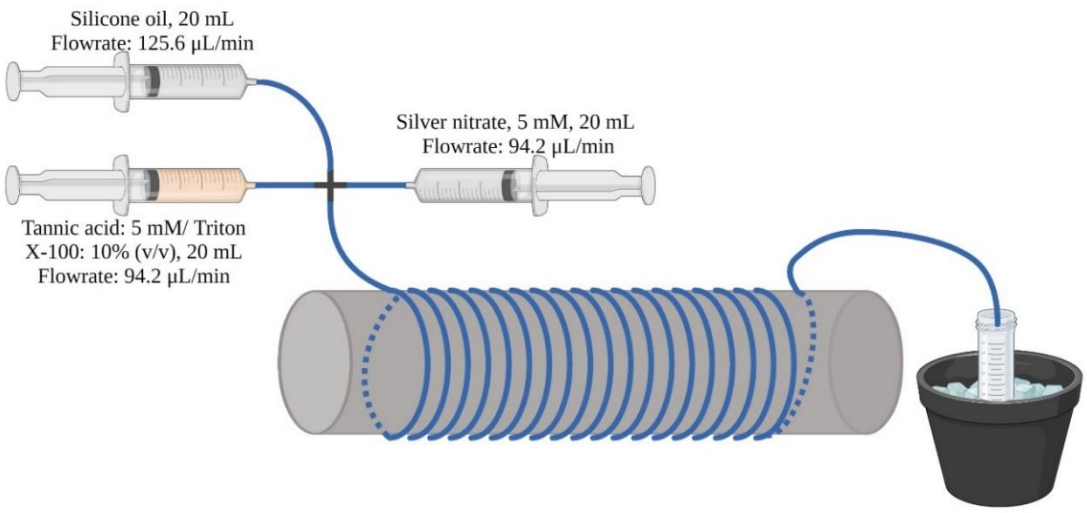

Figure 4.3: Configuration B of the millifluidic reactor: introduction of triton X-100 along with tannic acid. Created with BioRender.com.

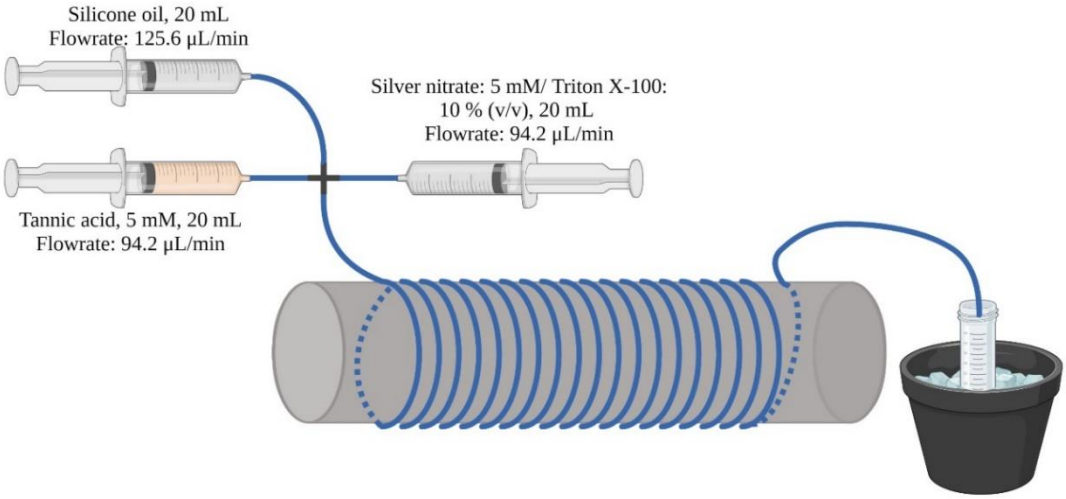

Figure 4.4: Configuration C of the millifluidic reactor: introduction of triton X-100 along with silver nitrate. Created with BioRender.com.

4.2.4. Ag^+ concentration measurements

The concentration of Ag^+ ions was measured similar to the approach in our previous study[485]. In this approach, which was inspired by a spectrophotometric method[407], TBF (1.5×10^{-3} M) and PHEN (4.5×10^{-3} M) are mixed with the Ag^+ containing solution from the reaction sample to make [PHEN. Ag-PHEN]$^{2+}$TBF^{2-} complexes that are detectable by UV-visible (UV-vis) spectroscopy where an absorbance peak at 550 nm can be observed. Prior to mixing with Ag^+, the pH of the PHEN-TBF solution (2 mL) was adjusted at 5.2 by adding 18 mL of the acetate buffer (mixture of sodium acetate (169 mM) and acetic acid (0.3 % v/v)). To measure the Ag^+ concentration at different time intervals, aliquots were taken from the reaction sample at different residence times (0, 16, 32, 48, 64, 80, and 96 minutes). For residence times shorter than 96 minutes, the reactor tubing was dissected and shortened to have the length corresponding to each residence time.

4.2.5. Characterization

4.2.5.1. Scanning electron microscopy (SEM)

The SEM images were collected by the FEI Quanta 600 Field-Emission Gun Environmental Scanning Electron Microscope at the Oklahoma State University's microscopy laboratory. For sample preparation, 100 μL of the nanostructure suspension was added to smooth carbon tabs which were placed on aluminum pins. The samples were maintained at room temperature for 24 hours to be dried. The samples were then placed in the SEM sample holder for characterization.

4.2.5.2. Transmission electron microscopy (TEM)

The TEM images were collected by the JEOL JEM-2100 Transmission Electron Microscope System (200 kV accelerating voltage) at the Oklahoma State University's microscopy laboratory. For sample preparation, 10 μL of the nanostructured suspension was added to carbon grids. After solvent removal, the grids were then moved to the TEM sample holder for characterization.

4.2.5.3. Energy dispersive X-ray spectroscopy (EDX)

EDS spectroscopy was performed by a built-in Evex Nanoanalysis EDX system in the TEM instrument.

4.2.5.4. Ultraviolet-visible spectroscopy (UV-vis)

The UV-vis spectroscopy was performed out by the Metler Toledo UV5 spectrophotometer. After adding the reaction solution into 3 mL cuvettes, the measurements were taken for wavelengths ranging from 190 to 1,100 nm.

4.2.5.5. Light measurements

The Dr. Meter 1330B-V light meter was used to measure light intensity (measured in LUX).

4.3. Results and discussion

4.3.1. Air and silicone oil effects

The use of segmented flow systems, in which a secondary phase is used as the carrier phase, can contribute to rapid mixing by creating small and separate droplets, which enhances product quality and reproducibility[486,487]. In such systems, the reaction is limited to single droplets, which allows for a uniform residence time and prevents the flow to be clogged by the accumulation of particles[486]. Depending on the type of the secondary phase, tubing material, and type of solvent, the flow can typically be obtained in three modes including droplet mode, plug mode, and slug mode (figure A.1)[486]. In the droplet mode, the droplets, in which the reaction is carried out, are totally separated from the walls by the carrier phase. In the plug mode, both the carrier and reaction phases are directly in contact with the walls. In the slug mode, the carrier phase is separated from the walls while the reaction phase is constantly in touch with the walls. If the reaction phase is an aqueous phase, the carrier phase shall contain fluid that is immiscible with water, such as oil or air. Choosing air can be beneficial to the process cost since the cost for any type of oil can be avoided. However, using air may result in fouling in the reactors and coating of the tubing inner walls depending on the tubing material and the reducing/capping agent used. Friedman et al.[488] demonstrated that different types of materials (composed of rubber, PVC, Teflon, and polyethylene plastic) can be coated in the case of silver nanoparticle synthesis. They used ethylene glycol as the reducing agent and silver nitrate as the metal precursor, in the presence of ammonia. They showed that all materials can be coated by silver nanoparticles regardless of the tubing material. However, Teflon was the least susceptible to coating compared to the three other materials used, suggesting the promising potential of Teflon (also known at PTFE) for the synthesis of metallic nanoparticles in fluidic reactors. It is important to mention that they did not use a segmented flow system, and carried out the process in the presence of ultrasonication. Nevertheless, if either air or oil is used as the carrier phase for a segmented flow,

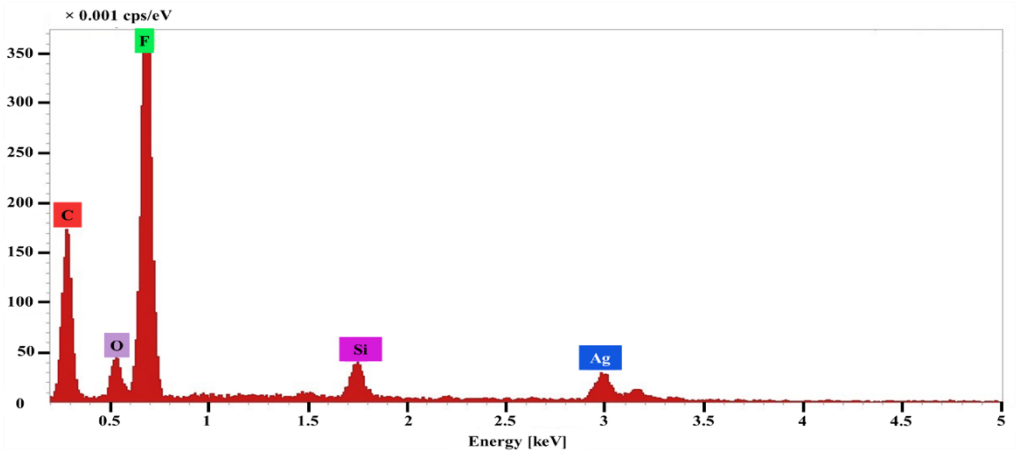

Figure 4.5: The EDX spectra collected from the tube surface (figure A.2) in which air was used as the secondary phase.

coating may be minimized. To test this hypothesis, we carried out the synthesis of silver nanostructures using tannic acid in the presence of air and silicone oil as the carrier phase. In the first experiment, the process was carried out similar to configuration A; however, air was used instead of silicone oil and triton X-100 was not present. After the completion of the synthesis process, inside the tubing was washed multiple times with acetone and water, and then dried with air. The results show that despite being resistant to coating, the PTFE tubing can significantly be coated by silver nanostructures, especially at the beginning of the tubing, just after the junction. To confirm the presence of silver nanostructures on the inner tubing wall, a small section of the PTFE tubing, just after the cross junction, was dissected along its long axis, and characterized by SEM and EDX. Figure A.2 shows the SEM image of the dissected piece of PTFE tubing. Figure 4.5 shows the EDX spectra collected from the same sample, in which the presence of the silver element can be confirmed. Furthermore, figure A.3 shows a map of different elements present at the surface of the tubing, where the significant presence of silver can be confirmed. It is important to note that although the tubing was even washed and dried rigorously before the analysis, silver particles were not removed from tubing wall, by which we can conclude that the tubing was coated with silver particles. Similarly, the process was repeated using silicone oil (10 cSt viscosity) instead of air. The results show a significant difference. The SEM image of the

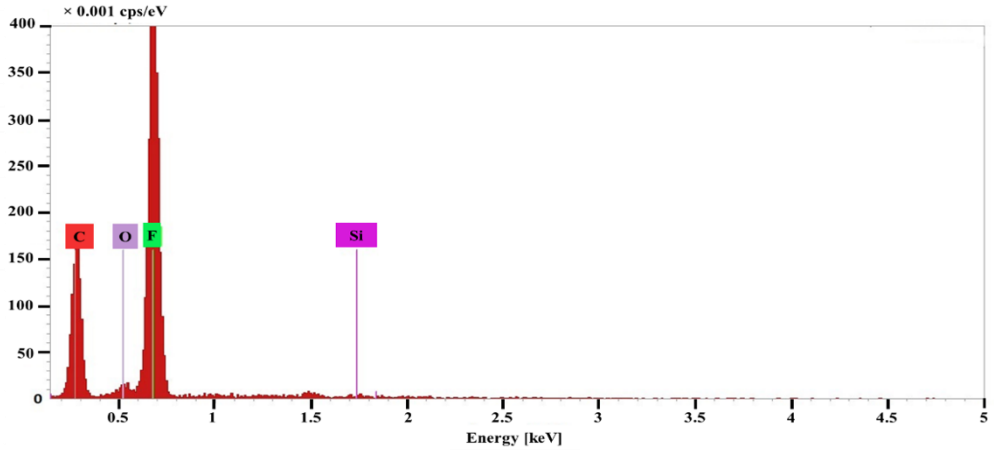

Figure 4.6: The EDX spectra collected from the same sample in figure A.4 in which silicone oil was used as the secondary phase.

dissected PTFE tube is provided in figure A.4. In this case, the PTFE tubing was almost fully resistant to coating as the absence of the silver element can be confirmed by EDX analysis (figures 4.6 and A.5) obtained by analyzing the same sample provided in figure A.4. Therefore, the presence of silicone oil was necessary to prevent coating in the millifluidic reactor.

When air is used as the carrier phase, the flow obtains either the plug or slug mode, as shown in figure A.1. In this case, the reaction phase is in direct contact with the tubing walls. The coating mainly occurs due to nanoparticles' tendency to minimize surface energy and achieve stability[489], which may be prevented using various stabilizers. However, some compounds that act as either reducing, capping, or stabilizing agents, may actually enhance the deposition of nanoparticles unto solid surfaces. For instance, polyphenols and their derivatives can adsorb onto a wide variety of solid substrates, regardless of their concentration[490–493]. It was also previously shown that a combination of polydopamine and tannic acid was used to coat steel and nylon substrates to prevent fouling by marine species[491]. It was also reported that polyphenols can cause strong fouling in filtration systems[492,493]. In our synthesis process, tannic acid—a polyphenol—is used as both the reducing and capping agents, which can adsorb onto the PTFE tubing inner walls. When silver nanostructures are synthesized by tannic acid at the vicinity of the wall, they form an assembly there, which grows over time. This is harmful to the process for several reasons. First,

nanoparticle deposition can result in channel clogging, which can lead to leakage. Second, the formed deposition layer at the walls weakens heat transfer in the system specifically if reactions are running at high temperature. Third, it affects the quality of the product as nanoparticle growth is more favorable at the tubing surface rather than inside the flow stream.

When silicone oil is used as the carrier phase, the flow tends to obtain a droplet mode where the reaction phase contact with the wall is minimized. In our setup, silicone oil's flow rate is higher than that of silver nitrate and tannic acid. This was done purposefully so that silicone oil reaches the reactor faster than silver nitrate and tannic acid, and wets the PTFE tubing inner wall before silver nitrate and tannic acid mixture enter the tubing. Afterward, the contact between silicone oil and PTFE is maintained throughout the process as both possess hydrophobic characteristics[494]. This phenomenon continuously keeps aqueous droplets away from the tubing wall and nanoparticle deposition is avoided. The results suggest that using silicone oil in continuous fluidic reactors is necessary in the case of silver nanostructure synthesis using tannic acid or any other compound (reducing/capping agent) that can adsorb onto PTFE surfaces. In addition to nanoparticle coating prevention, the droplet flow can help to enhance mixing in the reaction solution within each droplet, thereby increasing quality of the nanostructures (i.e. minimizing size distribution). Despite all the advantages, silicone oil itself can disrupt the formation of nanostructures in a homogeneous manner. This is discussed in detail in the following section.

4.3.2. Surfactant effect

When oil is used as the carrier phase, the synthesized silver nanostructures adsorb into the water-oil interface, which occurs due to their tendency to minimize surface energy[484,495]. This phenomenon leads to the formation of nanostructure assembly at the water-oil interface rather than in the droplets. This assembly becomes more stable as the size of the nanostructures increases[495], which in the case of a droplet-based fluidic reactor would mean that as

nanostructures grow, they will have a higher tendency to adsorb at the water-oil interface. This can be a disruptive process because mixing will become limited in the droplets and growth will be more favorable for the nanostructure assembly at the interface rather than nanostructures within the droplet. This can adversely affect nanostructures' uniformity in terms of size and morphology. Additionally, it is very challenging to separate synthesized nanostructures from the interface. To store the nanostructure suspension and use it for various applications, oil must be removed from the mixture, in which case the nanostructures might be removed along with oil during the separation process. One way to address this issue is to use a surfactant that can passivate the water-oil interface and prevent the migration of synthesized nanostructures to the interface. The use of common surfactants such as Cetyl Trimethyl Ammonium Bromide (CTAB) may not be favorable to prevent the interfacial adsorption of nanostructures as the nanostructures obtain an amphiphilic surface in the presence of CTAB molecules, which results in their migration to the water-oil interface[484]. Triton X-100, as a non-ionic surfactant, can passivate the water-oil interface and it does not interact with silver nanostructures. Figure A.6 shows the nanostructure suspension sample in the presence of silicone oil and in the absence of triton X-100. The setup had a configuration similar to A, but without the triton X-100 stream. As expected, the nanostructures formed an assembly at the water-silicone oil interface. On the other hand, the presence of triton X-100 is a significant game-changer in this process. Figure A.7 shows the nanostructure suspension sample in the presence of both silicone oil and triton X-100. In this case, the setup configuration was completely similar to configuration A. As expected, the nanostructures were separated and kept away from the water-oil interface. In this case, the formation of silver nanowires with a high yield and uniformity—the desired outcome—was more favorable, which is discussed in next section. In addition, the silicone oil can be removed and refluxed for reuse, in order to decrease the cost associated with silicone oil supply. A schematic of the synthesis process in the absence and presence of triton X-100 is shown in figure A.8, which demonstrates the journey of a droplet in the millifluidic reactor. When triton X-100 is present,

their molecules rearrange to have the hydrophilic end facing the aqueous solution in the droplet and the hydrophobic head being attached to the oil phase at the water-oil interface, thus preventing the migration of silver nanostructures to the interface. Furthermore, a similar study showed the advantages of triton X-100 as a surfactant in the presence of silicone oil, where it was shown that the use of triton X-100 does not affect the capping effect of PVP in the case of silver nanocube synthesis[484].

4.3.3. SEM/TEM results

4.3.3.1. Silver nanostructures synthesized in the presence of air and silicone oil as the carrier phase

When air is used as the carrier phase, the growth of silver nanostructures is affected in addition to the clogging issue and tube coating. Figure 4.7 shows the SEM image of the silver nanostructures synthesized in the presence of air as the carrier phase. The formation of large agglomerated particles with a wide size distribution and varied morphologies can be confirmed, which is undesirable. A probable reason is that when the tube is coated with nanostructures, homogeneous mixing is severely affected and the reduced atoms are adsorbed to the nanostructure assembly at the tube surface instead of assembling within the droplets. In the case of silicone oil and absence of triton X-100, the formation of nanostructure assembly at the water-oil interface affects the growth of silver nanostructures. The SEM image of the nanostructures is provided in figure 4.8, where the presence of large agglomerated particles can be confirmed. Similar to the air case, homogeneous mixing can be

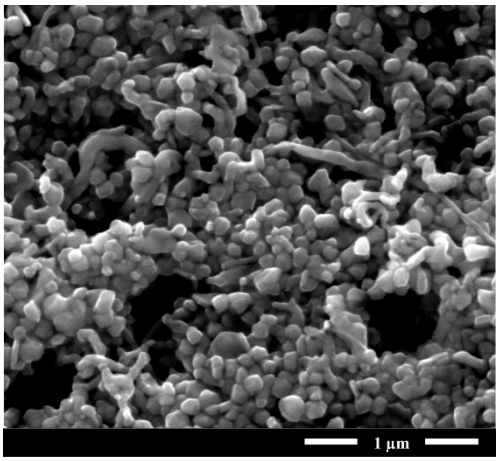

Figure 4.7: SEM image of silver nanostructures synthesized in the presence of air as the secondary phase.

affected when the nanostructures are merely assembled at the water-oil interface, causing the growth to be more favorable at the interface rather than within the droplet.

4.3.3.2. Silver nanowires (AgNWs) synthesized in configuration A

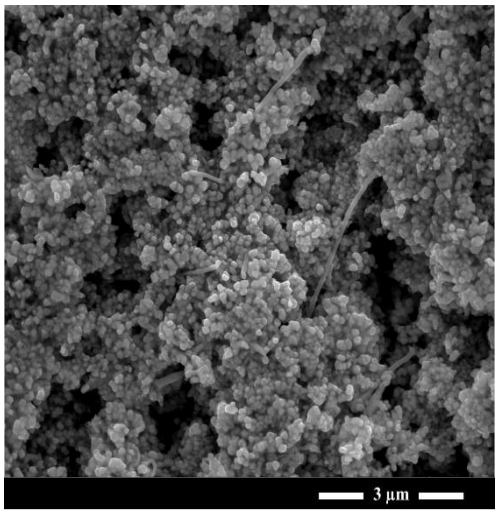

Figure 4.8: SEM image of silver nanostructures synthesized in the presence of silicone oil as the secondary phase.

To synthesize 1D silver nanostructures (e.g. AgNWs), the process should favor asymmetric growth facilitated by a controlled deposition rate of Ag^0 atoms, as well as thermodynamic control over nanocrystals' surface growth[377]. We previously showed in our recent study that tannic acid can be used as both the reducing and capping agents to synthesize AgNWs at room temperature with moderate yield, under controlled kinetics and reduction rate facilitated by photons[485]. However, that process was carried out in batch conditions, in which mixing and mass transfer is not as effective as in the millifluidic reactor. To synthesize AgNWs, configuration A was taken into consideration with the conditions shown in figure 4.2, which are similar to our batch process (room temperature, 5 mM tannic acid, and 5 mM silver nitrate). Additionally, the tubing was fully covered with aluminum foil to prevent the absorption of photons similar to the dark condition for our batch reactor in which the reactor was fully covered with aluminum foil. The reaction had a residence time of 96 minutes compared to the 240 minutes reaction time for the batch process. Figure 4.9.A shows the SEM image of the silver nanostructures, including mostly AgNWs, synthesized in the millifluidic reactor. The AgNWs had an average diameter of 47±18 nm, an average length of 5.8±4.1 µm, and the yield is estimated to be around 82%. The yield of AgNWs

synthesized at the dark condition was significantly higher compared to those synthesized in the batch process (the dark condition). An interesting phenomenon is that when the reaction is carried out in the batch reactor in the dark condition, the formation of silver nanoplates is more favorable due to a significantly slow reduction rate. In such case, a lower reduction rate leads to a lower atomic deposition rate, which promotes the formation of stacking faults favoring the growth of nanoplates. However, this is not the case for the millifluidic reactor. Although the reaction was carried out in the dark in the millifluidic reactor, the formation of AgNWs was more favorable compared to that of the batch. This indicates that the atomic deposition rate was adequately high in the millifluidic reactor compared to batch one due to enhanced mixing that contributes to anisotropic growth, which is why the yield of AgNWs is higher. The higher atomic deposition rate can be attributed to the miniaturized reaction environment as well as the droplet-based flow in which mass transfer is enhanced through molecular diffusion rather than advection, which is the dominant mechanism in the batch process. Furthermore, the yield of AgNWs in the millifluidic reactor was even higher compared to the best batch condition for the synthesis of AgNWs (%

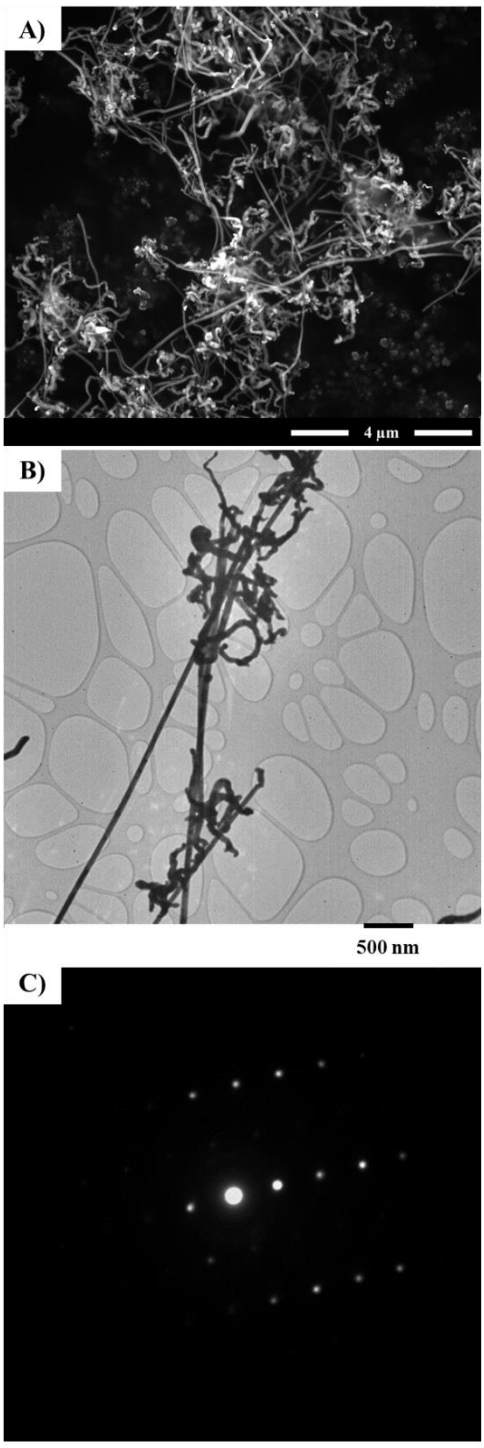

Figure 4.9: A) SEM image of AgNWs synthesized using configuration A. B) TEM image of AgNWs synthesized using configuration A. C) Diffraction pattern of AgNWs synthesized in the millifluidic reactor.

yield) where the reaction was partially exposed to photons. Furthermore, the TEM image of AgNWs is shown in figure 4.9.B. Figure 4.9.C shows diffraction patterns from AgNWs by which we can confirm the presence of single-crystal AgNWs.

4.3.3.3. Silver nanostructures synthesized at different mixing configurations

The surfactant (triton X-100) used in the synthesis of AgNWs can be used in different manners. Considering its inert properties, it can be mixed with either silver nitrate or tannic acid solutions prior to mixing of the two streams. This was carried out to observe how the yield of AgNWs was affected. For this purpose, the three different configurations discussed in section 2.3 were taken into consideration. The AgNWs synthesized using configuration A were discussed and analyzed in the previous section. Figure 4.10.A shows the SEM image of the silver nanostructures synthesized using configuration B. As demonstrated, the nanostructures consisted of particles with various morphologies and large size distribution along with a few nanorods. In this case, the yield of AgNWs was significantly lower compared to configuration A. A likely reason is the interaction of triton X-100 with tannic acid. Despite being inert to Ag^+ ions, triton X-100 can interact with tannic acid molecules via hydrogen bonding between triton X-100's etheric oxygens

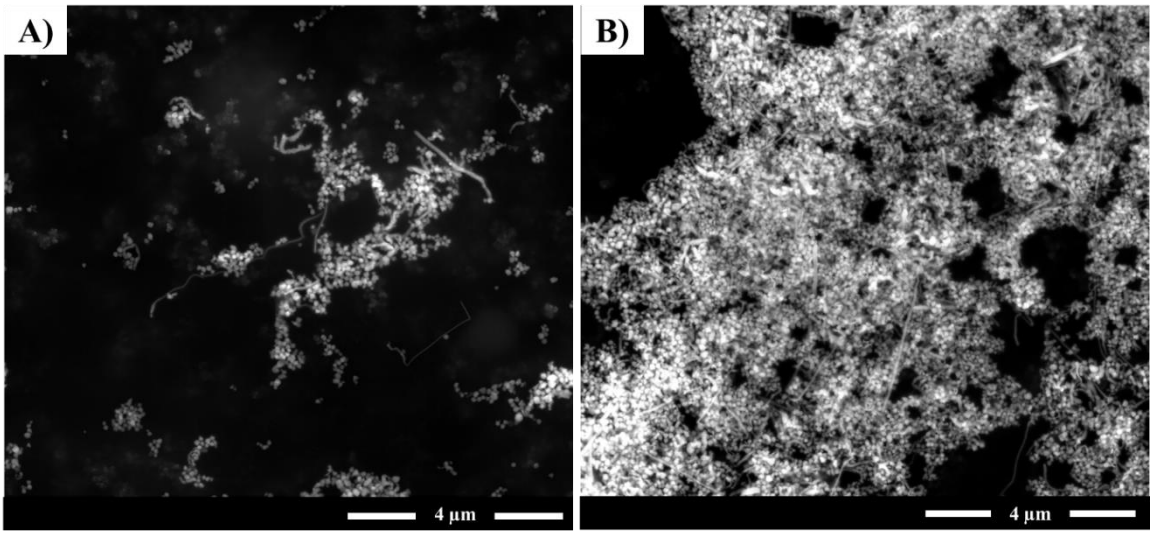

Figure 4.10: A) SEM image of silver nanostructures synthesized using configuration B. B) SEM image of silver nanostructures synthesized using configuration C.

and tannic acid's hydroxyl groups[496,497], thus disrupting the adsorption of Ag^+ ions and the formation of tannic acid-Ag^+ complex. It was previously shown that triton X-100 can disrupt phenolic-enzymatic interactions by interacting with the phenolic compounds, including tannic acid[496,498]. As a result of such interactions, less tannic acid molecules will be available to form the tannic acid-Ag^+ complex. In such case, it is as if the concentration of tannic acid is less than that of configuration A (5 mM). A less than 1 molar ratio of tannic acid/silver increases the incorporation of Ag^0 atoms into particles[485], which leads to higher nucleation and growth rates compared to that of configuration A, which is why the yield of AgNWs is lower in configuration B.

Figure 4.10.B shows the SEM image of the silver nanostructures synthesized using configuration C. As demonstrated, the nanostructures consisted of particles with varied morphologies, along with a few nanowires, somewhat similar to configuration B. However, the yield of AgNWs in this case was slightly higher compared to configuration B. Similarly, this could be due to the interaction of triton X-100 with tannic acid, but slightly differently. In configuration C, when tannic acid and silver nitrate/triton X-100 streams are being mixed at the junction, both Ag^+ ions and triton X-100 molecules diffuse through the tannic acid solution. As a result, there should be a competition between Ag^+ ions and triton X-100 molecules in interacting with tannic acid, while this is not the case for configuration B where tannic acid and triton X-100 are well-mixed before silver nitrate is introduced. As a result, more tannic acid molecules are available to form the complex with Ag^+ ions in configuration C, which is a closer scenario to configuration A. However, triton X-100 can still sever interactions of addition Ag^+ ions with tannic acid, causing configuration C to deviate significantly from configuration A.

Although this is possible that triton X-100 can still disrupt Ag^+-tannic acid interactions in configuration A after triton X-100 is introduced through the second junction, it has a weak effect which can be potentially considered to be negligible. When the triton X-100 stream is introduced

through the second junction, it will meet a two-phase flow where silicone oil and aqueous droplets are separated. In this case, the absorption of triton X-100 onto the water-oil interface is more favorable; thus, the diffusion of triton X-100 into the aqueous droplet is limited. The results demonstrated that configuration A was the most favorable setting for the synthesis of AgNWs with a higher yield; therefore, this setting was considered for further experiments.

4.3.3.4. Silver nanostructures synthesized at different light conditions

We previously showed that UV-vis irradiation can significantly enhance the reduction of Ag^+ ions in the batch synthesis of AgNWs using tannic acid, ultimately controlling the yield of AgNWs[485]. We demonstrated that this can be attributed to the strong absorption of UV light by tannic acid, which results in photoexcitation. The effect of UV-vis irradiation on the yield of AgNWs in the millifluidic reactor was similarly investigated in this study. The PTFE tubing used in this study was transparent, allowing the photons to pass through and reach the reaction environment. In order to carry out the experiments, different rounds of the tubing were covered with aluminum foil in a way that the rest of the tubing is exposed to irradiation. For this purpose, the first 10, 20, 30, and 40 rounds of the tubing were exposed to UV-vis irradiation in each experiment. In addition, an experiment was carried out with the reactor fully exposed to irradiation. The white fluorescent lamps in our laboratory were used as the illumination source. In order to quantify illumination, the light intensity was measured at the top of the reactor (placed horizontally), which is closer to the illumination source, and at the bottom of the reactor which is farther from the source. The readings were measured to be 592 and 317 LUX, respectively. This means that the reaction droplets will experience a maximum of 592 and minimum of 317 LUX light intensity; as a result, there will be an oscillation between those two values as the droplets take one turn to the next. Furthermore, the number of tubing rounds can be corresponded with their respective lengths and residence times, which are defined as exposure lengths and exposure residence times (ERT). These values are summarized in table 4.1.

Table 4.1: Residence times in the millifluidic reactor for exposure to UV-vis illumination.

Number of tubing rounds exposed to irradiation	0	10	20	30	40	All of the tubing exposed
Exposure length (ft)	0	6.2	12.4	18.6	24.8	50
ERT (exposure residence time) (minutes)	0	11.9	23.8	35.7	47.6	96

Figure A.9 shows the SEM images associated with different ERTs in addition to the SEM image of nanostructures synthesized in the dark (ERT of 0), which was discussed in the previous sections. In all cases, the nanostructures are a mixture of AgNWs and other nanoparticles such as nanorods, nanospheres, or structures with irregular morphologies. However, as the ERT increases, the yield of AgNWs decreases and 1D nanostructures tend to adapt a nanorod morphology. A significant difference in the yield of AgNWs between ERTs of 0 and 11.9 minutes can be observed. There is not a significant difference in the yield of AgNWs and the overall morphology of nanostructures when ERTs are equal to or higher than 11.9 minutes. This suggests that the first 12-minute span and earlier, at the beginning of the reaction, is crucial for the outcome of the process as controlling the reduction rate can change the morphology and yield of the nanostructures. A more detailed analysis is provided in section 3.4.3 using UV-vis spectroscopy analysis.

4.3.3.5. Silver nanowires/nanostructures synthesized at a different residence time

For tubular reactors, residence time is often regarded as the mean residence time due to the existence of residence time distribution. A large residence time distribution can adversely affect the quality of the product in the case of nanomaterials synthesis (i.e. high size distribution, non-uniform morphology). The residence time distribution can be reduced by either manipulating the flow regime or changing the geometry of the reactor. For instance, helical coil or preferably coil flow inverter reactors can induce Dean vortices, which can break stagnant regions, and therefore reduce residence time distribution[499–502]. This is necessary for a continuous flow. However, the

flow in our setup is different as aqueous reaction droplets are separated by silicone oil and a continuous one-phase flow does not exist. As a result, the residence time distribution for the particles inside the droplet is minimized. Therefore, a value of 96 minutes may be considered to be constant for all the particles passing through the reactor. To investigate the effect of residence time on the yield of AgNWs and the overall morphology of the silver nanostructures, the reactor inlet flowrates were halved to obtain an overall flowrate of 157 µL/min, equivalent to a residence time of 192 minutes, which is twice of the initial residence time. Figure 4.11 shows the SEM image of the silver nanostructures synthesized at 192 minutes residence time. As it can be observed, most nanostructures included AgNWs almost similar to the original condition where the residence time was 96 minutes. The process is still favorable for the synthesis of 1D nanostructures and the lower flowrate does not affect mixing significantly as both processes have a laminar flow regime, and Reynold's number (Re) is equal to 4.18 and 2.09 for the higher and lower flowrates, respectively. However, there are two main differences between the two processes. The first is the length of the AgNWs obtained at 192 minutes residence time, which was on average higher (8.5±4.4 µm) than that of those obtained at 96 minutes residence time. Another difference is the presence of other nanostructures with irregular morphologies along with AgNWs. As the residence time increases, the concentration of Ag^{+} ions is depleted in the flow resulting in a decrease in reduction and growth rates. A possible situation is that this may not favor further growth of AgNWs because of the inadequate atomic deposition rate, and instead, the reduced Ag^{0} atoms nucleate and the seeds grow, therefore producing a large number of small particles. These particles also exist in the case of 96 minutes residence time; however, they may be overshadowed by the larger presence of

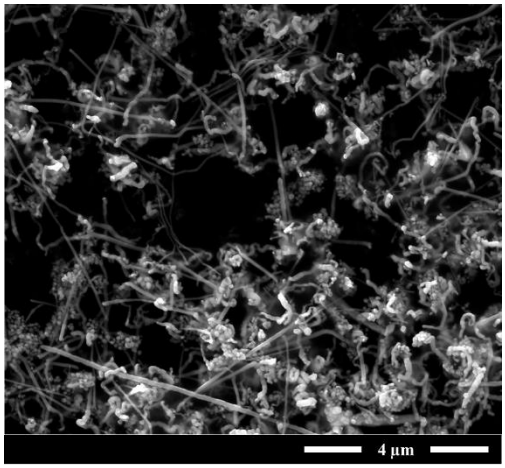

Figure 4.11: SEM image of silver nanostructures synthesized at 192 minutes residence time.

AgNWs. In general, the yield of AgNWs is higher for the 96 minutes residence time compared to 192 minutes residence time; however, AgNWs are longer in the case of 192 minutes residence time, and therefore have a higher aspect ratio since the average AgNW diameter (41±15 nm) is not significantly different from that of 96 minutes residence time.

4.3.3.6. Silver nanowires/nanostructures synthesized using different coil diameters

Controlling mixing in tubular reactors is crucial to mass and heat transfer. One particular method to enhance mixing is to have a curved flow path. This idea was previously used for the synthesis of nanomaterials in several studies[463,472,473,503–505], and the flow path design was essential in determining the final size and morphology of the products. It was first demonstrated by Dean in 1920's[506,507] that the helically-coiled tubes result in the creation of symmetrical vortices across the tube cross section as a result of centrifugal forces, where the Dean's number (De) is described as shown in equation 4.2.

$$De = Re\sqrt{\lambda} \qquad \text{Equation 4.2}$$

Where Re is the Reynold's number, and λ is the curvature ratio defined as the ratio of the tubing diameter to the coil diameter ($\frac{d}{D}$). The Dean's number is important in analyzing the effect of the secondary flow and mixing. The more the value of the Dean's number, the stronger the centrifugal effect, thus creating more circulating vortices within the droplet, which results in a more rapid mixing. This can be done either by increasing the curvature ratio or by increasing Re or both at the same time. We also recall Reynold and Schmidt's number, which are shown in equations 4.3 and 4.4, respectively.

$$Re = \frac{\rho v d}{\mu} \qquad \text{Equation 4.3}$$

$$Sc = \frac{\mu}{\rho D_{AB}} \qquad \text{Equation 4.4}$$

Where ρ is the fluid density, v the fluid velocity, d the tube diameter, D_{AB} the molecular diffusivity of component A in component B, and μ the fluid viscosity. The effect of Dean's vortices is stronger for higher Re, particularly in the turbulent region. However, Kumar et al.[508] analyzed both the laminar and turbulent flow behavior in helically curved tubes with a circular cross section. They showed that when the curvature ratio is increased from 5 to 10 (by changing the coil diameter, for a constant tubing diameter), the mixing greatly increases for Re values even as small as 10, which lies in the laminar region. Similarly, in a more recent study, Mansour et al.[509] demonstrated using computational fluid dynamics (CFD) simulations that decreasing the coil diameter (for a constant tubing diameter) enhances mixing for various Re values as small as 5. To see how this can affect the size and morphology of silver nanostructures in our system, the experiments were carried out for different coil diameters include 1.33, 2.37, and 5 inches, using configuration A. All previous experiments were carried out for the coil diameter of 2.37 inches. Figure 4.12 shows the SEM

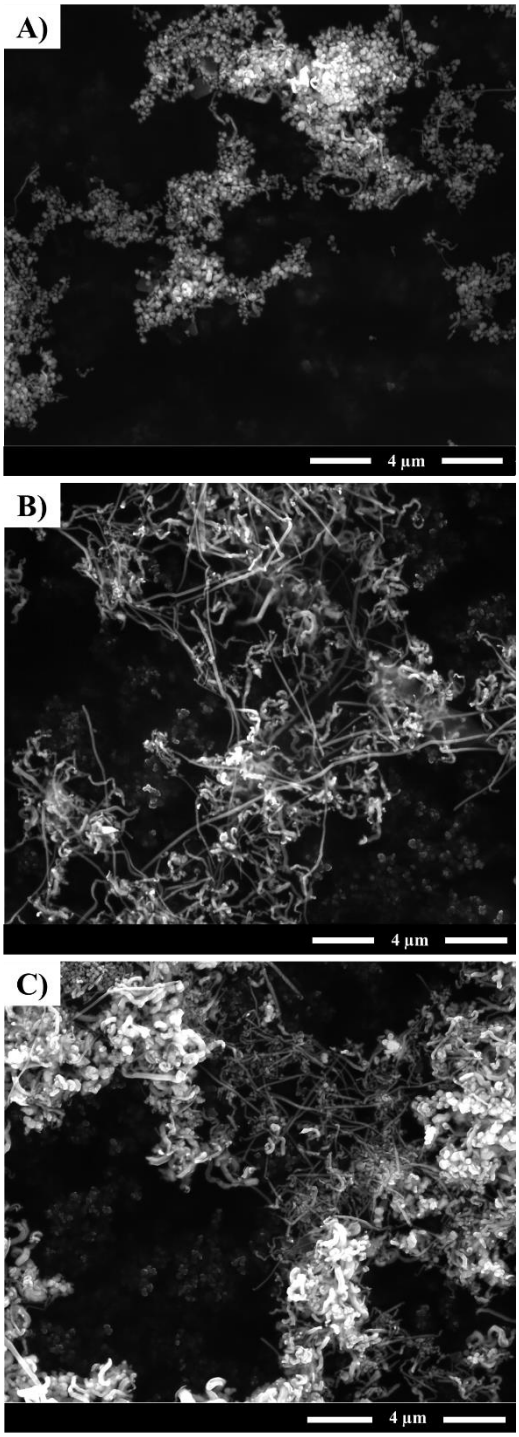

Figure 4.12: SEM images of silver nanostructures synthesized at different coil diameters. A) 1.33 in, B) 2.37 in, and C) 5 in.

images of the silver nanostructures synthesized at different coil diameters, corresponding to different curvature ratios. As demonstrated, the yield of AgNWs decreases significantly when the coil diameter is decreased to 1.33 inches. In this case, the product consisted mostly of nanoparticles with irregular morphologies. For 5 inches of coil diameter, the product consisted of large agglomerated particles along with AgNWs and thick nanorods (diameter >100 nm) with a twisted long axis. By comparison, there are more AgNWs for the 5-inch coil reactor compared to the 1.33-inch coil reactor, but less compared to the 2.37-inch coil reactor. An analysis of mixing in the flow can shine a light on the mechanism behind this difference. Typically, for small Re values, mixing is less dependent on the change in Re but more dependent on the change in Schmidt's number because mixing is dominated by diffusion rather than advection[509–512]. But in the case of helically coiled reactors, both effects come into play due to the presence of secondary flow. For two liquid droplets that are going to be mixed, mixing occurs more rapidly for lower Schmidt's number thanks to the effects from diffusion (larger D_{AB}). In Mansour et al.'s study[509], it was demonstrated that complete mixing between the two aqueous droplets can be achieved within the first 4 turns for a 118 mm (4.64 inches)-large coil. In that case, Schmidt's number was equal to 1,000, Re equal to 5, the coil pitch equal to 16 mm, the tube diameter equal to 10 mm, and the curvature ratio equal to 0.0423. By comparison, in our study, Re in the flow is equal to 4.18, which is close to the value of 5 in their study and the curvature ratio in our study is equal to 0.047 (for the 1.33-inch coil), which is almost identical to that of Mansour et al.'s study (0.042). However, the coil pitch in our study was equal to the tubing diameter (1/16 inches=1.59 mm), which is the minimal possible value for the pitch and Schmidt was equal to 606.8. From the Schmidt value, it can be deduced that the effects of diffusion are stronger in our setup. In our study, when the coil diameter is decreased from 2.37 to 1.33 inches (increasing curvature ratio), mixing is enhanced and the two droplets (one containing silver nitrate and the other containing tannic acid) are mixed more rapidly. Consequently, the reduction of Ag^+ ions and as a result,

nucleation and growth rates are faster. However, when the coil diameter is increased (decreasing curvature ratio), mixing is weaker and the two droplets take longer to fully mix. One particular reason for the agglomeration of particles and the presence of large nanostructures can be the movement of particles in the flow. In our study, the laminar flow is not strong enough to fluidize the nanostructures synthesized in the droplets; therefore, when nanostructures grow, they tend to settle at the bottom of the droplets because of gravity. When the coil diameter is larger, these nanostructures settle at the bottom of the droplet for longer periods of time, thus creating a stagnant presence within the droplets, which leads to the agglomeration of nanostructures and a non-uniform morphology. This can be worse for continuous flows or droplet-based reactors with large droplets or liquid slugs. A similar analysis was previously provided by Hohmann et al.[513]. This is a challenge for the synthesis of nanomaterials with uniform size and morphology, but it can be addressed by increasing the curvature ratio (i.e. decreasing the coil diameter).

4.3.4. UV-Vis results

4.3.4.1. Silver nanowires (AgNWs) synthesized using configuration A

Figure 4.13 shows the UV-vis spectra of AgNWs, in which a peak at 394 nm and a shoulder peak around 350 nm can be observed (corresponding to the transverse surface plasmon resonance of AgNWs). In general, in the case of AgNWs, a peak wavelength at or around 390 nm is expected. Depending on the yield of AgNWs, this wavelength can differ. The more the yield of AgNWs decreases, the peak wavelength will become more red-shifted.

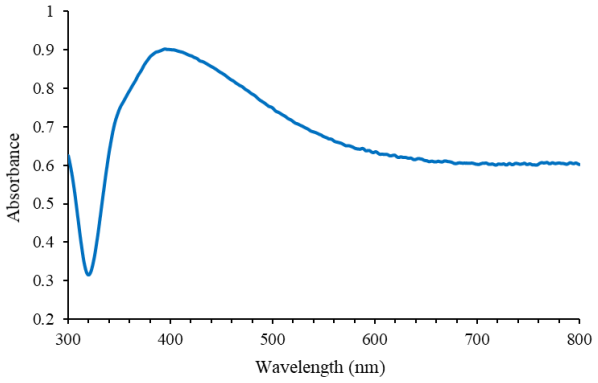

Figure 4.13: UV-vis spectra of AgNWs synthesized using configuration A.

4.3.4.2. Silver nanostructures synthesized at different mixing configurations

It is difficult to make a holistic judgement regarding the yield of silver nanowires based on the SEM images shown in figure 4.10. Figure 4.14 shows the spectra of silver nanostructures synthesized using both configurations. It can be seen that the peak for configuration C is more blue-shifted compared to that of configuration B (at 417 nm compared to 438 nm) due to more and longer 1D Ag nanostructure. This confirms that configuration C is slightly closer to configuration A and more favorable for the synthesis of AgNWs compared to configuration B.

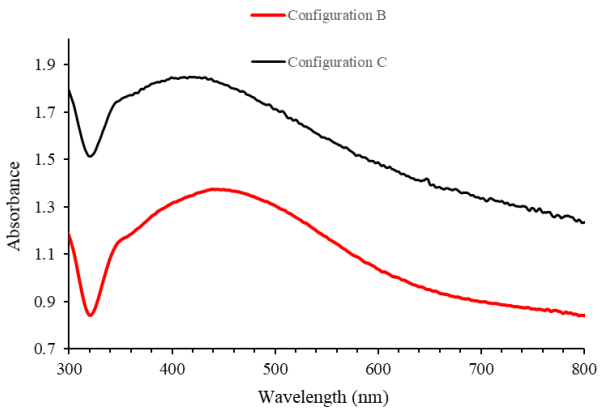

Figure 4.14: UV-vis spectra of silver nanostructures synthesized using configurations B and C.

4.3.4.3. Silver nanostructures synthesized at different light conditions

The UV-vis spectroscopy of silver nanostructures synthesized at different light conditions (figure 4.15) show that the wavelength is more red-shifted when the ERT increases, which is due to the lower yield of AgNWs as well as the presence of shorter 1D nanostructures such as nanorods. This is due to the enhanced Ag^{+} reduction rate, which results in fast nucleation and growth in which seeds adopt a symmetric morphology because it is thermodynamically more favorable[377]. This is not favorable

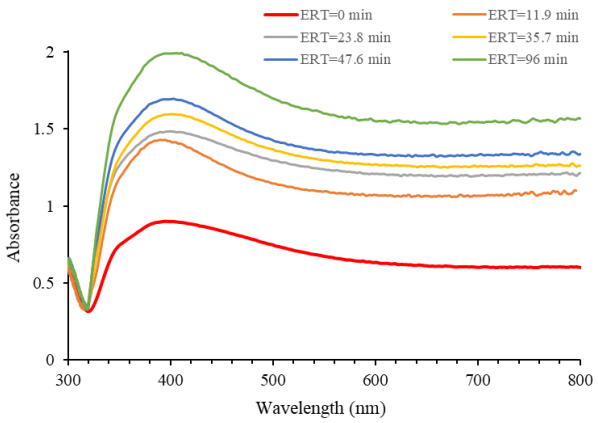

Figure 4.15: UV-vis spectra of silver nanostructures synthesized at different illumination or exposure residence times (ERTs).

for the synthesis of AgNWs, where symmetric breaking is preferred for 1D growth[377]. A particular analysis of the UV-vis spectra (figure 4.16) shows the peak wavelength vs. ERTs. As the ERT increases, the irradiation factor will have a weaker effect on changing the peak wavelength. This occurs because for a constant value of irradiation, the final morphology of Ag nanostructures is majorly dictated by the enhanced reduction rate at the beginning rather than throughout the reactor.

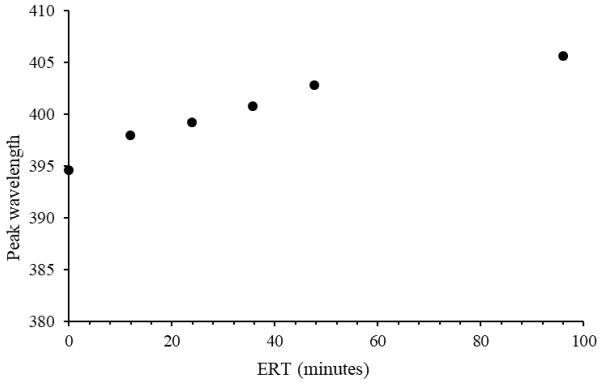

Figure 4.16: Change in UV-vis spectra peak wavelength with respect to exposure residence time (ERT).

4.3.4.4. Silver nanowires/nanostructures synthesized at a different residence time

The UV-vis spectra of silver nanostructures synthesized at 192 minutes residence time is demonstrated in figure 4.17. The thick black line represents the original UV-vis spectra of silver nanostructures. In this case, the main peak can be observed at 438 nm, which corresponds to the presence of nanoparticles. However, a slight shoulder peak may be observed around 390 nm. To confirm the presence of the AgNW peak at 390 nm, the UV-vis curve was analyzed by Origin's peak separation tool. In this analysis, the curve is mathematically broken down into different parabolic curves with peaks where the cumulative curve fits the original curve. Figure 4.17 also shows the separated fit peaks along with the original curve. The curve fitting information are provided in table A.1. As

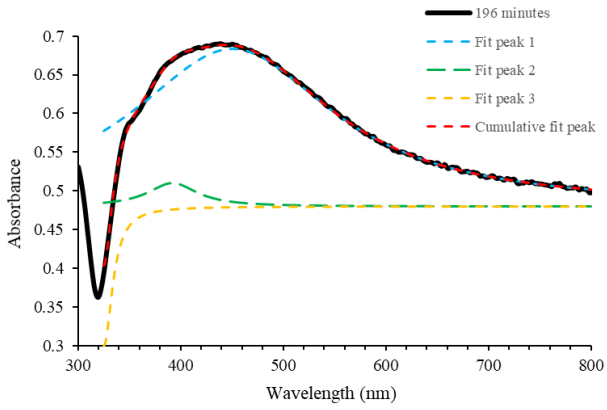

Figure 4.17: Peak separation of the UV-vis spectra. Performed using the Origin© software. Function used: Lorentz.

demonstrated, two separate peaks can be confirmed at 392 and 450 nm, which can correspond to the presence of AgNWs and silver nanoparticles, respectively, which is the expected spectroscopic behavior from AgNWs and silver nanoparticles. In addition, a third curve with a shoulder peak around 350 nm can be observed in figure 4.17, most likely corresponding to AgNW spectroscopic characteristics that is usually observed. For the third curve, there is another peak at 325 nm, which is derived mathematically, and is irrelevant because it is out of the AgNWs peak absorbance range.

4.3.4.5. Silver nanowires/nanostructures synthesized using different coil diameters

The UV-vis spectra of silver nanostructures for the three different coil diameters is provided in figure 4.18. The curve in the case of 2.37-in coil diameter is the same curve provided in figure 4.13, which is the case where AgNWs have the highest yield. For the higher coil diameter (5 in), the peak wavelength is slightly more red-shifted due to the presence of nanostructures other than wires. For the lower coil diameter (1.35 in), the absorbance band is spread-out and the peak wavelength is excessively red-shifted, which correspond to the presence of nanoparticles with high size distribution. These results are in agreement with the SEM images provided in section 4.3.3.6.

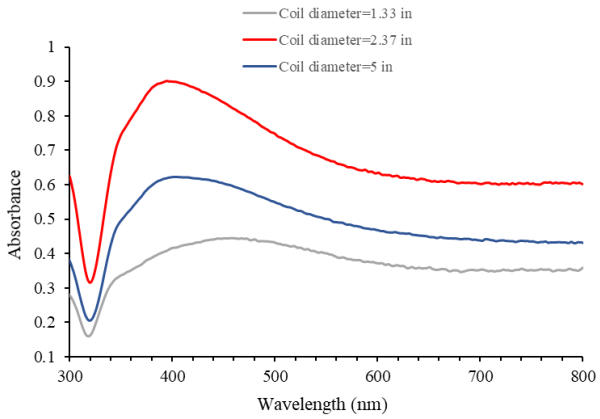

Figure 4.18: UV-vis spectra of silver nanostructures synthesized using different coil diameters.

4.3.5. Measurement of Ag^+ ions and analysis of the synthesis mechanism in the case of different coil diameters

To confirm the difference of reduction rate for different coil diameters, the concentration of Ag^+ ions was measured at different residence times (0, 16, 32, 48, 64, 80, and 96 minutes) by dissecting the tubing to obtain the corresponding residence times. The results are demonstrated in figure 4.19. As demonstrated, the consumption of Ag^+ ions is higher for the smaller-sized coil and lower for the larger-sized coil. This is an interesting phenomenon because it can be compared with the drop-wise addition of a precursor to the reducing agent in the case of batch AgNW synthesis. A slow and steady addition of Ag^+ to the reducing agent can be used as a tool to control the reduction of Ag^+ ions, and therefore the rate of atomic deposition for asymmetric growth as well as controlling supersaturation. This can similarly be done in our millifluidic setup by merely changing the coil diameter. We can define a time interval as "*mixing delay*", which would be the time interval beginning from when the droplets are just added together and ending when the droplets are fully mixed. The lower the mixing delay, which is the case for the smaller-sized coil, the faster the mixing of two droplets and therefore the stronger the reduction rate of Ag^+, and vice versa for the larger-sized coil. A stronger reduction results in a faster nucleation and growth, which are more favorable for symmetrical growth rather than asymmetrical growth needed for the growth of AgNWs. For the larger-sized coil (5 in), the mixing delay is higher; therefore, the reduction of Ag^+ ions is weaker

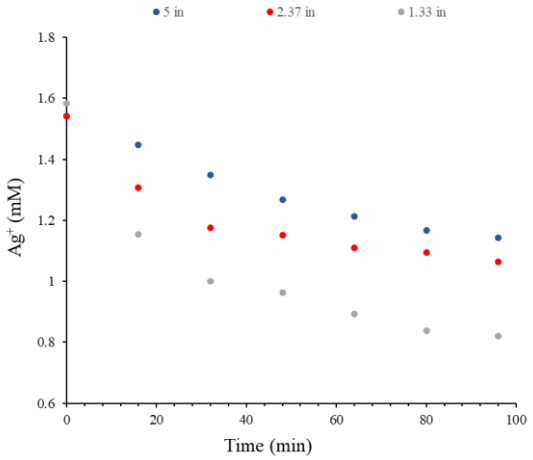

Figure 4.19: Change in Ag^+ concentration with respect to time for different coil diameters.

compared to both the 2.37-inch and 1.33-inch coils, but not significantly different from the 2.37-inch coil.

4.4. Conclusion

The continuous synthesis of AgNWs in a two-phase, droplet-based, and a helically-coiled millifluidic reactor, using tannic acid as both the reducing and capping agents, was investigated. To observe how the overall morphology and the yield of AgNWs is affected, different factors were taken into consideration. These include the effect of the secondary phase other than the aqueous phase, triton X-100 as the surfactant, different mixing configurations, UV-vis light, residence time, and the coil diameter. The results showed that the presence of silicone oil, rather than air, as the secondary phase was necessary to prevent the deposition of nanostructures on the tubing inner wall. The use of silicone oil, however, posed a challenge on the separation of silver nanostructures as the nanostructures adsorbed on the water-oil interface. This was resolved by the addition of triton X-100, as an inert surfactant. The synthesis of AgNWs was then carried out by three different configurations, in which triton X-100 was added to the reaction in different manners. In the first configuration, triton X-100 was introduced to the reactor after tannic acid and silver nitrate were mixed and the droplets were separated by silicone oil. This was the best condition for the synthesis of AgNWs. In second configuration, triton X-100 was mixed with tannic acid prior to mixing with silver nitrate. This was not the ideal condition for the synthesis of AgNWs as triton X-100 can limit tannic acid capabilities to interact with Ag^+ ions. In third configuration, triton X-100 was mixed with the silver nitrate solution prior to mixing with tannic acid. This was not either favorable for the synthesis of AgNWs as triton X-100 can still disrupt the absorption of Ag^+ ions to the tannic acid's dendritic structure. The disruption of triton X-100 can be avoided if it is added after silicone oil is introduced to the reactor and after tannic acid and silver nitrate streams are added together. The effect of UV-vis illumination was investigated by exposing different lengths of the tubing to illumination, which corresponded to different exposure

residence times (ERT) (0, 11.9, 23.8, 35.7, 47.6, and 96 minutes). The results showed that the yield of AgNWs significantly decreases as the exposure residence time increases. Furthermore, the effect of residence time on the yield of AgNWs was discussed. The results showed that a lower residence time (96 minutes) was more favorable for the synthesis of AgNWs with higher yield. However, a higher residence time (192 minutes) was more favorable for the synthesis of AgNWs with higher aspect ratio and also more favorable for the synthesis of silver nanoparticles, thus leading to a lower yield of AgNWs. Finally, the effect of coil diameter on the yield of AgNWs was investigated. A smaller coil diameter (1.33 inches) was more favorable for the synthesis of nanoparticles, while a larger coil diameter (5 inches) led to particle agglomeration. A coil diameter of 2.37 in was found to be the best condition for the synthesis of AgNWs. The reduction of Ag^+ ions was also analyzed by measuring the concentration of Ag^+ at different residence times (0,16, 32, 48, 64, 80, 96 minutes). It was shown that the reduction of Ag^+ ion was stronger in the case of reactors with lower coil diameters. By comparing with previous studies on continuous flow in pipes, it was deduced that rapid mixing was responsible for faster reduction in the lower-sized coiled-reactor (1.33 in), which lead to a significant decrease in the yield of AgNWs. For the larger-sized coiled-reactor (5 in), the deposition of nanostructures at the bottom of the droplets created a stagnant presence that led to particle agglomeration. The continuous process proposed in this study can resolve many challenges regarding the large-scale production of nanomaterials for manufacturing of electronics and many other applications. To name some advantages, the helically-coiled millifluidic reactor in our study is inexpensive to prepare, the process is strongly resistant to fouling and particle deposition, and thus the tubing can be used for a long period of time, the process is carried out at room temperature, only tannic acid is used as both the reducing and capping agents, and the mixing can be controlled by merely changing the coil diameter without needing to impose active mixing, such as by ultrasonication, which require additional energy. The high yield of AgNWs obtained from an inexpensive and continuous

process are promising for manufacturing transparent conductive films (TCFs), which are utilized for the production of flexible and wearable electronics.

CHAPTER V

INVESTIGATION OF THE RHEOLOGICAL BEHAVIOR OF GREEN AND SUSTAINABLY-SYNTHESIZED SILVER NANOWIRE-BASED CONDUCTIVE INK FOR PRINTING APPLICATIONS

5.1. Introduction

The development of metal-based colloidal conductive inks has emerged as a promising approach for manufacturing inexpensive, versatile, and flexible transparent conductive films (TCFs) used for the development of health-monitoring wearable devices, supercapacitors, photodetectors, and solar cells, to name a few[514–517]. Indium tin oxide (ITO) has been commonly applied in most TCFs, thanks to its high optical transmittance (> 90%) and its low sheet resistance (<10 Ω/square)[477]. However, the brittleness of the ITO limits its applications in flexible electronic materials and its manufacturing process is energy-intense.[477,478]. Alternatively, silver nanowire (AgNW)-based conductive inks are among the most prominent materials for TCF manufacturing due to their high electrical conductivity (with silver being the most conductive metal), enhanced transmittance, and their ability to sustain conductivity after a bending stress is applied [479,518]. In addition, the networks formed by interconnected nanowires, facilitates the flow of electrons and decreases sheet resistance.

To print TCFs with high quality (sharp line definition, high resolution, and minimum surface roughness), regardless of the printing process, the rheological properties of the ink (i.e. shear thinning or shear thickening characteristic, viscosity), and ink composition (i.e. organic binders, solvent, nanostructure conductive filler concentration and morphology) should be considered. However, these characteristics need to be tuned according to the corresponding printing application.

In the screen printing process, which is the most common printing process used to print conductive inks, the ink is placed on a frame with mesh on a substrate, and then subjected to shear stress applied by a squeegee. In a typical screen printing process, the applied shear rate lies in the region of 0.1-200 1/s[519–521]. The magnitude of the shear rate depends on the stress exerted by the squeegee, its movement rate, and more importantly the mess size [522,523]. For a smaller mesh size, the shear rate increases, and can exceed the 0.1-200 1/s range, especially if thin patterns (i.e. with hundreds of micrometers width) are needed. In such processes, the rheological properties of the ink determine the sharpness of the printed lines for uniform conductive patterns[362]. The relatively fast recovery of the shear viscosity (returning to the initial viscosity value by changing the shear rate) is vital for the formation of sharp-edged lines[524]. Due to the high shear rate, high-colloidal-content and viscous conductive ink is needed in order for the ink retain its original structure after screen printing. Screen printing method has several advantages such as versatility, simplicity, fine resolution, and high-volume printing; however, bears a main disadvantage, which is substantial material wastage during the printing process. Another useful printing method is inkjet printing, where the conductive ink is printed unto a substrate in miniaturized droplets, tens of micrometers in diameter [525,526]. In the inkjet printing process, ink droplets are shot to a substrate from multiple (hundreds) nozzles (10-100 μm) attached to a printhead [525]. The recommended viscosity range for inkjet printing lies in the region of 1-30 cP [527,528], which is typically lower compared to the viscosity needed for screen printing. Higher viscosities can result

in nozzle clogging. The inkjet printing process is highly advantageous for obtaining patterns with significantly high resolutions (dots per inch), and the ink does not need to be highly viscous to sustain high shear. However, the inkjet printing instrument is expensive and in the case of AgNW-based ink, nanowires with high aspect ratio can clog the nozzle, and are often cleaved using sonication to avoid that issue [529]. Another printing method is the direct writing approach, that is a mechanized printing process where the ink is directly printed through a nozzle (typically hundreds of μm wide in diameter) that is connected to an extruder, often operated by a 3D printing instrument. In order to maintain the desired shape after settlement, the conductive ink needs to flow in a smooth manner after being deposited from the nozzle [530]. The conductive ink to be printed using the direct writing approach should typically have a higher viscosity compared to the one used in inkjet printing, but a lower viscosity compared to the one used in screen printing. The direct writing process is advantageous in terms of being inexpensive, simple, versatile, customized printing, efficient usage of materials, and precision. Nevertheless, the process suffers from limited resolution and thick pattern lines, which limits its capability to print miniaturized circuits needed in small devices.

In all printing processes, the timescale for viscosity recovery is important in the determination of line sharpness and film leveling after printing [362]. A relationship between this timescale characteristic time and viscosity transition (from high to low shear rate) was previously proposed by the structure build-up or "Stretched Exponential" model [531,532] as shown in equation 5.1.

$$\eta = \eta_0 + (\eta_\infty - \eta_0)(1 - \exp(-\frac{t}{\tau})^r) \qquad \text{Equation 5.1}$$

Where η is the viscosity at time t, η_0 is the viscosity at the high shear rate, η_∞ the viscosity at the low shear rate, τ the transition characteristic time, and r a dimensionless constant, which is equal to one in most cases. The values for η_0 and η may be obtained using the peak hold test (applying

a step increase to the shear rate followed by a decrease to the initial shear rate to mimic the ink charging sequence[107]).

Furthermore, a considerable factor that affects the viscosity transition and recovery time is the type and weight percentage of the nanostructure content (i.e. AgNWs). Hemmati et al. [362] investigated the characteristic recovery time using the same equation (Equation 5.1) by testing inks with different commercially available AgNW content. They found that the characteristic time is decreased (down to 20.9 s) by increasing the Ag nanostructure content (up to 6 w%). In another study, Liang et al. [524] also investigated the rheological behavior of the AgNW ink by measuring the viscosity recovery percentage after an applied shear stress, for different AgNW compositions. They showed that for a medium AgNW composition of 6.6 w%, a maximum viscosity recovery percentage of 59.4 % can be obtained after 10 seconds of a step change in shear rate (from 200 to 0.1 S^{-1}). After 50 s, the viscosity recovery percentage increased to 85.9 %. However, for a higher content of AgNW (7.3 w%), 58.5 % of the initial viscosity value was obtained. This was attributed to the high viscosity of the ink at higher AgNW content. In addition, film leveling in the case of higher AgNW content was reported to be incomplete compared to the medium AgNW content. As a result, finding an optimal AgNW content is necessary for a relatively rapid viscosity recovery and higher recovery percentage. In both studies, screen printing was used to print the AgNW ink on the substrates. Another factor affecting the rheological behavior of the inks is the aspect ratio (ratio of length to diameter) of AgNWs. In the case of silver flakes, even at high content (>60 w%) the recovery rate is still lower compared to nanowires [524,533]. This difference is due to the high aspect ratio of the AgNWs compared to silver flakes that do not have a 1D structure, and therefore do not have a defined aspect ratio. By increasing aspect ratio, a more rapid viscosity retention can be achieved for an ink with the same AgNW content [524].

In the case of high-precision printing of colloidal inks using an automatic printing machine (i.e. direct writing), three criteria need to be satisfied [534,535]. Firstly, the initial viscosity of the ink should be in a region that allows its continuous and uniform printing. This depends on the printer properties and application. A significantly low viscosity will lead to the creation of satellite droplets and disrupts line uniformity after printing [536] while a significantly high viscosity does not allow the ink to be squeezed out of the nozzle. The conductive filler content, concentration of binder, and dispersing agent (if any) are essential in determining the viscosity of the ink. The second criterion is the ability of the ink to settle and recover its initial viscosity rapidly enough after flowing through the nozzle to facilitate shape retention of the deposited material. For this purpose, the ink should exhibit shear thinning behavior with relatively rapid viscosity recovery rate (within seconds) after shear stress removal [530]. Thirdly, shrinkage upon drying should be minimized, which can be done by using a high colloid volume fraction. However, it should be noted that a significantly high colloid content can result in nozzle clogging during the printing process. This issue can be addressed by using high aspect ratio AgNWs as they align under the shear and extensional flow, which is developed in the nozzle, thus reducing the risk of nozzle clogging [537,538].

AgNWs synthesized by the polyol process [426] have been widely used for conductive ink preparation. However, the application of green-synthesized AgNWs in conductive ink printing has not been studied to the best of our knowledge. We previously developed a green and sustainable method in which AgNWs with moderate yield were synthesized using tannic acid as both the reducing and capping agents at room temperature, unlike the polyol process that requires relatively high temperatures (>150 °C) and an additional capping agent. In this work, conductive ink using tannic acid-synthesized AgNWs as the conductive filler has been prepared. The rheological properties of the ink were investigated to analyze the shear thinning behavior of the ink, and simulate printing process in screen printing and direct writing. The characteristic

transition time for shape retention, and the effect of temperature and Ag nanostructure content on the rheological behavior of the ink was investigated. The direct writing of green AgNW-based conductive inks can be a promising approach for printed electronics thanks to its simplicity, minimal material wastage, low shear rate printing, and significantly low manufacturing cost starting from the initial material consumption to the final printing process.

5.2. Methodology

5.2.1. Materials

Silver nitrate ($AgNO_3$, MW: 169.87 g/mol, product number: S0139), tannic acid (MW: 1701.2 g/mol, product number: 403040), nitric acid (HNO_3, 70% ACS reagent, MW: 63.01 g/mol, product number: 438073), and sodium carboxymethyl cellulose (CMC, MW~90000 g/mol, product number: 419273) were purchased from Sigma Aldrich. Dispex ultra FA 4416 was purchased from BASF© as the dispersing agent and was used for conductive ink preparation. In addition, a commercial conductive ink (60 w%, manufacturer: Taylor Engineering©) was used for comparison with our laboratory-made conductive ink. Deionized water (DIW, ASTM type II) was used as the solvent to prepare aqueous $AgNO_3$ and tannic acid solutions, as well as the conductive ink.

5.2.2. Synthesis and isolation of AgNWs

For AgNWs synthesis with high throughput compared to our previously published study (5 mM tannic acid and $AgNO_3$ solutions), aqueous tannic acid and $AgNO_3$ solutions (both 20 mL,100 mM each) were prepared. The pH of the tannic acid solution was adjusted to 1.25 by adding HNO_3. The tannic acid solution was then added to a 100 mL round glass flask, and the $AgNO_3$ solution was added dropwise. The reaction was continued at room temperature for 4 hours. The flask was exposed to white fluorescent light at 676 LUX during the whole reaction because it

assists the reduction process [2]. After the synthesis process was completed, the AgNWs suspension was centrifuged 4 times in DIW at 5,000 rpm, with the supernatant being removed after each centrifugation step.

5.2.3. Scanning Electron Microscopy (SEM) characterization

AgNWs were characterized by the FEI Quanta 600 field-emission gun Environmental Scanning Electron Microscope at the Oklahoma State University microscopy laboratory. To do the characterization, 100 μL of the AgNWs suspension was pipetted unto smooth carbon tabs taped to aluminum pins. The samples were then kept at dry and room temperature conditions for 24 h to allow the samples to dry. The pins containing the AgNWs were then put on sample holders in the SEM instrument for characterization.

5.2.4. Conductive ink preparation

The AgNW-based conductive ink was prepared by mixing the AgNWs suspended in DIW, CMC, and the Dispex Ultra FA 4416 dispersing agent. The ink was prepared at different AgNWs weight percentages (2,5, 10, and 20%), while the weight percentage of CMC and the dispersing agent were both kept at 6%.

5.2.5. Rheological tests

To investigate the rheological properties of the prepared conductive ink, the ink sample was analyzed by TA Instrument's© Discovery HR-10 Rheometer. To do so, a 25 mm geometry was used and three main tests were performed including flow sweep, peak hold, and frequency sweep tests. After geometry definition and test setup, the ink sample was poured unto the sample holder disk (peltier plate) and trapped between the geometry and the disk. The trim gap (gap set for trimming the sample prior to the rheological test) was 1,050 μm and the test gap (gap set for

rheological testing) was 1000 µm. A 3-minute soak time was allowed for the ink to reach the desired temperature.

5.2.6. Conductive ink printing rheological simulation

To simulate the ink printing process using screen printing, the peak hold test was performed using the rheometer. In the first step of the peak hold test, the ink was subjected to a low shear rate of 0.1 1/s for 40 seconds to simulate ink at rest. In the second step, the ink was subjected to a high shear rate of 400 1/s for 20 seconds to simulate ink under printing shear stress. In the third step, the shear rate was reduced back to 0.1 1/s for 100 seconds to simulate ink at resting condition after printing. To simulate the ink printing process using the direct writing method, a laboratory-made 3D printer (figure 5.1) was considered as the model printer for the purpose of simulation, and its specifications were considered in the simulation process. The 3D printer extruder operated based on a syringe and piston system. To initiate the printing process, the syringe would be loaded by conductive ink, with the ink being pushed manually by the piston to reach the printing needle tip. The syringe inner diameter was set at 12 mm, the main tube inner diameter was set at 3.5 mm, and the needle diameter was set 0.69 mm. To operate the printer, the Repetier Host software can be used, which utilizes Gcode to define printing properties, such as the extruder movement rate, the flowrate, and the writing pattern.

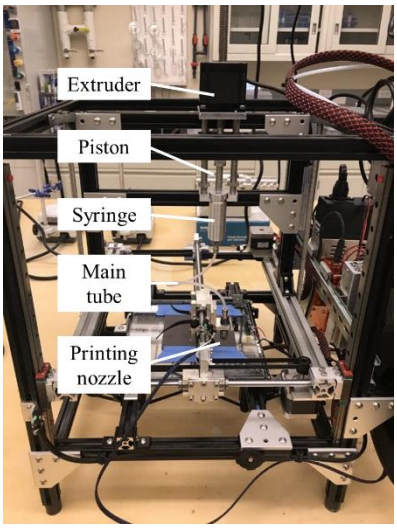

Figure 5.1: Laboratory-made 3D printer that its specifications were used for conductive inks printing process simulation.

5.3. Results and Discussion

5.3.1. Synthesis of AgNWs

We previously investigated the green synthesis of AgNWs using tannic acid and $AgNO_3$ at room temperature, as well as the effect of various factors such as light, Ag^+ ion and tannic acid concentration, and pH [2,3]. In such cases, AgNWs were produced at moderate yield using both batch and continuous millifuidic processes (50 and 82%, respectively). We demonstrated that light is a significant factor in controlling the reduction rate of Ag^+ ions by tannic acid, and the fact that reduction rate can increase by increasing pH and increasing the light intensity of UV-visible white fluorescent light. We also demonstrated that it is imperative that the ratio of tannic acid concentration to Ag^+ concentration is maintained at 1 in order to assist with the anisotropic growth of nanostructures which leads to the formation of nanowires[2]. The process by itself has several advantages, which are the minimal use of energy—due to the reaction being performed at room temperature—, using a single-step processes and just one reducing agent, which can also act as a capping and stabilizing agent, and using a sustainable and environmentally-friendly reducing/capping agent, thereby decreasing chemical waste production. Despite all these advantages, the overall productivity of those processes was limited and not feasible for preparation of conductive ink, which requires high silver nanostructure content, because $AgNO_3$ was used at a mere concentration of 5 mM. In this work, we were able to produce AgNWs with an approximate yield of 90% using $AgNO_3$ and tannic acid at a much

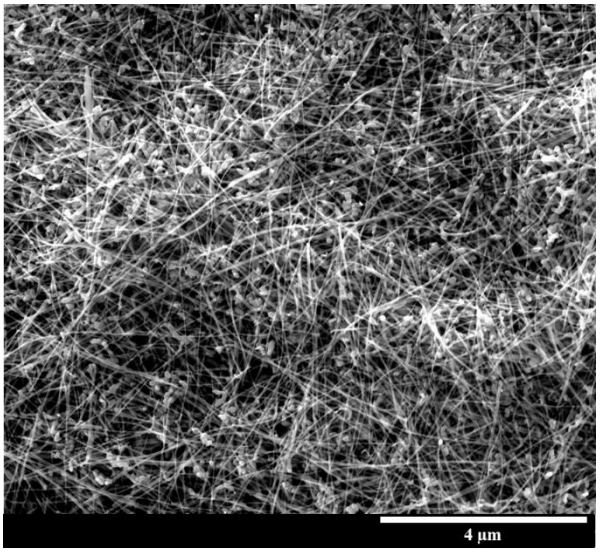

Figure 5.2: SEM image of silver nanowires (AgNWs) synthesized by tannic acid at room temperature. Average nanowire diameter: 32.9 ± 8.2 nm. Average nanowire length: 9.8 ± 4.1 µm.

higher concentration (100 mM) (figure 5.2). This yield was higher compared to the yield acquired by both batch and millifluidic processes (~50 and 82%, respectively) previously synthesized at 5 mM of $AgNO_3$ and tannic acid. This was done by adjusting both the pH and light to control the reduction kinetics in a manner that leads to a controlled anisotropic growth process. Furthermore, acquiring such a high yield at lower concentrations was more difficult for two main reasons. The first issue is the increased sensitivity to experimental conditions. When the concentration is too low, the reaction can become highly sensitive to temperature, pH, and reducing agent/precursor concentration, which may ultimately lead to non-uniform morphologies and low-yield. The second issue is the increased risk of contamination. When the concentration of the precursor (in this case, $AgNO_3$) is too low, the amount of impurities and contaminants in the reaction may be relatively large compared to concentration of Ag^+; therefore, interfering with the reaction in a disruptive manner. If the favorable experimental parameters at high precursor/reducing agent concentration is discovered, such two challenges can be minimized. The reduction rate increases when the concentration of Ag^+ ions is increased. However, the pH was reduced to a highly acidic value of 1.25, which decreases the reduction rate significantly and compensates for the increased reduction rate caused by high Ag^+ concentration. Lower or higher than pH of 1.25 will result in a lower yield of AgNWs. The combination of AgNWs and nanostructures other than nanowires were used for conductive ink preparation.

5.3.2. Rheological analysis

When investigating the rheological behavior of a printable nanostructure-based conductive ink, 6 main factors should be considered including viscosity, shear rate, weight percentage and morphology of nanostructures, solvent, temperature, and more importantly the printing conditions [107,530,539–542]. The first three were discussed in the introduction section. The effect of solvent is also important because solvents with higher surface tension tend to increase the viscosity of the ink. Temperature is also important because higher temperatures can reduce the viscosity of the

conductive ink while lower temperatures can increase it. This can be useful during the printing process because the rheological behavior of the ink can be tuned to suit the printing process by adjusting the temperature. Lastly, for the sake of proper rheological measurements, the specific printing condition needs to be considered. Printing conditions such as printing speed, ink flowrate, width/diameter of printing nozzle, and width/diameter of flow channel can affect the rheological behavior of the ink during printing process. Based on previous tests with our laboratory-made printer and its utilities, the overall viscosity of the ink (at rest) should be more than 5 Pa.s. Lower viscosities may result in nozzle drip, which leads to an inconsistent printing pattern. Higher viscosities can be used; however, this depends on the colloidal content and the concentration of the binder. One should note that there is not any defined viscosity range for printing applications, and the required viscosity and shear rate is application-specific.

5.3.2.1. Rheological behavior of AgNW-based conductive ink and the effect of silver (Ag) nanostructure content

5.3.2.1.1. Flow sweep test

To investigate the rheological behavior of the ink, the first test was the flow sweep test. This test shows the overall viscosity of the ink change with respect to shear rates, and determines whether the ink has shear-thinning or shear-thickening behavior. A conductive ink that is going to be used for screen printing or direct printing applications should have a shear thinning characteristic. Figure 5.3 shows the viscosity of the ink vs. shear rate for 2, 5, 10, and 20% weight percentage of Ag nanostructures at room

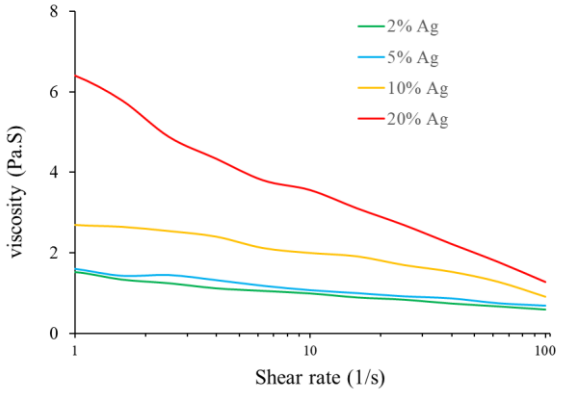

Figure 5.3: Flow sweep test for conductive ink with different silver nanostructure contents.

temperature (25 °C). As demonstrated, for all Ag nanostructure contents, the viscosity of the ink decreases with increase in shear rate, which shows the shear-thinning behavior of the ink. However, the decline in viscosity is more rapid for ink with higher Ag nanostructure content, while it is lower for ink with lower silver nanostructure content.

5.3.2.1.2. Frequency sweep test

The frequency sweep test was performed to analyze the viscoelastic behavior of the ink, and to extract valuable information about the effect of colloidal forces and the interaction of nanostructures. Two main variables are provided by the frequency sweep test including storage modulus and loss modulus. The storage modulus (G´) is a measure of the elastic behavior of the ink while the loss modulus (G″) is a measure of the viscous behavior of the ink. Figure 5.4 shows the frequency sweep test results, demonstrating storage and loss modulus vs. angular frequency for different Ag nanostructure contents, at room temperature (25 °C). Both the loss and storage modulus increase by increasing the Ag nanostructure content. This means that the resistance of the ink to deformation increases as the Ag nanostructure content increases. However, for all Ag nanostructure contents, and for the whole angular frequency spectrum, the loss modulus is more than the storage modulus, meaning that the viscous effect is dominant compared to the elastic effect. A more detailed analysis of the viscous/elastic effect can be provided by describing the tan delta variable (tan δ) as shown in equation 5.2.

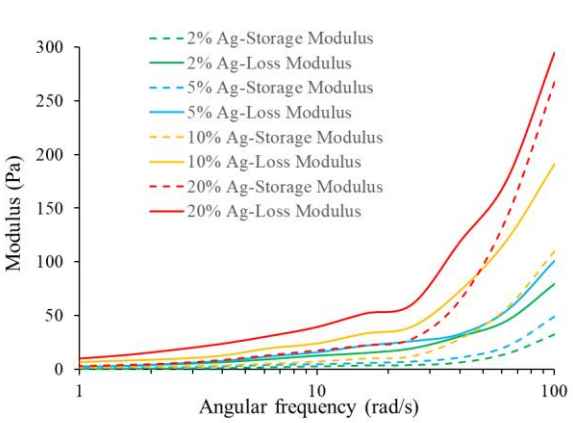

Figure 5.4: Frequency sweep test for conductive ink with different silver contents.

$$tan\delta = \frac{G''}{G'} \qquad \text{Equation 5.2}$$

Where G″(Pa) is the loss modulus and G´(Pa) the storage modulus. Thus, a higher tan δ accounts for a stronger viscous behavior while a lower tan δ accounts for a stronger elastic behavior. Figure 5.5, shows tan δ vs. angular frequency for different Ag nanostructure contents. As demonstrated, tan δ decreases overall for all Ag nanostructure contents, meaning that the elastic effects become stronger at higher frequencies. This is due to the fact that at lower frequencies, nanostructures have more time to move within the binder matrix, which can result in a more viscous response, while at higher frequencies, nanostructures have less time to move within binder matrix due to the high oscillation factor, which ultimately results in a more elastic response. The more the Ag nanostructure content, the lower the tan δ at high frequencies, meaning that the elastic response becomes stronger as the Ag nanostructure content increases. Nevertheless, for all Ag nanostructure contents and for the whole angular frequency spectrum, tan δ is higher than one, meaning that the viscous response is still dominant compared to the elastic response even for the highest angular frequencies. There is a "cross-over frequency" where the value of G´ equalizes G″, and tan δ becomes equal to 1. After this frequency, the elastic response will be more dominant rather than the viscous response. However, this frequency was not reached in the range of angular frequency used in this study.

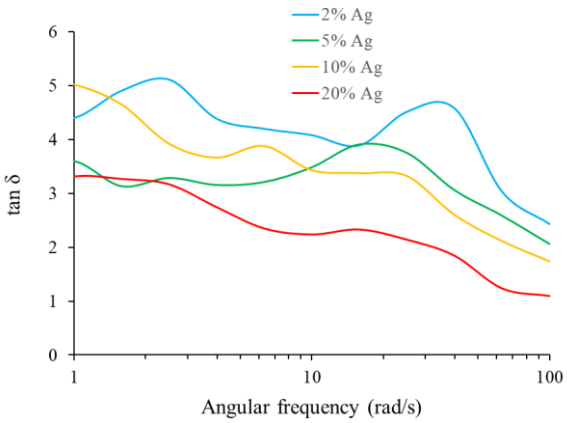

Figure 5.5: tan δ (ratio of viscous modulus to elastic modulus) for conductive ink with different silver contents.

5.3.2.1.3. Peak hold test: high-shear rate printing

In the peak hold test, the ink is first subjected to a low shear rate, simulating ink at rest, and then subjected to a high shear rate, simulating ink under increased stress during printing, and then back

to low shear rate, simulating ink at rest or recovery after printing. This is a very useful test for printing applications such as screen printing, inkjet printing, and direct writing or 3d printing because it can simulate the flow of the ink during the printing process, and therefore determine whether the ink is suitable for such applications based on its rheological characteristics. The peak hold test was performed for the inks with Ag nanostructures content of 2, 5, 10, and 20 weight percentages. The sample was first subjected to low shear rate at 0.1 1/s for 40 seconds, followed by high shear rate at 400 1/s for 20 seconds, and then back to 0.1 1/s for 100 seconds. Figure 5.6 shows the peak hold test for different Ag nanostructure contents at room temperature (25 °C). As demonstrated, the overall viscosity of the ink increases as the Ag nanostructure content is increased. However, it takes longer for the higher Ag nanostructure content ink to retain its original viscosity. By using the build-up structure model (equation 5.1), the characteristic time for transition can be identified. Table 5.1 shows the characteristic times of transition for Ag nanostructure contents of 10 and 20%. The characteristic time for transition in the case of 20% Ag nanostructure content is almost twice of that of 10% Ag nanostructure content, which explains the longer time for viscosity retention. For 2 and 5% of Ag nanostructure contents, the structure build-up model did not provide a statistically significant R^2 value, and therefore could not fit the data. One possible reason for this may be the high shear rate; because high shear rates—particularly for low colloidal content—can cause structural deformation in the ink, which causes the experimental data to deviate from the structure build-up model. Nevertheless, in both 2, and 5% Ag nanostructure contents, the viscosity retains its original value (viscosity just before being subjected to higher shear rate) in less than 60 seconds compared to 100 seconds for the 20% Ag

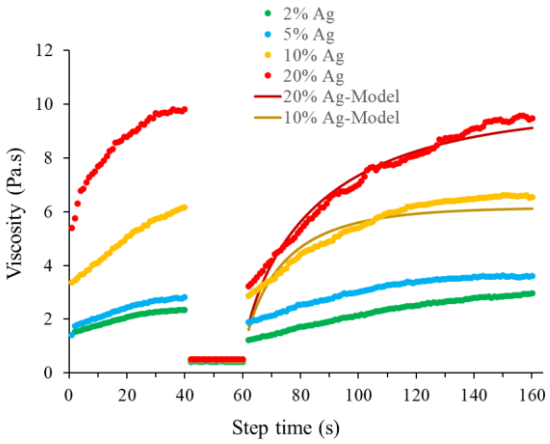

Figure 5.6: Peak hold test for conductive ink with different silver content (High shear rate= 400 1/s and Low shear rate= 0.1 1/s).

nanostructure content. We used the 400 1/s shear rate, as a significantly high shear rate value to observe the thixotropic behavior of the ink at very high shear. The high transition time caused by the 400 1/s shear rate suggests that this value may not be a proper shear rate in the printing process. When the shear rate increases, it also makes it harder for the ink to retain its original structure. Therefore, in this case, a lower shear rate is required to allow for a rapid transition.

Table 5.1: Model parameters from the structure build-up model for 10% and 20% silver nanostructure contents.

Ag nanostructure content	10 %	20 %
Characteristic time τ (s)	13.75	27.04
r (dimensionless constant)	0.78	0.73
R^2	0.91	0.97

5.3.2.2. Effect of temperature

5.3.2.2.1. Flow sweep test

The flow sweep test was performed at 30 and 40 °C to observe the change is viscosity and shear-thinning behavior with respect to temperature. This test and the next tests are done for the 20% Ag nanostructure content because 20% Ag nanostructure content was the most favorable condition for the direct writing application. Figure 5.7 shows the viscosity with respect to shear rate at 25, 30, and 40 °C. The curve for 25 °C is the same provided in figure 5.3. As demonstrated, the viscosity decreases by increasing the temperature. The decline in viscosity with respect to increasing shear rate is more rapid at lower temperatures; this behavior is similar to that of lower Ag nanostructure content ink.

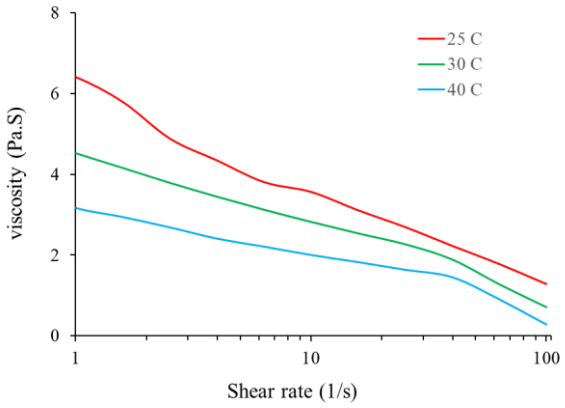

Figure 5.7: Flow sweep test for conductive ink with 20 w.% silver content at different temperatures.

5.3.2.2.2. Frequency sweep test

The frequency sweep test was performed at 30 and 40 °C to observe the viscoelastic behavior of the ink. Figure 5.8 shows the storage and loss modulus of the ink with respect to angular frequency for different temperatures. As shown, both storage and loss modulus decrease as the temperature increases. With increasing temperature, overall resistance of the ink to deformation decreases. This is an important phenomenon and should be considered for printing processes at other temperature than that of room temperature. To analyze the dominance of either the storage or loss modulus, tan δ with respect to angular frequency for all temperatures should be considered, and Figure 5.9 shows this comparison. As demonstrated, for all temperatures, tan δ decreases by increasing angular frequency, which means that the elastic response becomes more dominant at higher frequencies. However, there is a noticeable difference between the curves. After the frequency of approximately 4 rad/s, tan δ for inks at 30 and 40 °C surpasses the one at room temperature, meaning that at low frequencies, the viscous response is more dominant in the case of lower temperatures, while at higher frequencies, the elastic response is more dominant. This

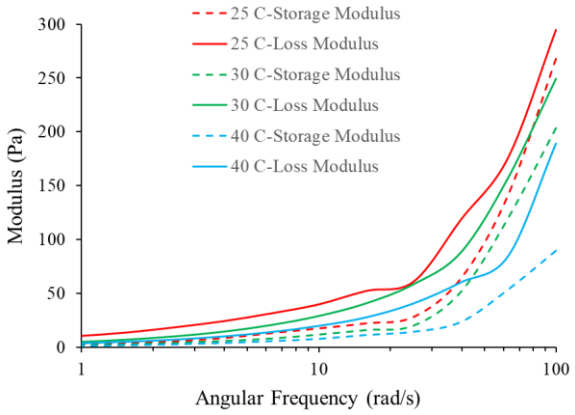

Figure 5.8: Frequency sweep test for conductive ink with 20 w.% silver content at different temperatures.

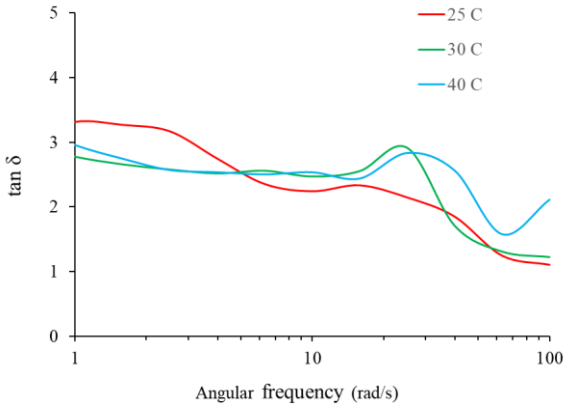

Figure 5.9: tan δ (ratio of viscous modulus to elastic modulus) for conductive ink with 20 w.% silver content at different temperatures.

phenomenon occurs due to the fact that at higher temperatures, the nanostructures can move slightly easier, and therefore allow the ink to maintain its viscous response.

5.3.2.2.3. Peak hold test: high-shear rate printing

Similar to the peak hold test performed for different Ag nanostructure contents at room temperature, the peak hold test was performed to observe the shear thinning thixotropic behavior of the ink at different temperatures. Figure 5.10 shows the peak hold test, for the viscosity sketched with respect to time at different temperatures. In all cases, the ink experiences a relatively high transition time to retain its original viscosity. To compare the characteristic times for transition, the build-up structure model was used to fit the data for three temperatures. Table 5.2 shows the model parameters for all temperatures.

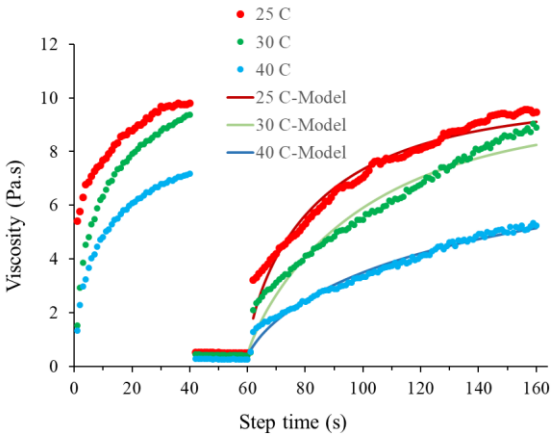

Figure 5.10: Peak hold test for conductive ink with 20 w% silver content at different temperatures. High shear rate= 400 1/s. Low shear rate= 0.1 1/s.

Table 5.2: Stretched Exponential model parameters from the structure build-up model for different temperatures.

Temperature	25 °C	30 °C	40 °C
Characteristic time τ (s)	27.04	42.37	75.72
r (dimensionless constant)	0.73	0.86	0.73
R^2	0.97	0.96	0.98

5.3.2.3. Printing simulation: low-shear rate printing

To simulate the printing process, the situation that the ink undergoes inside the printer needs to be analyzed in detail. In a syringe-piston system, where the ink is squeezed through a cylindrical

tube (figure 5.11), the shear rate for a shear-thinning material can be calculated by equation 5.3[543].

$$\dot{\gamma}_w = \frac{Q}{\pi r^3}\left[3 + \frac{1}{n}\right] \qquad \text{Equation 5.3}$$

Where Q is the flowrate inside the tube (mm^3/s), r the tube radius (mm), $\dot{\gamma}_w$ the shear rate at the wall of the tube (1/s), and n the dimensionless power law index, which will be derived from the power-law as shown in equation 5.4.

$$\sigma = k\dot{\gamma}^n \qquad \text{Equation 5.4}$$

Where σ is the shear stress (pa), $\dot{\gamma}$ the shear rate (1/s), k the consistency index (pa.s), and n the power-law index. The power-law equation relates shear rate and shear stress for a non-Newtonian fluid. In the case of n=1, the fluid is Newtonian; in the case of n>1, the fluid has a shear-thickening behavior, and in the case of n<1, the fluid has a shear-thinning behavior. To determine n, one should fit the power-law model with the experimental data describing shear stress with respect to shear rate. The rheometer was used to simulate the printing process by performing the peak hold test on the AgNW-based ink, with 20% Ag nanostructure content. To do so, n should be calculated by fitting the power-law equation (equation 5.4) with the experimental data. Figure 5.12 shows shear stress vs. shear rate for the experimental data (obtained by flow sweep test with the rheometer) and the fitted model.

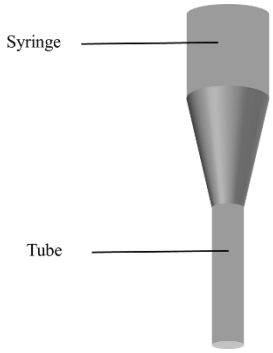

Figure 5.11: Schematic of the syringe and main tube in the 3D printer

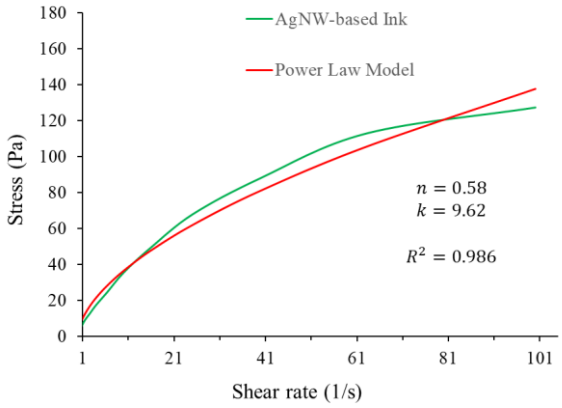

Figure 5.12: Shear stress vs. shear rate, and the fitted power-law model for the tannic acid-synthesized AgNWs-based conductive ink (result obtained by the flow sweep test)

After calculating n, equation 5.3 was used to calculate the shear rate inside the main tube of the printer. With n being equal to 0.58, the shear rate was 22.24 1/s inside the main tube. After the shear rate is calculated, the peak hold test can be performed using the calculated value. It was assumed that the printing process has already reached a steady state. It was also assumed that the shear rate within the nozzle and tube fittings can be neglected compared to the shear rate within the main tube. This assumption was made based on the fact that the time the ink is under shear stress inside the nozzle and tube fittings is a fraction of a second, and therefore negligible compared to 34.53 seconds in the main tube. Therefore, a consistent shear rate of 22.24 1/s was used for the high-shear rate step in the peak hold test, which lasted for 34.53 seconds. The low shear rate, simulating the ink at rest, was considered as 0.1 1/s. The first low-shear rate step lasted for 40 seconds and the second low-shear rate step lasted for 100 seconds. The test was done at room temperature as the printing process is also performed at room temperature. Figure 5.13 shows the peak hold test performed for AgNW-based conductive ink. As demonstrated, after undergoing stress at 22.24 1/s for 34.53 seconds, the ink follows smooth transition back to its original viscosity. The structure build-up model was used to fit the experimental data after high shear rate removal. The characteristic time for transition in this case was equal to 1.78 s, which is significantly lower compared to the one previously calculated for 20%-Ag nanostructure-content ink, undergoing 400 1/s shear rate. This suggests that the low shear rate of 22.24 1/s allows for a rapid and smooth transition during the ink printing process.

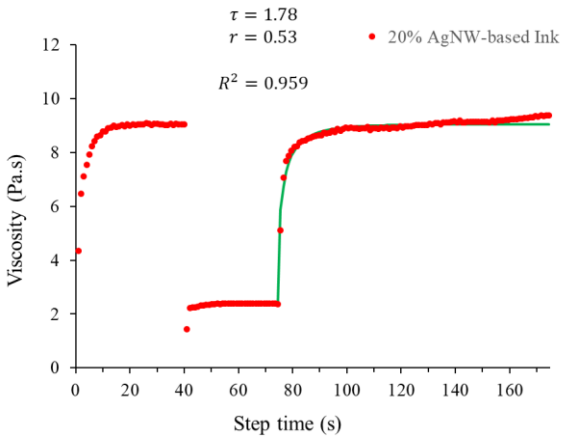

Figure 5.13: Peak hold test for tannic acid-synthesized AgNWs-based conductive ink. High shear rate= 22.24 1/s. Low shear rate= 0.1 1/s.

5.4. Conclusion

This study investigated the rheological behavior of AgNW-based conductive ink for printing applications. The silver nanowires used as the conductive filler for conductive ink preparation were synthesized using an environmentally-friendly and sustainable process at room temperature, in which the yield of AgNWs was 90%. The rheological behavior of the conductive ink was investigated by performing rheological tests at different contents of silver nanostructures and temperatures. The conductive ink demonstrated a shear-thinning thixotropic behavior for all silver contents (2, 5, 10, and 20%), and all temperatures (25, 30, and 40 °C). Three general rheological tests were performed, namely, the flow sweep, frequency sweep, and peak hold tests. The flow sweep test showed the shear-thinning behavior of the ink, and the decline in viscosity for different shear rates. For higher silver contents, and for lower temperatures, the decline in viscosity was stronger. The frequency sweep test demonstrated the viscoelastic behavior of the ink and its overall resistance to deformation. The results showed that for higher silver content, both the storage and loss modulus of the material increases, accounting for higher resistance to deformation. Also, it was shown that the viscous response is more dominant compared to the elastic response, regardless of the silver content and temperature. However, the elastic response is stronger for higher silver content, and increases with respect to oscillation frequency. In addition, the viscous response for the ink at 25 °C was stronger at lower oscillation frequencies compared to ink at 30 and 40 °C. At higher oscillation frequencies, the elastic response was more dominant for the ink at 25 °C compared to 30 and 40 °C. The peak hold tests showed that the time for viscosity and shape retention after subjection to high shear rate (400 1/s) was longer for higher silver content and higher temperatures. Finally, the direct writing process using a laboratory-made printer was simulated by performing the peak hold test on the green and sustainably-produced AgNW-based ink. The ink showed a smooth transition to retain its structure after being subjected to the shear rate of 22.24 1/s during printing process. The characteristic time for transition was

significantly lower compared to that of ink subjected to significantly high shear rate of 400 1/s, suggesting that the direct writing procedure is more favorable to print ink at low colloidal content due to its lower shear rate, while screen printing is more favorable for printing high-content, and high-viscosity ink, due to its high shear rates.

CHAPTER VI

CONCLUSION REMARKS AND FUTURE DIRECTIONS

6.1. Conclusion remarks and summary

In this dissertation, the green and sustainable synthesis of silver nanostructures, with the focus on silver nanowires (AgNWs) was investigated. In chapter II, the conventional physical and solution-based chemical methods for the synthesis of silver nanostructures and their advantages and disadvantages were initially reviewed. Afterward, the novel green and sustainable synthesis of silver nanostructures with different morphologies using biological reagents, bio-extracts, sugars, vitamins, viruses, and plant extracts were reviewed. Then the effect of various parameters such as pH, temperature, reducing and capping agent concentrations on the size and morphology of silver nanostructures and the growth of one-dimensional (1D) nanostructures was reviewed. The possibility of the one-dimensional growth of silver nanostructures using plant-based compounds was discussed. It was discussed how some of such compounds such as polyphenols can act as moderate reducing agents at room temperature, facilitating the growth of AgNWs, if the experimental conditions are met. It was then discussed how the utilization of green and sustainable compounds for the synthesis of silver nanowires can be economically and environmentally promising for transparent conductive film manufacturing.

In chapter III, a novel method for the green, sustainable, and room-temperature synthesis of AgNWs using tannic acid in a one-step, 4-hour batch process was proposed. It was shown how tannic acid can be used as both the reducing and capping agents to synthesize AgNWs with an approximate yield of 50% in a one-step process. It was then demonstrated how various parameters can be tuned to increase the yield of AgNWs. One of these parameters was light. The light wavelength absorbance of tannic acid was investigated and it was shown that tannic acid molecules can become excited due to the absorption of UV light, which can lead to an increased reduction rate. It was shown that a moderate light intensity of 90 LUX (from white fluorescent lamps) is necessary for the synthesis of AgNWs, while lower and higher light intensities can reduce the yield of AgNWs. Another parameter that was investigated was the concentration ratio of tannic acid to silver nitrate, which shall be kept at one to allow for a moderate reduction rate. Using two kinetic models, it was demonstrated that a moderate reduction rate was necessary for 1D growth, which leads to nanowire formation. It was also shown that pH can significantly affect the reduction process, in the manner that higher pH leads to a higher reduction rate, and a lower yield of AgNWs. A pH of 4 was necessary for a more moderate reduction rate, which leads to 1D growth. Stirring rate, on the other hand, did not have a significant effect on the yield of AgNWs.

In chapter IV, the continuous synthesis of AgNWs in a millifluidic reactor was investigated. It was demonstrated that the millifluidic reactor can be used as an improved tool for the synthesis of AgNWs with a higher yield compared to the batch process. It was discussed how enhanced mass and heat transfer in the millifluidic reactor allow for a more homogenous reaction and growth process, leading to a more uniform morphology and a higher yield of AgNWs. It was shown that the yield of AgNWs can be increased by 32% (from 50 to 82%) using the same conditions used in the batch reactor, except that the reaction had to be performed in the dark. The results showed that the millilfuidic reactor can synthesize AgNWs with a high yield at a lower time compared to that of the batch (96 minutes compared to 240 minutes), and that the reduction rate can be

increased in the millifluidic reactor without the need for an external light source. The effect of light exposure on the yield of AgNWs in the millilfuidic reactor was also investigated, and it was shown that increased exposure to white fluorescent light increases the reduction rate and reduces the yield of AgNWs. In addition, it was demonstrated that silicone oil is required as a secondary phase in the millifluidic reactor to prevent tube coating caused by particle deposition. Also, the use of triton X-100 was shown to be necessary to prevent the migration of formed nanostructures to the water-oil interface, which is a disruptive phenomenon. It was also illustrated how triton X-100, tannic acid, and silver nitrate streams need to be introduced to the millifluidic reactor to maintain a uniform mixing process without disrupting the reduction of Ag^{+} ions. It was then demonstrated how different coil diameters in the case of helically-coiled millilfuidic reactor can affect the reduction rate and therefore the yield of AgNWs. The results showed that increased diameter can lead to a slower reduction rate, while decreased diameter can lead to an increased reduction rate. As discussed, the reason can be attributed to the rate of mixing when the coil diameter changes.

In Chapter V, the utilization of AgNWS—synthesized by tannic acid—in conductive ink manufacturing, with the aim of printing, was investigated. It was initially demonstrated that AgNWs can be synthesized at a larger scale, using an improved batch process, compared to the one provided in chapter III. The measured yield of AgNWs stood at approximately 90%, facilitating their use for conductive ink preparation. The rheological properties of the silver nanostructure-based (~90% silver nanowires) conductive ink were investigated by performing flow sweep, frequency sweep, and peak hold tests by the rheometer. The flow sweep test performed for different silver nanostructure contents (at 25 °C) showed that the decrease in viscosity vs. shear rate is more rapid for higher silver nanostructure contents. Furthermore, the flow sweep test performed for different temperatures (at 20% silver nanostructures), showed that the decrease in viscosity is more rapid in the case of lower temperatures. The frequency sweep

test at different silver nanostructure content (at 25 °C) showed that higher contents will lead to a more elastic response by the ink at increased frequencies. The frequency sweep test for different temperatures (at 20% silver nanostructures) showed that a lower temperature leads to a more elastic response at increased frequencies, while the response for higher temperatures tends to be more viscous at increased frequencies. The peak hold test demonstrated that increasing the silver nanostructure content (at 25 °C) results in a longer transition time after the ink is subjected to a high shear rate. The peak hold test at different temperatures (at 20% silver nanostructures) showed that higher temperatures increase the transition time after the ink is subjected to high shear rate. To simulate the direct writing printing method, the peak hold test was carried out based on the shear rate inside the printing system. The peak hold test results showed that the transition time for recovery was significantly faster in the case of direct writing compared to that of screen printing (1.78 vs. 27.04 s), which leads to faster shape retention after printing.

6.2. Perspective and future directions

The synthesis of AgNWs using tannic acid, as athe green reducing/capping agents, can open up a new window of possibilities for the green and sustainable synthesis of AgNWs. Such possibilities can be satisfied by a wide selection of green and sustainable reducing/capping agents. The recent *in-situ* analytical techniques such as *in-situ* FTIR, in-situ UV-Vis, and *in-situ* TEM can provide a more detailed information from the reaction including but not limited to reduction, nucleation, and growth. The *in-situ* FTIR technique can provide minute-by-minute information about the functional groups involved in the reduction and stabilization process throughout the reaction. Similar responsible functional groups involved may also be found in a different “green and sustainable” compound, which can lead to similar reduction and stabilization processes. *In situ* UV-Vis can provide minute-by-minute information about the light absorbance behavior of nanostructures throughout the reaction caused by their surface plasmon resonance behavior. For instance, *in-situ* UV-Vis spectra can provide insight regarding how an absorbance peak can

develop during the course of a reaction, in which case the peaks correspond to a specific size and morphology of nanostructures. *In situ* TEM can provide momentary information on the growth of nanostructures where one can see the growth of a certain morphology throughout the reaction. Combining this information allows the identification of different reaction steps and how one step develops to a different one (i.e. from reduction to nucleation, and nucleation to growth). In addition, such information can be used to alter the parameters in a manner that allows for a desired control over the size and morphology of nanostructures, and the yield of AgNWs in the case of AgNW synthesis. Furthermore, artificial neural networks can serve as a strong tool to optimize the synthesis of silver nanostructures with desired yield (i.e. AgNWs). This can be carried out by the data obtained from various characterization techniques such as FTIR, SEM, TEM, and UV-Vis. A prominent advantage of this tool is saving time and material in the testing process, thus facilitating process development. An advantageous aspect of green and sustainably-synthesized AgNWs is their high-scale production capability and economical feasibility. Based on our calculations, silver nanowires synthesized by our developed tannic acid-based synthesis process cost less than those synthesized in an average batch polyol process. On average, the production cost for each gram of AgNWs synthesized by an average batch polyol process[471] is approximately 29.34 $, while this production cost is reduced to ~21.16 $/g silver nanowires in the case of our tannic acid-based synthesis process, pointing to a 28% reduction in production costs (material and utility usage costs). In addition, waste removal would be much easier and more inexpensive in the case of tannic acid-based synthesis, and environmental regulations can be easily met. This is an important aspect for industrial manufacturing, and can finally contribute to the production of high-quality AgNW-based transparent conductive films.

REFERENCES

(1) Kaabipour, S.; Hemmati, S. A Review on the Green and Sustainable Synthesis of Silver Nanoparticles and One-Dimensional Silver Nanostructures. *Beilstein J. Nanotechnol.* **2021**. https://doi.org/10.3762/bjnano.12.9.

(2) Kaabipour, S.; Hemmati, S. Green, Sustainable, and Room-Temperature Synthesis of Silver Nanowires Using Tannic Acid – Kinetic and Parametric Study. *Colloids Surfaces A Physicochem. Eng. Asp.* **2022**, *641*. https://doi.org/10.1016/j.colsurfa.2022.128495.

(3) Kaabipour, S.; Hemmati, S. Continuous, Green, and Room-Temperature Synthesis of Silver Nanowires in a Helically-Coiled Millifluidic Reactor. *Colloids Surfaces A Physicochem. Eng. Asp.* **2023**, *659* (130806). https://doi.org/https://doi.org/10.1016/j.colsurfa.2022.130806.

(4) Seaberg, J.; Kaabipour, S.; Hemmati, S.; Ramsey, J. D. A Rapid Millifluidic Synthesis of Tunable Polymer-Protein Nanoparticles. *Eur. J. Pharm. Biopharm.* **2020**, *154*, 127–135. https://doi.org/10.1016/j.ejpb.2020.07.006.

(5) Austin, L. A.; MacKey, M. A.; Dreaden, E. C.; El-Sayed, M. A. The Optical, Photothermal, and Facile Surface Chemical Properties of Gold and Silver Nanoparticles in Biodiagnostics, Therapy, and Drug Delivery. *Arch. Toxicol.* **2014**, *88* (7), 1391–1417. https://doi.org/10.1007/s00204-014-1245-3.

(6) Abadeer, N. S.; Murphy, C. J. Recent Progress in Cancer Thermal Therapy Using Gold Nanoparticles. *J. Phys. Chem. C* **2016**, *120* (9), 4691–4716. https://doi.org/10.1021/acs.jpcc.5b11232.

(7) Mirzaei, H.; Darroudi, M. Zinc Oxide Nanoparticles: Biological Synthesis and Biomedical Applications. *Ceram. Int.* **2017**, *43* (1), 907–914. https://doi.org/10.1016/j.ceramint.2016.10.051.

(8) Jahangirian, H.; Lemraski, E. G.; Webster, T. J.; Rafiee-Moghaddam, R.; Abdollahi, Y. A Review of Drug Delivery Systems Based on Nanotechnology and Green Chemistry: Green Nanomedicine. *Int. J. Nanomedicine* **2017**, *12*, 2957–2978. https://doi.org/10.2147/IJN.S127683.

(9) Wen, M. M.; El-Salamouni, N. S.; El-Refaie, W. M.; Hazzah, H. A.; Ali, M. M.; Tosi, G.; Farid, R. M.; Blanco-Prieto, M. J.; Billa, N.; Hanafy, A. S. Nanotechnology-Based Drug Delivery Systems for Alzheimer's Disease Management: Technical, Industrial, and Clinical Challenges. *J. Control. Release* **2017**, *245*, 95–107. https://doi.org/10.1016/j.jconrel.2016.11.025.

(10) Dos Santos Ramos, M. A.; Da Silva, P. B.; Spósito, L.; De Toledo, L. G.; Bonifácio, B. vidal; Rodero, C. F.; Dos Santos, K. C.; Chorilli, M.; Bauab, T. M. Nanotechnology-

Based Drug Delivery Systems for Control of Microbial Biofilms: A Review. *Int. J. Nanomedicine* **2018**, *13*, 1179–1213. https://doi.org/10.2147/IJN.S146195.

(11) Chen, F.; Hableel, G.; Zhao, E. R.; Jokerst, J. V. Multifunctional Nanomedicine with Silica: Role of Silica in Nanoparticles for Theranostic, Imaging, and Drug Monitoring. *J. Colloid Interface Sci.* **2018**, *521*, 261–279. https://doi.org/10.1016/j.jcis.2018.02.053.

(12) Wilhelm, S.; Tavares, A. J.; Dai, Q.; Ohta, S.; Audet, J.; Dvorak, H. F.; Chan, W. C. W. Analysis of Nanoparticle Delivery to Tumours. *Nat. Rev. Mater.* **2016**, *1* (5), 1–12. https://doi.org/10.1038/natrevmats.2016.14.

(13) Shi, J.; Kantoff, P. W.; Wooster, R.; Farokhzad, O. C. Cancer Nanomedicine: Progress, Challenges and Opportunities. *Nat. Rev. Cancer* **2017**, *17* (1), 20–37. https://doi.org/10.1038/nrc.2016.108.

(14) Brownlee, W. J.; Seib, F. P. Impact of the Hypoxic Phenotype on the Uptake and Efflux of Nanoparticles by Human Breast Cancer Cells. *Sci. Rep.* **2018**, *8* (1), 1–11. https://doi.org/10.1038/s41598-018-30517-3.

(15) Cano, A. I.; Chiralt, A.; González-Martínez, C. Silver Composite Materials and Food Packaging. In *Composites Materials for Food Packaging*; 2018; pp 123–152. https://doi.org/10.1002/9781119160243.ch3.

(16) Kumar, S.; Shukla, A.; Baul, P.; … A. M.-F. packaging and shelf; 2018, U. Biodegradable Hybrid Nanocomposites of Chitosan/gelatin and Silver Nanoparticles for Active Food Packaging Applications. *Elsevier* **2018**, *16*, 178–184.

(17) Al-Shabib, N. A.; Husain, F. M.; Ahmed, F.; Khan, R. A.; Ahmad, I.; Alsharaeh, E.; Khan, M. S.; Hussain, A.; Rehman, M. T.; Yusuf, M.; et al. Biogenic Synthesis of Zinc Oxide Nanostructures from Nigella Sativa Seed: Prospective Role as Food Packaging Material Inhibiting Broad-Spectrum Quorum Sensing and Biofilm. *Sci. Rep.* **2016**, *6*, 36761. https://doi.org/10.1038/srep36761.

(18) Wang, R.; Neoh, K. G.; Kang, E. T.; Tambyah, P. A.; Chiong, E. Antifouling Coating with Controllable and Sustained Silver Release for Long-Term Inhibition of Infection and Encrustation in Urinary Catheters. *J. Biomed. Mater. Res. - Part B Appl. Biomater.* **2015**, *103* (3), 519–528. https://doi.org/10.1002/jbm.b.33230.

(19) Wu, K.; Yang, Y.; Zhang, Y.; Deng, J.; Lin, C. A Ntimicrobial Activity and Cytocompatibility of Silver Nanoparticles Coated Catheters via a Biomimetic Surface Functionalization Strategy. *Int. J. Nanomedicine* **2015**, *10*, 7241–7252. https://doi.org/10.2147/IJN.S92307.

(20) Bhargava, A.; Pareek, V.; Roy Choudhury, S.; Panwar, J.; Karmakar, S. Superior Bactericidal Efficacy of Fucose-Functionalized Silver Nanoparticles against Pseudomonas Aeruginosa PAO1 and Prevention of Its Colonization on Urinary Catheters. *ACS Appl. Mater. Interfaces* **2018**, *10* (35), 29325–29337. https://doi.org/10.1021/acsami.8b09475.

(21) van Hest, J. J. H. A.; Agronskaia, A. V.; Fokkema, J.; Montanarella, F.; Gregorio Puig, A.; de Mello Donega, C.; Meijerink, A.; Blab, G. A.; Gerritsen, H. C. Towards Robust and Versatile Single Nanoparticle Fiducial Markers for Correlative Light and Electron Microscopy. *J. Microsc.* **2019**, *274* (1), 13–22. https://doi.org/10.1111/jmi.12778.

(22) Varna, M.; Xuan, H. V.; Fort, E. Gold Nanoparticles in Cardiovascular Imaging. *Wiley Interdiscip. Rev. Nanomedicine Nanobiotechnology* **2018**, *10* (1), e1470. https://doi.org/10.1002/wnan.1470.

(23) Zhang, K.; Zhao, Q.; Qin, S.; Fu, Y.; Liu, R.; Zhi, J.; Shan, C. Nanodiamonds Conjugated Upconversion Nanoparticles for Bio-Imaging and Drug Delivery. *J. Colloid Interface Sci.* **2019**, *537*, 316–324. https://doi.org/10.1016/j.jcis.2018.11.028.

(24) Sharma, R. K.; Nigam, S.; Chouryal, Y. N.; Nema, S.; Bera, S. P.; Bhargava, Y.; Ghosh, P. Eu-Doped BaF 2 Nanoparticles for Bioimaging Applications. *ACS Appl. Nano Mater.* **2019**, *2* (2), 927–936. https://doi.org/10.1021/acsanm.8b02180.

(25) Jafari, S.; Derakhshankhah, H.; Alaei, L.; … A. F.-B. &; 2019, U. Mesoporous Silica Nanoparticles for Therapeutic/diagnostic Applications. *Biomed. Pharmacother.* **2019**, *109*, 1100–1111.

(26) Zhou, Z.; Yang, L.; Gao, J.; Chen, X. Structure–Relaxivity Relationships of Magnetic Nanoparticles for Magnetic Resonance Imaging. *Adv. Mater.* **2019**, *31*, 1804567. https://doi.org/10.1002/adma.201804567.

(27) Dash, S. P.; Patnaik, S. K.; Tripathy, S. K. Investigation of a Low Cost Tapered Plastic Fiber Optic Biosensor Based on Manipulation of Colloidal Gold Nanoparticles. *Opt. Commun.* **2019**, *437*, 388–391. https://doi.org/10.1016/j.optcom.2018.12.088.

(28) Liu, J.; Zhao, F.; Wang, H.; Zhang, W.; Hu, X.; Li, X.; Wang, Y. Generation of Dark Solitons in Erbium-Doped Fiber Laser Based on Black Phosphorus Nanoparticles. *Opt.*

Mater. (Amst). **2019**, *89*, 100–105. https://doi.org/10.1016/j.optmat.2018.12.055.

(29) Sharma, A.; Srivastava, A.; Jeon, Y.; Ahn, B. Template-Assisted Fabrication of Nanostructured Tin (β-Sn) Arrays for Bulk Microelectronic Packaging Devices. *Metals (Basel).* **2018**, *8* (5), 347. https://doi.org/10.3390/met8050347.

(30) Wang, Y.; Liu, W.; Liu, W.; He, P.; Fan, Z.; Wang, X.; Yu, D.; Guo, J.; Guo, B.; Shen, H. Synthesis of SnAgCu Nanoparticles with Low Melting Point by the Chemical Reduction Method. *Microelectron. Reliab.* **2017**, *78*, 17–24. https://doi.org/10.1016/j.microrel.2017.07.069.

(31) Sochol, R. D.; Sweet, E.; Glick, C. C.; Wu, S. Y.; Yang, C.; Restaino, M.; Lin, L. 3D Printed Microfluidics and Microelectronics. *Microelectron. Eng.* **2018**, *189*, 52–68. https://doi.org/10.1016/j.mee.2017.12.010.

(32) Mihyun, L.; M Zenobi-Wong - US Patent App. 16/000, 679; 2019. Nanocomposite Materials Comprising Cationic Nanoparticles and Anionic Polymers Useful in Methods for 3d Printing Thereof, 2019.

(33) Fantino, E.; Chiappone, A.; Roppolo, I.; Manfredi, D.; Bongiovanni, R.; Pirri, C. F.; Calignano, F. 3D Printing of Conductive Complex Structures with in Situ Generation of Silver Nanoparticles. *Adv. Mater.* **2016**, *28* (19), 3712–3717. https://doi.org/10.1002/adma.201505109.

(34) Zhu, W.; Webster, T. J.; Zhang, L. G. How Can 3D Printing Be a Powerful Tool in Nanomedicine? *Nanomedicine* **2018**, *13* (3), 251–253. https://doi.org/10.2217/nnm-2017-

0369.

(35) Tavakoli, M.; Malakooti, M. H.; Paisana, H.; Ohm, Y.; Green Marques, D.; Alhais Lopes, P.; Piedade, A. P.; de Almeida, A. T.; Majidi, C. EGaIn-Assisted Room-Temperature Sintering of Silver Nanoparticles for Stretchable, Inkjet-Printed, Thin-Film Electronics. *Adv. Mater.* **2018**, *30*, 1801852. https://doi.org/10.1002/adma.201801852.

(36) Suresh, S.; Unni, G. E.; Satyanarayana, M.; Sreekumaran Nair, A.; Mahadevan Pillai, V. P. Silver Nanoparticles-Incorporated Nb2O5 Surface Passivation Layer for Efficiency Enhancement in Dye-Sensitized Solar Cells. *J. Colloid Interface Sci.* **2018**, *524*, 236–244. https://doi.org/10.1016/j.jcis.2018.03.086.

(37) Wongrat, E.; Wongkrajang, S.; Chuejetton, A.; Bhoomanee, C.; Choopun, S. Rapid Synthesis of Au, Ag and Cu Nanoparticles by DC Arc-Discharge for Efficiency Enhancement in Polymer Solar Cells. *Mater. Res. Innov.* **2019**, *23* (2), 66–72. https://doi.org/10.1080/14328917.2017.1376786.

(38) Xie, H.; Yin, X.; Chen, P.; Liu, J.; Yang, C.; Que, W.; Wang, G. Solvothermal Synthesis of Highly Crystalline SnO 2 Nanoparticles for Flexible Perovskite Solar Cells Application. *Mater. Lett.* **2019**, *234*, 311–314. https://doi.org/10.1016/j.matlet.2018.09.117.

(39) Li, H.; He, Y.; Wang, X.; Liu, D.; Liu, Z. Bilayer Films Using Broadband Nanoparticles and Mesoporous TiO2 for High Efficient Dye Sensitized Solar Cells. *J. Alloys Compd.* **2019**, *773*, 743–751. https://doi.org/10.1016/j.jallcom.2018.09.279.

(40) Huang, S.; Wang, Y.; Shen, S.; Tang, Y.; Yu, A.; Kang, B.; Silva, S. R. P.; Lu, G. Enhancing the Performance of Polymer Solar Cells Using Solution-Processed Copper Doped Nickel Oxide Nanoparticles as Hole Transport Layer. *J. Colloid Interface Sci.* **2019**, *535*, 308–317. https://doi.org/10.1016/j.jcis.2018.10.013.

(41) Zhao, F.; Chen, S.; Hu, Q.; Xue, G.; Ni, Q.; Jiang, Q.; Qiu, Y. Antimicrobial Three Dimensional Woven Filters Containing Silver Nanoparticle Doped Nanofibers in a Membrane Bioreactor for Wastewater Treatment. *Sep. Purif. Technol.* **2017**, *175*, 130–139. https://doi.org/10.1016/j.seppur.2016.11.024.

(42) Morsi, R. E.; Alsabagh, A. M.; Nasr, S. A.; Zaki, M. M. Multifunctional Nanocomposites of Chitosan, Silver Nanoparticles, Copper Nanoparticles and Carbon Nanotubes for Water Treatment: Antimicrobial Characteristics. *Int. J. Biol. Macromol.* **2017**, *97*, 264–269. https://doi.org/10.1016/j.ijbiomac.2017.01.032.

(43) Bindhu, M. R.; Umadevi, M. Antibacterial and Catalytic Activities of Green Synthesized Silver Nanoparticles. *Spectrochim. Acta - Part A Mol. Biomol. Spectrosc.* **2015**, *135*, 373–378. https://doi.org/10.1016/j.saa.2014.07.045.

(44) Veisi, H.; Azizi, S.; Mohammadi, P. Green Synthesis of the Silver Nanoparticles Mediated by Thymbra Spicata Extract and Its Application as a Heterogeneous and Recyclable Nanocatalyst for Catalytic Reduction of a Variety of Dyes in Water. *J. Clean. Prod.* **2018**, *170*, 1536–1543. https://doi.org/10.1016/j.jclepro.2017.09.265.

(45) Choudhary, M. K.; Kataria, J.; Sharma, S. Evaluation of the Kinetic and Catalytic Properties of Biogenically Synthesized Silver Nanoparticles. *J. Clean. Prod.* **2018**, *198*,

882–890. https://doi.org/10.1016/j.jclepro.2018.09.015.

(46) Yan, Z.; Fu, L.; Zuo, X.; Yang, H. Green Assembly of Stable and Uniform Silver Nanoparticles on 2D Silica Nanosheets for Catalytic Reduction of 4-Nitrophenol. *Appl. Catal. B Environ.* **2018**, *226*, 23–30. https://doi.org/10.1016/j.apcatb.2017.12.040.

(47) Khoshnamvand, M.; Huo, C.; Liu, J. Silver Nanoparticles Synthesized Using Allium Ampeloprasum L. Leaf Extract: Characterization and Performance in Catalytic Reduction of 4-Nitrophenol and Antioxidant Activity. *J. Mol. Struct.* **2019**, *1175*, 90–96. https://doi.org/10.1016/j.molstruc.2018.07.089.

(48) Alexander, J. W. History of the Medical Use of Silver. *Surg. Infect. (Larchmt).* **2009**, *10* (3), 289–292. https://doi.org/10.1089/sur.2008.9941.

(49) Srikar, S. K.; Giri, D. D.; Pal, D. B.; Mishra, P. K.; Upadhyay, S. N. Green Synthesis of Silver Nanoparticles: A Review. *Green Sustain. Chem.* **2016**, *6* (1), 34–56. https://doi.org/10.4236/gsc.2016.61004.

(50) Wang, B.; Zhang, L.; Zhou, X. Synthesis of Silver Nanocubes as a SERS Substrate for the Determination of Pesticide Paraoxon and Thiram. *Spectrochim. Acta - Part A Mol. Biomol. Spectrosc.* **2014**, *121*, 63–69. https://doi.org/10.1016/j.saa.2013.10.013.

(51) Zhou, S.; Li, J.; Gilroy, K. D.; Tao, J.; Zhu, C.; Yang, X.; Sun, X.; Xia, Y. Facile Synthesis of Silver Nanocubes with Sharp Corners and Edges in an Aqueous Solution. *ACS Nano* **2016**, *10* (11), 9861–9870. https://doi.org/10.1021/acsnano.6b05776.

(52) Khatoon, U. T.; Nageswara Rao, G. V. S.; Mohan, K. M.; Ramanaviciene, A.; Ramanavicius, A. Antibacterial and Antifungal Activity of Silver Nanospheres Synthesized by Tri-Sodium Citrate Assisted Chemical Approach. *Vacuum* **2017**, *146*, 259–265. https://doi.org/10.1016/j.vacuum.2017.10.003.

(53) Khatami, M.; Zafarnia, N.; Heydarpoor Bami, M.; Sharifi, I.; Singh, H. Antifungal and Antibacterial Activity of Densely Dispersed Silver Nanospheres with Homogeneity Size Which Synthesized Using Chicory: An in Vitro Study. *J. Mycol. Med.* **2018**, *28* (4), 637–644. https://doi.org/10.1016/j.mycmed.2018.07.007.

(54) Nair, A. K.; Sukumaran Nair, K. M.; Thomas, S.; Rouxel, D.; Alwarappan, S.; Kalarikkal, N. In Situ Synthesis of Silver Nanospheres, Nanocubes, and Nanowires over Boron-Doped Graphene Sheets for Surface-Enhanced Raman Scattering Application and Enzyme-Free Detection of Hydrogen Peroxide. *Langmuir* **2018**, *34* (45), 13603–13614. https://doi.org/10.1021/acs.langmuir.8b02005.

(55) Wu, C.; Zhou, X.; Wei, J. Localized Surface Plasmon Resonance of Silver Nanotriangles Synthesized by a Versatile Solution Reaction. *Nanoscale Res. Lett.* **2015**, *10* (1), 1–6. https://doi.org/10.1186/s11671-015-1058-1.

(56) Amirjani, A.; Koochak, N. N.; Haghshenas, D. F. Synthesis of Silver Nanotriangles with Tunable Edge Length: A Promising Candidate for Light Harvesting Purposes within Visible and near-Infrared Ranges. *Mater. Res. Express* **2019**, *6* (3), 36204. https://doi.org/10.1088/2053-1591/aaf624.

(57) Debnath, B.; Das, R. Controlled Synthesis of Saponin-Capped Silver Nanotriangles and

Their Optical Properties. *Plasmonics* **2019**, *14* (6), 1365–1375. https://doi.org/10.1007/s11468-019-00923-y.

(58) Haber, J.; Sokolov, K. Synthesis of Stable Citrate-Capped Silver Nanoprisms. *Langmuir* **2017**, *33* (40), 10525–10530. https://doi.org/10.1021/acs.langmuir.7b01362.

(59) Tsuji, M.; Gomi, S.; Maeda, Y.; Matsunaga, M.; Hikino, S.; Uto, K.; Tsuji, T.; Kawazumi, H. Rapid Transformation from Spherical Nanoparticles, Nanorods, Cubes, or Bipyramids to Triangular Prisms of Silver with PVP, Citrate, and H 2O 2. *Langmuir* **2012**, *28* (24), 8845–8861. https://doi.org/10.1021/la3001027.

(60) He, Y.; Wu, X.; Lu, G.; Shi, G. A Facile Route to Silver Nanosheets. *Mater. Chem. Phys.* **2006**, *98* (1), 178–182. https://doi.org/10.1016/j.matchemphys.2005.09.008.

(61) Jang, H. S.; Seong, B.; Zang, X.; Lee, H.; Bae, J. W.; Cho, D. H.; Kao, E.; Yang, C.; Kang, G.; Liu, Y.; et al. Ultrafast Growth of Large 2D Silver Nanosheets by Highly Ordered Biological Template at Air/Gel Interface. *Adv. Mater. Interfaces* **2018**, *5* (10), 1701491. https://doi.org/10.1002/admi.201701491.

(62) Ahn, H. Y.; Cha, J. R.; Gong, M. S. Preparation of Sintered Silver Nanosheets by Coating Technique Using Silver Carbamate Complex. *Mater. Chem. Phys.* **2015**, *153*, 390–395. https://doi.org/10.1016/j.matchemphys.2015.01.030.

(63) Bashir, O.; Khan, Z. Silver Nano-Disks: Synthesis, Encapsulation, and Role of Water Soluble Starch. *J. Mol. Liq.* **2014**, *199*, 524–529. https://doi.org/10.1016/j.molliq.2014.09.041.

(64) Kim, B. H.; Lee, J. S. One-Pot Photochemical Synthesis of Silver Nanodisks Using a Conventional Metal-Halide Lamp. *Mater. Chem. Phys.* **2015**, *149*, 678–685. https://doi.org/10.1016/j.matchemphys.2014.11.026.

(65) Mohapatra, B.; Kuriakose, S.; Mohapatra, S. Rapid Green Synthesis of Silver Nanoparticles and Nanorods Using Piper Nigrum Extract. *J. Alloys Compd.* **2015**, *637*, 119–126. https://doi.org/10.1016/j.jallcom.2015.02.206.

(66) Patarroyo, J.; Genç, A.; Arbiol, J.; Bastús, N. G.; Puntes, V. One-Pot Polyol Synthesis of Highly Monodisperse Short Green Silver Nanorods. *Chem. Commun.* **2016**, *52* (73), 10960–10963. https://doi.org/10.1039/c6cc04796c.

(67) Zhang, Q.; Moran, C. H.; Xia, X.; Rycenga, M.; Li, N.; Xia, Y. Synthesis of Ag Nanobars in the Presence of Single-Crystal Seeds and a Bromide Compound, and Their Surface-Enhanced Raman Scattering (SERS) Properties. *Langmuir* **2012**, *28* (24), 9047–9054. https://doi.org/10.1021/la300253a.

(68) Wiley, B. J.; Chen, Y.; McLellan, J. M.; Xiong, Y.; Li, Z. Y.; Ginger, D.; Xia, Y. Synthesis and Optical Properties of Silver Nanobars and Nanorice. *Nano Lett.* **2007**, *7* (4), 1032–1036. https://doi.org/10.1021/nl070214f.

(69) Hemmati, S.; Barkey, D. P. Parametric Study, Sensitivity Analysis, and Optimization of Polyol Synthesis of Silver Nanowires. *ECS J. Solid State Sci. Technol.* **2017**, *6* (4), 132–137. https://doi.org/10.1149/2.0141704jss.

(70) Hemmati, S.; Barkey, D. P.; Eggleston, L.; Zukas, B.; Gupta, N.; Harris, M. Silver

Nanowire Synthesis in a Continuous Millifluidic Reactor. *ECS J. Solid State Sci. Technol.* **2017**, *6* (4), 144–149. https://doi.org/10.1149/2.0171704jss.

(71) Wang, H.; Wang, Y.; Chen, X. Synthesis of Uniform Silver Nanowires from AgCl Seeds for Transparent Conductive Films via Spin-Coating at Variable Spin-Speed. *Colloids Surfaces A Physicochem. Eng. Asp.* **2019**, *565*, 154–161. https://doi.org/10.1016/j.colsurfa.2018.11.050.

(72) Khodashenas, B.; Ghorbani, H. R. Synthesis of Silver Nanoparticles with Different Shapes. *Arab. J. Chem.* **2015**, *12* (8), 1823–1838. https://doi.org/10.1016/j.arabjc.2014.12.014.

(73) Wei, L.; Lu, J.; Xu, H.; Patel, A.; Chen, Z. S.; Chen, G. Silver Nanoparticles: Synthesis, Properties, and Therapeutic Applications. *Drug Discov. Today* **2015**, *20* (5), 595–601. https://doi.org/10.1016/j.drudis.2014.11.014.

(74) Bhakya, S.; Muthukrishnan, S.; Sukumaran, M.; Grijalva, M.; Cumbal, L.; Franklin Benjamin, J. H.; Senthil Kumar, T.; Rao, M. V. Antimicrobial, Antioxidant and Anticancer Activity of Biogenic Silver Nanoparticles-an Experimental Report. *RSC Adv.* **2016**, *6* (84), 81436–81446. https://doi.org/10.1039/c6ra17569d.

(75) Zheng, K.; Setyawati, M. I.; Leong, D. T.; Xie, J. Antimicrobial Silver Nanomaterials. *Coord. Chem. Rev.* **2018**, *357*, 1–17. https://doi.org/10.1016/j.ccr.2017.11.019.

(76) Ventola, C. L. The Antibiotic Resistance Crisis: Part 1: Causes and Threats. *Pharm. Ther.* **2015**, *40* (4), 277–283.

(77) Andersson, D. I.; Hughes, D. Microbiological Effects of Sublethal Levels of Antibiotics. *Nat. Rev. Microbiol.* **2014**, *12* (7), 465–478. https://doi.org/10.1038/nrmicro3270.

(78) Besinis, A.; De Peralta, T.; Handy, R. D. The Antibacterial Effects of Silver, Titanium Dioxide and Silica Dioxide Nanoparticles Compared to the Dental Disinfectant Chlorhexidine on Streptococcus Mutans Using a Suite of Bioassays. *Nanotoxicology* **2014**, *8* (1), 1–16. https://doi.org/10.3109/17435390.2012.742935.

(79) Seil, J. T.; Webster, T. J. Antimicrobial Applications of Nanotechnology: Methods and Literature. *Int. J. Nanomedicine* **2012**, *7*, 2767–2781. https://doi.org/10.2147/IJN.S24805.

(80) Morones, J. R.; Elechiguerra, J. L.; Camacho, A.; Holt, K.; Kouri, J. B.; Ramírez, J. T.; Yacaman, M. J. The Bactericidal Effect of Silver Nanoparticles. *Nanotechnology* **2005**, *16* (10), 2346–2353. https://doi.org/10.1088/0957-4484/16/10/059.

(81) Wang, F.; Yao, Y.; Zeng, X.; Huang, T.; Sun, R.; Xu, J.; Wong, C. P. Highly Thermally Conductive Polymer Nanocomposites Based on Boron Nitride Nanosheets Decorated with Silver Nanoparticles. *RSC Adv.* **2016**, *6* (47), 41630–41636. https://doi.org/10.1039/c6ra00358c.

(82) Wang, F.; Zeng, X.; Yao, Y.; Sun, R.; Xu, J.; Wong, C. P. Silver Nanoparticle-Deposited Boron Nitride Nanosheets as Fillers for Polymeric Composites with High Thermal Conductivity. *Sci. Rep.* **2016**, *6* (1), 1–9. https://doi.org/10.1038/srep19394.

(83) Patole, A.; Lubineau, G. Carbon Nanotubes with Silver Nanoparticle Decoration and Conductive Polymer Coating for Improving the Electrical Conductivity of Polycarbonate

Composites. *Carbon N. Y.* **2015**, *81*, 720–730. https://doi.org/10.1016/j.carbon.2014.10.014.

(84) Li, F.; Weir, M. D.; Chen, J.; Xu, H. H. K. Comparison of Quaternary Ammonium-Containing with Nano-Silver-Containing Adhesive in Antibacterial Properties and Cytotoxicity. *Dent. Mater.* **2013**, *29* (4), 450–461. https://doi.org/10.1016/j.dental.2013.01.012.

(85) Corrêa, J. M.; Mori, M.; Sanches, H. L.; Cruz, A. D. Da; Poiate, E.; Poiate, I. A. V. P. Silver Nanoparticles in Dental Biomaterials. *Int. J. Biomater.* **2015**, 485275. https://doi.org/10.1155/2015/485275.

(86) Slane, J.; Vivanco, J.; Rose, W.; Ploeg, H. L.; Squire, M. Mechanical, Material, and Antimicrobial Properties of Acrylic Bone Cement Impregnated with Silver Nanoparticles. *Mater. Sci. Eng. C* **2015**, *48*, 188–196. https://doi.org/10.1016/j.msec.2014.11.068.

(87) Dadosh, T. Synthesis of Uniform Silver Nanoparticles with a Controllable Size. *Mater. Lett.* **2009**, *63* (26), 2236–2238. https://doi.org/10.1016/j.matlet.2009.07.042.

(88) Jeong, S. H.; Choi, H.; Kim, J. Y.; Lee, T. W. Silver-Based Nanoparticles for Surface Plasmon Resonance in Organic Optoelectronics. *Part. Part. Syst. Charact.* **2015**, *32* (2), 164–175. https://doi.org/10.1002/ppsc.201400117.

(89) Qu, L. L.; Geng, Y. Y.; Bao, Z. N.; Riaz, S.; Li, H. Silver Nanoparticles on Cotton Swabs for Improved Surface-Enhanced Raman Scattering, and Its Application to the Detection of Carbaryl. *Microchim. Acta* **2016**, *183* (4), 1307–1313. https://doi.org/10.1007/s00604-

016-1760-4.

(90) Dissanayake, M. A. K. L.; Kumari, J. M. K. W.; Senadeera, G. K. R.; Thotawatthage, C. A. Efficiency Enhancement in Plasmonic Dye-Sensitized Solar Cells with TiO2 Photoanodes Incorporating Gold and Silver Nanoparticles. *J. Appl. Electrochem.* **2016**, *46* (1), 47–58. https://doi.org/10.1007/s10800-015-0886-0.

(91) Saravanan, S.; Kato, R.; Balamurugan, M.; Kaushik, S.; Soga, T. Efficiency Improvement in Dye Sensitized Solar Cells by the Plasmonic Effect of Green Synthesized Silver Nanoparticles. *J. Sci. Adv. Mater. Devices* **2017**, *2* (4), 418–424. https://doi.org/10.1016/j.jsamd.2017.10.004.

(92) Meschi Amoli, B.; Trinidad, J.; Hu, A.; Zhou, Y. N.; Zhao, B. Highly Electrically Conductive Adhesives Using Silver Nanoparticle (Ag NP)-Decorated Graphene: The Effect of NPs Sintering on the Electrical Conductivity Improvement. *J. Mater. Sci. Mater. Electron.* **2014**, *26* (1), 590–600. https://doi.org/10.1007/s10854-014-2440-y.

(93) He, L.; Tjong, S. C. Nanostructured Transparent Conductive Films: Fabrication, Characterization and Applications. *Mater. Sci. Eng. R Reports* **2016**, *109*, 1–101. https://doi.org/10.1016/j.mser.2016.08.002.

(94) Zhang, P.; Wyman, I.; Hu, J.; Lin, S.; Zhong, Z.; Tu, Y.; Huang, Z.; Wei, Y. Silver Nanowires: Synthesis Technologies, Growth Mechanism and Multifunctional Applications. *Mater. Sci. Eng. B Solid-State Mater. Adv. Technol.* **2017**, *223*, 1–23. https://doi.org/10.1016/j.mseb.2017.05.002.

(95) Jiu, J.; Sugahara, T.; Nogi, M.; Nagao, S.; Suganuma, K. Silver Nanowires Transparent Conductive Films: Fabrication Using Different Sintering Techniques. In *Proceedings of the IEEE Conference on Nanotechnology*; 2013; pp 15–18. https://doi.org/10.1109/NANO.2013.6720806.

(96) Bobinger, M.; Keddis, S.; Hinterleuthner, S.; Becherer, M.; Kluge, F.; Schwesinger, N.; Salmeron, J. F.; Lugli, P.; Rivadeneyra, A. Light and Pressure Sensors Based on PVDF with Sprayed and Transparent Electrodes for Self-Powered Wireless Sensor Nodes. *IEEE Sens. J.* **2019**, *19* (3), 1114–1126. https://doi.org/10.1109/JSEN.2018.2879122.

(97) Youn, D. Y.; Jung, U.; Naqi, M.; Choi, S. J.; Lee, M. G.; Lee, S.; Park, H. J.; Kim, I. D.; Kim, S. Wireless Real-Time Temperature Monitoring of Blood Packages: Silver Nanowire-Embedded Flexible Temperature Sensors. *ACS Appl. Mater. Interfaces* **2018**, *10* (51), 44678–44685. https://doi.org/10.1021/acsami.8b11928.

(98) De Guzman, N.; Ramos, M.; Balela, M. D. Improvements in the Electroless Deposition of Ag Nanowires in Hot Ethylene Glycol for Resistive Touchscreen Device. *Mater. Res. Bull.* **2018**, *106*, 446–454. https://doi.org/10.1016/j.materresbull.2018.06.030.

(99) Richard Swartwout. Smoothing Silver Nanowires for Optoelectronic Applications, Massachusetts Institute of Technology, 2018.

(100) Li, D.; Han, T.; Ruan, H. Solution-Assembled Ordered Grids Constructed with Silver Nanowires as Transparent Conductive Electrodes. *ACS Omega* **2018**, *3* (7), 7191–7195. https://doi.org/10.1021/acsomega.8b01320.

(101) Ha, B.; Jo, S. Hybrid Ag Nanowire Transparent Conductive Electrodes with Randomly Oriented and Grid-Patterned Ag Nanowire Networks. *Sci. Rep.* **2017**, *7* (1), 1–8. https://doi.org/10.1038/s41598-017-11964-w.

(102) Cheng, Y.; Wang, R.; Zhai, H.; Sun, J. Stretchable Electronic Skin Based on Silver Nanowire Composite Fiber Electrodes for Sensing Pressure, Proximity, and Multidirectional Strain. *Nanoscale* **2017**, *9* (11), 3834–3842. https://doi.org/10.1039/c7nr00121e.

(103) Chebeleu, L. *Using Nanowire Film in LCD Displays for Flexible Placement of Chip-on-Glass*; 2017.

(104) Park, H. G.; Heo, G. S.; Park, S. G.; Jeong, H. C.; Lee, J. H.; Seo, D. S. Silver Nanowire Networks as Transparent Conducting Films for Liquid Crystal Displays. *ECS Solid State Lett.* **2015**, *4* (10), 50–52. https://doi.org/10.1149/2.0031510ssl.

(105) Mallikarjuna, K.; Kim, H. Highly Transparent Conductive Reduced Graphene Oxide/Silver Nanowires/Silver Grid Electrodes for Low-Voltage Electrochromic Smart Windows. *ACS Appl. Mater. Interfaces* **2019**, *11* (2), 1969–1978. https://doi.org/10.1021/acsami.8b14086.

(106) Wang, J. L.; Lu, Y. R.; Li, H. H.; Liu, J. W.; Yu, S. H. Large Area Co-Assembly of Nanowires for Flexible Transparent Smart Windows. *J. Am. Chem. Soc.* **2017**, *139* (29), 9921–9926. https://doi.org/10.1021/jacs.7b03227.

(107) Hemmati, S.; Barkey, D. P.; Gupta, N.; Banfield, R. Synthesis and Characterization of

Silver Nanowire Suspensions for Printable Conductive Media. *ECS J. Solid State Sci. Technol.* **2015**, *4* (4), 3075–3079. https://doi.org/10.1149/2.0121504jss.

(108) Rafique, M.; Sadaf, I.; Rafique, M. S.; Tahir, M. B. A Review on Green Synthesis of Silver Nanoparticles and Their Applications. *Artif. Cells, Nanomedicine Biotechnol.* **2017**, *45* (7), 1272–1291. https://doi.org/10.1080/21691401.2016.1241792.

(109) Khayati, G. R.; Janghorban, K. An Investigation on the Application of Process Control Agents in the Preparation and Consolidation Behavior of Nanocrystalline Silver by Mechanochemical Method. *Adv. Powder Technol.* **2012**, *23* (6), 808–813. https://doi.org/10.1016/j.apt.2011.11.001.

(110) Khayati, G. R.; Janghorban, K. The Nanostructure Evolution of Ag Powder Synthesized by High Energy Ball Milling. *Adv. Powder Technol.* **2012**, *23* (3), 393–397. https://doi.org/10.1016/j.apt.2011.05.005.

(111) Jayaramudu, T.; Raghavendra, G. M.; Varaprasad, K.; Reddy, G. V. S.; Reddy, A. B.; Sudhakar, K.; Sadiku, E. R. Preparation and Characterization of Poly(ethylene Glycol) Stabilized Nano Silver Particles by a Mechanochemical Assisted Ball Mill Process. *J. Appl. Polym. Sci.* **2016**, *133* (7), 43027. https://doi.org/10.1002/app.43027.

(112) Boutinguiza, M.; Comesaña, R.; Lusquiños, F.; Riveiro, A.; Del Val, J.; Pou, J. Production of Silver Nanoparticles by Laser Ablation in Open Air. *Appl. Surf. Sci.* **2015**, *336*, 108–111. https://doi.org/10.1016/j.apsusc.2014.09.193.

(113) Verma, S.; Rao, B. T.; Srivastava, A. P.; Srivastava, D.; Kaul, R.; Singh, B. A Facile

Synthesis of Broad Plasmon Wavelength Tunable Silver Nanoparticles in Citrate Aqueous Solutions by Laser Ablation and Light Irradiation. *Colloids Surfaces A Physicochem. Eng. Asp.* **2017**, *527*, 23–33. https://doi.org/10.1016/j.colsurfa.2017.05.003.

(114) Boutinguiza, M.; Fernández-Arias, M.; del Val, J.; Buxadera-Palomero, J.; Rodríguez, D.; Lusquiños, F.; Gil, F. J.; Pou, J. Synthesis and Deposition of Silver Nanoparticles on Cp Ti by Laser Ablation in Open Air for Antibacterial Effect in Dental Implants. *Mater. Lett.* **2018**, *231*, 126–129. https://doi.org/10.1016/j.matlet.2018.07.134.

(115) Arboleda, D. M.; Santillán, J. M. J.; Arce, V. B.; Fernández van Raap, M. B.; Muraca, D.; Fernández, M. A.; Torres Sanchez, R. M.; Schinca, D. C.; Scaffardi, L. B. A Simple and "green" Technique to Synthesize Long-Term Stability Colloidal Ag Nanoparticles: Fs Laser Ablation in a Biocompatible Aqueous Medium. *Mater. Charact.* **2018**, *140*, 320–332. https://doi.org/10.1016/j.matchar.2018.04.021.

(116) Sportelli, M.; Izzi, M.; Volpe, A.; Clemente, M.; Picca, R.; Ancona, A.; Lugarà, P.; Palazzo, G.; Cioffi, N. The Pros and Cons of the Use of Laser Ablation Synthesis for the Production of Silver Nano-Antimicrobials. *Antibiotics* **2018**, *7* (3), 67. https://doi.org/10.3390/antibiotics7030067.

(117) Simchi, A.; Ahmadi, R.; Reihani, S. M. S.; Mahdavi, A. Kinetics and Mechanisms of Nanoparticle Formation and Growth in Vapor Phase Condensation Process. *Mater. Des.* **2007**, *28* (3), 850–856. https://doi.org/10.1016/j.matdes.2005.10.017.

(118) Baker, C.; Pradhan, A.; Pakstis, L.; Pochan, D.; Shah, S. I. Synthesis and Antibacterial Properties of Silver Nanoparticles. *J. Nanosci. Nanotechnol.* **2005**, *5* (2), 244–249.

https://doi.org/10.1166/jnn.2005.034.

(119) Malekzadeh, M.; Halali, M. Production of Silver Nanoparticles by Electromagnetic Levitation Gas Condensation. *Chem. Eng. J.* **2011**, *168* (1), 441–445. https://doi.org/10.1016/j.cej.2010.12.081.

(120) Hui, K. S.; Hui, K. N.; Dinh, D. A.; Tsang, C. H.; Cho, Y. R.; Zhou, W.; Hong, X.; Chun, H. H. Green Synthesis of Dimension-Controlled Silver Nanoparticle-Graphene Oxide with in Situ Ultrasonication. *Acta Mater.* **2014**, *64*, 326–332. https://doi.org/10.1016/j.actamat.2013.10.045.

(121) Park, M.; Sohn, Y.; Shin, W. G.; Lee, J.; Ko, S. H. Ultrasonication Assisted Production of Silver Nanowires with Low Aspect Ratio and Their Optical Properties. *Ultrason. Sonochem.* **2015**, *22*, 35–40. https://doi.org/10.1016/j.ultsonch.2014.05.007.

(122) Raghavendra, G. M.; Jung, J.; Kim, D.; Varaprasad, K.; Seo, J. Identification of Silver Cubic Structures during Ultrasonication of Chitosan AgNO3 Solution. *Carbohydr. Polym.* **2016**, *152*, 558–565. https://doi.org/10.1016/j.carbpol.2016.07.045.

(123) Jung, J.; Raghavendra, G. M.; Kim, D.; Seo, J. One-Step Synthesis of Starch-Silver Nanoparticle Solution and Its Application to Antibacterial Paper Coating. *Int. J. Biol. Macromol.* **2018**, *107*, 2285–2290. https://doi.org/10.1016/j.ijbiomac.2017.10.108.

(124) Javey, A.; Dai, H. Regular Arrays of 2 Nm Metal Nanoparticles for Deterministic Synthesis of Nanomaterials. *J. Am. Chem. Soc.* **2005**, *127* (34), 11942–11943. https://doi.org/10.1021/ja0536668.

(125) Wu, J.; Zan, X.; Li, S.; Liu, Y.; Cui, C.; Zou, B.; Zhang, W.; Xu, H.; Duan, H.; Tian, D.; et al. In Situ Synthesis of Large-Area Single Sub-10 Nm Nanoparticle Arrays by Polymer Pen Lithography. *Nanoscale* **2014**, *6* (2), 749–752. https://doi.org/10.1039/c3nr05033e.

(126) Shih, S. J.; Chien, I. C. Preparation and Characterization of Nanostructured Silver Particles by One-Step Spray Pyrolysis. *Powder Technol.* **2013**, *237*, 436–441. https://doi.org/10.1016/j.powtec.2012.12.032.

(127) Jang, H. D.; Kim, S. K.; Chang, H.; Jo, E. H.; Roh, K. M.; Choi, J. H.; Choi, J. W. Synthesis of 3D Silver-Graphene-Titanium Dioxide Composite via Aerosol Spray Pyrolysis for Sensitive Glucose Biosensor. *Aerosol Sci. Technol.* **2015**, *49* (7), 538–546. https://doi.org/10.1080/02786826.2015.1050086.

(128) Keskar, M.; Sabatini, C.; Cheng, C.; Swihart, M. T. Synthesis and Characterization of Silver Nanoparticle-Loaded Amorphous Calcium Phosphate Microspheres for Dental Applications. *Nanoscale Adv.* **2019**, *1* (2), 627–635. https://doi.org/10.1039/c8na00281a.

(129) Ramnani, S. P.; Biswal, J.; Sabharwal, S. Synthesis of Silver Nanoparticles Supported on Silica Aerogel Using Gamma Radiolysis. *Radiat. Phys. Chem.* **2007**, *76* (8–9), 1290–1294. https://doi.org/10.1016/j.radphyschem.2007.02.074.

(130) Juby, K.; Dwivedi, C.; Kumar, M.; Kota, S.; … H. M.-C.; 2012, U. Silver Nanoparticle-Loaded PVA/gum Acacia Hydrogel: Synthesis, Characterization and Antibacterial Study. *Carbohydr. Polym.* **2012**, *89* (3), 906–913.

(131) Biswal, J.; Misra, N.; Borde, L. C.; Sabharwal, S. Synthesis of Silver Nanoparticles in

Methacrylic Acid Solution by Gamma Radiolysis and Their Application for Estimation of Dopamine at Low Concentrations. *Radiat. Phys. Chem.* **2013**, *83*, 67–73. https://doi.org/10.1016/j.radphyschem.2012.10.003.

(132) Uttayarat, P.; Eamsiri, J.; Tangthong, T.; Suwanmala, P. Radiolytic Synthesis of Colloidal Silver Nanoparticles for Antibacterial Wound Dressings. *Adv. Mater. Sci. Eng.* **2015**, 376082. https://doi.org/10.1155/2015/376082.

(133) Ashkarran, A. A. A Novel Method for Synthesis of Colloidal Silver Nanoparticles by Arc Discharge in Liquid. *Curr. Appl. Phys.* **2010**, *10* (6), 1442–1447. https://doi.org/10.1016/j.cap.2010.05.010.

(134) Kumar, P.; Singh, P. K.; Hussain, M.; Das, A. K. Synthesis of Silver Metal Nanoparticles through Electric Arc Discharge Method: A Review. *Adv. Sci. Lett.* **2016**, *22* (1), 3–7. https://doi.org/10.1166/asl.2016.6772.

(135) Zhang, H.; Zou, G.; Liu, L.; Tong, H.; Li, Y.; Bai, H.; Wu, A. Synthesis of Silver Nanoparticles Using Large-Area Arc Discharge and Its Application in Electronic Packaging. *J. Mater. Sci.* **2017**, *52* (6), 3375–3387. https://doi.org/10.1007/s10853-016-0626-9.

(136) Tseng, K. H.; Chou, C. J.; Liu, T. C.; Tien, D. C.; Wu, T. C.; Stobinski, L. Interactive Relationship between Silver Ions and Silver Nanoparticles with PVA Prepared by the Submerged Arc Discharge Method. *Adv. Mater. Sci. Eng.* **2018**, 3240959. https://doi.org/10.1155/2018/3240959.

(137) Tseng, K. H.; Chou, C. J.; Liu, T. C.; Tien, D. C.; Chang, C. Y.; Stobinski, L. Relationship between Ag Nanoparticles and Ag Ions Prepared by Arc Discharge Method. *Nanotechnol. Rev.* **2018**, *7* (1), 1–9. https://doi.org/10.1515/ntrev-2017-0167.

(138) Liu, J.; Zhang, X.; Yu, M.; Li, S.; Small, J. Z.-; 2012, U. Photoinduced Silver Nanoparticles/nanorings on Plasmid DNA Scaffolds. *Small* **2012**, *8* (2), 310–316.

(139) Manikprabhu, D.; Lingappa, K. Antibacterial Activity of Silver Nanoparticles against Methicillin-Resistant Staphylococcus Aureus Synthesized Using Model Streptomyces Sp. Pigment by Photo-Irradiation Method. *J. Pharm. Res.* **2013**, *6* (2), 255–260. https://doi.org/10.1016/j.jopr.2013.01.022.

(140) Zhang, J. D.; Yu, M.; Liu, J. H.; Li, S. M.; Meng, Y. B. Effect of Plasmid DNA Dimension Evolution on the Size of Ag Nanoparticles during Photoirradiation. *Mater. Sci. Forum* **2016**, *847*, 194–199. https://doi.org/10.4028/www.scientific.net/msf.847.194.

(141) Natsuki, J. A Review of Silver Nanoparticles: Synthesis Methods, Properties and Applications. *Int. J. Mater. Sci. Appl.* **2016**, *4* (5), 325–332. https://doi.org/10.11648/j.ijmsa.20150405.17.

(142) Thanh, N. T. K.; Maclean, N.; Mahiddine, S. Mechanisms of Nucleation and Growth of Nanoparticles in Solution. *Chem. Rev.* **2014**, *114* (15), 7610–7630. https://doi.org/10.1021/cr400544s.

(143) Lee, J.; Yang, J.; Kwon, S. G.; Hyeon, T. Nonclassical Nucleation and Growth of Inorganic Nanoparticles. *Nat. Rev. Mater.* **2016**, *1* (8), 1–16.

https://doi.org/10.1038/natrevmats.2016.34.

(144) Khan, M.; Shaik, M. R.; Adil, S. F.; Khan, S. T.; Al-Warthan, A.; Siddiqui, M. R. H.; Tahir, M. N.; Tremel, W. Plant Extracts as Green Reductants for the Synthesis of Silver Nanoparticles: Lessons from Chemical Synthesis. *Dalt. Trans.* **2018**, *47* (35), 11988–12010. https://doi.org/10.1039/C8DT01152D.

(145) Mourdikoudis, S.; Liz-Marzán, L. M. Oleylamine in Nanoparticle Synthesis. *Chem. Mater.* **2013**, *25* (9), 1465–1476. https://doi.org/10.1021/cm4000476.

(146) Montes-García, V.; Pérez-Juste, J.; Pastoriza-Santos, I.; Liz-Marzán, L. M. Metal Nanoparticles and Supramolecular Macrocycles: A Tale of Synergy. *Chem. - A Eur. J.* **2014**, *20* (35), 10874–10883. https://doi.org/10.1002/chem.201403107.

(147) Jadalannagari, S.; Deshmukh, K.; Ramanan, S. R.; Kowshik, M. Antimicrobial Activity of Hemocompatible Silver Doped Hydroxyapatite Nanoparticles Synthesized by Modified Sol–gel Technique. *Appl. Nanosci.* **2014**, *4* (2), 133–141. https://doi.org/10.1007/s13204-013-0197-x.

(148) Ueno, S.; Nakashima, K.; Sakamoto, Y.; Wada, S. Synthesis of Silver-Strontium Titanate Hybrid Nanoparticles by Sol-Gel-Hydrothermal Method. *Nanomaterials* **2015**, *5* (2), 386–397. https://doi.org/10.3390/nano5020386.

(149) Arun Kumar, K. V.; John, J.; Sooraj, T. R.; Raj, S. A.; Unnikrishnan, N. V.; Selvaraj, N. B. Surface Plasmon Response of Silver Nanoparticles Doped Silica Synthesised via Sol-Gel Route. *Appl. Surf. Sci.* **2019**, *472*, 40–45.

https://doi.org/10.1016/j.apsusc.2018.05.178.

(150) Li, X.; Kim, N.; Youn, S.; An, T. K.; Kim, J.; Lim, S.; Kim, S. H. Sol-Gel-Processed Organic-Inorganic Hybrid for Flexible Conductive Substrates Based on Gravure-Printed Silver Nanowires and Graphene. *Polymers (Basel).* **2019**, *11* (1), 158. https://doi.org/10.3390/polym11010158.

(151) Lee, S. J.; Heo, M.; Lee, D.; Han, S.; Moon, J. H.; Lim, H. N.; Kwon, I. K. Preparation and Characterization of Antibacterial Orthodontic Resin Containing Silver Nanoparticles. *Appl. Surf. Sci.* **2018**, *432*, 317–323. https://doi.org/10.1016/j.apsusc.2017.04.030.

(152) Wang, Y.; Zheng, Y.; Huang, C. Z.; Xia, Y. Synthesis of Ag Nanocubes 18-32 Nm in Edge Length: The Effects of Polyol on Reduction Kinetics, Size Control, and Reproducibility. *J. Am. Chem. Soc.* **2013**, *135* (5), 1941–1951. https://doi.org/10.1021/ja311503q.

(153) Dugandžić, V.; Hidi, I. J.; Weber, K.; Cialla-May, D.; Popp, J. In Situ Hydrazine Reduced Silver Colloid Synthesis – Enhancing SERS Reproducibility. *Anal. Chim. Acta* **2016**, *946*, 73–79. https://doi.org/10.1016/j.aca.2016.10.018.

(154) Zhu, J.; Xu, X.; Liu, J.; Zheng, Y.; Hou, S. Facile Synthesis of Oleylamine-Capped Silver Nanowires and Their Application in Transparent Conductive Electrodes. *RSC Adv.* **2015**, *5* (90), 74126–74131. https://doi.org/10.1039/c5ra13884a.

(155) Raza, M.; Kanwal, Z.; Rauf, A.; Sabri, A.; Riaz, S.; Naseem, S. Size- and Shape-Dependent Antibacterial Studies of Silver Nanoparticles Synthesized by Wet Chemical

Routes. *Nanomaterials* **2016**, *6* (4), 74. https://doi.org/10.3390/nano6040074.

(156) Singha, D.; Barman, N.; Sahu, K. A Facile Synthesis of High Optical Quality Silver Nanoparticles by Ascorbic Acid Reduction in Reverse Micelles at Room Temperature. *J. Colloid Interface Sci.* **2014**, *413*, 37–42. https://doi.org/10.1016/j.jcis.2013.09.009.

(157) Matsuhisa, N.; Inoue, D.; Zalar, P.; Jin, H.; Matsuba, Y.; Itoh, A.; Yokota, T.; Hashizume, D.; Someya, T. Printable Elastic Conductors by in Situ Formation of Silver Nanoparticles from Silver Flakes. *Nat. Mater.* **2017**, *16* (8), 834–840. https://doi.org/10.1038/nmat4904.

(158) Yang, J.; Li, Y.; Jiang, B.; Fu, Y. Synthesis and Mechanism Study of the Highly Monodispersed Extra-Small Silver Nanoparticles in Reverse Micelles. *J. Nanophotonics* **2018**, *12* (3), 36008. https://doi.org/10.1117/1.jnp.12.036008.

(159) Ciobanu, C. S.; Iconaru, S. L.; Chifiriuc, M. C.; Costescu, A.; Le Coustumer, P.; Predoi, D. Synthesis and Antimicrobial Activity of Silver-Doped Hydroxyapatite Nanoparticles. *Biomed Res. Int.* **2013**, 916218. https://doi.org/10.1155/2013/916218.

(160) Bahlawane, N.; Premkumar, P. A.; Brechling, A.; Reiss, G.; Kohse-Höinghaus, K. Alcohol-Assisted CVD of Silver Using Commercially Available Precursors. *Chem. Vap. Depos.* **2007**, *13* (8), 401–407. https://doi.org/10.1002/cvde.200706610.

(161) Kuzminova, A.; Beranová, J.; Polonskyi, O.; Shelemin, A.; Kylián, O.; Choukourov, A.; Slavínská, D.; Biederman, H. Antibacterial Nanocomposite Coatings Produced by Means of Gas Aggregation Source of Silver Nanoparticles. *Surf. Coatings Technol.* **2016**, *294*, 225–230. https://doi.org/10.1016/j.surfcoat.2016.03.097.

(162) Zhang, K. X.; Wen, X.; Yao, C. B.; Li, J.; Zhang, M.; Li, Q. H.; Sun, W. J.; Wu, J. Da. Synthesis, Structural and Optical Properties of Silver Nanoparticles Uniformly Decorated ZnO Nanowires. *Chem. Phys. Lett.* **2018**, *698*, 147–151. https://doi.org/10.1016/j.cplett.2018.03.018.

(163) Wani, I. A.; Khatoon, S.; Ganguly, A.; Ahmed, J.; Ganguli, A. K.; Ahmad, T. Silver Nanoparticles: Large Scale Solvothermal Synthesis and Optical Properties. *Mater. Res. Bull.* **2010**, *45* (8), 1033–1038. https://doi.org/10.1016/j.materresbull.2010.03.028.

(164) Chen, D.; Qiao, X.; Qiu, X.; Chen, J.; Jiang, R. Large-Scale Synthesis of Silver Nanowires via a Solvothermal Method. *J. Mater. Sci. Mater. Electron.* **2011**, *22* (1), 6–13. https://doi.org/10.1007/s10854-010-0074-2.

(165) Du, D.; Yang, X.; Yang, Y.; Zhao, Y.; Wang, Y. Silver Nanowire Ink for Flexible Circuit on Textiles. *Micromachines* **2019**, *10* (1), 42. https://doi.org/10.3390/mi10010042.

(166) Guzmán, M.G., Dille, J., Godet, S. Synthesis of Silver Nanoparticles by Chemical Reduction Method and Their Antibacterial Activity. *Int. J. Chem. Biomol. Eng.* **2009**, *2* (3), 104–111.

(167) Khaydarov, R. A.; Khaydarov, R. R.; Gapurova, O.; Estrin, Y.; Scheper, T. Electrochemical Method for the Synthesis of Silver Nanoparticles. *J. Nanoparticle Res.* **2009**, *11* (5), 1193–1200. https://doi.org/10.1007/s11051-008-9513-x.

(168) Reicha, F. M.; Sarhan, A.; Abdel-Hamid, M. I.; El-Sherbiny, I. M. Preparation of Silver Nanoparticles in the Presence of Chitosan by Electrochemical Method. *Carbohydr. Polym.*

2012, *89* (1), 236–244. https://doi.org/10.1016/j.carbpol.2012.03.002.

(169) Nasretdinova, G. R.; Fazleeva, R. R.; Mukhitova, R. K.; Nizameev, I. R.; Kadirov, M. K.; Ziganshina, A. Y.; Yanilkin, V. V. Electrochemical Synthesis of Silver Nanoparticles in Solution. *Electrochem. commun.* **2015**, *50*, 69–72. https://doi.org/10.1016/j.elecom.2014.11.016.

(170) Chitsazi, M. R.; Korbekandi, H.; Asghari, G.; Najafi, R. B.; Badii, A.; Iravani, S. Synthesis of Silver Nanoparticles Using Methanol and Dichloromethane Extracts of Pulicaria Gnaphalodes (Vent.) Boiss. Aerial Parts. *Artif. Cells, Nanomedicine Biotechnol.* **2016**, *44* (1), 328–333. https://doi.org/10.3109/21691401.2014.949726.

(171) Divya, M.; Kiran, G. S.; Hassan, S.; Selvin, J. Biogenic Synthesis and Effect of Silver Nanoparticles (AgNPs) to Combat Catheter-Related Urinary Tract Infections. *Biocatal. Agric. Biotechnol.* **2019**, *18*, 101037. https://doi.org/10.1016/j.bcab.2019.101037.

(172) Saravanan, M.; Barik, S. K.; MubarakAli, D.; Prakash, P.; Pugazhendhi, A. Synthesis of Silver Nanoparticles from Bacillus Brevis (NCIM 2533) and Their Antibacterial Activity against Pathogenic Bacteria. *Microb. Pathog.* **2018**, *116*, 221–226. https://doi.org/10.1016/j.micpath.2018.01.038.

(173) Saravanan, C.; Rajesh, R.; Kaviarasan, T.; Muthukumar, K.; Kavitake, D.; Shetty, P. H. Synthesis of Silver Nanoparticles Using Bacterial Exopolysaccharide and Its Application for Degradation of Azo-Dyes. *Biotechnol. Reports* **2017**, *15*, 33–40. https://doi.org/10.1016/j.btre.2017.02.006.

(174) Rajora, N.; Kaushik, S.; Jyoti, A.; Kothari, S. L. Rapid Synthesis of Silver Nanoparticles by Pseudomonas Stutzeri Isolated from Textile Soil under Optimised Conditions and Evaluation of Their Antimicrobial and Cytotoxicity Properties. *IET Nanobiotechnology* **2016**, *10* (6), 367–373. https://doi.org/10.1049/iet-nbt.2015.0107.

(175) Srivastava, S.; Bhargava, A.; Pathak, N.; Srivastava, P. Production, Characterization and Antibacterial Activity of Silver Nanoparticles Produced by Fusarium Oxysporum and Monitoring of Protein-Ligand Interaction through in-Silico Approaches. *Microb. Pathog.* **2019**, *129*, 136–145. https://doi.org/10.1016/j.micpath.2019.02.013.

(176) Khalil, N. M.; Abd El-Ghany, M. N.; Rodríguez-Couto, S. Antifungal and Anti-Mycotoxin Efficacy of Biogenic Silver Nanoparticles Produced by Fusarium Chlamydosporum and Penicillium Chrysogenum at Non-Cytotoxic Doses. *Chemosphere* **2019**, *218*, 477–486. https://doi.org/10.1016/j.chemosphere.2018.11.129.

(177) Sanguiñedo, P.; Fratila, R.; … M. E.-N. B. and; 2018, U. Extracellular Biosynthesis of Silver Nanoparticles Using Fungi and Their Antibacterial Activity. *Nano. Biomed. Eng* **2018**, *10* (2), 156–164.

(178) Ma, L.; Su, W.; Liu, J. X.; Zeng, X. X.; Huang, Z.; Li, W.; Liu, Z. C.; Tang, J. X. Optimization for Extracellular Biosynthesis of Silver Nanoparticles by Penicillium Aculeatum Su1 and Their Antimicrobial Activity and Cytotoxic Effect Compared with Silver Ions. *Mater. Sci. Eng. C* **2017**, *77*, 963–971. https://doi.org/10.1016/j.msec.2017.03.294.

(179) Bayram, S.; Zahr, O.; Del Re, J.; Blum, A. S. TMV Disk Scaffolds for Making Sub-30

Nm Silver Nanorings. In *Methods in Molecular Biology*; 2018; pp 109–118. https://doi.org/10.1007/978-1-4939-7893-9_9.

(180) Yang, C.; Jung, S.; Yi, H. A Biofabrication Approach for Controlled Synthesis of Silver Nanoparticles with High Catalytic and Antibacterial Activities. *Biochem. Eng. J.* **2014**, *89*, 10–20. https://doi.org/10.1016/j.bej.2013.12.008.

(181) Daphne, J.; Francis, A.; Mohanty, R.; Ojha, N.; Das, N. Green Synthesis of Antibacterial Silver Nanoparticles Using Yeast Isolates and Its Characterization. *Res. J. Pharm. Technol.* **2018**, *11* (1), 83–92. https://doi.org/10.5958/0974-360X.2018.00016.1.

(182) Fernández, J. G.; Fernández-Baldo, M. A.; Berni, E.; Camí, G.; Durán, N.; Raba, J.; Sanz, M. I. Production of Silver Nanoparticles Using Yeasts and Evaluation of Their Antifungal Activity against Phytopathogenic Fungi. *Process Biochem.* **2016**, *51* (9), 1306–1313. https://doi.org/10.1016/j.procbio.2016.05.021.

(183) Korbekandi, H.; Mohseni, S.; Jouneghani, R. M.; Pourhossein, M.; Iravani, S. Biosynthesis of Silver Nanoparticles Using Saccharomyces Cerevisiae. *Artif. Cells, Nanomedicine Biotechnol.* **2016**, *44* (1), 235–239. https://doi.org/10.3109/21691401.2014.937870.

(184) Kumar, V.; Yadav, S. K. Plant-Mediated Synthesis of Silver and Gold Nanoparticles and Their Applications. *J. Chem. Technol. Biotechnol.* **2009**, *84* (2), 151–157. https://doi.org/10.1002/jctb.2023.

(185) Iravani, S. Green Synthesis of Metal Nanoparticles Using Plants. *Green Chem.* **2011**, *13*

(10), 2638–2650. https://doi.org/10.1039/c1gc15386b.

(186) Mashwani, Z. ur R.; Khan, T.; Khan, M. A.; Nadhman, A. Synthesis in Plants and Plant Extracts of Silver Nanoparticles with Potent Antimicrobial Properties: Current Status and Future Prospects. *Appl. Microbiol. Biotechnol.* **2015**, *99* (23), 9923–9934. https://doi.org/10.1007/s00253-015-6987-1.

(187) Rajeshkumar, S.; Bharath, L. V. Mechanism of Plant-Mediated Synthesis of Silver Nanoparticles – A Review on Biomolecules Involved, Characterisation and Antibacterial Activity. *Chem. Biol. Interact.* **2017**, *273*, 219–227. https://doi.org/10.1016/j.cbi.2017.06.019.

(188) Sri Ramkumar, S. R.; Sivakumar, N.; Selvakumar, G.; Selvankumar, T.; Sudhakar, C.; Ashokkumar, B.; Karthi, S. Green Synthesized Silver Nanoparticles from: Garcinia Imberti Bourd and Their Impact on Root Canal Pathogens and HepG2 Cell Lines. *RSC Adv.* **2017**, *7* (55), 34548–34555. https://doi.org/10.1039/c6ra28328d.

(189) Ahmed, S.; Ahmad, M.; Swami, B. L.; Ikram, S. A Review on Plants Extract Mediated Synthesis of Silver Nanoparticles for Antimicrobial Applications: A Green Expertise. *J. Adv. Res.* **2016**, *7* (1), 17–28. https://doi.org/10.1016/j.jare.2015.02.007.

(190) Shaik, M. R.; Khan, M.; Kuniyil, M.; Al-Warthan, A.; Alkhathlan, H. Z.; Siddiqui, M. R. H.; Shaik, J. P.; Ahamed, A.; Mahmood, A.; Khan, M.; et al. Plant-Extract-Assisted Green Synthesis of Silver Nanoparticles Using Origanum Vulgare L. Extract and Their Microbicidal Activities. *Sustain.* **2018**, *10* (4), 913. https://doi.org/10.3390/su10040913.

(191) Behravan, M.; Hossein Panahi, A.; Naghizadeh, A.; Ziaee, M.; Mahdavi, R.; Mirzapour, A. Facile Green Synthesis of Silver Nanoparticles Using Berberis Vulgaris Leaf and Root Aqueous Extract and Its Antibacterial Activity. *Int. J. Biol. Macromol.* **2019**, *124*, 148–154. https://doi.org/10.1016/j.ijbiomac.2018.11.101.

(192) Ranoszek-Soliwoda, K.; Tomaszewska, E.; Małek, K.; Celichowski, G.; Orlowski, P.; Krzyzowska, M.; Grobelny, J. The Synthesis of Monodisperse Silver Nanoparticles with Plant Extracts. *Colloids Surfaces B Biointerfaces* **2019**, *177*, 19–24. https://doi.org/10.1016/j.colsurfb.2019.01.037.

(193) Dahoumane, S. A.; Mechouet, M.; Wijesekera, K.; Filipe, C. D. M.; Sicard, C.; Bazylinski, D. A.; Jeffryes, C. Algae-Mediated Biosynthesis of Inorganic Nanomaterials as a Promising Route in Nanobiotechnology-a Review. *Green Chem.* **2017**, *19* (3), 552–587. https://doi.org/10.1039/c6gc02346k.

(194) Dahoumane, S.; Jeffryes, C.; Mechouet, M.; Agathos, S. Biosynthesis of Inorganic Nanoparticles: A Fresh Look at the Control of Shape, Size and Composition. *Bioengineering* **2017**, *4* (1), 14. https://doi.org/10.3390/bioengineering4010014.

(195) Dahoumane, S. A.; Mechouet, M.; Alvarez, F. J.; Agathos, S. N.; Jeffryes, C. Microalgae: An Outstanding Tool in Nanotechnology. *Bionatura* **2016**, *1* (4), 196–201. https://doi.org/10.21931/rb/2016.01.04.7.

(196) Rahman, A.; Kumar, S.; Bafana, A.; Dahoumane, S. A.; Jeffryes, C. Biosynthetic Conversion of Ag + to Highly Stable Ag 0 Nanoparticles by Wild Type and Cell Wall Deficient Strains of Chlamydomonas Reinhardtii. *Molecules* **2019**, *24* (1), 98.

https://doi.org/10.3390/molecules24010098.

(197) Abdel-Raouf, N.; Al-Enazi, N. M.; Ibraheem, I. B. M.; Alharbi, R. M.; Alkhulaifi, M. M. Biosynthesis of Silver Nanoparticles by Using of the Marine Brown Alga Padina Pavonia and Their Characterization. *Saudi J. Biol. Sci.* **2018**, *26* (6), 1207–1215. https://doi.org/10.1016/j.sjbs.2018.01.007.

(198) Talekar, S.; Joshi, G.; Chougle, R.; Nainegali, B.; Desai, S.; Joshi, A.; Kambale, S.; Kamat, P.; Haripurkar, R.; Jadhav, S.; et al. Preparation of Stable Cross-Linked Enzyme Aggregates (CLEAs) of NADH-Dependent Nitrate Reductase and Its Use for Silver Nanoparticle Synthesis from Silver Nitrate. *Catal. Commun.* **2014**, *53*, 62–66. https://doi.org/10.1016/j.catcom.2014.05.003.

(199) Talekar, S.; Joshi, A.; Chougle, R.; Nakhe, A.; Bhojwani, R. Immobilized Enzyme Mediated Synthesis of Silver Nanoparticles Using Cross-Linked Enzyme Aggregates (CLEAs) of NADH-Dependent Nitrate Reductase. *Nano-Structures and Nano-Objects* **2016**, *6*, 23–33. https://doi.org/10.1016/j.nanoso.2016.03.002.

(200) Mukherjee, K.; Gupta, R.; Kumar, G.; Kumari, S.; Biswas, S.; Padmanabhan, P. Synthesis of Silver Nanoparticles by Bacillus Clausii and Computational Profiling of Nitrate Reductase Enzyme Involved in Production. *J. Genet. Eng. Biotechnol.* **2018**, *16* (2), 527–536. https://doi.org/10.1016/j.jgeb.2018.04.004.

(201) Philip, D. Honey Mediated Green Synthesis of Silver Nanoparticles. *Spectrochim. Acta - Part A Mol. Biomol. Spectrosc.* **2010**, *75* (3), 1078–1081. https://doi.org/10.1016/j.saa.2009.12.058.

(202) Anuradha, K.; Bangal, P.; Madhavendra, S. S. Macromolecular Arabinogalactan Polysaccharide Mediated Synthesis of Silver Nanoparticles, Characterization and Evaluation. *Macromol. Res.* **2016**, *24* (2), 152–162. https://doi.org/10.1007/s13233-016-4018-4.

(203) Hemmati, S.; Retzlaff-Roberts, E.; Scott, C.; Harris, M. T. Artificial Sweeteners and Sugar Ingredients as Reducing Agent for Green Synthesis of Silver Nanoparticles. *J. Nanomater.* **2019**, 9641860. https://doi.org/10.1155/2019/9641860.

(204) Gade, A. K.; Bonde, S. R.; Meshram, S. M.; Gupta, I. R.; Rai, M. K. Green Synthesis of Silver Nanoparticles Using White Sugar. *IET Nanobiotechnology* **2013**, *7* (1), 28–32. https://doi.org/10.1049/iet-nbt.2012.0002.

(205) May, B. M. M.; Oluwafemi, O. S. Sugar-Reduced Gelatin-Capped Silver Nanoparticles with High Selectivity for Colorimetric Sensing of Hg 2+ and Fe 2+ Ions in the Midst of Other Metal Ions in Aqueous Solutions. *Int. J. Electrochem. Sci.* **2016**, *11*, 8096–8108. https://doi.org/10.20964/2016.09.29.

(206) Nadagouda, M. N.; Varma, R. S. Green and Controlled Synthesis of Gold and Platinum Nanomaterials Using Vitamin B2: Density-Assisted Self-Assembly of Nanospheres, Wires and Rods. *Green Chem.* **2006**, *8* (6), 516–518. https://doi.org/10.1039/b601271j.

(207) Malassis, L.; Dreyfus, R.; Murphy, R. J.; Hough, L. A.; Donnio, B.; Murray, C. B. One-Step Green Synthesis of Gold and Silver Nanoparticles with Ascorbic Acid and Their Versatile Surface Post-Functionalization. *RSC Adv.* **2016**, *6* (39), 33092–33100. https://doi.org/10.1039/c6ra00194g.

(208) Nadagouda, M. N.; Varma, R. S. Green Synthesis of Ag and Pd Nanospheres, Nanowires, and Nanorods Using Vitamin B2: Catalytic Polymerisation of Aniline and Pyrrole. *J. Nanomater.* **2008**, *2008*, 782358. https://doi.org/10.1155/2008/782358.

(209) Akhavan, O. Bacteriorhodopsin as a Superior Substitute for Hydrazine in Chemical Reduction of Single-Layer Graphene Oxide Sheets. *Carbon N. Y.* **2015**, *81*, 158–166. https://doi.org/10.1016/j.carbon.2014.09.044.

(210) Granata, G.; Yamaoka, T.; Pagnanelli, F.; Fuwa, A. Study of the Synthesis of Copper Nanoparticles: The Role of Capping and Kinetic towards Control of Particle Size and Stability. *J. Nanoparticle Res.* **2016**, *18* (5), 133. https://doi.org/10.1007/s11051-016-3438-6.

(211) Lee, Y. I.; Kwon, Y. T.; Kim, S.; Lee, K. J.; Choa, Y. H. Hydrazine Vapor-Based Rapid and Low Temperature Post-Processing for Inkjet Printed Conductive Copper Patterns. *Thin Solid Films* **2016**, *616*, 260–264. https://doi.org/10.1016/j.tsf.2016.08.032.

(212) Guzman, M.; Dille, J.; Godet, S. Synthesis and Antibacterial Activity of Silver Nanoparticles against Gram-Positive and Gram-Negative Bacteria. *Nanomedicine Nanotechnology, Biol. Med.* **2012**, *8* (1), 37–45. https://doi.org/10.1016/j.nano.2011.05.007.

(213) Szczepanowicz, K.; Stefańska, J.; Socha, R. P.; Warszyński, P. Preparation of Silver Nanoparticles via Chemical Reduction and Their Antimicrobial Activity. *Physicochem. Probl. Miner. Process.* **2010**, *45* (2010), 85–98.

(214) Chumachenko, V.; Kutsevol, N.; Rawiso, M.; Schmutz, M.; Blanck, C. In Situ Formation of Silver Nanoparticles in Linear and Branched Polyelectrolyte Matrices Using Various Reducing Agents. *Nanoscale Res. Lett.* **2014**, *9* (1), 164. https://doi.org/10.1186/1556-276X-9-164.

(215) Gurusamy, V.; Krishnamoorthy, R.; Gopal, B.; Veeraravagan, V.; Periyasamy. Systematic Investigation on Hydrazine Hydrate Assisted Reduction of Silver Nanoparticles and Its Antibacterial Properties. *Inorg. Nano-Metal Chem.* **2017**, *47* (5), 761–767. https://doi.org/10.1080/15533174.2015.1137074.

(216) Dai, L.; Nadeau, B.; An, X.; Cheng, D.; Long, Z.; Ni, Y. Silver Nanoparticles-Containing Dual-Function Hydrogels Based on a Guar Gum-Sodium Borohydride System. *Sci. Rep.* **2016**, *6*, 36497. https://doi.org/10.1038/srep36497.

(217) Zamiri, R.; Azmi, B. Z.; Sadrolhosseini, A. R.; Ahangar, H. A.; Zaidan, A. W.; Mahdi, M. A. Preparation of Silver Nanoparticles in Virgin Coconut Oil Using Laser Ablation. *Int. J. Nanomedicine* **2011**, *6*, 71–75. https://doi.org/10.2147/IJN.S14005.

(218) Iravani, S.; Korbekandi, H.; Mirmohammadi, S. V.; Zolfaghari, B. Synthesis of Silver Nanoparticles: Chemical, Physical and Biological Methods. *Res. Pharm. Sci.* **2014**, *9* (6), 385–406.

(219) Mostafa, A. A.; Sayed, S. R. M.; Solkamy, E. N.; Khan, M.; Shaik, M. R.; Al-Warthan, A.; Adil, S. F. Evaluation of Biological Activities of Chemically Synthesized Silver Nanoparticles. *J. Nanomater.* **2015**, 789178. https://doi.org/10.1155/2015/789178.

(220) Siddiqi, K. S.; Husen, A.; Rao, R. A. K. A Review on Biosynthesis of Silver Nanoparticles and Their Biocidal Properties. *J. Nanobiotechnology* **2018**, *16* (1), 14. https://doi.org/10.1186/s12951-018-0334-5.

(221) Mousavi, S. M.; Hashemi, S. A.; Ghasemi, Y.; Atapour, A.; Amani, A. M.; Savar Dashtaki, A.; Babapoor, A.; Arjmand, O. Green Synthesis of Silver Nanoparticles toward Bio and Medical Applications: Review Study. *Artif. Cells, Nanomedicine Biotechnol.* **2018**, *46* (S3), S855–S872. https://doi.org/10.1080/21691401.2018.1517769.

(222) Jorge de Souza, T. A.; Rosa Souza, L. R.; Franchi, L. P. Silver Nanoparticles: An Integrated View of Green Synthesis Methods, Transformation in the Environment, and Toxicity. *Ecotoxicol. Environ. Saf.* **2019**, *171*, 691–700. https://doi.org/10.1016/j.ecoenv.2018.12.095.

(223) Mittal, A. K.; Chisti, Y.; Banerjee, U. C. Synthesis of Metallic Nanoparticles Using Plant Extracts. *Biotechnol. Adv.* **2013**, *31* (2), 346–356. https://doi.org/10.1016/j.biotechadv.2013.01.003.

(224) Xing, T.; Sunarso, J.; Yang, W.; Yin, Y.; Glushenkov, A. M.; Li, L. H.; Howlett, P. C.; Chen, Y. Ball Milling: A Green Mechanochemical Approach for Synthesis of Nitrogen Doped Carbon Nanoparticles. *Nanoscale* **2013**, *5* (17), 7970–7976. https://doi.org/10.1039/c3nr02328a.

(225) Khayati, G. R.; Janghorban, K. Preparation of Nanostructure Silver Powders by Mechanical Decomposing and Mechanochemical Reduction of Silver Oxide. *Trans. Nonferrous Met. Soc. China (English Ed.* **2013**, *23* (5), 1520–1524.

https://doi.org/10.1016/S1003-6326(13)62625-4.

(226) Ullah, M.; Ali, M. E.; Hamid, S. B. A. Surfactant-Assisted Ball Milling: A Novel Route to Novel Materials with Controlled Nanostructure-A Review. *Rev. Adv. Mater. Sci.* **2014**, *37*, 1–14.

(227) Cui, B. Z.; Zheng, L. Y.; Waryoba, D.; Marinescu, M.; Hadjipanayis, G. C. Anisotropic SmCo5flakes and Nanocrystalline Particles by High Energy Ball Milling. *J. Appl. Phys.* **2011**, *109* (7), 07A728. https://doi.org/10.1063/1.3562447.

(228) Raffi, M.; Rumaiz, A. K.; Hasan, M. M.; Shah, S. I. Studies of the Growth Parameters for Silver Nanoparticle Synthesis by Inert Gas Condensation. *J. Mater. Res.* **2007**, *22* (12), 3378–3384. https://doi.org/10.1557/jmr.2007.0420.

(229) Kruis, F. E.; Fissan, H.; Rellinghaus, B. Sintering and Evaporation Characteristics of Gas-Phase Synthesis of Size-Selected PbS Nanoparticles. *Mater. Sci. Eng. B* **2002**, *69*, 329–334. https://doi.org/10.1016/s0921-5107(99)00298-6.

(230) Magnusson, M. H.; Deppert, K.; Malm, J. O.; Bovin, J. O.; Samuelson, L. Gold Nanoparticles: Production, Reshaping, and Thermal Charging. *J. Nanoparticle Res.* **1999**, *1* (2), 243–251. https://doi.org/10.1023/A:1010012802415.

(231) Tien, D. C.; Tseng, K. H.; Liao, C. Y.; Huang, J. C.; Tsung, T. T. Discovery of Ionic Silver in Silver Nanoparticle Suspension Fabricated by Arc Discharge Method. *J. Alloys Compd.* **2008**, *463* (1–2), 408–411. https://doi.org/10.1016/j.jallcom.2007.09.048.

(232) Amendola, V.; Meneghetti, M. Laser Ablation Synthesis in Solution and Size Manipulation of Noble Metal Nanoparticles. *Phys. Chem. Chem. Phys.* **2009**, *11* (20), 3805–3821. https://doi.org/10.1039/b900654k.

(233) Amendola, V.; Meneghetti, M. What Controls the Composition and the Structure of Nanomaterials Generated by Laser Ablation in Liquid Solution? *Phys. Chem. Chem. Phys.* **2013**, *15* (9), 3027–3046. https://doi.org/10.1039/c2cp42895d.

(234) Ghaffarian, H.; Saiedi, M.; … M. S.-I. J. of; 2011, U. Synthesis of ZnO Nanoparticles by Spray Pyrolysis Method. *Iran. J. Chem. Chem. Eng.* **2011**, *30* (1), 1–6.

(235) Thota, S.; Crans, D. C.; Iravani, S. Methods for Preparation of Metal Nanoparticles. In *Metal Nanoparticles*; 2017; pp 15–32. https://doi.org/10.1002/9783527807093.ch2.

(236) Niederberger, M. Nonaqueous Sol-Gel Routes to Metal Oxide Nanoparticles. *Acc. Chem. Res.* **2007**, *40* (9), 793–800. https://doi.org/10.1021/ar600035e.

(237) Muromachi, T.; Tsujino, T.; Kamitani, K.; Maeda, K. Application of Functional Coatings by Sol-Gel Method. *J. Sol-Gel Sci. Technol.* **2006**, *40* (2–3), 267–272. https://doi.org/10.1007/s10971-006-8386-7.

(238) Milea, C. A.; Bogatu, C.; Duta, A. The Influence of Parameters in Silica Sol-Gel Process. *Bull. Transilv. Univ. Brasov Ser. I Eng. Sci.* **2011**, *4* (53), 1.

(239) Noritomi, H.; Umezawa, Y.; Miyagawa, S.; Kato, S. Preparation of Highly Concentrated Silver Nanoparticles in Reverse Micelles of Sucrose Fatty Acid Esters through Solid-

Liquid Extraction Method. *Adv. Chem. Eng. Sci.* **2011**, *1* (4), 299–304. https://doi.org/10.4236/aces.2011.14041.

(240) Setua, P.; Ghatak, C.; Rao, V. G.; Das, S. K.; Sarkar, N. Dynamics of Solvation and Rotational Relaxation of Coumarin 480 in Pure Aqueous-AOT Reverse Micelle and Reverse Micelle Containing Different-Sized Silver Nanoparticles inside Its Core: A Comparative Study. *J. Phys. Chem. B* **2012**, *116* (12), 3704–3712. https://doi.org/10.1021/jp203043k.

(241) Zhang, W.; Qiao, X.; And, J. C.-C. and S. A. P.; 2007, U. Synthesis of Nanosilver Colloidal Particles in Water/oil Microemulsion. *Physicochem. Eng. Asp.* **2007**, *299* (1–3), 22–28.

(242) Setua, P.; Pramanik, R.; Sarkar, S.; Seth, D.; Sarkar, N. Direct Observation of Solvation Dynamics in an Aqueous Reverse Micellar System Containing Silver Nanoparticles in the Reverse Micellar Core. *J. Phys. Chem. B* **2009**, *113* (17), 5677–5680. https://doi.org/10.1021/jp810229m.

(243) Egorova, E. M.; Revina, A. A. Synthesis of Metallic Nanoparticles in Reverse Micelles in the Presence of Quercetin. *Colloids Surfaces A Physicochem. Eng. Asp.* **2000**, *168* (1), 87–96. https://doi.org/10.1016/S0927-7757(99)00513-0.

(244) Solanki, J.; Chemistry, Z. M.-I. & E.; 2011, U. Reduction of Nitro Aromatic Compounds over Ag/Al2O3 Nanocatalyst Prepared in Water-in-Oil Microemulsion: Effects of Water-to-Surfactant Mole Ratio and Type of. *Ind. Eng. Chem. Res.* **2011**, *50* (12), 7338–7344.

(245) Piszczek, P.; Radtke, A. Silver Nanoparticles Fabricated Using Chemical Vapor Deposition and Atomic Layer Deposition Techniques: Properties, Applications and Perspectives: Review. In *Noble and Precious Metals - Properties, Nanoscale Effects and Applications*; 2018; pp 187–213. https://doi.org/10.5772/intechopen.71571.

(246) Goswami, S.; Aich, K.; Das, S.; Basu Roy, S.; Pakhira, B.; Sarkar, S. A Reaction Based Colorimetric as Well as Fluorescence "Turn On" Probe for the Rapid Detection of Hydrazine. *RSC Adv.* **2014**, *4* (27), 14210–14214. https://doi.org/10.1039/c3ra46663a.

(247) Mahapatra, A. K.; Karmakar, P.; Manna, S.; Maiti, K.; Mandal, D. Benzthiazole-Derived Chromogenic, Fluorogenic and Ratiometric Probes for Detection of Hydrazine in Environmental Samples and Living Cells. *J. Photochem. Photobiol. A Chem.* **2017**, *334*, 1–12. https://doi.org/10.1016/j.jphotochem.2016.10.032.

(248) Epa, U.; Risk Information System Division, I. *Hydrazine/Hydrazine Sulfate (CASRN 302-01-2) | IRIS | US EPA*.

(249) Epa, U.; Risk Information System Division, I. *N,N-Dimethylformamide (CASRN 68-12-2) | IRIS | US EPA*.

(250) New Jersey Department of Health and Senior Services. *Hazardous Substance Fact Sheet on Sodium Borohydride*; 1999.

(251) Titkov, A. I.; Gerasimov, E. Y.; Shashkov, M. V.; Logutenko, O. A.; Bulina, N. V.; Yukhin, Y. M.; Lyakhov, N. Z. Specific Features of Polyol Synthesis of Silver Nanoparticles with the Use of Solid Carboxylates as Precursors. *Colloid J.* **2016**, *78* (4),

515–524. https://doi.org/10.1134/S1061933X16040189.

(252) Kim, D.; Jeong, S.; Moon, J. Synthesis of Silver Nanoparticles Using the Polyol Process and the Influence of Precursor Injection. *Nanotechnology* **2006**, *17* (16), 4019–4024. https://doi.org/10.1088/0957-4484/17/16/004.

(253) Zhao, T.; Sun, R.; Yu, S.; Zhang, Z.; Zhou, L.; Huang, H.; Du, R. Size-Controlled Preparation of Silver Nanoparticles by a Modified Polyol Method. *Colloids Surfaces A Physicochem. Eng. Asp.* **2010**, *366* (1–3), 197–202. https://doi.org/10.1016/j.colsurfa.2010.06.005.

(254) Chen, C.; Wang, L.; Yu, H.; Jiang, G.; Yang, Q.; Zhou, J.; Xiang, W.; Zhang, J. Study on the Growth Mechanism of Silver Nanorods in the Nanowire-Seeding Polyol Process. *Mater. Chem. Phys.* **2008**, *107* (1), 13–17. https://doi.org/10.1016/j.matchemphys.2007.06.048.

(255) Parveen, K.; Banse, V.; Ledwani, L. Green Synthesis of Nanoparticles: Their Advantages and Disadvantages. In *AIP Conference Proceedings*; 2016; p Vol 1724, 020048. https://doi.org/10.1063/1.4945168.

(256) Sharma, V. K.; Yngard, R. A.; Lin, Y. Silver Nanoparticles: Green Synthesis and Their Antimicrobial Activities. *Adv. Colloid Interface Sci.* **2009**, *145* (1–2), 83–96. https://doi.org/10.1016/j.cis.2008.09.002.

(257) Hussain, I.; Singh, N. B.; Singh, A.; Singh, H.; Singh, S. C. Green Synthesis of Nanoparticles and Its Potential Application. *Biotechnol. Lett.* **2016**, *38* (4), 545–560.

https://doi.org/10.1007/s10529-015-2026-7.

(258) Chen, J.; Wang, J.; Zhang, X.; Jin, Y. Microwave-Assisted Green Synthesis of Silver Nanoparticles by Carboxymethyl Cellulose Sodium and Silver Nitrate. *Mater. Chem. Phys.* **2008**, *108* (2–3), 421–424. https://doi.org/10.1016/j.matchemphys.2007.10.019.

(259) Francis, S.; Joseph, S.; Koshy, E. P.; Mathew, B. Microwave Assisted Green Synthesis of Silver Nanoparticles Using Leaf Extract of Elephantopus Scaber and Its Environmental and Biological Applications. *Artif. Cells, Nanomedicine Biotechnol.* **2018**, *46* (4), 795–804. https://doi.org/10.1080/21691401.2017.1345921.

(260) Long, D.; Wu, G.; Chen, S. Preparation of Oligochitosan Stabilized Silver Nanoparticles by Gamma Irradiation. *Radiat. Phys. Chem.* **2007**, *76* (7), 1126–1131. https://doi.org/10.1016/j.radphyschem.2006.11.001.

(261) Varaprasad, K.; Sadiku, R.; Malegowd Raghavendra, G.; Jayaramudu, T.; Sinha Ray, S.; Mohana Raju, K. Cellulose-Polymer-Ag Nanocomposite Fibers for Antibacterial Fabrics/skin Scaffolds Article in Carbohydrate Polymers · April 2013 CITATIONS 33 READS 357 Cellulose-Polymer-Ag Nanocomposite Fibers for Antibacterial Fabrics/skin Scaffolds. *Carbohydr. Polym.* **2013**, *93* (2), 553–560. https://doi.org/10.1016/j.carbpol.2012.12.035.

(262) Raghavendra, G. M.; Jayaramudu, T.; Varaprasad, K.; Mohan Reddy, G. S.; Raju, K. M. Antibacterial Nanocomposite Hydrogels for Superior Biomedical Applications: A Facile Eco-Friendly Approach. *RSC Adv.* **2015**, *5* (19), 14351–14358. https://doi.org/10.1039/c4ra15995k.

(263) Shivaji, S.; Madhu, S.; Singh, S. Extracellular Synthesis of Antibacterial Silver Nanoparticles Using Psychrophilic Bacteria. *Process Biochem.* **2011**, *46* (9), 1800–1807. https://doi.org/10.1016/j.procbio.2011.06.008.

(264) Sastry, M.; Ahmad, A.; Islam Khan, M.; Kumar, R. Biosynthesis of Metal Nanoparticles Using Fungi and Actinomycete. *Curr. Sci.* **2003**, *85* (2), 162–170.

(265) Dujardin, E.; Peet, C.; Stubbs, G.; Culver, J. N.; Mann, S. Organization of Metallic Nanoparticles Using Tobacco Mosaic Virus Templates. *Nano Lett.* **2003**, *3* (3), 413–417. https://doi.org/10.1021/nl034004o.

(266) Lee, S. Y.; Royston, E.; Culver, J. N.; Harris, M. T. Improved Metal Cluster Deposition on a Genetically Engineered Tobacco Mosaic Virus Template. *Nanotechnology* **2005**, *16* (7), S435–S441. https://doi.org/10.1088/0957-4484/16/7/019.

(267) Thangavelu, R. M.; Ganapathy, R.; Ramasamy, P.; Krishnan, K. Fabrication of Virus Metal Hybrid Nanomaterials: An Ideal Reference for Bio Semiconductor. *Arab. J. Chem.* **2020**, *13* (1), 2750–2765. https://doi.org/10.1016/j.arabjc.2018.07.006.

(268) Sathishkumar, R. S.; Sundaramanickam, A.; Srinath, R.; Ramesh, T.; Saranya, K.; Meena, M.; Surya, P. Green Synthesis of Silver Nanoparticles by Bloom Forming Marine Microalgae Trichodesmium Erythraeum and Its Applications in Antioxidant, Drug-Resistant Bacteria, and Cytotoxicity Activity. *J. Saudi Chem. Soc.* **2019**, *23* (8), 1180–1191. https://doi.org/10.1016/j.jscs.2019.07.008.

(269) Dahoumane, S. A.; Wujcik, E. K.; Jeffryes, C. Noble Metal, Oxide and Chalcogenide-

Based Nanomaterials from Scalable Phototrophic Culture Systems. *Enzyme Microb. Technol.* **2016**, *95*, 13–27. https://doi.org/10.1016/j.enzmictec.2016.06.008.

(270) Naghdi, M.; Taheran, M.; Brar, S. K.; Verma, M.; Surampalli, R. Y.; Valero, J. R. Green and Energy-Efficient Methods for the Production of Metallic Nanoparticles. *Beilstein J. Nanotechnol.* **2015**. https://doi.org/10.3762/bjnano.6.243.

(271) Kalimuthu, K.; Suresh Babu, R.; Venkataraman, D.; Bilal, M.; Gurunathan, S. Biosynthesis of Silver Nanocrystals by Bacillus Licheniformis. *Colloids Surfaces B Biointerfaces* **2008**, *65* (1), 150–153. https://doi.org/10.1016/j.colsurfb.2008.02.018.

(272) Shahverdi, A. R.; Minaeian, S.; Shahverdi, H. R.; Jamalifar, H.; Nohi, A. A. Rapid Synthesis of Silver Nanoparticles Using Culture Supernatants of Enterobacteria: A Novel Biological Approach. *Process Biochem.* **2007**, *42* (5), 919–923. https://doi.org/10.1016/j.procbio.2007.02.005.

(273) Lateef, A.; Adelere, I. A.; Gueguim-Kana, E. B.; Asafa, T. B.; Beukes, L. S. Green Synthesis of Silver Nanoparticles Using Keratinase Obtained from a Strain of Bacillus Safensis LAU 13. *Int. Nano Lett.* **2015**, *5* (1), 29–35. https://doi.org/10.1007/s40089-014-0133-4.

(274) Ahmad, A.; Mukherjee, P.; Senapati, S.; Mandal, D. Extracellular Biosynthesis of Silver Nanoparticles Using the Fungus Fusarium Oxysporum. *Colloids and Surfaces* **2003**, *28* (4), 313–318. https://doi.org/10.1016/S0927-7765(02)00174-1.

(275) Naqvi, S. Z. H.; Kiran, U.; Ali, M. I.; Jamal, A.; Hameed, A.; Ahmed, S.; Ali, N.

Combined Efficacy of Biologically Synthesized Silver Nanoparticles and Different Antibiotics against Multidrug-Resistant Bacteria. *Int. J. Nanomedicine* **2013**, *8*, 3187–3195. https://doi.org/10.2147/IJN.S49284.

(276) Young, M.; Debbie, W.; Uchida, M.; Douglas, T. Plant Viruses as Biotemplates for Materials and Their Use in Nanotechnology. *Annu. Rev. Phytopathol.* **2008**, *46*, 361–384. https://doi.org/10.1146/annurev.phyto.032508.131939.

(277) Adigun, O. O.; Retzlaff-Roberts, E. L.; Novikova, G.; Wang, L.; Kim, B. S.; Ilavsky, J.; Miller, J. T.; Loesch-Fries, L. S.; Harris, M. T. BSMV as a Biotemplate for Palladium Nanomaterial Synthesis. *Langmuir* **2017**. https://doi.org/10.1021/acs.langmuir.6b03341.

(278) Lee, K. Z.; Pussepitiyalage, V. B.; Lee, Y.; Loesch-Fries, S.; Harris, M. T.; Hemmati, S.; Solomon, K. V. Engineering Tobacco Mosaic Virus and Its Virus-Like-Particles for Synthesis of Biotemplated Nanomaterials. *Biotechnol. J.* **2020**. https://doi.org/10.1002/biot.202000311.

(279) da Silva Ferreira, V.; ConzFerreira, M. E.; Lima, L. M. T. R.; Frasés, S.; de Souza, W.; Sant'Anna, C. Green Production of Microalgae-Based Silver Chloride Nanoparticles with Antimicrobial Activity against Pathogenic Bacteria. *Enzyme Microb. Technol.* **2017**, *97*, 114–121. https://doi.org/10.1016/j.enzmictec.2016.10.018.

(280) Monteiro, C. M.; Castro, P. M. L.; Malcata, F. X. Metal Uptake by Microalgae: Underlying Mechanisms and Practical Applications. *Biotechnol. Prog.* **2012**, *28* (2), 299–311. https://doi.org/10.1002/btpr.1504.

(281) Barwal, I.; Ranjan, P.; Kateriya, S.; Yadav, S. C. Cellular Oxido-Reductive Proteins of Chlamydomonas Reinhardtii Control the Biosynthesis of Silver Nanoparticles. *J. Nanobiotechnology* **2011**, *9* (1), 56. https://doi.org/10.1186/1477-3155-9-56.

(282) Jena, J.; Pradhan, N.; Prasad Dash, B.; Behari Sukla, L.; kumar Panda Affiliations, P. Biosynthesis and Characterization of Silver Nanoparticles Using Microalga Chlorococcum Humicola and Its Antibacterial Activity. *Int. J. Nanomater. Biostructures* **2013**, *3* (1), 1–8.

(283) Muthusamy, G.; Thangasamy, S.; Raja, M.; Chinnappan, S.; Kandasamy, S. Biosynthesis of Silver Nanoparticles from Spirulina Microalgae and Its Antibacterial Activity. *Environ. Sci. Pollut. Res.* **2017**, *24* (23), 19459–19464. https://doi.org/10.1007/s11356-017-9772-0.

(284) Galvez, A. M.; Ramos, K. M.; Teja, A. J.; Baculi, R. Bacterial Exopolysaccharide-Mediated Synthesis of Silver Nanoparticles and Their Application on Bacterial Biofilms. *J. Microbiol. Biotechnol. Food Sci.* **2019**, *2019*, 970–978. https://doi.org/10.15414/jmbfs.2019.8.4.970-978.

(285) Muthulakshmi, K.; Uma, C.; Sivagurunathan, P.; Yoganathan, K.; Satheeshkumar, S. Extracellular, Biosynthesis of Silver Nanoparticles Using Enterobacter Cloacae (mk163462) and Their Antibacterial Activity against Certain Multidrug Resistant Pathogens. *J. Pharmacogn. Phytochem.* **2018**, *7* (6), 741–747.

(286) Wang, C.; Kim, Y. J.; Singh, P.; Mathiyalagan, R.; Jin, Y.; Yang, D. C. Green Synthesis of Silver Nanoparticles by Bacillus Methylotrophicus, and Their Antimicrobial Activity. *Artif. Cells, Nanomedicine Biotechnol.* **2016**, *44* (4), 1127–1132. https://doi.org/10.3109/21691401.2015.1011805.

(287) Gurunathan, S.; Kalishwaralal, K.; Vaidyanathan, R.; Venkataraman, D.; Pandian, S. R. K.; Muniyandi, J.; Hariharan, N.; Eom, S. H. Biosynthesis, Purification and Characterization of Silver Nanoparticles Using Escherichia Coli. *Colloids Surfaces B Biointerfaces* **2009**, *74* (1), 328–335. https://doi.org/10.1016/j.colsurfb.2009.07.048.

(288) Nanda, A.; Saravanan, M. Biosynthesis of Silver Nanoparticles from Staphylococcus Aureus and Its Antimicrobial Activity against MRSA and MRSE. *Nanomedicine Nanotechnology, Biol. Med.* **2009**, *5* (4), 452–456. https://doi.org/10.1016/j.nano.2009.01.012.

(289) Husain, S.; Afreen, S.; Hemlata; Yasin, D.; Afzal, B.; Fatma, T. Cyanobacteria as a Bioreactor for Synthesis of Silver Nanoparticles-an Effect of Different Reaction Conditions on the Size of Nanoparticles and Their Dye Decolorization Ability. *J. Microbiol. Methods* **2019**, *162*, 77–82. https://doi.org/10.1016/j.mimet.2019.05.011.

(290) Rolim, W. R.; Pelegrino, M. T.; de Araújo Lima, B.; Ferraz, L. S.; Costa, F. N.; Bernardes, J. S.; Rodigues, T.; Brocchi, M.; Seabra, A. B. Green Tea Extract Mediated Biogenic Synthesis of Silver Nanoparticles: Characterization, Cytotoxicity Evaluation and Antibacterial Activity. *Appl. Surf. Sci.* **2019**, *463*, 66–74. https://doi.org/10.1016/j.apsusc.2018.08.203.

(291) Flores-González, M.; Talavera-Rojas, M.; Soriano-Vargas, E.; Rodríguez-González, V. Practical Mediated-Assembly Synthesis of Silver Nanowires Using Commercial: Camellia Sinensis Extracts and Their Antibacterial Properties. *New J. Chem.* **2018**, *42* (3), 2133–2139. https://doi.org/10.1039/c7nj03812g.

(292) Kumar, B.; Smita, K.; Cumbal, L.; Debut, A. Green Synthesis of Silver Nanoparticles Using Andean Blackberry Fruit Extract. *Saudi J. Biol. Sci.* **2017**, *24* (1), 45–50. https://doi.org/10.1016/j.sjbs.2015.09.006.

(293) Dhand, V.; Soumya, L.; Bharadwaj, S.; Chakra, S.; Bhatt, D.; Sreedhar, B. Green Synthesis of Silver Nanoparticles Using Coffea Arabica Seed Extract and Its Antibacterial Activity. *Mater. Sci. Eng. C* **2016**, *58*, 36–43. https://doi.org/10.1016/j.msec.2015.08.018.

(294) Hu, S.; Hsieh, Y. Lo. Silver Nanoparticle Synthesis Using Lignin as Reducing and Capping Agents: A Kinetic and Mechanistic Study. *Int. J. Biol. Macromol.* **2016**, *82*, 856–862. https://doi.org/10.1016/j.ijbiomac.2015.09.066.

(295) Dong, L. One Pod Synthesis of Single-Crystal Silver Nanowires for Selective Detection of Pb(II). *Micro Nano Lett.* **2019**, *14* (2), 137–141. https://doi.org/10.1049/mnl.2018.5110.

(296) Jeevika, A.; Ravi Shankaran, D. Seed-Free Synthesis of 1D Silver Nanowires Ink Using Clove Oil (Syzygium Aromaticum) at Room Temperature. *J. Colloid Interface Sci.* **2015**, *458*, 155–159. https://doi.org/10.1016/j.jcis.2015.07.045.

(297) Nthunya, L. N.; Derese, S.; Gutierrez, L.; Verliefde, A. R.; Mamba, B. B.; Barnard, T. G.; Mhlanga, S. D. Green Synthesis of Silver Nanoparticles Using One-Pot and Microwave-Assisted Methods and Their Subsequent Embedment on PVDF Nanofibre Membranes for Growth Inhibition of Mesophilic and Thermophilic Bacteria. *New J. Chem.* **2019**, *43* (10), 4168–4180. https://doi.org/10.1039/C8NJ06160B.

(298) Ahmed, S.; Saifullah; Ahmad, M.; Swami, B. L.; Ikram, S. Green Synthesis of Silver

Nanoparticles Using Azadirachta Indica Aqueous Leaf Extract. *J. Radiat. Res. Appl. Sci.* **2016**, *9* (1), 1–7. https://doi.org/10.1016/j.jrras.2015.06.006.

(299) Anjum, S.; Jacob, G.; Gupta, B. Investigation of the Herbal Synthesis of Silver Nanoparticles Using Cinnamon Zeylanicum Extract. *Emergent Mater.* **2019**, *2* (1), 113–122. https://doi.org/10.1007/s42247-019-00023-x.

(300) Ibrahim, H. M. M. Green Synthesis and Characterization of Silver Nanoparticles Using Banana Peel Extract and Their Antimicrobial Activity against Representative Microorganisms. *J. Radiat. Res. Appl. Sci.* **2015**, *8* (3), 265–275. https://doi.org/10.1016/j.jrras.2015.01.007.

(301) Alsammarraie, F. K.; Wang, W.; Zhou, P.; Mustapha, A.; Lin, M. Green Synthesis of Silver Nanoparticles Using Turmeric Extracts and Investigation of Their Antibacterial Activities. *Colloids Surfaces B Biointerfaces* **2018**, *171*, 398–405. https://doi.org/10.1016/j.colsurfb.2018.07.059.

(302) Padalia, H.; Moteriya, P.; Chanda, S. Green Synthesis of Silver Nanoparticles from Marigold Flower and Its Synergistic Antimicrobial Potential. *Arab. J. Chem.* **2015**, *8* (5), 732–741. https://doi.org/10.1016/j.arabjc.2014.11.015.

(303) Kumar, B.; Smita, K.; Cumbal, L.; Debut, A.; Pathak, R. N. Sonochemical Synthesis of Silver Nanoparticles Using Starch: A Comparison. *Bioinorg. Chem. Appl.* **2014**, *2014*, 784268. https://doi.org/10.1155/2014/784268.

(304) El-Refai, A. A.; Ghoniem, G. A.; El-Khateeb, A. Y.; Hassaan, M. M. Eco-Friendly

Synthesis of Metal Nanoparticles Using Ginger and Garlic Extracts as Biocompatible Novel Antioxidant and Antimicrobial Agents. *J. Nanostructure Chem.* **2018**, *8* (1), 71–81. https://doi.org/10.1007/s40097-018-0255-8.

(305) Qin, Y.; Ji, X.; Jing, J.; Liu, H.; Wu, H.; Yang, W. Size Control over Spherical Silver Nanoparticles by Ascorbic Acid Reduction. *Colloids Surfaces A Physicochem. Eng. Asp.* **2010**, *372* (1–3), 172–176. https://doi.org/10.1016/j.colsurfa.2010.10.013.

(306) Han, C.; Nagendra, V.; Baig, R. B. N.; Varma, R. S.; Nadagouda, M. N. Expeditious Synthesis of Noble Metal Nanoparticles Using Vitamin B12 under Microwave Irradiation. *Appl. Sci.* **2015**, *5* (3), 415–426. https://doi.org/10.3390/app5030415.

(307) AbdelRahim, K.; Mahmoud, S. Y.; Ali, A. M.; Almaary, K. S.; Mustafa, A. E. Z. M. A.; Husseiny, S. M. Extracellular Biosynthesis of Silver Nanoparticles Using Rhizopus Stolonifer. *Saudi J. Biol. Sci.* **2017**, *24* (1), 208–216. https://doi.org/10.1016/j.sjbs.2016.02.025.

(308) Amooaghaie, R.; Saeri, M. R.; Azizi, M. Synthesis, Characterization and Biocompatibility of Silver Nanoparticles Synthesized from Nigella Sativa Leaf Extract in Comparison with Chemical Silver Nanoparticles. *Ecotoxicol. Environ. Saf.* **2015**, *120*, 400–408. https://doi.org/10.1016/j.ecoenv.2015.06.025.

(309) Komes, D.; Belščak-Cvitanović, A.; Horžić, D.; Rusak, G.; Likić, S.; Berendika, M. Phenolic Composition and Antioxidant Properties of Some Traditionally Used Medicinal Plants Affected by the Extraction Time and Hydrolysis. *Phytochem. Anal.* **2011**, *22* (2), 172–180. https://doi.org/10.1002/pca.1264.

(310) Rice-evans, C. A.; Miller, N. J.; Bolwell, P. G.; Bramley, P. M.; Pridham, J. B. The Relative Antioxidant Activities of Plant-Derived Polyphenolic Flavonoids. *Free Radic. Res.* **1995**, *22* (4), 375–383. https://doi.org/10.3109/10715769509145649.

(311) Khan, M.; Khan, M.; Adil, S. F.; Tahir, M. N.; Tremel, W.; Alkhathlan, H. Z.; Al-Warthan, A.; Siddiqui, M. R. H. Green Synthesis of Silver Nanoparticles Mediated by Pulicaria Glutinosa Extract. *Int. J. Nanomedicine* **2013**, *8*, 1507–1516. https://doi.org/10.2147/IJN.S43309.

(312) Tangahu, B. V.; Sheikh Abdullah, S. R.; Basri, H.; Idris, M.; Anuar, N.; Mukhlisin, M. A Review on Heavy Metals (As, Pb, and Hg) Uptake by Plants through Phytoremediation. *Int. J. Chem. Eng.* **2011**, *2011*, 939161. https://doi.org/10.1155/2011/939161.

(313) Ali, H.; Khan, E.; Sajad, M. A. Phytoremediation of Heavy Metals-Concepts and Applications. *Chemosphere* **2013**, *91* (7), 869–881. https://doi.org/10.1016/j.chemosphere.2013.01.075.

(314) Callahan, D. L.; Hare, D. J.; Bishop, D. P.; Doble, P. A.; Roessner, U. Elemental Imaging of Leaves from the Metal Hyperaccumulating Plant Noccaea Caerulescens Shows Different Spatial Distribution of Ni, Zn and Cd. *RSC Adv.* **2016**, *6* (3), 2337–2344. https://doi.org/10.1039/c5ra23953b.

(315) De Oliveira, L. M.; Ma, L. Q.; Santos, J. A. G.; Guilherme, L. R. G.; Lessl, J. T. Effects of Arsenate, Chromate, and Sulfate on Arsenic and Chromium Uptake and Translocation by Arsenic Hyperaccumulator Pteris Vittata L. *Environ. Pollut.* **2014**, *184*, 187–192. https://doi.org/10.1016/j.envpol.2013.08.025.

(316) Ma, Y.; Oliveira, R. S.; Nai, F.; Rajkumar, M.; Luo, Y.; Rocha, I.; Freitas, H. The Hyperaccumulator Sedum Plumbizincicola Harbors Metal-Resistant Endophytic Bacteria That Improve Its Phytoextraction Capacity in Multi-Metal Contaminated Soil. *J. Environ. Manage.* **2015**, *156*, 62–69. https://doi.org/10.1016/j.jenvman.2015.03.024.

(317) Antoniadis, V.; Levizou, E.; Shaheen, S. M.; Ok, Y. S.; Sebastian, A.; Baum, C.; Prasad, M. N. V.; Wenzel, W. W.; Rinklebe, J. Trace Elements in the Soil-Plant Interface: Phytoavailability, Translocation, and phytoremediation–A Review. *Earth-Science Rev.* **2017**, *171*, 621–645. https://doi.org/10.1016/j.earscirev.2017.06.005.

(318) Gardea-Torresdey, J. L.; Gomez, E.; Peralta-Videa, J. R.; Parsons, J. G.; Troiani, H.; Jose-Yacaman, M. Alfalfa Sprouts: A Natural Source for the Synthesis of Silver Nanoparticles. *Langmuir* **2003**, *19* (4), 1357–1361. https://doi.org/10.1021/la020835i.

(319) Marchiol, L. Synthesis of Metal Nanoparticles in Living Plants. *Ital. J. Agron.* **2012**, *7* (e37), 274–282. https://doi.org/10.4081/ija.2012.e37.

(320) Haverkamp, R. G.; Marshall, A. T.; Van Agterveld, D. Pick Your Carats: Nanoparticles of Gold-Silver-Copper Alloy Produced in Vivo. *J. Nanoparticle Res.* **2007**, *9* (4), 697–700. https://doi.org/10.1007/s11051-006-9198-y.

(321) Harris, A. T.; Bali, R. On the Formation and Extent of Uptake of Silver Nanoparticles by Live Plants. *J. Nanoparticle Res.* **2008**, *10* (4), 691–695. https://doi.org/10.1007/s11051-007-9288-5.

(322) Haverkamp, R. G.; Marshall, A. T. The Mechanism of Metal Nanoparticle Formation in

Plants: Limits on Accumulation. *J. Nanoparticle Res.* **2009**, *11* (6), 1453–1463. https://doi.org/10.1007/s11051-008-9533-6.

(323) Beattie, I. R.; Haverkamp, R. G. Silver and Gold Nanoparticles in Plants: Sites for the Reduction to Metal. *Metallomics* **2011**, *3* (6), 628–632. https://doi.org/10.1039/c1mt00044f.

(324) Park, Y.; Hong, Y. N.; Weyers, A.; Kim, Y. S.; Linhardt, R. J. Polysaccharides and Phytochemicals: A Natural Reservoir for the Green Synthesis of Gold and Silver Nanoparticles. *IET Nanobiotechnology* **2011**, *5* (3), 69–78. https://doi.org/10.1049/iet-nbt.2010.0033.

(325) Ratan, Z. A.; Haidere, M. F.; Nurunnabi, M.; Shahriar, S. M.; Ahammad, A. J. S.; Shim, Y. Y.; Reaney, M. J. T.; Cho, J. Y. Green Chemistry Synthesis of Silver Nanoparticles and Their Potential Anticancer Effects. *Cancers (Basel).* **2020**, *12*, 855. https://doi.org/10.3390/cancers12040855.

(326) Makarov, V. V.; Love, A. J.; Sinitsyna, O. V.; Makarova, S. S.; Yaminsky, I. V.; Taliansky, M. E.; Kalinina, N. O. "Green" nanotechnologies: Synthesis of Metal Nanoparticles Using Plants. *Acta Naturae* **2014**, *6*, 35–44. https://doi.org/10.32607/20758251-2014-6-1-35-44.

(327) Mukunthan, K. S.; Balaji, S. Cashew Apple Juice (Anacardium Occidentale L.) Speeds up the Synthesis of Silver Nanoparticles. *Int. J. Green Nanotechnol. Biomed.* **2012**, *4* (2), 71–79. https://doi.org/10.1080/19430892.2012.676900.

(328) Antonysamy Johnson, M. A.; Shibila, T.; Amutha, S.; Menezes, I. R. A.; da Costa, J. G. M.; Sampaio, N. F. L.; Coutinho, H. D. M. Synthesis of Silver Nanoparticles Using Odontosoria Chinensis (L.) J. Sm. and Evaluation of Their Biological Potentials. *Pharmaceuticals* **2020**, *13*, 66. https://doi.org/10.3390/ph13040066.

(329) Sivakumar, M.; Surendar, S.; Jayakumar, M.; Seedevi, P.; Sivasankar, P.; Ravikumar, M.; Anbazhagan, M.; Murugan, T.; Siddiqui, S. S.; Loganathan, S. Parthenium Hysterophorus Mediated Synthesis of Silver Nanoparticles and Its Evaluation of Antibacterial and Antineoplastic Activity to Combat Liver Cancer Cells. *J. Clust. Sci.* **2020**, 1–11. https://doi.org/10.1007/s10876-020-01775-x.

(330) Nouri, A.; Tavakkoli Yaraki, M.; Lajevardi, A.; Rezaei, Z.; Ghorbanpour, M.; Tanzifi, M. Ultrasonic-Assisted Green Synthesis of Silver Nanoparticles Using Mentha Aquatica Leaf Extract for Enhanced Antibacterial Properties and Catalytic Activity. *Colloids Interface Sci. Commun.* **2020**, *35*, 100252. https://doi.org/10.1016/j.colcom.2020.100252.

(331) Tanase, C.; Berta, L.; Mare, A.; Man, A.; Talmaciu, A. I.; Roșca, I.; Mircia, E.; Volf, I.; Popa, V. I. Biosynthesis of Silver Nanoparticles Using Aqueous Bark Extract of Picea Abies L. and Their Antibacterial Activity. *Eur. J. Wood Wood Prod.* **2020**, *78* (2), 281–291. https://doi.org/10.1007/s00107-020-01502-3.

(332) Mohaghegh, S.; Osouli-Bostanabad, K.; Nazemiyeh, H.; Javadzadeh, Y.; Parvizpur, A.; Barzegar-Jalali, M.; Adibkia, K. A Comparative Study of Eco-Friendly Silver Nanoparticles Synthesis Using Prunus Domestica Plum Extract and Sodium Citrate as Reducing Agents. *Adv. Powder Technol.* **2020**, *31* (3), 1169–1180. https://doi.org/10.1016/j.apt.2019.12.039.

(333) Ranoszek-Soliwoda, K.; Tomaszewska, E.; Socha, E.; Krzyczmonik, P.; Ignaczak, A.; Orlowski, P.; Krzyzowska, M.; Celichowski, G.; Grobelny, J. The Role of Tannic Acid and Sodium Citrate in the Synthesis of Silver Nanoparticles. *J. Nanoparticle Res.* **2017**, *19* (8), 273. https://doi.org/10.1007/s11051-017-3973-9.

(334) Phongtongpasuk, S.; Norasingsatorn, T.; Yongvanich, N. Effect of Ph on the Environmentally Friendly Fabrication of Silver Nanoparticles Using Rambutan Peel Extract. *Key Eng. Mater.* **2019**, *824*, 149–155. https://doi.org/10.4028/www.scientific.net/KEM.824.149.

(335) Singh, A.; Gaud, B.; Jaybhaye, S. Optimization of Synthesis Parameters of Silver Nanoparticles and Its Antimicrobial Activity. *Mater. Sci. Energy Technol.* **2020**, *3*, 232–236. https://doi.org/10.1016/j.mset.2019.08.004.

(336) Handayani, W.; Ningrum, A. S.; Imawan, C. The Role of pH in Synthesis Silver Nanoparticles Using Pometia Pinnata (Matoa) Leaves Extract as Bioreductor. *J. Phys* **2020**, *1428*, 12021. https://doi.org/10.1088/1742-6596/1428/1/012021.

(337) Dada, A. O.; Adekola, F. A.; Adeyemi, O. S.; Bello, O. M.; Oluwaseun, A. C.; Awakan, O. J.; Grace, F.-A. A. Exploring the Effect of Operational Factors and Characterization Imperative to the Synthesis of Silver Nanoparticles. In *Silver Nanoparticles - Fabrication, Characterization and Applications*; 2018; pp 165–184. https://doi.org/10.5772/intechopen.76947.

(338) Ghodake, G. S.; Deshpande, N. G.; Lee, Y. P.; Jin, E. S. Pear Fruit Extract-Assisted Room-Temperature Biosynthesis of Gold Nanoplates. *Colloids Surfaces B Biointerfaces*

2010, *75* (2), 584–589. https://doi.org/10.1016/j.colsurfb.2009.09.040.

(339) Raut, R. W.; Mendhulkar, V. D.; Kashid, S. B. Photosensitized Synthesis of Silver Nanoparticles Using Withania Somnifera Leaf Powder and Silver Nitrate. *J. Photochem. Photobiol. B Biol.* **2014**, *132*, 45–55. https://doi.org/10.1016/j.jphotobiol.2014.02.001.

(340) Kanipandian, N.; Thirumurugan, R. A Feasible Approach to Phyto-Mediated Synthesis of Silver Nanoparticles Using Industrial Crop Gossypium Hirsutum (Cotton) Extract as Stabilizing Agent and Assessment of Its in Vitro Biomedical Potential. *Ind. Crops Prod.* **2014**, *55*, 1–10. https://doi.org/10.1016/j.indcrop.2014.01.042.

(341) Singh, M.; Sinha, I.; Mandal, R. K. Role of pH in the Green Synthesis of Silver Nanoparticles. *Mater. Lett.* **2009**, *63* (3–4), 425–427. https://doi.org/10.1016/j.matlet.2008.10.067.

(342) Madivoli, E. S.; Kareru, P. G.; Gachanja, A. N.; Mugo, S. M.; Makhanu, D. S.; Wanakai, S. I.; Gavamukulya, Y. Facile Synthesis of Silver Nanoparticles Using Lantana Trifolia Aqueous Extracts and Their Antibacterial Activity. *J. Inorg. Organomet. Polym. Mater.* **2020**, *30*, 2842–2850. https://doi.org/10.1007/s10904-019-01432-5.

(343) Anbu, P.; Gopinath, S. C. B.; Yun, H. S.; Lee, C. G. Temperature-Dependent Green Biosynthesis and Characterization of Silver Nanoparticles Using Balloon Flower Plants and Their Antibacterial Potential. *J. Mol. Struct.* **2019**, *1177*, 302–309. https://doi.org/10.1016/j.molstruc.2018.09.075.

(344) Sun, Q.; Cai, X.; Li, J.; Zheng, M.; Chen, Z.; Yu, C. P. Green Synthesis of Silver

Nanoparticles Using Tea Leaf Extract and Evaluation of Their Stability and Antibacterial Activity. *Colloids Surfaces A Physicochem. Eng. Asp.* **2014**, *444*, 226–231. https://doi.org/10.1016/j.colsurfa.2013.12.065.

(345) Cruz, D.; Falé, P. L.; Mourato, A.; Vaz, P. D.; Luisa Serralheiro, M.; Lino, A. R. L. Preparation and Physicochemical Characterization of Ag Nanoparticles Biosynthesized by Lippia Citriodora (Lemon Verbena). *Colloids Surfaces B Biointerfaces* **2010**, *81* (1), 67–73. https://doi.org/10.1016/j.colsurfb.2010.06.025.

(346) Jiang, X. C.; Chen, W. M.; Chen, C. Y.; Xiong, S. X.; Yu, A. B. Role of Temperature in the Growth of Silver Nanoparticles Through a Synergetic Reduction Approach. *Nanoscale Res. Lett.* **2011**, *6* (1), 32. https://doi.org/10.1007/s11671-010-9780-1.

(347) Liu, H.; Zhang, H.; Wang, J.; Wei, J. Effect of Temperature on the Size of Biosynthesized Silver Nanoparticle: Deep Insight into Microscopic Kinetics Analysis. *Arab. J. Chem.* **2020**, *13* (1), 1011–1019. https://doi.org/10.1016/j.arabjc.2017.09.004.

(348) Hasnain, M. S.; Javed, M. N.; Alam, M. S.; Rishishwar, P.; Rishishwar, S.; Ali, S.; Nayak, A. K.; Beg, S. Purple Heart Plant Leaves Extract-Mediated Silver Nanoparticle Synthesis: Optimization by Box-Behnken Design. *Mater. Sci. Eng. C* **2019**, *99*, 1105–1114. https://doi.org/10.1016/j.msec.2019.02.061.

(349) Htwe, Y. Z. N.; Chow, W. S.; Suda, Y.; Mariatti, M. Effect of Silver Nitrate Concentration on the Production of Silver Nanoparticles by Green Method. *Mater. Today Proc.* **2019**, *17* (3), 568–573. https://doi.org/10.1016/j.matpr.2019.06.336.

(350) Khan, S.; Singh, S.; Gaikwad, S.; Nawani, N.; Junnarkar, M.; Pawar, S. V. Optimization of Process Parameters for the Synthesis of Silver Nanoparticles from Piper Betle Leaf Aqueous Extract, and Evaluation of Their Antiphytofungal Activity. *Environ. Sci. Pollut. Res.* **2019**, *27*, 27221–27233. https://doi.org/10.1007/s11356-019-05239-2.

(351) Parashar, V.; Parashar, R.; Sharma, B.; Pandey, A. C. Parthenium Leaf Extract Mediated Synthesis of Silver Nanoparticles: A Novel Approach towards Weed Utilization. *Dig. J. Nanomater. Biostructures* **2009**, *4* (1), 45–50.

(352) Kowalska, D.; Krajnik, B.; Olejnik, M.; Twardowska, M.; Czechowski, N.; Hofmann, E.; MacKowski, S. Metal-Enhanced Fluorescence of Chlorophylls in Light-Harvesting Complexes Coupled to Silver Nanowires. *Sci. World J.* **2013**, *2013*, 670412. https://doi.org/10.1155/2013/670412.

(353) Ćwik, M.; Buczyńska, D.; Sulowska, K.; Roźniecka, E.; Mackowski, S.; Niedziółka-Jönsson, J. Optical Properties of Submillimeter Silver Nanowires Synthesized Using the Hydrothermal Method. *Materials (Basel).* **2019**, *12* (5), 721. https://doi.org/10.3390/ma12050721.

(354) Kim, S.; Yun, T. G.; Kang, C.; Son, M. J.; Kang, J. G.; Kim, I. H.; Lee, H. J.; An, C. H.; Hwang, B. Facile Fabrication of Paper-Based Silver Nanostructure Electrodes for Flexible Printed Energy Storage System. *Mater. Des.* **2018**, *151*, 1–7. https://doi.org/10.1016/j.matdes.2018.04.047.

(355) Yu, C. H.; Chi, H. H.; Hsiao, C. C. 42.3: *Invited Paper:* Silver Nanowire for Next Generation Touch Solution. *SID Symp. Dig. Tech. Pap.* **2019**, *50* (S1), 476–478.

https://doi.org/10.1002/sdtp.13533.

(356) Dai, H.; Spaid, M. 31-2: *Invited Paper:* Silver Nanowire Transparent Conductive Films for Flexible/Foldable Devices. *SID Symp. Dig. Tech. Pap.* **2018**, *49* (1), 397–400. https://doi.org/10.1002/sdtp.12583.

(357) Yi, P.; Zhu, Y.; Deng, Y. Fabrication and Applications of Flexible Transparent Electrodes Based on Silver Nanowires. *Flex. Electron.* **2018**. https://doi.org/10.5772/intechopen.77506.

(358) Zhu, Y.; Deng, Y.; Yi, P.; Peng, L.; Lai, X.; Lin, Z. Flexible Transparent Electrodes Based on Silver Nanowires: Material Synthesis, Fabrication, Performance, and Applications. *Adv. Mater. Technol.* **2019**, *4* (10), 1900413. https://doi.org/10.1002/admt.201900413.

(359) Li, B.; Ye, S.; Stewart, I. E.; Alvarez, S.; Wiley, B. J. Synthesis and Purification of Silver Nanowires to Make Conducting Films with a Transmittance of 99%. *Nano Lett.* **2015**, *15* (10), 6722–6726. https://doi.org/10.1021/acs.nanolett.5b02582.

(360) Du, Y.; Shi, L.; He, T.; Sun, X.; Mo, Y. SERS Enhancement Dependence on the Diameter and Aspect Ratio of Silver-Nanowire Array Fabricated by Anodic Aluminium Oxide Template. *Appl. Surf. Sci.* **2008**, *255* (5), 1901–1905. https://doi.org/10.1016/j.apsusc.2008.06.140.

(361) Bergin, S. M.; Chen, Y. H.; Rathmell, A. R.; Charbonneau, P.; Li, Z. Y.; Wiley, B. J. The Effect of Nanowire Length and Diameter on the Properties of Transparent, Conducting Nanowire Films. *Nanoscale* **2012**. https://doi.org/10.1039/c2nr30126a.

(362) Hemmati, S.; Barkey, D. P.; Gupta, N. Rheological Behavior of Silver Nanowire Conductive Inks during Screen Printing. *J. Nanoparticle Res.* **2016**, *18* (8), 249. https://doi.org/10.1007/s11051-016-3561-4.

(363) Govindaraj, A.; Satishkumar, B. C.; Nath, M.; Rao, C. N. R. Metal Nanowires and Intercalated Metal Layers in Single-Walled Carbon Nanotube Bundles. *Chem. Mater.* **2000**, *12*, 202–205. https://doi.org/10.1021/cm990546o.

(364) Zhang, D.; Qi, L.; Ma, J.; Cheng, H. Formation of Silver Nanowires in Aqueous Solutions of a Double-Hydrophilic Block Copolymer. *Chem. Mater.* **2001**, *13* (9), 2753–2755. https://doi.org/10.1021/cm0105007.

(365) Junaidi; Yunus, M.; Harsojo; Suharyadi, E.; Triyana, K. Effect of Stirring Rate on the Synthesis Silver Nanowires Using Polyvinyl Alcohol as a Capping Agent by Polyol Process. *Int. J. Adv. Sci. Eng. Inf. Technol.* **2016**, *6* (3), 365–369. https://doi.org/10.18517/ijaseit.6.3.808.

(366) Fahad, S.; Yu, H.; Wang, L.; Zain-ul-Abdin; Haroon, M.; Ullah, R. S.; Nazir, A.; Naveed, K. ur R.; Elshaarani, T.; Khan, A. Recent Progress in the Synthesis of Silver Nanowires and Their Role as Conducting Materials. *J. Mater. Sci.* **2019**, *54* (2), 997–1035. https://doi.org/10.1007/s10853-018-2994-9.

(367) Sun, Y.; Gates, B.; Mayers, B.; Xia, Y. Crystalline Silver Nanowires by Soft Solution Processing. *Nano Lett.* **2002**, *2* (2), 165–168. https://doi.org/10.1021/nl010093y.

(368) Sun, Y.; Xia, Y. Large-Scale Synthesis of Uniform Silver Nanowires through a Soft, Self-

Seeding, Polyol Process. *Adv. Mater.* **2002**, *14* (11), 833–837. https://doi.org/10.1002/1521-4095(20020605)14:11<833::AID-ADMA833>3.0.CO;2-K.

(369) Wiley, B.; Sun, Y.; Xia, Y. Polyol Synthesis of Silver Nanostructures: Control of Product Morphology with Fe(II) or Fe(III) Species. *Langmuir* **2005**, *21* (18), 8077–8080. https://doi.org/10.1021/la050887i.

(370) Korte, K. E.; Skrabalak, S. E.; Xia, Y. Rapid Synthesis of Silver Nanowires through a CuCl- or CuCl2-Mediated Polyol Process. *J. Mater. Chem.* **2008**, *18* (4), 437–441. https://doi.org/10.1039/b714072j.

(371) Hemmati, S.; Harris, M. T.; Barkey, D. P. Polyol Silver Nanowire Synthesis and the Outlook for a Green Process. *J. Nanomater.* **2020**, *2020*, 9341983. https://doi.org/10.1155/2020/9341983.

(372) Tian, X.; Li, J.; Pan, S. Facile Synthesis of Single-Crystal Silver Nanowires through a Tannin-Reduction Process. *J. Nanoparticle Res.* **2009**, *11* (7), 1839. https://doi.org/10.1007/s11051-009-9700-4.

(373) Barnaby, S. N.; Yu, S. M.; Fath, K. R.; Tsiola, A.; Khalpari, O.; Banerjee, I. A. Ellagic Acid Promoted Biomimetic Synthesis of Shape-Controlled Silver Nanochains. *Nanotechnology* **2011**. https://doi.org/10.1088/0957-4484/22/22/225605.

(374) Lin, L.; Wang, W.; Huang, J.; Li, Q.; Sun, D.; Yang, X.; Wang, H.; He, N.; Wang, Y. Nature Factory of Silver Nanowires: Plant-Mediated Synthesis Using Broth of Cassia Fistula Leaf. *Chem. Eng. J.* **2010**, *162* (2), 852–858.

https://doi.org/10.1016/j.cej.2010.06.023.

(375) Soleimani, F. F.; Saleh, T.; Shojaosadati, S. A.; Poursalehi, R. Green Synthesis of Different Shapes of Silver Nanostructures and Evaluation of Their Antibacterial and Cytotoxic Activity. *Bionanoscience* **2018**, *8* (1), 72–80. https://doi.org/10.1007/s12668-017-0423-1.

(376) Peng, H. C.; Park, J.; Zhang, L.; Xia, Y. Toward a Quantitative Understanding of Symmetry Reduction Involved in the Seed-Mediated Growth of Pd Nanocrystals. *J. Am. Chem. Soc.* **2015**. https://doi.org/10.1021/jacs.5b03040.

(377) Huo, D.; Kim, M. J.; Lyu, Z.; Shi, Y.; Wiley, B. J.; Xia, Y. One-Dimensional Metal Nanostructures: From Colloidal Syntheses to Applications. *Chemical Reviews*. 2019. https://doi.org/10.1021/acs.chemrev.8b00745.

(378) Bulut, E.; Özacar, M. Rapid, Facile Synthesis of Silver Nanostructure Using Hydrolyzable Tannin. *Ind. Eng. Chem. Res.* **2009**. https://doi.org/10.1021/ie801779f.

(379) Yi, Z.; Li, X.; Xu, X.; Luo, B.; Luo, J.; Wu, W.; Yi, Y.; Tang, Y. Green, Effective Chemical Route for the Synthesis of Silver Nanoplates in Tannic Acid Aqueous Solution. *Colloids Surfaces A Physicochem. Eng. Asp.* **2011**, *392* (1), 131–136. https://doi.org/10.1016/j.colsurfa.2011.09.045.

(380) Tian, X.; Wang, W.; Cao, G. A Facile Aqueous-Phase Route for the Synthesis of Silver Nanoplates. *Mater. Lett.* **2007**. https://doi.org/10.1016/j.matlet.2006.04.021.

(381) Cruz, B. H.; Díaz-Cruz, J. M.; Ariño, C.; Esteban, M. Heavy Metal Binding by Tannic Acid: A Voltammetric Study. *Electroanalysis* **2000**. https://doi.org/10.1002/1521-4109(200010)12:14<1130::AID-ELAN1130>3.0.CO;2-7.

(382) Ahmad, T. Reviewing the Tannic Acid Mediated Synthesis of Metal Nanoparticles. *Journal of Nanotechnology*. 2014. https://doi.org/10.1155/2014/954206.

(383) Martínez-Castañón, G. A.; Niño-Martínez, N.; Martínez-Gutierrez, F.; Martínez-Mendoza, J. R.; Ruiz, F. Synthesis and Antibacterial Activity of Silver Nanoparticles with Different Sizes. *J. Nanoparticle Res.* **2008**. https://doi.org/10.1007/s11051-008-9428-6.

(384) Liu, J.; Qin, G.; Raveendran, P.; Ikushima, Y. Facile "Green" Synthesis, Characterization, and Catalytic Function of β-D-Glucose-Stabilized Au Nanocrystals. *Chem. - A Eur. J.* **2007**. https://doi.org/10.1002/chem.200790050.

(385) Schuette, W. M.; Buhro, W. E. Polyol Synthesis of Silver Nanowires by Heterogeneous Nucleation; Mechanistic Aspects Influencing Nanowire Diameter and Length. *Chem. Mater.* **2014**, *26*, 6410–6417. https://doi.org/10.1021/cm502827b.

(386) Villalpando, M.; Saavedra-Molina, A.; Rosas, G. A Facile Synthesis of Silver Nanowires and Their Evaluation in the Mitochondrial Membrane Potential. *Mater. Sci. Eng. C* **2020**, *114*, 110973. https://doi.org/10.1016/j.msec.2020.110973.

(387) Tiwari, P.; Joshi, A.; Dubey, B. . Phytochemical Screening and Thin Layer Chromatographic Studies of Annona Squamosa (Seeds), Azadirachta Indica (Leaves) and Lavandula Angustifolia (Flower) Aqueous Extract. *Asian J. Pharm. Educ. Res.* **2017**, *6*

(2), 45–53.

(388) Chen, J.; Herricks, T.; Geissler, M.; Xia, Y. Single-Crystal Nanowires of Platinum Can Be Synthesized by Controlling the Reaction Rate of a Polyol Process. *J. Am. Chem. Soc.* **2004**, *126* (35), 10854–10855. https://doi.org/10.1021/ja0468224.

(389) You, H.; Fang, J. Particle-Mediated Nucleation and Growth of Solution-Synthesized Metal Nanocrystals: A New Story beyond the LaMer Curve. *Nano Today* **2016**, *11* (2), 145–167. https://doi.org/10.1016/j.nantod.2016.04.003.

(390) Jang, H. W.; Hwang, B. Y.; Lee, K. W.; Kim, Y. M.; Kim, J. Y. Controlling the Size of Silver Nanowires Produced by a Tetrabutylammonium Dichlorobromide Salt-Based Polyol Process: Kinetics of Silver Crystal Growth. *AIP Adv.* **2018**, *8*, 25303. https://doi.org/10.1063/1.5011263.

(391) Dong, B.; Hadinoto, K. Direct Comparison between Millifluidic and Bulk-Mixing Platform in the Synthesis of Amorphous Drug-Polysaccharide Nanoparticle Complex. *Int. J. Pharm.* **2017**, *523* (1), 42–51. https://doi.org/10.1016/j.ijpharm.2017.03.021.

(392) Meshram, S. M.; Bonde, S. R.; Gupta, I. R.; Gade, A. K.; Rai, M. K. Green Synthesis of Silver Nanoparticles Using White Sugar. *IET Nanobiotechnology* **2013**, *7* (1), 28–32. https://doi.org/10.1049/iet-nbt.2012.0002.

(393) Nadagouda, M. N.; Varma, R. S. Green Synthesis of Ag and Pd Nanospheres, Nanowires, and Nanorods Using Vitamin B2: Catalytic Polymerisation of Aniline and Pyrrole. *J. Nanomater.* **2008**, *2008*, 782358. https://doi.org/10.1155/2008/782358.

(394) Moulton, M. C.; Braydich-Stolle, L. K.; Nadagouda, M. N.; Kunzelman, S.; Hussain, S. M.; Varma, R. S. Synthesis, Characterization and Biocompatibility Of “green” synthesized Silver Nanoparticles Using Tea Polyphenols. *Nanoscale* **2010**. https://doi.org/10.1039/c0nr00046a.

(395) Aswathy Aromal, S.; Philip, D. Facile One-Pot Synthesis of Gold Nanoparticles Using Tannic Acid and Its Application in Catalysis. *Phys. E Low-Dimensional Syst. Nanostructures* **2012**. https://doi.org/10.1016/j.physe.2012.04.022.

(396) Shakibaie, M.; Forootanfar, H.; Mollazadeh-Moghaddam, K.; Bagherzadeh, Z.; Nafissi-Varcheh, N.; Shahverdi, A. R.; Faramarzi, M. A. Green Synthesis of Gold Nanoparticles by the Marine Microalga Tetraselmis Suecica . *Biotechnol. Appl. Biochem.* **2010**. https://doi.org/10.1042/ba20100196.

(397) Hagerman, A. E.; Riedl, K. M.; Jones, G. A.; Sovik, K. N.; Ritchard, N. T.; Hartzfeld, P. W.; Riechel, T. L. High Molecular Weight Plant Polyphenolics (Tannins) as Biological Antioxidants. *J. Agric. Food Chem.* **1998**. https://doi.org/10.1021/jf970975b.

(398) Ashok, P.; Upadhyaya, K. Tannins Are Astringent. *J. Pharmacogn. Phytochem.* **2012**. https://doi.org/10.11648/j.ijnfs.20140304.18.

(399) Sivaraman, S. K.; Elango, I.; Kumar, S.; Santhanam, V. A Green Protocol for Room Temperature Synthesis of Silver Nanoparticles in Seconds. *Curr. Sci.* **2009**.

(400) McDonald, M.; Mila, I.; Scalbert, A. Precipitation of Metal Ions by Plant Polyphenols: Optimal Conditions and Origin of Precipitation. *J. Agric. Food Chem.* **1996**.

https://doi.org/10.1021/jf950459q.

(401) Chen, S.; Drehmel, J. R.; Penn, R. L. Facile Synthesis of Monodispersed Ag NPs in Ethylene Glycol Using Mixed Capping Agents. *ACS Omega* **2020**. https://doi.org/10.1021/acsomega.9b04492.

(402) Rainville, L.; Dorais, M. C.; Boudreau, D. Controlled Synthesis of Low Polydispersity Ag@SiO2 Core-Shell Nanoparticles for Use in Plasmonic Applications. *RSC Adv.* **2013**. https://doi.org/10.1039/c3ra41677a.

(403) Călinescu, I.; Pătraşcu, M.; Gavrilă, A. I.; Trifan, A.; Boscornea, C. Synthesis and Characterisation of Silver Nanoparticles in the Presence of PVA and Tannic Acid. *UPB Sci. Bull. Ser. B Chem. Mater. Sci.* **2011**.

(404) Alshammari, A.; Köckritz, A.; Narayana Kalevaru, V.; Bagabas, A.; Martin, A. Influence of Single Use and Combination of Reductants on the Size, Morphology and Growth Steps of Gold Nanoparticles in Colloidal Mixture. *Open J. Phys. Chem.* **2012**. https://doi.org/10.4236/ojpc.2012.24033.

(405) Mahl, D.; Diendorf, J.; Ristig, S.; Greulich, C.; Li, Z. A.; Farle, M.; Köller, M.; Epple, M. Silver, Gold, and Alloyed Silver-Gold Nanoparticles: Characterization and Comparative Cell-Biologic Action. *J. Nanoparticle Res.* **2012**. https://doi.org/10.1007/s11051-012-1153-5.

(406) Hao, Y.; Zhang, N.; Luo, J.; Liu, X. Green Synthesis of Silver Nanoparticles by Tannic Acid with Improved Catalytic Performance Towards the Reduction of Methylene Blue.

Nano **2018**. https://doi.org/10.1142/S1793292018500030.

(407) El-Ghamry, M. T.; Frei, R. W. Spectrophotometric Determination of Trace Amounts of Silver(I). *Anal. Chem.* **1968**, *40* (13), 1986–1990. https://doi.org/10.1021/ac60269a034.

(408) Sakamoto, M.; Fujistuka, M.; Majima, T. Light as a Construction Tool of Metal Nanoparticles: Synthesis and Mechanism. *Journal of Photochemistry and Photobiology C: Photochemistry Reviews*. 2009, pp 33–56. https://doi.org/10.1016/j.jphotochemrev.2008.11.002.

(409) Hada, H.; Yonezawa, Y.; Yoshida, A.; Kurakake, A. Photoreduction of Silver Ion in Aqueous and Alcoholic Solutions. *J. Phys. Chem.* **1976**, *80* (25), 2728–2731. https://doi.org/10.1021/j100566a003.

(410) Yonezawa, Y.; Sato, T.; Ohno, M.; Hada, H. Photochemical Formation of Colloidal Metals. *J. Chem. Soc. Faraday Trans. 1 Phys. Chem. Condens. Phases* **1987**, *83* (5), 1559–1567. https://doi.org/10.1039/F19878301559.

(411) Condorelli, G. G.; Costanzo, L. L.; Fragalà, I. L.; Giuffrida, S.; Ventimiglia, G. A Single Photochemical Route for the Formation of Both Copper Nanoparticles and Patterned Nanostructured Films. *J. Mater. Chem.* **2003**, *13* (10), 2409–2411. https://doi.org/10.1039/b308418c.

(412) Giuffrida, S.; Condorelli, G. G.; Costanzo, L. L.; Fragalà, I. L.; Ventimiglia, G.; Vecchio, G. Photochemical Mechanism of the Formation of Nanometer-Sized Copper by UV Irradiation of Ethanol Bis(2,4-pentandionato)copper(II) Solutions. *Chem. Mater.* **2004**, *16*

(7), 1260–1266. https://doi.org/10.1021/cm034782h.

(413) Judai, K.; Nishijo, J.; Okabe, C.; Ohishi, O.; Sawa, H.; Nishi, N. Carbon-Skinned Metallic Wires and Magnetic Nanocrystals Prepared from Metal Acetylides. In *Synthetic Metals*; 2005; Vol. 155, pp 352–356. https://doi.org/10.1016/j.synthmet.2005.09.012.

(414) Nishijo, J.; Okabe, C.; Bushiri, J.; Kosugi, K.; Nishi, N.; Sawa, H. Formation of Carbon-Encapsulated Metallic Nano-Particles from Metal Acetylides by Electron Beam Irradiation. *Eur. Phys. J. D* **2005**, *34* (1–3), 219–222. https://doi.org/10.1140/epjd/e2005-00146-1.

(415) Kapoor, S.; Mukherjee, T. Photochemical Formation of Copper Nanoparticles in poly(N-Vinylpyrrolidone). *Chem. Phys. Lett.* **2003**, *370* (1–2), 83–87. https://doi.org/10.1016/S0009-2614(03)00073-3.

(416) Scaiano, J. C.; Aliaga, C.; Maguire, S.; Wang, D. Magnetic Field Control of Photoinduced Silver Nanoparticle Formation. *J. Phys. Chem. B* **2006**, *110* (26), 12856–12859. https://doi.org/10.1021/jp061723t.

(417) Wood, A.; Giersig, M.; Mulvaney, P. Fermi Level Equilibration in Quantum Dot-Metal Nanojunctions. *J. Phys. Chem. B* **2001**, *105* (37), 8810–8815. https://doi.org/10.1021/jp011576t.

(418) Kamat, P. V. Photophysical, Photochemical and Photocatalytic Aspects of Metal Nanoparticles. *J. Phys. Chem. B* **2002**, *106* (32), 7729–7744. https://doi.org/10.1021/jp0209289.

(419) Saleh, R.; Djaja, N. F. Transition-Metal-Doped ZnO Nanoparticles: Synthesis, Characterization and Photocatalytic Activity under UV Light. *Spectrochim. Acta - Part A Mol. Biomol. Spectrosc.* **2014**, *130*, 581–590. https://doi.org/10.1016/j.saa.2014.03.089.

(420) Srikar, S. K.; Giri, D. D.; Pal, D. B.; Mishra, P. K.; Upadhyay, S. N. Light Induced Green Synthesis of Silver Nanoparticles Using Aqueous Extract of <i>Prunus Amygdalus</i> *Green Sustain. Chem.* **2016**. https://doi.org/10.4236/gsc.2016.61003.

(421) Stellacci, F.; Bauer, C. A.; Meyer-Friedrichsen, T.; Wenseleers, W.; Alain, V.; Kuebler, S. M.; Pond, S. J. K.; Zhang, Y.; Marder, S. R.; Perry, J. W. Laser and Electron-Beam Induced Growth of Nanoparticles for 2D and 3D Metal Patterning. *Adv. Mater.* **2002**, *14* (3), 194–198. https://doi.org/10.1002/1521-4095(20020205)14:3<194::AID-ADMA194>3.0.CO;2-W.

(422) Mironava, T.; Hadjiargyrou, M.; Simon, M.; Rafailovich, M. H. The Effects of UV Emission from Compact Fluorescent Light Exposure on Human Dermal Fibroblasts and Keratinocytes in Vitro. *Photochem. Photobiol.* **2012**, *88* (6), 1497–1506. https://doi.org/10.1111/j.1751-1097.2012.01192.x.

(423) Khazova, M.; O'Hagan, J. B. Optical Radiation Emissions from Compact Fluorescent Lamps. *Radiat. Prot. Dosimetry* **2008**, *131* (4), 521–525. https://doi.org/10.1093/rpd/ncn234.

(424) Azizi, M.; Golmohammadi, R.; Aliabadi, M. Comparative Analysis of Lighting Characteristics and Ultraviolet Emissions from Commercial Compact Fluorescent and

Incandescent Lamps. *J. Res. Health Sci.* **2016**, *16* (4), 200–205. https://doi.org/10.34172/jrhs162489.

(425) Haridy, M. A.; Reda, S. M.; Mohmed, A. N. A. Illuminance and Ultra Violet Emissions Radiated from White Compact Fluorescent Lamps. *Int. J. Metrol. Qual. Eng.* **2016**, *7* (4). https://doi.org/10.1051/ijmqe/2016025.

(426) Sun, Y.; Mayers, B.; Herricks, T.; Xia, Y. Polyol Synthesis of Uniform Silver Nanowires: A Plausible Growth Mechanism and the Supporting Evidence. *Nano Lett.* **2003**, *3* (7), 955–960. https://doi.org/10.1021/nl034312m.

(427) Zhang, S. H.; Jiang, Z. Y.; Xie, Z. X.; Xu, X.; Huang, R. Bin; Zheng, L. S. Growth of Silver Nanowires from Solutions: A Cyclic Penta-Twinned-Crystal Growth Mechanism. *J. Phys. Chem. B* **2005**, *109* (19), 9416–9421. https://doi.org/10.1021/jp0441036.

(428) Da Silva, R. R.; Yang, M.; Choi, S. Il; Chi, M.; Luo, M.; Zhang, C.; Li, Z. Y.; Camargo, P. H. C.; Ribeiro, S. J. L.; Xia, Y. Facile Synthesis of Sub-20 Nm Silver Nanowires through a Bromide-Mediated Polyol Method. *ACS Nano* **2016**, *10* (8), 7892–7900. https://doi.org/10.1021/acsnano.6b03806.

(429) Luo, M.; Huang, H.; Choi, S. Il; Zhang, C.; Da Silva, R. R.; Peng, H. C.; Li, Z. Y.; Liu, J.; He, Z.; Xia, Y. Facile Synthesis of Ag Nanorods with No Plasmon Resonance Peak in the Visible Region by Using Pd Decahedra of 16 Nm in Size as Seeds. *ACS Nano* **2015**, *9* (10), 10523–10532. https://doi.org/10.1021/acsnano.5b05053.

(430) Xia, Y.; Xiong, Y.; Lim, B.; Skrabalak, S. E. Shape-Controlled Synthesis of Metal

Nanocrystals: Simple Chemistry Meets Complex Physics? *Angewandte Chemie - International Edition*. 2009, pp 60–103. https://doi.org/10.1002/anie.200802248.

(431) Wiley, B. J.; Wang, Z.; Wei, J.; Yin, Y.; Cobden, D. H.; Xia, Y. Synthesis and Electrical Characterization of Silver Nanobeams. *Nano Lett.* **2006**, *6* (10), 2273–2278. https://doi.org/10.1021/nl061705n.

(432) Zheng, Y.; Zeng, J.; Ruditskiy, A.; Liu, M.; Xia, Y. Oxidative Etching and Its Role in Manipulating the Nucleation and Growth of Noble-Metal Nanocrystals. *Chemistry of Materials*. 2014, pp 22–33. https://doi.org/10.1021/cm402023g.

(433) Gunckel, S.; Santander, P.; Cordano, G.; Ferreira, J.; Munoz, S.; Nunez-Vergara, L. J.; Squella, J. A. Antioxidant Activity of Gallates: An Electrochemical Study in Aqueous Media. *Chem. Biol. Interact.* **1998**, *114* (1–2). https://doi.org/10.1016/S0009-2797(98)00041-6.

(434) Marciniak, B.; Buono-Core, G. E. Photochemical Properties of 1,3-Diketonate Transition Metal Chelates. *Journal of Photochemistry and Photobiology, A: Chemistry*. 1990, pp 1–25. https://doi.org/10.1016/1010-6030(90)87085-P.

(435) Roberts, G. M.; Chatterley, A. S.; Young, J. D.; Stavros, V. G. Direct Observation of Hydrogen Tunneling Dynamics in Photoexcited Phenol. *J. Phys. Chem. Lett.* **2012**, *3* (3), 348–352. https://doi.org/10.1021/jz2016318.

(436) Iqbal, A.; Pegg, L. J.; Stavros, V. G. Direct versus Indirect H Atom Elimination from Photoexcited Phenol Molecules. *J. Phys. Chem. A* **2008**, *112* (39), 9531–9534.

https://doi.org/10.1021/jp802155b.

(437) Iqbal, A.; Cheung, M. S. Y.; Nix, M. G. D.; Stavros, V. G. Exploring the Time-Scales of H-Atom Detachment from Photoexcited Phenol-h6 and Phenol-d5: Statistical vs Nonstatistical Decay. *J. Phys. Chem. A* **2009**, *113* (29), 8157–8163. https://doi.org/10.1021/jp9031223.

(438) Tatarchuk, V. V.; Sergievskaya, A. P.; Korda, T. M.; Druzhinina, I. A.; Zaikovsky, V. I. Kinetic Factors in the Synthesis of Silver Nanoparticles by Reduction of Ag+ with Hydrazine in Reverse Micelles of Triton N-42. *Chem. Mater.* **2013**, *25* (18), 3570–3579. https://doi.org/10.1021/cm304115j.

(439) Yang, T. H.; Gilroy, K. D.; Xia, Y. Reduction Rate as a Quantitative Knob for Achieving Deterministic Synthesis of Colloidal Metal Nanocrystals. *Chemical Science*. 2017, pp 6730–6749. https://doi.org/10.1039/c7sc02833d.

(440) Wang, Y.; Peng, H. C.; Liu, J.; Huang, C. Z.; Xia, Y. Use of Reduction Rate as a Quantitative Knob for Controlling the Twin Structure and Shape of Palladium Nanocrystals. *Nano Lett.* **2015**, *15* (2), 1445–1450. https://doi.org/10.1021/acs.nanolett.5b00158.

(441) Zhou, M.; Wang, H.; Vara, M.; Hood, Z. D.; Luo, M.; Yang, T. H.; Bao, S.; Chi, M.; Xiao, P.; Zhang, Y.; et al. Quantitative Analysis of the Reduction Kinetics Responsible for the One-Pot Synthesis of Pd-Pt Bimetallic Nanocrystals with Different Structures. *J. Am. Chem. Soc.* **2016**, *138* (37), 12263–12270. https://doi.org/10.1021/jacs.6b07213.

(442) Pacławski, K.; Sak, T. Kinetics and Mechanism of the Reaction of gold(III) Chloride Complexes with Formic Acid. *J. Min. Metall. Sect. B Metall.* **2015**, *51* (2), 133–142. https://doi.org/10.2298/JMMB141024017P.

(443) Boruah, S. K. Green Synthesis Of Gold Nanoparticles Using Camellia Sinensis And Kinetics Of The Reaction. *Adv. Mater. Lett.* **2012**, *3* (6), 481–486. https://doi.org/10.5185/amlett.2012.icnano.103.

(444) Yang, T. H.; Peng, H. C.; Zhou, S.; Lee, C. T.; Bao, S.; Lee, Y. H.; Wu, J. M.; Xia, Y. Toward a Quantitative Understanding of the Reduction Pathways of a Salt Precursor in the Synthesis of Metal Nanocrystals. *Nano Lett.* **2017**, *17* (1), 334–340. https://doi.org/10.1021/acs.nanolett.6b04151.

(445) Harada, M.; Kizaki, S. Formation Mechanism of Gold Nanoparticles Synthesized by Photoreduction in Aqueous Ethanol Solutions of Polymers Using in Situ Quick Scanning X-Ray Absorption Fine Structure and Small-Angle X-Ray Scattering. *Cryst. Growth Des.* **2016**, *16* (3), 1200–1212. https://doi.org/10.1021/acs.cgd.5b01168.

(446) Watzky, M. A.; Finke, R. G. Transition Metal Nanocluster Formation Kinetic and Mechanistic Studies. A New Mechanism When Hydrogen Is the Reductant: Slow, Continuous Nucleation and Fast Autocatalytic Surface Growth. *J. Am. Chem. Soc.* **1997**, *119* (43), 10382–10400. https://doi.org/10.1021/ja9705102.

(447) Özkar, S.; Finke, R. G. Palladium(0) Nanoparticle Formation, Stabilization, and Mechanistic Studies: Pd(acac)2 as a Preferred Precursor, [Bu4N]2HPO4 Stabilizer, plus the Stoichiometry, Kinetics, and Minimal, Four-Step Mechanism of the Palladium

Nanoparticle Formation and Subsequ. *Langmuir* **2016**, *32* (15), 3699–3716. https://doi.org/10.1021/acs.langmuir.6b00013.

(448) Levenspiel, O. *Chemical Reaction Engineering O. Levenspiel*; 1999.

(449) Ma, J.; Zhan, M. Rapid Production of Silver Nanowires Based on High Concentration of AgNO3 Precursor and Use of FeCl3 as Reaction Promoter. *RSC Adv.* **2014**, *4* (40), 21060–21071. https://doi.org/10.1039/c4ra00711e.

(450) Qi, L.; Zhang, K.; Qin, W.; Hu, Y. Highly Efficient Flow-through Catalytic Reduction of Methylene Blue Using Silver Nanoparticles Functionalized Cotton. *Chem. Eng. J.* **2020**, *388*. https://doi.org/10.1016/j.cej.2020.124252.

(451) Wu, K.; Su, D.; Liu, J.; Saha, R.; Wang, J. P. Magnetic Nanoparticles in Nanomedicine: A Review of Recent Advances. *Nanotechnology* **2019**, *30* (50). https://doi.org/10.1088/1361-6528/ab4241.

(452) Wu, Y.; Ali, M. R. K.; Chen, K.; Fang, N.; El-Sayed, M. A. Gold Nanoparticles in Biological Optical Imaging. *Nano Today*. 2019, pp 120–140. https://doi.org/10.1016/j.nantod.2018.12.006.

(453) Chen, F.; Si, P.; De La Zerda, A.; Jokerst, J. V.; Myung, D. Gold Nanoparticles to Enhance Ophthalmic Imaging. *Biomaterials Science*. 2021, pp 367–390. https://doi.org/10.1039/d0bm01063d.

(454) Kumar, S.; Shukla, A.; Baul, P. P.; Mitra, A.; Halder, D. Biodegradable Hybrid

Nanocomposites of Chitosan/gelatin and Silver Nanoparticles for Active Food Packaging Applications. *Food Packag. Shelf Life* **2018**, *16*, 178–184. https://doi.org/10.1016/j.fpsl.2018.03.008.

(455) Yadav, S.; Mehrotra, G. K.; Dutta, P. K. Chitosan Based ZnO Nanoparticles Loaded Gallic-Acid Films for Active Food Packaging. *Food Chem.* **2021**, *334*. https://doi.org/10.1016/j.foodchem.2020.127605.

(456) Prosposito, P.; Burratti, L.; Venditti, I. Silver Nanoparticles as Colorimetric Sensors for Water Pollutants. *Chemosensors*. 2020. https://doi.org/10.3390/CHEMOSENSORS8020026.

(457) Zhu, X.; Wang, X.; Han, L.; Chen, T.; Wang, L.; Li, H.; Li, S.; He, L.; Fu, X.; Chen, S.; et al. Reverse Transcription Loop-Mediated Isothermal Amplification Combined with Nanoparticles-Based Biosensor for Diagnosis of COVID-19. *medRxiv* **2020**. https://doi.org/10.1101/2020.03.17.20037796.

(458) Nakamoto, M. Microelectronics Packaging by Metal Nanoparticle Pastes. In *Nanoparticle Technology Handbook*; 2018; pp 647–650. https://doi.org/10.1016/B978-0-444-64110-6.00053-6.

(459) Yang, Z.; Wang, W.; Bi, L.; Chen, L.; Wang, G.; Chen, G.; Ye, C.; Pan, J. Wearable Electronics for Heating and Sensing Based on a Multifunctional PET/silver nanowire/PDMS Yarn. *Nanoscale* **2020**, *12* (31), 16562–16569. https://doi.org/10.1039/d0nr04023a.

(460) Li, X.; Wang, Y.; Yin, C.; Yin, Z. Copper Nanowires in Recent Electronic Applications: Progress and Perspectives. *Journal of Materials Chemistry C*. 2020, pp 849–872. https://doi.org/10.1039/c9tc04744a.

(461) An, T.; Anaya, D. V.; Gong, S.; Yap, L. W.; Lin, F.; Wang, R.; Yuce, M. R.; Cheng, W. Self-Powered Gold Nanowire Tattoo Triboelectric Sensors for Soft Wearable Human-Machine Interface. *Nano Energy* **2020**, *77*. https://doi.org/10.1016/j.nanoen.2020.105295.

(462) Zhang, L.; Xia, Y. Scaling up the Production of Colloidal Nanocrystals: Should We Increase or Decrease the Reaction Volume? *Adv. Mater.* **2014**, *26* (16), 2600–2606. https://doi.org/10.1002/adma.201304897.

(463) Roberts, E. J.; Karadaghi, L. R.; Wang, L.; Malmstadt, N.; Brutchey, R. L. Continuous Flow Methods of Fabricating Catalytically Active Metal Nanoparticles. *ACS Appl. Mater. Interfaces* **2019**, *11* (31), 27479–27502. https://doi.org/10.1021/acsami.9b07268.

(464) Pussepitiyalage, V. B.; Hemmati, S. Sustainable, Green, and Continuous Synthesis of Fivefold Palladium Nanorods Using L-Ascorbic Acid in a Segmented Millifluidic Flow Reactor. *Langmuir* **2022**, *38* (14), 4200–4212. https://doi.org/https://doi.org/10.1021/acs.langmuir.1c03133.

(465) Hartman, R. L.; McMullen, J. P.; Jensen, K. F. Deciding Whether to Go with the Flow: Evaluating the Merits of Flow Reactors for Synthesis. *Angewandte Chemie - International Edition*. 2011. https://doi.org/10.1002/anie.201004637.

(466) Ottino, J. M.; Wiggins, S. Introduction: Mixing in Microfluidics. *Philosophical*

Transactions of the Royal Society A: Mathematical, Physical and Engineering Sciences. 2004. https://doi.org/10.1098/rsta.2003.1355.

(467) R. Byron Bird Warren E. Stewart Edwin N. Lightfoo; Bird, R. B.; Stewart, W. E.; Lightfoot, E. N. Transport Phenomena, Revised 2nd Edition. *John Wiley Sons, Inc.* **2006**.

(468) Luty-Błocho, M.; Fitzner, K.; Hessel, V.; Löb, P.; Maskos, M.; Metzke, D.; Pacławski, K.; Wojnicki, M. Synthesis of Gold Nanoparticles in an Interdigital Micromixer Using Ascorbic Acid and Sodium Borohydride as Reducers. *Chem. Eng. J.* **2011**, *171* (1), 279–290. https://doi.org/10.1016/j.cej.2011.03.104.

(469) Köhler, J. M.; Abahmane, L.; Wagner, J.; Albert, J.; Mayer, G. Preparation of Metal Nanoparticles with Varied Composition for Catalytical Applications in Microreactors. *Chem. Eng. Sci.* **2008**, *63* (20), 5048–5055. https://doi.org/10.1016/j.ces.2007.11.038.

(470) Wagner, J.; Köhler, J. M. Continuous Synthesis of Gold Nanoparticles in a Microreactor. *Nano Lett.* **2005**, *5* (4), 685–691. https://doi.org/10.1021/nl050097t.

(471) Hemmati, S.; Barkey, D. P.; Eggleston, L.; Zukas, B.; Gupta, N.; Harris, M. Silver Nanowire Synthesis in a Continuous Millifluidic Reactor. *ECS J. Solid State Sci. Technol.* **2017**, *6* (4), 144–149. https://doi.org/10.1149/2.0171704jss.

(472) V Kinhal, K.; Bhatt, N.; Subramaniam, P. Transport and Kinetic Effects on the Morphology of Silver Nanoparticles in a Millifluidic System. *Ind. Eng. Chem. Res.* **2019**, *58* (15), 5820–5829. https://doi.org/10.1021/acs.iecr.8b04156.

(473) Li, Y.; Sanampudi, A.; Raji Reddy, V.; Biswas, S.; Nandakumar, K.; Yemane, D.; Goettert, J.; Kumar, C. S. S. R. Size Evolution of Gold Nanoparticles in a Millifluidic Reactor. *ChemPhysChem* **2012**. https://doi.org/10.1002/cphc.201100726.

(474) Biswas, S.; Miller, J. T.; Li, Y.; Nandakumar, K.; Kumar, C. S. S. R. Developing a Millifluidic Platform for the Synthesis of Ultrasmall Nanoclusters: Ultrasmall Copper Nanoclusters as a Case Study. *Small* **2012**, *8* (5), 688–698. https://doi.org/10.1002/smll.201102100.

(475) Ravi Kumar, D. V.; Prasad, B. L. V.; Kulkarni, A. A. Segmented Flow Synthesis of Ag Nanoparticles in Spiral Microreactor: Role of Continuous and Dispersed Phase. *Chem. Eng. J.* **2012**, *192*, 357–368. https://doi.org/10.1016/j.cej.2012.02.084.

(476) Li, W.; Zhang, H.; Shi, S.; Xu, J.; Qin, X.; He, Q.; Yang, K.; Dai, W.; Liu, G.; Zhou, Q.; et al. Recent Progress in Silver Nanowire Networks for Flexible Organic Electronics. *J. Mater. Chem. C* **2020**, *8* (14), 4636–4674. https://doi.org/10.1039/c9tc06865a.

(477) Lee, S.; Jang, J.; Park, T.; Park, Y. M.; Park, J. S.; Kim, Y. K.; Lee, H. K.; Jeon, E. C.; Lee, D. K.; Ahn, B.; et al. Electrodeposited Silver Nanowire Transparent Conducting Electrodes for Thin-Film Solar Cells. *ACS Appl. Mater. Interfaces* **2020**, *12* (5), 6169–6175. https://doi.org/10.1021/acsami.9b17168.

(478) Gonzalez-Garcia, L.; Maurer, J. H. M.; Reiser, B.; Kanelidis, I.; Kraus, T. Ultrathin Gold Nanowires for Transparent Electronics: Breaking Barriers. *Procedia Eng.* **2016**, *141*, 152–156. https://doi.org/10.1016/j.proeng.2015.08.1120.

(479) Yang, X.; Du, D.; Wang, Y.; Zhao, Y. Silver Nanowires Inks for Flexible Circuit on Photographic Paper Substrate. *Micromachines* **2018**, *10* (1), 22. https://doi.org/10.3390/mi10010022.

(480) Yang, L.; Xu, X.; Yuan, Y.; Li, Z.; He, S. Meter-Scale Transparent Conductive Circuits Based on Silver Nanowire Networks for Rigid and Flexible Transparent Light-Emitting Diode Screens. *Opt. Mater. Express* **2019**, *9* (12), 4483–4496. https://doi.org/10.1364/ome.9.004483.

(481) Marus, M.; Hubarevich, A.; Lim, R. J. W.; Huang, H.; Smirnov, A.; Wang, H.; Fan, W.; Sun, X. W. Effect of Silver Nanowire Length in a Broad Range on Optical and Electrical Properties as a Transparent Conductive Film. *Opt. Mater. Express* **2017**, *7* (3), 1105–1112. https://doi.org/10.1364/ome.7.001105.

(482) Nekahi, A.; Marashi, S. P. H.; Fatmesari, D. H. High Yield Polyol Synthesis of Round- and Sharp-End Silver Nanowires with High Aspect Ratio. *Mater. Chem. Phys.* **2016**. https://doi.org/10.1016/j.matchemphys.2016.09.033.

(483) Gottesman, R.; Tangy, A.; Oussadon, I.; Zitoun, D. Silver Nanowires and Nanoparticles from a Millifluidic Reactor: Application to Metal Assisted Silicon Etching. *New J. Chem.* **2012**, *36* (12), 2456–2459. https://doi.org/10.1039/c2nj40763a.

(484) Zhang, L.; Wang, Y.; Tong, L.; Xia, Y. Synthesis of Colloidal Metal Nanocrystals in Droplet Reactors: The Pros and Cons of Interfacial Adsorption. *Nano Lett.* **2014**, *14* (7), 4189–4194. https://doi.org/10.1021/nl501994q.

(485) Kaabipour, S.; Hemmati, S. Green, Sustainable, and Room-Temperature Synthesis of Silver Nanowires Using Tannic Acid – Kinetic and Parametric Study. *Colloids Surfaces A Physicochem. Eng. Asp.* **2022**, *641*, 128495. https://doi.org/https://doi.org/10.1016/j.colsurfa.2022.128495.

(486) Niu, G.; Ruditskiy, A.; Vara, M.; Xia, Y. Toward Continuous and Scalable Production of Colloidal Nanocrystals by Switching from Batch to Droplet Reactors. *Chem. Soc. Rev.* **2015**, *44* (16), 5806–5820. https://doi.org/10.1039/c5cs00049a.

(487) Elvira, K. S.; I Solvas, X. C.; Wootton, R. C. R.; Demello, A. J. The Past, Present and Potential for Microfluidic Reactor Technology in Chemical Synthesis. *Nature Chemistry*. 2013, pp 905–915. https://doi.org/10.1038/nchem.1753.

(488) Friedman, A.; Perkas, N.; Koltypin, Y.; Gedanken, A. Depositing Nanoparticles inside Millimeter-Size Hollow Tubing. *Appl. Surf. Sci.* **2012**, *258* (7), 2368–2372. https://doi.org/10.1016/j.apsusc.2011.10.033.

(489) Ponticorvo, E.; Iuliano, M.; Cirillo, C.; Maiorino, A.; Aprea, C.; Sarno, M. Fouling Behavior and Dispersion Stability of Nanoparticle-Based Refrigeration Fluid. *Energies* **2022**, *15* (9), 3059.

(490) Reitzer, F.; Allais, M.; Ball, V.; Meyer, F. Polyphenols at Interfaces. *Advances in Colloid and Interface Science*. 2018. https://doi.org/10.1016/j.cis.2018.06.001.

(491) Kim, S.; Gim, T.; Kang, S. M. Versatile, Tannic Acid-Mediated Surface PEGylation for Marine Antifouling Applications. *ACS Appl. Mater. Interfaces* **2015**.

https://doi.org/10.1021/acsami.5b01304.

(492) Vernhet, A.; Moutounet, M. Fouling of Organic Microfiltration Membranes by Wine Constituents: Mportance, Relative Impact of Wine Polysccharides and Polyphenols and Incidence of Membrane Properties. *J. Memb. Sci.* **2002**. https://doi.org/10.1016/S0376-7388(01)00723-2.

(493) Chu, K. H.; Huang, Y.; Yu, M.; Her, N.; Flora, J. R. V.; Park, C. M.; Kim, S.; Cho, J.; Yoon, Y. Evaluation of Humic Acid and Tannic Acid Fouling in Graphene Oxide-Coated Ultrafiltration Membranes. *ACS Appl. Mater. Interfaces* **2016**. https://doi.org/10.1021/acsami.6b08020.

(494) Niu, G.; Zhang, L.; Ruditskiy, A.; Wang, L.; Xia, Y. A Droplet-Reactor System Capable of Automation for the Continuous and Scalable Production of Noble-Metal Nanocrystals. *Nano Lett.* **2018**, *18* (6), 3879–3884. https://doi.org/10.1021/acs.nanolett.8b01200.

(495) Lin, Y.; Skaff, H.; Emrick, T.; Dinsmore, A. D.; Russell, T. P. Nanoparticle Assembly and Transport at Liquid-Liquid Interfaces. *Science (80-.).* **2003**, *299* (5604), 226–229. https://doi.org/10.1126/science.1078616.

(496) Liu, Y.; Liu, Z.; Zeng, G.; Chen, M.; Jiang, Y.; Shao, B.; Li, Z.; Liu, Y. Effect of Surfactants on the Interaction of Phenol with Laccase: Molecular Docking and Molecular Dynamics Simulation Studies. *J. Hazard. Mater.* **2018**, *357*, 10–18. https://doi.org/10.1016/j.jhazmat.2018.05.042.

(497) Li, X.; Zheng, Y. Lignin-Enzyme Interaction: Mechanism, Mitigation Approach,

Modeling, and Research Prospects. *Biotechnology Advances*. 2017, pp 466–489. https://doi.org/10.1016/j.biotechadv.2017.03.010.

(498) Olsen, S. N.; Bohlin, C.; Murphy, L.; Borch, K.; McFarland, K. C.; Sweeny, M. D.; Westh, P. Effects of Non-Ionic Surfactants on the Interactions between Cellulases and Tannic Acid: A Model System for Cellulase-Poly-Phenol Interactions. *Enzyme Microb. Technol.* **2011**, *49* (4), 353–359. https://doi.org/10.1016/j.enzmictec.2011.06.015.

(499) Kurt, S. K.; Akhtar, M.; Nigam, K. D. P.; Kockmann, N. Continuous Reactive Precipitation in a Coiled Flow Inverter: Inert Particle Tracking, Modular Design, and Production of Uniform CaCO3 Particles. *Ind. Eng. Chem. Res.* **2017**, *56* (39), 11320–11335. https://doi.org/10.1021/acs.iecr.7b02240.

(500) Kurt, S. K.; Gelhausen, M. G.; Kockmann, N. Axial Dispersion and Heat Transfer in a Milli/Microstructured Coiled Flow Inverter for Narrow Residence Time Distribution at Laminar Flow. *Chem. Eng. Technol.* **2015**, *38* (7), 1122–1130. https://doi.org/10.1002/ceat.201400515.

(501) Klutz, S.; Kurt, S. K.; Lobedann, M.; Kockmann, N. Narrow Residence Time Distribution in Tubular Reactor Concept for Reynolds Number Range of 10-100. *Chem. Eng. Res. Des.* **2015**, *95*, 22–33. https://doi.org/10.1016/j.cherd.2015.01.003.

(502) Rossi, D.; Gargiulo, L.; Valitov, G.; Gavriilidis, A.; Mazzei, L. Experimental Characterization of Axial Dispersion in Coiled Flow Inverters. *Chem. Eng. Res. Des.* **2017**, *120*, 159–170. https://doi.org/10.1016/j.cherd.2017.02.011.

(503) Richard, C.; McGee, R.; Goenka, A.; Mukherjee, P.; Bhargava, R. On-Demand Milifluidic Synthesis of Quantum Dots in Digital Droplet Reactors. *Ind. Eng. Chem. Res.* **2020**. https://doi.org/10.1021/acs.iecr.9b04230.

(504) Gelber, M. K.; Kole, M. R.; Kim, N.; Aluru, N. R.; Bhargava, R. Quantitative Chemical Imaging of Nonplanar Microfluidics. *Anal. Chem.* **2017**. https://doi.org/10.1021/acs.analchem.6b03943.

(505) Song, H.; Tice, J. D.; Ismagilov, R. F. A Microfluidic System for Controlling Reaction Networks in Time. *Angew. Chemie - Int. Ed.* **2003**. https://doi.org/10.1002/anie.200390203.

(506) Dean, W. R. XVI. Note on the Motion of Fluid in a Curved Pipe . *London, Edinburgh, Dublin Philos. Mag. J. Sci.* **1927**. https://doi.org/10.1080/14786440708564324.

(507) Dean, W. R. LXXII. The Stream-Line Motion of Fluid in a Curved Pipe (Second Paper) . *London, Edinburgh, Dublin Philos. Mag. J. Sci.* **1928**. https://doi.org/10.1080/14786440408564513.

(508) Kumar, V.; Aggarwal, M.; Nigam, K. D. P. Mixing in Curved Tubes. *Chem. Eng. Sci.* **2006**. https://doi.org/10.1016/j.ces.2006.04.040.

(509) Mansour, M.; Khot, P.; Thévenin, D.; Nigam, K. D. P.; Zähringer, K. Optimal Reynolds Number for Liquid-Liquid Mixing in Helical Pipes. *Chem. Eng. Sci.* **2020**, *214*. https://doi.org/10.1016/j.ces.2018.09.046.

(510) Mansour, M.; Thévenin, D.; Zähringer, K. Numerical Study of Flow Mixing and Heat Transfer in Helical Pipes, Coiled Flow Inverters and a Novel Coiled Configuration. *Chem. Eng. Sci.* **2020**, *221*. https://doi.org/10.1016/j.ces.2020.115690.

(511) Kováts, P.; Velten, C.; Mansour, M.; Thévenin, D.; Zähringer, K. Mixing Characterization in Different Helically Coiled Configurations by Laser-Induced Fluorescence. *Exp. Fluids* **2020**, *61* (9). https://doi.org/10.1007/s00348-020-03035-0.

(512) Mansour, M.; Liu, Z.; Janiga, G.; Nigam, K. D. P.; Sundmacher, K.; Thévenin, D.; Zähringer, K. Numerical Study of Liquid-Liquid Mixing in Helical Pipes. *Chem. Eng. Sci.* **2017**, *172*, 250–261. https://doi.org/10.1016/j.ces.2017.06.015.

(513) Hohmann, L.; Schmalenberg, M.; Prasanna, M.; Matuschek, M.; Kockmann, N. Suspension Flow Behavior and Particle Residence Time Distribution in Helical Tube Devices. *Chem. Eng. J.* **2019**, *360*, 1371–1389. https://doi.org/10.1016/j.cej.2018.10.166.

(514) Hasan, M. M.; Hossain, M. M. Nanomaterials-Patterned Flexible Electrodes for Wearable Health Monitoring: A Review. *Journal of Materials Science*. 2021, pp 14900–14942. https://doi.org/10.1007/s10853-021-06248-8.

(515) Manjakkal, L.; Núñez, C. G.; Dang, W.; Dahiya, R. Flexible Self-Charging Supercapacitor Based on Graphene-Ag-3D Graphene Foam Electrodes. *Nano Energy* **2018**, *51*, 604–612. https://doi.org/10.1016/j.nanoen.2018.06.072.

(516) Lin, C. H.; Fu, H. C.; Cheng, B.; Tsai, M. L.; Luo, W.; Zhou, L.; Jang, S. H.; Hu, L.; He, J. H. A Flexible Solar-Blind 2D Boron Nitride Nanopaper-Based Photodetector with High

Thermal Resistance. *npj 2D Mater. Appl.* **2018**, *2* (1). https://doi.org/10.1038/s41699-018-0070-6.

(517) Tseberlidis, G.; Trifiletti, V.; Le Donne, A.; Frioni, L.; Acciarri, M.; Binetti, S. Kesterite Solar-Cells by Drop-Casting of Inorganic Sol–gel Inks. *Sol. Energy* **2020**, *208*, 532–538. https://doi.org/10.1016/j.solener.2020.07.093.

(518) Yang, L.; Xu, X.; Yuan, Y.; Li, Z.; He, S. Meter-Scale Transparent Conductive Circuits Based on Silver Nanowire Networks for Rigid and Flexible Transparent Light-Emitting Diode Screens. *Opt. Mater. Express* **2019**, *9* (12), 4483–4496. https://doi.org/10.1364/OME.9.004483.

(519) Zeng, P.; Tian, B.; Tian, Q.; Yao, W.; Li, M.; Wang, H.; Feng, Y.; Liu, L.; Wu, W. Screen-Printed, Low-Cost, and Patterned Flexible Heater Based on Ag Fractal Dendrites for Human Wearable Application. *Adv. Mater. Technol.* **2019**, *4* (3). https://doi.org/10.1002/admt.201800453.

(520) Faddoul, R.; Reverdy-Bruas, N.; Blayo, A. Formulation and Screen Printing of Water Based Conductive Flake Silver Pastes onto Green Ceramic Tapes for Electronic Applications. *Mater. Sci. Eng. B Solid-State Mater. Adv. Technol.* **2012**, *177* (13), 1053–1066. https://doi.org/10.1016/j.mseb.2012.05.015.

(521) Ke, S. H.; Xue, Q. W.; Pang, C. Y.; Guo, P. W.; Yao, W. J.; Zhu, H. P.; Wu, W. Printing the Ultra-Long Ag Nanowires Inks onto the Flexible Textile Substrate for Stretchable Electronics. *Nanomaterials*. 2019. https://doi.org/10.3390/infrastructures4020020.

(522) Li, W.; Yang, S.; Shamim, A. Screen Printing of Silver Nanowires: Balancing Conductivity with Transparency While Maintaining Flexibility and Stretchability. *npj Flex. Electron.* **2019**, *3* (1). https://doi.org/10.1038/s41528-019-0057-1.

(523) He, X.; Shen, G.; Xu, R.; Yang, W.; Zhang, C.; Liu, Z.; Chen, B.; Liu, J.; Song, M. Hexagonal and Square Patterned Silver nanowires/PEDOT:PSS Composite Grids by Screen Printing for Uniformly Transparent Heaters. *Polymers (Basel).* **2019**, *11* (3). https://doi.org/10.3390/polym11030468.

(524) Liang, J.; Tong, K.; Pei, Q. A Water-Based Silver-Nanowire Screen-Print Ink for the Fabrication of Stretchable Conductors and Wearable Thin-Film Transistors. *Adv. Mater.* **2016**. https://doi.org/10.1002/adma.201600772.

(525) Patil, P.; Patil, S.; Kate, P.; Kulkarni, A. A. Inkjet Printing of Silver Nanowires on Flexible Surfaces and Methodologies to Improve the Conductivity and Stability of the Printed Patterns. *Nanoscale Adv.* **2021**, *3* (1), 240–248. https://doi.org/10.1039/d0na00684j.

(526) Huang, Q.; Al-Milaji, K. N.; Zhao, H. Inkjet Printing of Silver Nanowires for Stretchable Heaters. *ACS Appl. Nano Mater.* **2018**, *1* (9), 4528–4536. https://doi.org/10.1021/acsanm.8b00830.

(527) Lee, H. H.; Chou, K. Sen; Huang, K. C. Inkjet Printing of Nanosized Silver Colloids. *Nanotechnology* **2005**, *16* (10), 2436–2441. https://doi.org/10.1088/0957-4484/16/10/074.

(528) Liu, Z.; Su, Y.; Varahramyan, K. Inkjet-Printed Silver Conductors Using Silver Nitrate

Ink and Their Electrical Contacts with Conducting Polymers. *Thin Solid Films* **2005**, *478* (1–2), 275–279. https://doi.org/10.1016/j.tsf.2004.11.077.

(529) Finn, D. J.; Lotya, M.; Coleman, J. N. Inkjet Printing of Silver Nanowire Networks. *ACS Appl. Mater. Interfaces* **2015**, *7* (17), 9254–9261. https://doi.org/10.1021/acsami.5b01875.

(530) Kuzmenko, V.; Karabulut, E.; Pernevik, E.; Enoksson, P.; Gatenholm, P. Tailor-Made Conductive Inks from Cellulose Nanofibrils for 3D Printing of Neural Guidelines. *Carbohydr. Polym.* **2018**, *189*, 22–30. https://doi.org/10.1016/j.carbpol.2018.01.097.

(531) Barnes, H. A. Thixotropy - A Review. *Journal of Non-Newtonian Fluid Mechanics*. 1997. https://doi.org/10.1016/S0377-0257(97)00004-9.

(532) Mallik, S. Study of the Time-Dependent Rheological Behaviour of Lead-Free Solder Pastes and Flux Mediums Used for Flip-Chip Assembly Applications Study of the Time-Dependent Rheological Behaviour of Lead-Free Solder Pastes and Flux Mediums Used for Flip-Chip Assembl, University of Greenwich, 2009.

(533) Rudež, R.; Pavlič, J.; Bernik, S. Preparation and Influence of Highly Concentrated Screen-Printing Inks on the Development and Characteristics of Thick-Film Varistors. *J. Eur. Ceram. Soc.* **2015**. https://doi.org/10.1016/j.jeurceramsoc.2015.04.035.

(534) Smay, J. E.; Gratson, G. M.; Shepherd, R. F.; Cesarano, J.; Lewis, J. A. Directed Colloidal Assembly of 3D Periodic Structures. *Adv. Mater.* **2002**. https://doi.org/10.1002/1521-4095(20020916)14:18<1279::AID-ADMA1279>3.0.CO;2-A.

(535) Nair, N. M.; Daniel, K.; Vadali, S. C.; Ray, D.; Swaminathan, P. Direct Writing of Silver Nanowire-Based Ink for Flexible Transparent Capacitive Touch Pad. *Flex. Print. Electron.* **2019**, *4* (4). https://doi.org/10.1088/2058-8585/ab4b04.

(536) Martin, G. D.; Hoath, S. D.; Hutchings, I. M. Inkjet Printing - The Physics of Manipulating Liquid Jets and Drops. *J. Phys. Conf. Ser.* **2008**, *105* (1). https://doi.org/10.1088/1742-6596/105/1/012001.

(537) Yan, P.; Brown, E.; Su, Q.; Li, J.; Wang, J.; Xu, C.; Zhou, C.; Lin, D. 3D Printing Hierarchical Silver Nanowire Aerogel with Highly Compressive Resilience and Tensile Elongation through Tunable Poisson's Ratio. *Small* **2017**. https://doi.org/10.1002/smll.201701756.

(538) Compton, B. G.; Lewis, J. A. 3D-Printing of Lightweight Cellular Composites. *Adv. Mater.* **2014**. https://doi.org/10.1002/adma.201401804.

(539) Hong, H.; Jiyong, H.; Moon, K. S.; Yan, X.; Wong, C. ping. Rheological Properties and Screen Printability of UV Curable Conductive Ink for Flexible and Washable E-Textiles. *J. Mater. Sci. Technol.* **2021**, *67*, 145–155. https://doi.org/10.1016/j.jmst.2020.06.033.

(540) Dzisah, P.; Ravindra, N. M. Modeling of Rheological Properties of Metal Nanoparticle Conductive Inks for Printed Electronics. In *Minerals, Metals and Materials Series*; 2021; Vol. 5, pp 964–979. https://doi.org/10.1007/978-3-030-65261-6_86.

(541) Yoon, I. S.; Oh, Y.; Kim, S. H.; Choi, J.; Hwang, Y.; Park, C. H.; Ju, B. K. 3D Printing of Self-Wiring Conductive Ink with High Stretchability and Stackability for Customized

Wearable Devices. *Adv. Mater. Technol.* **2019**, *4* (9). https://doi.org/10.1002/admt.201900363.

(542) Hatala, M.; Gemeiner, P.; Hvojnik, M.; Mikula, M. The Effect of the Ink Composition on the Performance of Carbon-Based Conductive Screen Printing Inks. *J. Mater. Sci. Mater. Electron.* **2019**, *30* (2), 1034–1044. https://doi.org/10.1007/s10854-018-0372-7.

(543) No Title. *Center for Industrial Rheology, Hampshire, U.K.* https://www.rheologylab.com/articles/viscosity-testing-for-process-design/

APPENDICES

Supplementary information

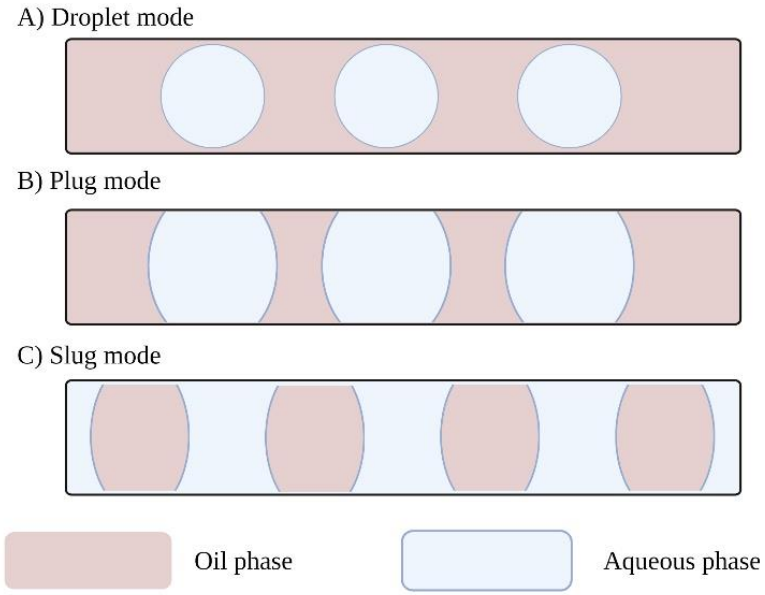

Figure A.1: Different modes of flow in two-phase continuous flows.
Created with BioRender.com.

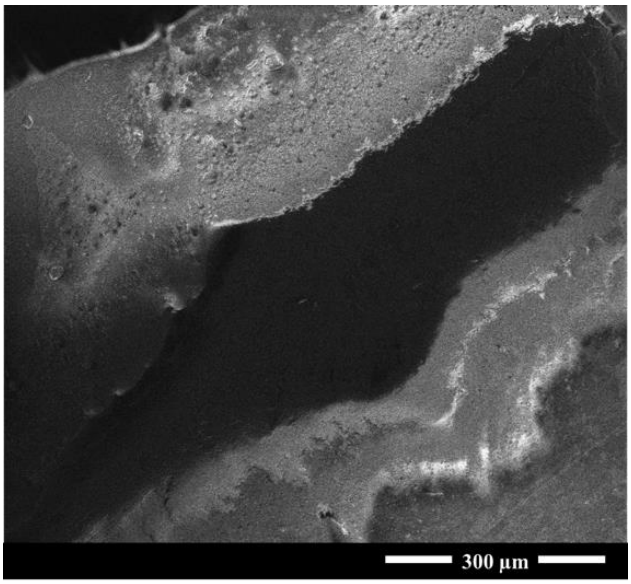

Figure A.2: SEM image of the surface of a dissected part of the PTFE tubing in the case of air as the secondary phase.

Figure A.3: The elemental map collected by EDX analysis of the same sample in figure A.2 in which air was used as the secondary phase.

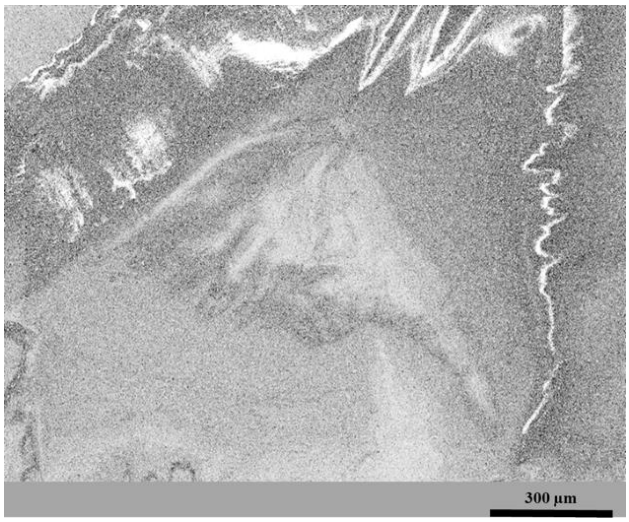

Figure A.4: The SEM image of the surface of a dissected part of the PTFE tubing in the case of silicone oil as the secondary phase

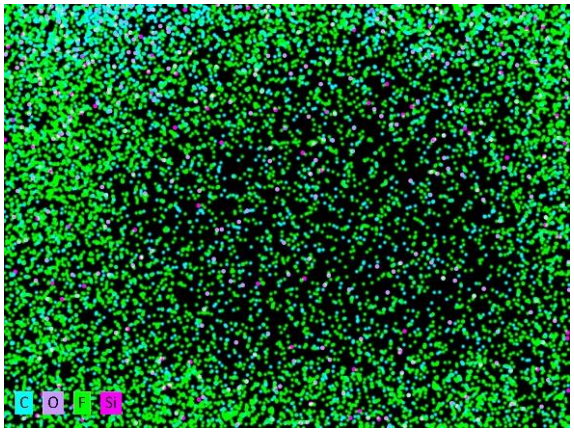

Figure A.5: The elemental map collected by EDX analysis of the same sample in figure A.4 in which silicone oil was used as the secondary phase

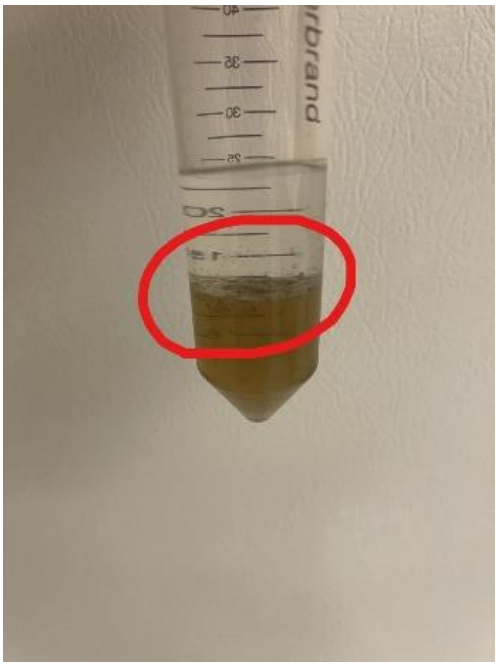

Figure A.6: Adsorption of nanostructures to the water-oil interface in the absence of triton X-100.

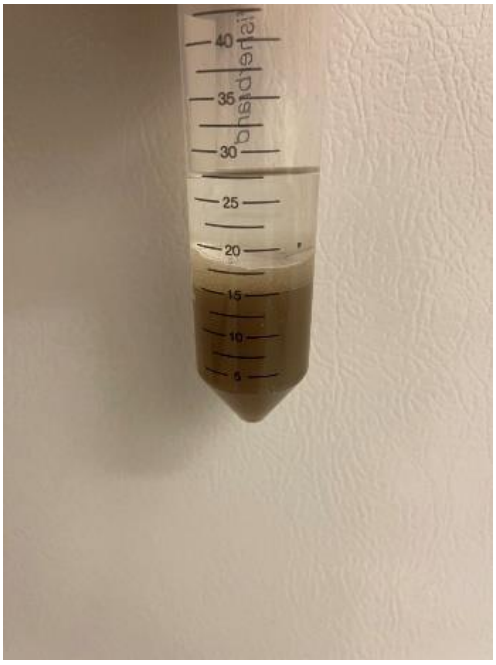

Figure A.7: Prevention of the adsorption of nanostructures to the water-oil interface in the presence of triton X-100.

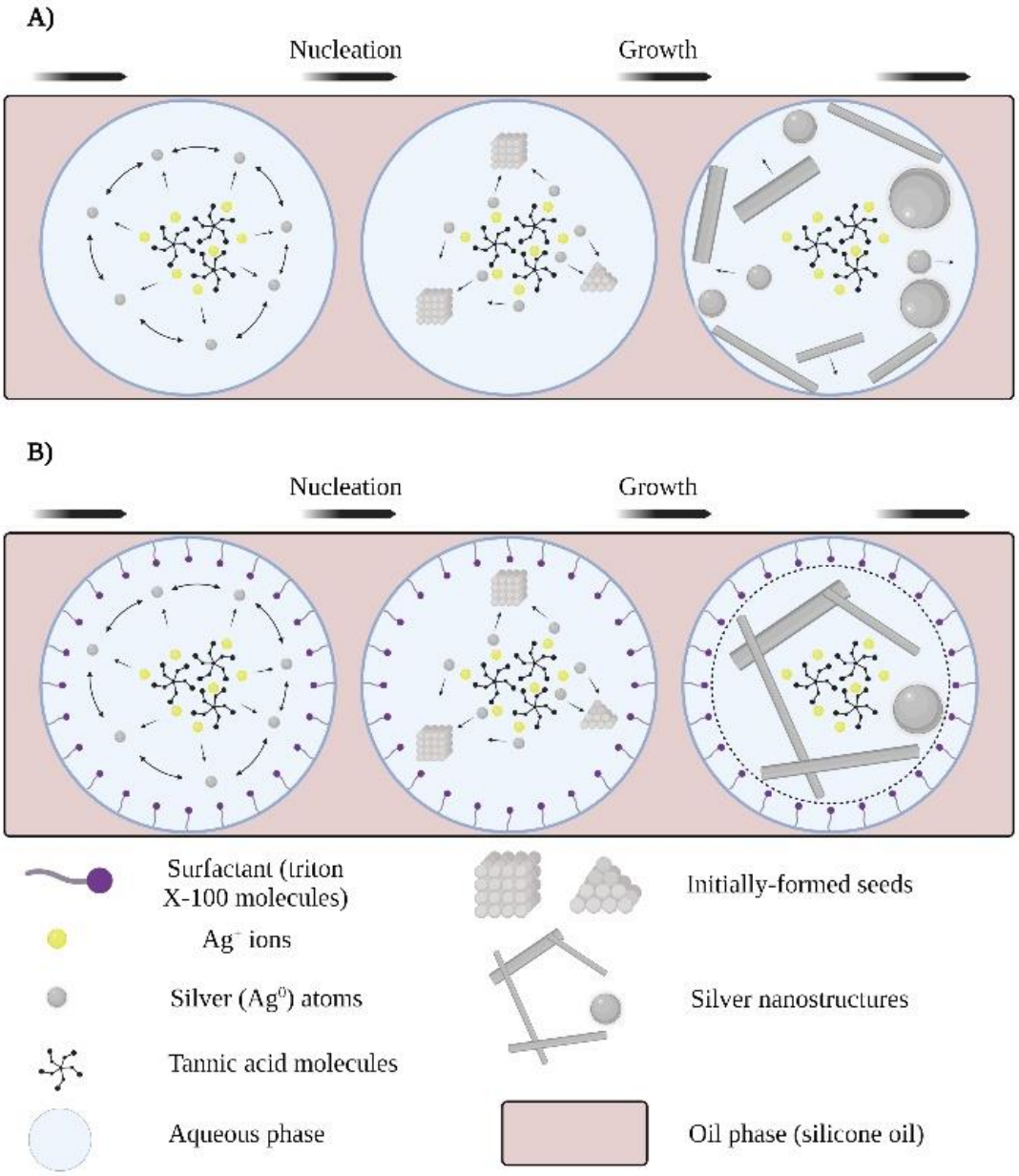

Figure A.8: A schematic of the synthesis of silver nanostructures through the millifluidic reactor in the absence and presence of triton X-100. Created with BioRender.com.

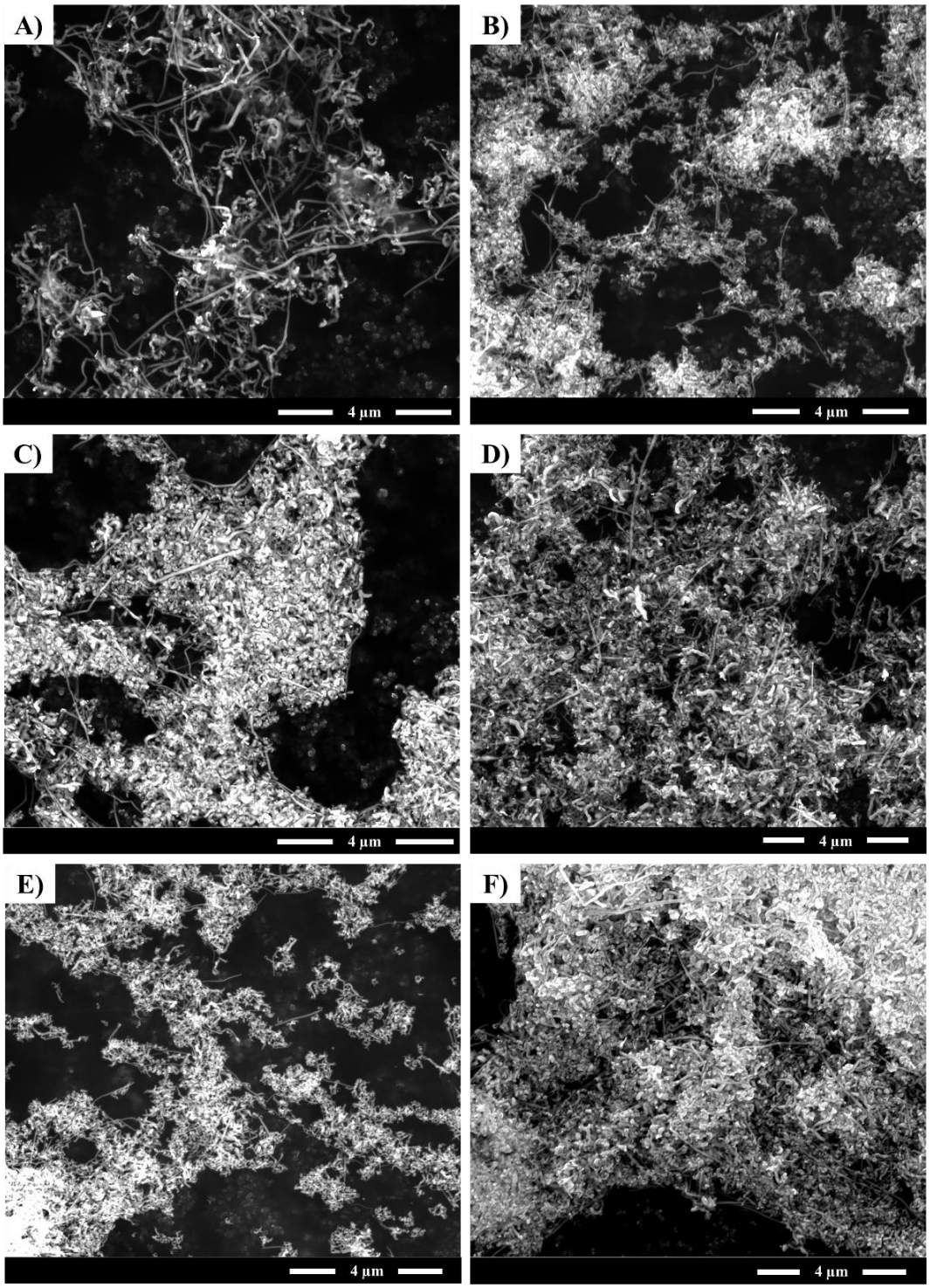

Figure A.9: SEM images of silver nanostructures synthesized at different illumination or different exposure residence times (ERTs): A) 0 min, B) 11.9 min, C) 23.8 min, D) 35.7 min, E) 47.6 min, and F) 96 min.

Table A.1: Parameters of the peak separation model determined by curve fitting.

Model	Lorentz		
Equation	$y = y_0 + \left(\frac{2A}{\pi}\right)\frac{w}{(4(x-x_c)^2 + w^2)}$		
Plot	Peak1(Absorbance)	Peak2(Absorbance)	Peak3(Absorbance)
y_0	0.47978 ± 2.08107×10^{-4}	0.47978 ± 2.08107×10^{-4}	0.47978 ± 2.08107×10^{-4}
x_c	450.6996 ± 0.46001	392.01906 ± 0.20819	325.05167 ± 0.08803
w	241.16194 ± 0.74797	59.0227 ± 1.93455	20.17493 ± 0.16227
A	77.01164 ± 0.49776	2.7732 ± 0.17695	-5.66678 ± 0.06755
Reduced Chi-Sqr	3.14×10^{-6}		
R-Square (COD)	0.99935		
Adj. R-Square	0.99935		

VITA

Sina Kaabipour

Candidate for the Degree of Chemical Engineering

Doctor of Philosophy

Dissertation: GREEN AND SUSTAINABLE SYNTHESIS OF SILVER NANOWIRES USING BATCH AND MILLIFLUIDIC PROCESSES AND THEIR APPLICATIONS IN CONDUCTIVE INKS

Major Field: Chemical Engineering

Biographical:

Completed the requirements for the Doctor of Philosophy in Chemical Engineering at Oklahoma State University, Stillwater, Oklahoma in May 2023.

Completed the requirements for the Master of Science in Chemical Engineering at Lamar University, Beaumont, Texas in Dec 2018.

Completed the requirements for the Bachelor of Science in Chemical Engineering at Shiraz University, Shiraz, Iran in Sep 2015.

Experience:

Graduate Research Assistant/Associate, from Jan 2019 to May 2023

Graduate Teaching Associate, from Jan 2021 to May 2023

Professional Memberships:

Chemical Engineering Graduate Student Association at Oklahoma State University